Modeling of Mass Timber Components Subjected to Blast Loads

by

Damian Oliveira

A thesis submitted in partial fulfillment of the requirements for the degree of

Master of Applied Science

in Civil Engineering

Under the auspices of the Ottawa-Carleton Institute for Civil Engineering

University of Ottawa

ABSTRACT

Recent interest in sustainable design has resulted in timber products being considered for a variety of construction projects. This has especially been the case for engineered wood products (EWPs), such as glue-laminated timber (glulam) and cross-laminated timber (CLT). Research into the performance of these massive timber products has been ongoing, where the methodology employed has generally favoured experimental approaches on undamaged members, combined with simplified analytical methods. Relatively little attention has been given to more sophisticated numerical methodologies and to the effects of repeated loadings on the same specimen. This study intends to contribute to the literature by investigating the viability of full-scale finite element models to simulate the behaviour of timber elements at high strain rates and proposing a generalized structure for dynamic models that is capable of adequately recreating realistic failure modes.

Three glulam specimens and three CLT specimens were subjected to simulated blast loads under four-point bending with simply supported boundary conditions using the University of Ottawa Shock Tube Test Facility. The behaviour of the glulam specimens during the dynamic testing was consistently linear-elastic until flexural failure was reached. Conversely, the failure behaviour of CLT panels was more complex and included flexural failure, rolling shear failure, or a combined behaviour where both modes developed simultaneously.

Single-degree-of-freedom (SDOF) and finite element analysis (FEA) methodologies were used to predict the behaviour in terms of displacement-time histories and failure modes. The inputs for the analytical methods relied on values sourced from literature or manufacturer data. A finite element (FE) material model was implemented into ABAQUS/Explicit through a dynamic user subroutine (VUMAT). The model used continuum damage mechanics to alter the material stiffness matrix once the elastic strengths were exceeded.

SDOF analysis was shown to effectively predict the maximum mid-span displacement of glulam members subjected to blast loads, within a 20% error margin. However, the model was found to be incapable of consistently predicting the displacement and time of failure, especially for CLT panels, where up to 50% error was observed. This degree of error was attributed to the model's inability to account for multiple failure modes, namely rolling shear and flexural failure. The

resistance curves implemented in the SDOF models generally agreed with experimental results, particularly with regard to initial stiffness, and were deemed sufficiently accurate from the perspective of design.

The finite element models simulated specimen ultimate behaviour reasonably well. Relatively accurate analytical predictions were also obtained for both maximum mid-span displacements and corresponding times. However, computational issues with damage transfer prevented the modeling of repeated tests on CLT panels. The FE model was capable of producing resistance-displacement relationships which correlated well to experimental results, despite the presence of numerical fluctuations. This is a significant outcome for the potential application of FEA to blast behaviour of timber components, since SDOF models require resistance curves as input and are unable to predict the force-displacement response of members.

ACKNOWLEDGEMENTS

Completing a thesis is no small task for any graduate student. Generally speaking, the process involves developing academic skills, committing to goals, and learning to make practical compromises to solve problems. Finalizing a thesis also involves the author confronting shortcomings, both in the work and themselves. These challenges are inherent in the undertaking, even before considering the global pandemic which my contemporaries and I find ourselves in. Needless to say, I could not have navigated these times or produced this document without the assistance of several others.

First, I would like to thank my supervisors, Dr. Ghasan Doudak and Dr. Christian Viau, for their patience, guidance, and time both in the lab and across the screen. Without their help, this thesis would be nowhere near its current quality and far from finished. I would also like to thank Dr. Doudak again for his financial support, which allowed this study to be completed without unnecessary delays.

I would also like to thank my colleagues and friends who shared the lab with me and kept things enjoyable during the hot summer days in the lab, namely Antoine Bérubé, Andrew McGrath and Laith Gharaibeh. I wish you the best in your own projects, and let me know if you need more foils cut.

Lastly, I would like to extend my thanks to my parents, who kept me determined and focused when timelines went long; to my friends, who organized online game nights that kept these four walls from closing in; and of course to my wife Tara, who supported me unconditionally and who has my heart, always.

TABLE OF CONTENTS

Abstract ii

Acknowledgements iv

Table of Contents v

List of Figures ix

List of Tables xv

Nomenclature and Symbols xvi

Chapter 1- Introduction 1

1.1 Background 1

1.2 Material Behaviour 2

1.3 Mass Timber 4

1.4 Blast Loads 5

1.5 Dynamic Analysis 8

1.6 Finite Element Modeling 11

1.7 Research Objective and Scope 12

1.8 Structure of Thesis 13

Chapter 2- Literature Review 14

2.1 Flexural Timber Response 14

2.2 Response of Lumber to High Strain Rates 16

2.3 Behaviour of Mass and Heavy Timber Subjected to Blast Loading 18

2.4 Blast Analysis of Timber Components 21

2.5 Finite Element Analysis of Timber 23

2.6 Summary 30

Chapter 3- Experimental Program 31

3.1 General 31
3.2 Specimen Description 32
3.3 Shock Tube Description 33
3.4 Experimental Setup 36
3.5 Instrumentation and Methods of Measurement 41
Chapter 4- Experimental Results 43
4.1 General 43
4.2 Nomenclature 43
4.3 Glulam Members 45
4.3.1 Test GL1.1 45
4.3.2 Test GL2.1 46
4.3.3 Test GL2.2 47
4.3.4 Test GL3.1 48
4.3.5 Test GL3.2 49
4.3.6 Test GL3.3 50
4.4 CLT Members 51
4.4.1 Test CLT1.1 52
4.4.2 Test CLT2.1 53
4.4.3 Test CLT2.2 55
4.4.4 Test CLT2.3 56
4.4.5 Test CLT3.1 57
4.4.6 Test CLT3.2 58
4.5 Experimental Data Analysis 59
4.6 Resistance Curves 62

Chapter 5- Analytical Methods 67
5.1 General 67
5.2 Single-Degree-of-Freedom Model 69
5.2.1 Model Inputs 69
5.2.2 Model Results 72
5.3 Finite Element Analysis 75
5.3.1 Choice of Software 75
5.3.2 Modeling Assumptions 77
5.3.3 Model Algorithm 79
5.3.4 Model Equations 81
5.3.5 Programming Details 86
5.3.6 Mesh Sensitivity Analysis 87
5.3.7 Modeling Techniques 89
5.3.8 Material Inputs 92
5.3.9 Finite Element Results 94
Chapter 6- Discussion 104
6.1 Behaviour of Mass Timber Elements Under Dynamic Loading 104
6.1.1 Glulam Specimens 104
6.1.2 CLT Specimens 106
6.2 Experimental Comparison with SDOF Analysis 107
6.2.1 Resistance Curves 107
6.2.2 Glulam Displacement and Failure 110
6.2.3 CLT Displacement and Failure 113
6.3 Experimental Comparison with FEA 117

6.3.1 Displacement and Failure Behaviour ... 117
6.3.2 Resistance Curves ... 126
6.4 Comparison Between the Analytical Methods ... 132
Chapter 7- Conclusions ... 139
7.1 General ... 139
7.2 Conclusions ... 139
7.3 Recommendations for Future Work ... 140
References ... 142
Appendix A: Dyanmic Testing Results ... 150
Appendix B: Strength Increase Factor Determination ... 199
Appendix C: Glulam Resistance Curve for Single-Degree-of-Freedom Analysis ... 202
Appendix D: Single-Degree-of-Freedom Results ... 204
Appendix E: ABAQUS VUMAT Code ... 218
Appendix F: Finite Element Analysis Results ... 226

LIST OF FIGURES

Figure 1.1: Illustration of wood cell structure (a) and general pith/ring structure (b) [6] 2

Figure 1.2 Illustration showing knot formation, a type of defect occuring during growth [6] 4

Figure 1.3: Comparison of CLT and glulam composition [11] 5

Figure 1.4: Typical pressure-time history of a shock wave [13] 7

Figure 2.1: Stress-strain relationship for timber materials [20] 14

Figure 2.2: Moment-curvature relationship and ranges for flexural failure modes [20] 15

Figure 2.3: Illustration of CLT failure modes in a three-ply CLT panel: a) Rolling shear b) Flexural [10] 19

Figure 2.4: Idealized flexural resistance curves for three- and five-ply CLT [10] 20

Figure 2.5: Resistance curve for three-ply CLT failing in rolling shear [10] 21

Figure 2.6: Effect of damage for a) Ductile modes b) Brittle modes [39] 27

Figure 2.7: Doubly symmetric model of a bolted timber connection [42] 28

Figure 2.8: Behaviour comparison images from Kaliyanda et al.: a)ABAQUS joint model b)Deformed bolt head c)Timber crushing damage [42] 29

Figure 3.1: Expansion section (a) and rear view of driver chamber and retraction mechanism (b). 35

Figure 3.2: Closed diaphragm section, with pressure lines and foils... 35

Figure 3.3: View of the end frame side, showing vents and expansion section. (a) View of Load Transfer Device without specimen, with retaining strap. (b)... 36

Figure 3.4: Image of experimental setup for glulam, annotated lower components..................... 37

Figure 3.5:Image of experimental setup for CLT 38

Figure 3.6: Reaction assembly detail for glulam, with mounted load cell and notched plate support system 38

Figure 3.7: CLT end details 39

Figure 3.8: Head-on diagram of load transfer device 39

Figure 3.9: Side diagram of experimental setup for glulam 40

Figure 3.10: Side diagram of experimental setup for cross-laminated timber............................. 40

Figure 3.11: Labelled top-view diagram of general testing setup, not scaled. 42

Figure 4.1: Specimen face nomenclature, with reference to experimental setup 44

Figure 4.2: CLT specimen end, left side, with annotated ply order... 44

Figure 4.3: a) Specimen GL1 before testing b) Failure during test GL1.1 c) Failure cracks, left side 46

Figure 4.4: Minor splitting failure in test GL2.1, post-test.. 47

Figure 4.5: a) Initiation cracks during test GL2.2 b) Failure cracks left side c) Failure cracks right side 48

Figure 4.6:Specimen after test GL3.1 49

Figure 4.7: a) Location of superficial crack after test GL3.2 b) Close-up of damaged section.... 50

Figure 4.8: Failure cracks for test GL3.3: a) Left side b)Tension face c)Right side 51

Figure 4.9:Failed state overview of specimen CLT1: a) Left side b) Right side.......................... 52

Figure 4.10: CLT1.1 failure details: a) Finger joint failure b) Compression wrinkling 53

Figure 4.11: a) Transverse gaps in CLT2 before testing b) Minor damage on tension face c) Rolling shear damage, lower right side... 54

Figure 4.12:a) Vertical crack on right side b) Right side rolling shear cracks 55

Figure 4.13: Propagation of transverse shear cracks: a) Left side b) Right side 56

Figure 4.14: a) Tension face, with flexural fractures b) Point of maximum displacement, illustrating failure behaviour c) Crack extension past support and through end of panel 57

Figure 4.15: a) Undamaged specimen before testing b) Development of rolling shear cracks during test c) Damaged state of panel, right side 58

Figure 4.16: Typical pressure- and impulse- time histories, from blast test CLT2.1 59

Figure 4.17: Typical reaction-time history, from test CLT2.1 60

Figure 4.18: Typical (elastic) mid-span displacement-time history, from test CLT2.1 60

Figure 4.19:Idealized system for the derivation of resistance equations [49] 61

Figure 4.20: Dynamic resistance curve for test GL1.1 62

Figure 4.21:Dynamic resistance curves for GL2 63

Figure 4.22: Dynamic resistance curves for GL3 63

Figure 4.23:Dynamic resistance curve for test CLT1.1 64

Figure 4.24: Dynamic resistance curves for CLT2 64

Figure 4.25: Dynamic resistance curves for CLT3 65

Figure 5.1: Experimental and simplified pressure-time histories for shot GL1.1 68

Figure 5.2: Five-ply CLT resistance curve for SDOF analysis 70

Figure 5.3: Three-ply CLT resistance curve for SDOF analysis 71

Figure 5.4: Glulam resistance curve for SDOF analysis.. 72

Figure 5.5: RCBlast output window for CLT2.2 73

Figure 5.6: Displacement results for CLT3.2 74

Figure 5.7: Material model flowchart 81

Figure 5.8: Displacement comparison for glulam meshes.. 88

Figure 5.9: Displacement comparison for CLT meshes 89

Figure 5.10: Main member model and coordinate systems for glulam (a) and CLT (b).............. 90

Figure 5.11: Model assemblies, with loads and support points, for glulam (a) and CLT (b)....... 91

Figure 5.12: Final state of model GL1.1, mapping tensile damage parallel to grain.................... 96

Figure 5.13: Damage in model GL2.1: a) Tension parallel to grain b) Tension perpendicular to grain (Global Y), at midspan 96

Figure 5.14: Initial mid-span deletion (a) and failed state (b) of model GL2.2............................ 97

Figure 5.15: Damage development at maximum displacement for GL3.2: a) Tension parallel to grain b) Tension perpendicular to grain (Global Z) 98

Figure 5.16: Failed state of model GL3.3 99

Figure 5.17: Failure behaviour of model CLT1.1: a) Initiation of rolling shear damage b)Failed state of panel, with view of tension face 99

Figure 5.18: Positive phase parallel to grain damage in model CLT2.1 100

Figure 5.19: Parallel to grain tensile damage in model CLT3.1 101

Figure 5.20: Modeled resistance curve for CLT3.1 102

Figure 5.21: Displacement history for model CLT3.1 102

Figure 6.1: a) Superficial cracking resulting from test GL3.2 b) Comparison of pre-peak resistance curves for GL3.2 and GL3.3 104

Figure 6.2: Failure initiation in glulam specimens, with the point of crack origin circled: a) GL1.1 b) GL2.2 c) GL3.3 105

Figure 6.3: Resistance curves for glulam specimen failures 106

Figure 6.4: a) Flexural cracks developed in test GL1.1 b) Displacement-time history for test GL1.1 106

Figure 6.5: Experimental CLT resistance curves displaying both initial stiffness and failure development 107

Figure 6.6: SDOF resistance curve comparisons for glulam: a) GL1 b) GL2 c) GL3 108

Figure 6.7: SDOF resistance curve comparison for CLT: a) CLT1 b) CLT2 c) CLT3 109

Figure 6.8: Displacement comparison for SDOF model of shot GL1.1 111

Figure 6.9: Displacement comparison for SDOF model of shots GL2.1 (a) and GL2.2(b) with experimental and analytical time of failure indicated 112

Figure 6.10: Displacement comparison for SDOF model of shots GL3.1 (a), GL3.2 (b), and GL3.3 (c)with experimental and analytical time of failure indicated 113

Figure 6.11: Displacement comparison for SDOF model of shot CLT1.1, with times of key experimental and analytical behaviour indicated 114

Figure 6.12: Displacement comparison for SDOF model of shots CLT2.1 (a), CLT 2.2 (b), and CLT2.3 (c) with key experimental and analytical behaviour indicated 116

Figure 6.13: Displacement comparison for SDOF model of shots CLT3.1 (a) and CLT3.2 with experimental and analytical behaviour indicated (b) 117

Figure 6.14: Displacement comparison for FEA of shot GL1.1 118

Figure 6.15: Displacement comparison for FEA of shot GL2.1 119

Figure 6.16: Displacement comparison for FEA of shot GL2.2, with experimental and analytical failure observations 120

Figure 6.17: Side-by-side comparison between experimental cracking and model deletion for GL2.2 120

Figure 6.18: Displacement comparison for FEA of shot GL3.1 121

Figure 6.19: Displacement comparison for FEA of shot GL3.2 121

Figure 6.20: Side-by-side comparison between experimental cracking and model deletion for GL3.3 122

Figure 6.21: Displacement comparison for FEA of shot GL3.3, with key experimental and analytical behaviour indicated 123

Figure 6.22:Experimental displacement comparison for FEA of shot CLT1.1, including points of initial and ultimate failure 124

Figure 6.23: Side-by-side comparison of central failure behaviour for CLT1.1 124

Figure 6.24: Displacement comparison for FEA of shot CLT2.1 125

Figure 6.25: Displacement comparison for FEA of shot CLT3.1 126

Figure 6.26:Finite element resistance curve comparison for shot GL1.1 127

Figure 6.27:Finite element resistance curve comparison for shots GL2.1 (a) and GL2.2 (b) 128

Figure 6.28:Finite element resistance curve comparison for shots GL3.1 (a), GL3.2 (b), and GL3.3 (c) ... 129

Figure 6.29:Finite element resistance curve comparison for shots CLT1.1 (a), CLT2.1 (b), and CLT3.1(c)... 130

Figure 6.30:Experimental displacements versus analytical predictions ... 136

Figure 6.31:Experimental versus predicted times for key behaviours... 137

LIST OF TABLES

Table 3.1 Specimen Testing Outline 32

Table 4.1: Summary of Full-Scale Dynamic Test Results 66

Table 5.1: Equivalent Blast Pressure-Time Histories for Analysis 68

Table 5.2: Analytical Increase Factors for Parallel to Grain Capacities 69

Table 5.3: Summary of SDOF Analysis Results 75

Table 5.4: Mesh Sensitivity Results 88

Table 5.5: Units for Material Model 92

Table 5.6: Material Properties for Finite Element Subroutine 94

Table 5.7: Summary of FEA Displacement Results 103

Table 6.1: Model Comparison Table for Simple Displacement Responses 133

Table 6.2: FEA Behavioural Summary and Comparison 135

NOMENCLATURE AND SYMBOLS

CLT	Cross Laminated Timber
COV	Coefficient of Variation
CSA	Canadian Standards Association
DAS	Data Acquisition System
DIF	Dynamic Increase Factor
EWP	Engineered Wood Product
FE	Finite Element
FEA	Finite Element Analysis
FENTAB	Finite Element Nonlinear Transient Analysis of Beams
GL	Glulam
LTD	Load Transfer Device
LVDT	Linear Variable Differential Transducer
MC	Moisture Content
SDOF	Single-Degree-of-Freedom
SDV	State Dependent Variable
SIF	Strength Increase Factor
TDOF	Two Degree of Freedom
TNT	Trinitrotoluene
UMAT	User Material
VUMAT	Dynamic User Material

0	(subscript) Parallel to grain
90	(subscript) Perpendicular to grain
b	Waveform parameter
c	Coefficient of damping
c	(subscript) Compression component
C^{dam}	Damaged material compliance matrix
d	Component damage
D	Material stiffness matrix
D^{dam}	Damaged material stiffness matrix
d^{eff}	Effective composite damage
d_S	Stabilized component damage
dt	Time increment
E	Young's modulus
F	Total system forces
f	Material capacity

F(t)	Load as a function of time
F(σ)	Damage criterion
F_e	Equivalent lumped force
f_{max}	General component capacity
G	Shear modulus
G_f	Fracture energy
G_{roll}	Rolling shear modulus
I	Moment of inertia
i_s	Positive phase impulse
k	Spring constant
K	Equivalent dynamic stiffness
K_L	Load transformation factor
K_{LM}	Load-mass transformation factor
K_M	Mass transformation factor
K_R	Resistance transformation factor
L	Length
L	(subscript) Longitudinal direction
m	Mass
M	Total system mass
m_c	Concentrated mass
M_e	Equivalent lumped mass
M_R	Dynamic moment resistance
$\overline{m}$	Specimen linearly distributed mass
$\overline{m}(x)$	Distributed mass function
p(x)	Distributed load function
$P_s(t)$	Overpressure as a function of time
p_{so}	Peak overpressure
R	Standoff distance
R	(subscript) Radial direction
R(t)	Dynamic resistance of a member
R(y)	Resistance-displacement function
R_F	Member dynamic resistance at failure
R_{max}	Maximum experimental resistance
t	Time
T	(subscript) Tangential direction
t	(subscript) Tension component
t_d	Equivalent positive phase duration

t_o	Positive phase duration
u(t)	Displacement
$\dot{u}(t)$	Velocity
$\ddot{u}(t)$	Acceleration
v	(subscript) Shear component
V(t)	Dynamic reaction
W	Equivalent charge weight in TNT
x_{eq}	Equivalent distance to resultant inertial force
Z	Scaled distance
κ	Stress-history variable
σ	Stress
σ^{dam}	Damaged stress
υ	Poisson's ratio
φ	Evaluated shape function for discrete systems
$\varphi(x)$	Shape function for distributed systems
ϵ	Strain

CHAPTER 1- INTRODUCTION

1.1 Background

Recent interest in sustainable design has resulted in timber products being increasingly considered for a variety of construction projects. This has especially been the case for engineered wood products (EWPs), such as glue-laminated timber (glulam) and cross-laminated timber (CLT), due to their enhanced structural properties, ease of assembly onsite, and aesthetic properties [1]. Research into the performance of these massive timber products has been ongoing, and both manufacturing (e.g. ANSI/APA PRG 320) and design standards (e.g. CSA O86, ANSI/AWC NDS-2015) have been developed in several countries. Recently, studies have primarily focused on topics not completely covered in contemporary standards, such as fire performance (e.g. [2]) and composite assemblies where timber is combined with other materials (e.g. [3]). Another topic of interest that has been investigated in the past decade is the dynamic response of timber structures, especially when subjected to extreme loading. Such a topic is particularly critical to the broadening of applications of timber into taller (i.e. mid- and high-rise structures) and larger buildings with inherent heightened risk of exposure to blast and earthquake loadings.

The established knowledge related to the behaviour of timber structural elements under blast loads is limited, when compared to that of steel or reinforced concrete. While most buildings considered to be at risk for targeted blast attacks are constructed of materials with higher inherent blast resistance, there are recent Canadian examples of high-importance buildings with a significant portion of the structure made of timber products (e.g. Olympic Oval, Richmond B.C.; Condos Origines residential tower, Quebec City, QC.). Any blast event also has the potential to cause significant damage to all surrounding structures, some of which are likely wood structures (e.g. residential buildings) even if the targeted building or location of the accident is built using blast-resistant materials.

At the University of Ottawa, the majority of research developments in the blast performance of wood materials have largely focused on establishing reliable response parameters (e.g. [4]) and retrofits (e.g. [5]). The methodology employed has generally favoured experimental approaches on undamaged members, combined with simplified analytical methods. Relatively little attention has been given to more sophisticated numerical methodologies and to the effects of repeated loadings on the same specimen.

The current study investigates the adequacy of finite element analysis (FEA) to describe the dynamic behaviour of timber elements when subjected to simulated blast loading. The outcome from this study is expected contribute to future research efforts in timber behaviour and propose a generalized structure for dynamic models of timber elements that is capable of adequately recreating realistic failure modes.

1.2 Material Behaviour

Wood is a highly variable construction material, with properties varying depending on grain directions, moisture content, species, and growing conditions of the origin tree. Wood's internal structure consists of fibres comprised of slender cells. These cells are connected together with a relatively weak binding component called lignin. This structure is illustrated in Figure 1.1a [6], with annotations for the cell wall and lignin binder. Broadly speaking all wood grows in concentric rings centered on the tree's core (pith), as presented in Figure 1.1b, and is sawn into shape (typically square or rectangular) after felling. However, the distribution of these cells and the density and layering of the cell walls varies according to species. Additionally, the exact arrangement of these cells is dependant on the various environmental conditions (e.g. wind, pests, water quantity) during the origin tree's growth periods.

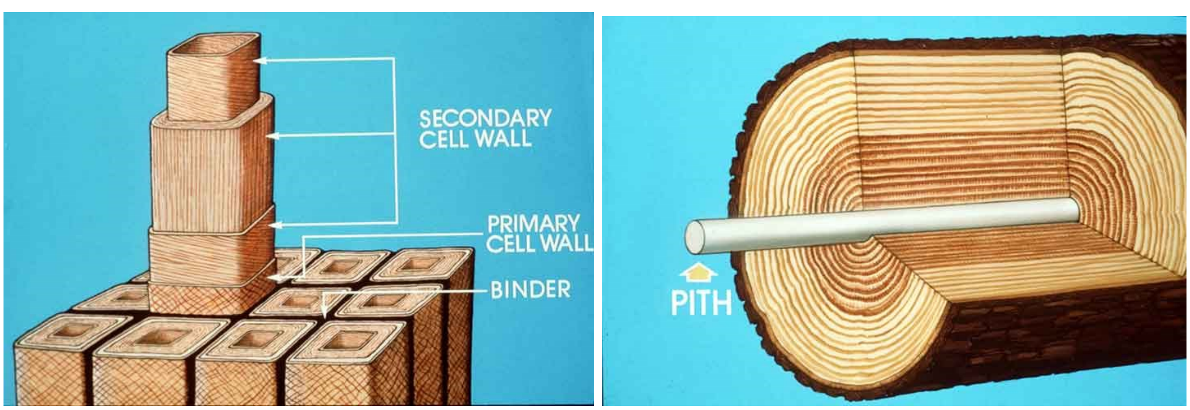

(a) (b)

Figure 1.1: Illustration of wood cell structure (a) and general pith/ring structure (b) [6]

The growth structure causes wood to exhibit different properties relative to the annual rings. Wood can therefore be considered a cylindrically orthotropic material, with consistent behaviour in the longitudinal, radial, and tangential directions. However, the radial and tangential properties are similar, especially when considered relative to the properties parallel to grain. As such, wood is typically idealized as transversely isotropic, with the same properties assigned to the perpendicular to grain directions. Wood is stronger when loaded parallel to its grain direction, where stresses can engage the entirety of the cell's length and the majority of the cell wall structure. When loaded perpendicular to the grain, the strength relies on either the weak lignin bonds or reduced portions of the cell wall.

While the behaviour of wood can be considered strong and ductile in compression (both parallel and perpendicular to grain) due to material densification, splits and fractures occur when the material is subjected to tension or shear, resulting in brittle failure modes. This is particularly apparent when a member is loaded in tension perpendicular to the grain, due to the weakness of the lignin bonds. In addition, defects such as knots or cracks cause localized weaknesses that can act as a point of initial fracture and may cause premature and unwanted failure in the member. The knot formation process is illustrated in Figure 1.2 [6]. Defects, as well as other variations in properties, are accounted for through grading systems (e.g. machine-stress rating, visual grade) and addressed in design by means of appropriate modification factors.

Figure 1.2 Illustration showing knot formation, a type of defect occuring during growth [6]

The overall strength of timber members is also affected by the duration of applied loads. At long-term or permanent durations there is a significant loss in capacity, which can mainly be attributed to changes in the lignin matrix over time, while loadings with shorter durations (e.g. lateral wind loads) prompt a relative increase in capacity [7]. Research shows that further strength increases can be obtained as a result of high strain rates that occur when loads are rapidly applied (e.g. blast events) (e.g. [8] [9] [10]).

1.3 Mass Timber

Mass timber products are a type of EWP consisting of small dimension laminations of lumber bonded together into a structural member. The two types of mass-timber products frequently used in current timber construction are glulam and CLT. The main difference between the two products is the orientation of the laminates. In a glulam member all laminates have the same grain direction which coincides with the long axis of the member. CLT is composed of several plies, each typically with a single layer of laminates oriented in the same direction. The panel usually comprises of an odd number of plies with alternating orientation. Commonly available lay-ups include three to nine plies, although custom lay-ups can also be made available by some manufacturers. CLT panels typically have a major axis along the panel length that matches the grain direction of the outer laminates, where stronger material is used. The fewer transverse plies are typically made of weaker grades of timber and provide splitting resistance and strength in minor direction of the panel, allowing for the possibility of two-way bending action. The panels are typically oriented such that the span length or gravity load is parallel to the major longitudinal axis. An illustration of the sectional differences between glulam members and CLT panels is presented in Figure 1.3 [11]. In general, EWP tend to be more consistent than traditional lumber, because they consist of smaller dimension lumber elements that are less likely to contain significant concealed defects.

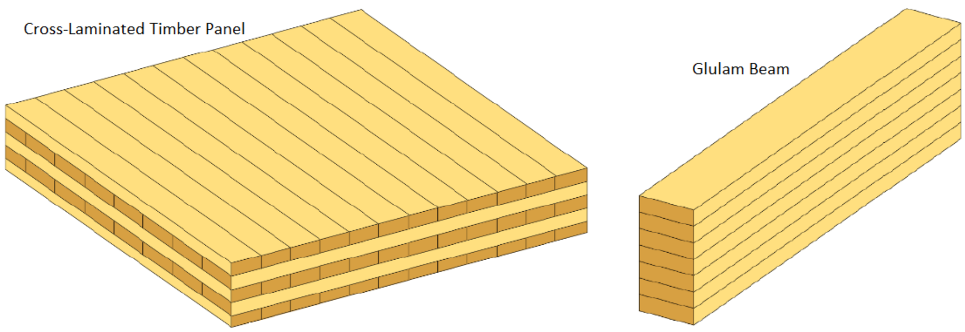

Figure 1.3: Comparison of CLT and glulam composition [11]

Glulam members are typically used as beams or columns while CLT panels can be installed as floors, walls, or roofs. In both cases, prefabrication of such systems help quicken on-site construction [12]. Although outside the scope of the current project, connections in mass timber structures are of paramount importance. They typically consist of dowel type connections such as large bolts or screws, often in combination with steel plates.

1.4 Blast Loads

Blast loads consist of short, high intensity loads caused by explosions, which can be generally defined as a sudden release of energy that results in an increase in ambient pressure (overpressure) that propagates away from the source [13]. Explosions are commonly caused by chemical reactions or physical events, although other types of explosion are possible (e.g. nuclear). In chemical explosions a volatile reaction takes place and generates large amounts of heat and gas, often through oxidation. Depending on the chemical reaction involved, the substance is referred to as a high or low explosive. High explosives tend to detonate, creating an expanding sphere of overpressure that travels at supersonic speeds and compresses the air it displaces. This phenomenon is referred to as a blast or shock wave. Examples of high explosives include trinitrotoluene (TNT) and nitroglycerine. Low explosives tend to deflagrate, creating waves of pressure that are subsonic and do not generate blast waves. Examples of low explosives include propellants such as gunpowder and gasoline. Physical explosions occur when pressure fronts, similar to detonations, are generated without a chemical reaction, such as the rupture of a pressurized vessel or the generation of large amounts of steam through contact between water and high temperature substances.

The energy released by explosions is typically measured in mass equivalencies of TNT due to its consistency and availability. The resulting loads are categorized by the relationship between the point of origin and the affected structure. When the structure's surface is perpendicular to the path of the blast front, the resulting pressure experienced by that section is referred to as reflected overpressure. If the surface is parallel to the path of the shock wave (or otherwise not directly facing the origin) the resulting pressure distribution is referred to as side-on overpressure [13]. The impact of the event is heavily influenced by the distance from the point of origin to the structure in question, termed standoff distance, due to the reduction in blast pressure as the wave travels from its source. Different equivalencies of explosive can generate the same overpressures by altering their standoff distance, as described by scaling distance Z in Equation [1-1] where R is the standoff distance and W is the equivalent charge weight in TNT [14]. This cube-root scaling allows for the characterization of a variety of blast loads.

$$Z = \frac{R}{W^{\frac{1}{3}}} \qquad [1\text{-}1]$$

Shock waves are primarily characterized by their peak overpressure, positive phase duration, and impulse. These blast characteristics can be determined using the scaled distance in combination with established charts [15] for different patterns of propagation (e.g. hemispherical ground burst, free-air burst).

When a shock wave interacts with the surface of a structure, a large overpressure is applied across the surface in question. This peak pressure then dissipates as the blast front moves past the structure, with stagnation and drag lengthening the time of the overpressure as the structure prevents the free expansion of the shockwave. The period between the arrival of the blast wave and the degradation back to ambient pressure is referred to as the positive phase. The positive phase is followed by the negative phase, a period of negative pressure caused by the over-expansion of the gases and subsequent suction as disturbed air flows back and equalizes ambient pressure. This can be described by Equation [1-2], which is modified from Friedlander's equation for the propagation of sound pulses [16]. The corresponding pressure-time history is visually represented in Figure 1.4 with additional labeling for impulses and time of arrival (t_A).

$$P_s(t) = p_{so}\left(1 - \frac{t}{t_o}\right) e^{-\frac{bt}{t_o}} \qquad [1\text{-}2]$$

Where p_{so} is the peak overpressure, t is the elapsed time, t_o is the positive phase duration and b is a waveform coefficient.

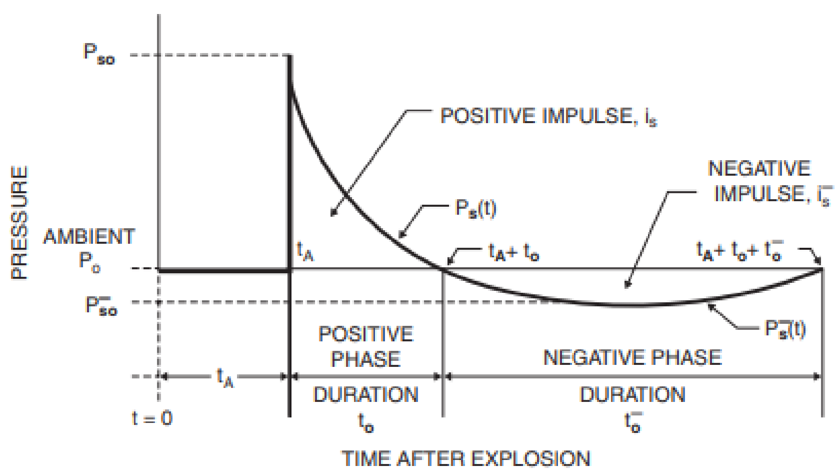

Figure 1.4: Typical pressure-time history of a shock wave [13]

It is common for the pressure-time history of a blast to be simplified for use in design. Since the maximum response of the structural element is of interest, the negative phase is often disregarded for the design of structures [17]. Furthermore, the positive phase can be simplified into a triangular pressure-time history, where the total positive impulse (i_s) and peak pressure are maintained but the equivalent duration is found according to Equation [1-3]. These simplifications allow for the use of various closed-form solutions during analysis of blast effects.

$$t_d = \frac{2i_s}{P_{so}} \tag{1-3}$$

1.5 Dynamic Analysis

Single-degree-of-freedom (SDOF) modeling is commonly used to predict and evaluate the dynamic behavior of structural elements. By mathematically reducing the real structural system to a lumped mass with a spring, the characteristic displacement curve can be obtained using the equation of dynamic equilibrium, as seen in Equation [1-4]. The equation states that the sum of applied forces $F(t)$ is equal to the total resisting forces, which consist of inertia ($m\ddot{u}(t)$), damping ($c\dot{u}(t)$), and collective spring forces ($ku(t)$).

$$m\ddot{u}(t) + c\dot{u}(t) + ku(t) = F(t) \tag{1-4}$$

The inertial resistance scales with the mass of the system, acting opposite to the systems acceleration according to Newton's second law. The effect of inertial force is one reason that heavier materials, such as reinforced concrete, have inherent blast resistance. The damping force accounts for factors such as friction and air resistance and consists of a damping coefficient and the velocity of the lumped mass. The spring forces collectively account for any resistance that scales with displacements, such as structural stiffness or the resistance of a deforming spring support. When a system is reduced to a single characteristic displacement, such as the mid-span displacement of a beam, closed form solutions become possible provided the forcing function is well-defined.

As blasts occur over short timeframes, it is generally accepted that damping has insufficient time to influence the behaviour of the maximum displacement and is typically disregarded in the analysis [17]. Furthermore, the reduction of a system of distributed mass, load, and stiffness into a single lumped point requires that equivalency be maintained between the actual continuous system and the idealized lumped system. This is done through a set of transformation factors, denoted as K_M, K_R, and K_L for mass, resistance, and load, respectively. Equation [1-5] presents a modified form of the dynamic equation of equilibrium which takes these factors into account, as well as changes the spring force term *ku(t)* in favour of a general resistance function *R(y)* and generic mass *m* for total mass *M*.

$$K_M M\ddot{u}(t) + K_R R(y) = K_L P(t) \qquad [1\text{-}5]$$

The formulation of the transformation factors depends on whether the original system is considered as a continuously distributed system (e.g. structural beam, wind loads) or a discretely concentrated system (e.g. supported machinery, shock absorbers). Equations [1-6] and [1-7] show the formulations for concentrated mass and load transformation factors respectively, while Equations [1-8] and [1-9] present the distributed formulations. The resistance factor and load factor are taken as equal, due to the relationship between applied load and resistance [17]. These equations introduce the defected shape function *φ(x)* to describe the deformed shape of the actual system and to convert the behaviour to an equivalent single point.

$$K_M = \frac{M_e}{M} = \frac{\sum_r^i m_r \phi_r^2}{\sum_r^i m_r} \qquad [1\text{-}6]$$

Where M_e is the equivalent system mass for single degree analysis, and m_r is the concentrated mass at point *r* of *i* points.

$$K_L = \frac{F_e}{F} = \frac{\sum_r^i F_r \phi_r}{\sum_r^i F_r} \qquad [1\text{-}7]$$

Where F_e and *F* are respectively the equivalent and total forces on a system, and F_r is the force applied to the system at point *r* of *i* points.

$$K_M = \frac{M_e}{M} = \frac{\int_0^L \bar{m}(x)\phi(x)^2 dx}{\int_0^L \bar{m}(x) dx} \quad [1\text{-}8]$$

Where $\bar{m}(x)$ is the mass distribution function with respect to length.

$$K_L = \frac{F_e}{F} = \frac{\int_0^L p(x)\phi(x) dx}{\int_0^L p(x) dx} \quad [1\text{-}9]$$

Where p(x) is the applied force distribution function with respect to length.

The load and mass factors can also be combined into a single variable, denoted as the load-mass factor K_{LM}, as shown in Equation [1-10]. This is often done as a matter of convenience, as the dynamic equation of equilibrium can be written in terms of the load-mass transformation factor alone as seen in Equation [1-11].

$$K_{LM} = \frac{K_M}{K_L} \quad [1\text{-}10]$$

$$K_{LM} M \ddot{u}(t) + R(y) = P(t) \quad [1\text{-}11]$$

The use of SDOF analysis for the purpose of blast analysis and design of structural elements has been well documented (e.g. [8] [15] [17]), with displacement functions, transformation factors, and tables available for a variety of loading functions and systems.

The resistance-displacement relationship *R(y)* is critical to the analysis of structural elements under dynamic loading. The relationship, typically referred to as a member's resistance curve, defines the member's resistance at specific characteristic displacements. Therefore, the stiffness, maximum response, and failure behaviour of a member can all be characterized using this relationship. Resistance curves can be linear or non-linear, with values for positive and negative displacements.

1.6 Finite Element Modeling

Modeling the blast-structure interaction can be quite challenging to analysts and engineers, due to the many unknown variables present within the shock wave itself and within the structural members and assemblies. For this reason, closed-form solutions may be impractical or impossible to derive and are replaced by simplified and idealized analytical solutions, which may require many assumptions. One possible solution is to subdivide the problem into smaller elements. Equations can then be solved numerically for each of these elements, and values at specific points, called nodes, can be determined. Nodes often act as connections between elements, in some cases supplemented by shared surfaces or edges. The common nodes facilitate the combination of the localized solutions through the continuity of variables from one element to another. This continuity between elements is enforced through compatibility conditions, such as equilibrium of forces. The compatibility between elements can then be leveraged to assemble and solve a global system of equations. Generally, the accuracy of a FEA method largely depends on its internal assumptions and inputs, both in terms of element properties (e.g. type, size, mechanical properties) and boundary conditions [18].

Finite element (FE) methods have many possible applications, including structural analysis and heat transfer. However, many applications require a degree of complexity and number of elements that is not feasible to evaluate by hand. Therefore, computer processing is often required. Several software environments for general finite element analysis are commercially available, with examples including ABAQUS, ANSYS, and SAP2000. For specific applications, however, it may be preferable to use a more specialized finite element package (e.g. LS-DYNA) or program an entirely unique solver.

A wide variety of element types can address different properties or sets of unknowns, but elements for material simulation can be separated into two broad categories: discrete and continuum elements. An analysis using discrete elements consists of a lattice-like assembly of linear, one-dimensional elements which are assigned well-defined mechanical behaviours. Discrete finite element methods are ideal when the relationship between nodes can be isolated as sets of connections. These one-dimensional elements are well suited to structural analysis, for example, where an element can represent an entire member and compatibility can be enforced using equilibrium at the nodes.

Contrarily, continuum elements assign material properties into a two- or three-dimensional continuous element connected at exterior nodes, as well as edges and surfaces if applicable. Continuum elements are suited for analyses requiring detailed results, where each element represents a small part of a whole entity rather than a functional component or link. Accordingly, continuous techniques are generally a better match to member-scale analyses, such as a single bending member or joint. The compatibility equations generally take the form of differential equations, which must be solved numerically. Element size, element shape, and number of nodes per element have significant influence on the accuracy of the numerical approximation but can also significantly increase the computational cost of the analysis.

1.7 Research Objective and Scope

This study seeks to investigate the behaviour of glulam and CLT members subjected to multiple simulated blast loads. This research project also aims to evaluate the capability of different analytical methods to simulate the failure behaviour and compare the modeled results to the experimental data.

These research objectives will be achieved through the following:

- Experimental testing of glulam and CLT specimens at the University of Ottawa Shock Tube Test Facility, focusing on repeated tests and characterisation of failure behaviour.
- Modeling and analyzing the behaviour of the tested specimens using a single-degree-of-freedom (SDOF) analysis.
- Developing a customized material model to be used in a commercial finite element software.
- Comparing the experimental and analytical results to evaluate the accuracy of the afore-mentioned modeling techniques.

1.8 Structure of Thesis

Chapter 1 contains an overview of relevant theory as well as an outline of the scope and purpose of the study.

Chapter 2 provides a review of literature relevant to the research topics, focusing on the performance of timber under blast loads and the numerical analysis of timber materials.

Chapter 3 consists of a description of the experimental component of this study, including the testing outline and laboratory set up.

Chapter 4 contains the results of the shock tube tests conducted on CLT and glulam members.

Chapter 5 provides details on the analytical methods and their implementation. The SDOF and FEA programmes used in this research are described, including development choices and assumptions for the material model. It also contains a thorough description of the various inputs and the modeling practices.

Chapter 6 presents and compares the results of the SDOF and FEA models, including failure patterns and resistance curve analysis. The analytical results are further compared to the experimental data, and the observations are discussed.

Chapter 7 summarizes the findings of this study and identifies possible further research.

Appendix A presents detailed figures for the dynamic test results.

Appendix B provides the process used to determine the strength increase factor.

Appendix C presents the derivation of the glulam resistance curve for SDOF approach.

Appendix D presents detailed outputs for the SDOF models.

Appendix E provides the code for the material model subroutine developed for ABAQUS/Explicit.

Appendix F presents detailed results for the FE model.

CHAPTER 2- LITERATURE REVIEW

2.1 Flexural Timber Response

As addressed in Chapter 1, timber tends to experience brittle failure modes when loaded in tension, shear and flexure, while the response in compression tends to be ductile crushing [19]. Buchanan [20] developed a sectional relationship for commercially graded lumber and timber under flexural loads, modifying earlier work by Bazan [21] which was applicable only to clear (i.e. defect-free) wood.

The stress-strain relationship outlined by Buchanan [20] consisted of linear-elastic behaviour in tension up to point of failure while the compressive behaviour was bi-linear and featured a descending branch past a maximum stress and yield strain. This relationship is presented in Figure 2.1, where it is shown that a constant ratio of the elastic modulus as the descending compressive branch is implemented [20].

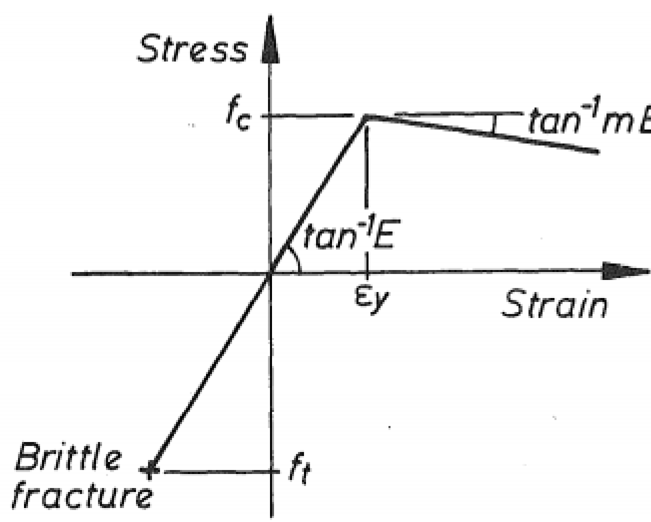

Figure 2.1: Stress-strain relationship for timber materials [20]

Four modes of flexural failure were established as a function of the relative strength in compression and tension. Modes one ($M_U(1)$) and two ($M_U(2)$) were primarily dependent on tension: in the first mode, the sectional stresses were entirely linearly distributed before tension failure occurred, while in mode two, compression yielding had begun at time of fracture. Mode three ($M_U(3)$) occurred when the bending capacity was controlled by compression rather than tension. The failure of a member in mode three was identified by a reduction in moment capacity as significant yielding occurred in the compressive zone, followed by tensile rupture. The fourth mode ($M_U(4)$) was an extreme case noted to only be common in green (i.e. high moisture-content or living) wood, where compressive yielding continued to the formation of a plastic hinge and no tensile failure occurred. It was noted that clear wood often exhibits failure modes two or three and commercially graded wood most often fails in modes one or two, due to the presence of defects reducing the tensile strength of the material while having a less significant impact on compressive behaviour. The distinction between clear and in-grade wood was critical, as it has been shown that the behaviour of commercial specimens cannot be accurately described by tests on clear specimens (e.g. [22], [23]). The relationship between the modes is illustrated along a theoretical moment-curvature relationship in Figure 2.2, accompanied by comments on the relative strengths in tension and compression [20].

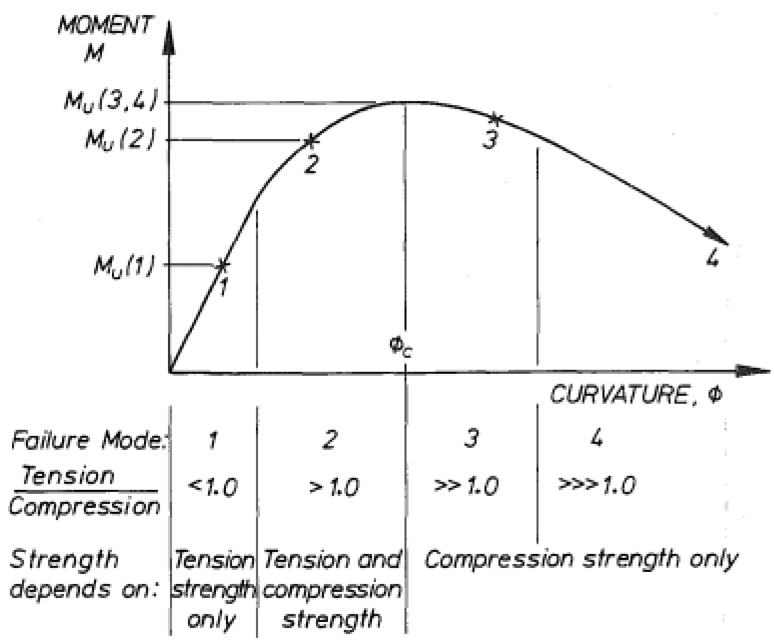

Figure 2.2: Moment-curvature relationship and ranges for flexural failure modes [20]

2.2 Response of Lumber to High Strain Rates

Early investigation of the effect of strain rates on the behaviour of wood focused on small scale clear wood specimens. Liska [24] conducted impact tests on clear and straight-grained specimens and evaluated the compressive and flexural strength at timeframes between 0.3 seconds and a control of 750 seconds. It was determined that softwood and hardwood specimens showed an increase of up to 40% in compressive and flexural capacities as the time-to-failure decreased from the control. No significant effects on the modulus of elasticity were observed. Further research by Nadeau and Bennett [25] indicated that the effect of increased strain rates can vary based on member strength, a result which was corroborated with earlier findings [26].

Nadeau and Bennett [25] performed tests on small, clear specimens of Douglas-fir using a hydraulic machine capable of applying consistent strain rates. Prior to testing, many of the specimens were notched on the tension face using a saw, either 20% or 50% through their section, to evaluate the effects of initial cracks or weaknesses. Tests for unnotched members had loading rates between 2.6 x 10^{-3} MPa s^{-1} and 529 MPa s^{-1}, while notched specimens were tested at rates between 2.6 x 10^{-3} MPa s^{-1} and 68.9 MPa s^{-1}. Increases in capacity up to 30% were observed at high strain rates, however those significant increases were only found in the unnotched specimens. Almost no increase was observed in the heavily notched specimens (i.e. with 50% of their section removed), while specimens which had small notches showed a moderate increase of approximately 20% in capacity. The resulting increases in strength due to strain rate coincided with the observations made by Spencer [26], which were a product of similar testing performed on numerous small-scale clear specimens. The strain rate effects observed by Nadeau and Bennett [25] for the unnotched, moderately notched, and heavily notched members were similar to those observed in the strong (95th percentile), average, and weak (5th percentile) specimens tested by Spencer [26], respectively. Nadeau and Bennett [25] also examined the fracture and crack growth of specimens during testing and concluded that the connection between crack growth and strain rate can be used to predict the performance of timber at various strengths and strain rates. However, the authors determined that the failure behaviour was often shown to be mixed-mode, and that the failure in heavily notched specimens was not strictly described by cracks developing through the cross-section at the notch.

Jansson [22] investigated strain rate effects on timber through the testing and analysis of commercial grade lumber. A total of 651 specimens were cut from commercial machine-graded lumber and separated into two groups. The first group was as defect-free as possible within the sample set, while the second was representative of the variety of commercially available timber. The specimens were tested non-destructively in bending, followed by either destructive static testing or single-blow impact testing. It was determined that the specimens containing clear wood were notably stronger than the commercially representative group, which was of generally of lower quality and contained more defects. The specimen group containing the clearer wood also exhibited less variability in properties when compared to the group containing defects. It was concluded that data obtained though clear wood testing should not be taken as representative of graded commercial lumber. Similar conclusions were made by Barrett and Lau [23].

Jansson [22] also implemented and compared several analytical approaches to predict the failure stress of the specimens. Three methods of analysis were investigated: a single-degree-of-freedom (SDOF) approach which described the failure stress through a generalized inertial load based on experimental readings, a discrete finite element model of the specimen, and another SDOF approach that considers the modulus of elasticity (obtained through the non-destructive static testing) and modes of vibration of the specimen. Additional damping tests were performed and concluded that negligible damping occurred during impact tests, and as such the system was considered undamped in all cases. The former SDOF approach was found to be problematic to implement due to difficulties arising in obtaining reliable accelerometer measurements during testing. The finite element analysis (FEA) utilized FENTAB (Finite Element Nonlinear Transient Analysis of Beams) to create a model of the specimens using one-dimensional beam elements. The model's domain was reduced to half the specimen via symmetry, and implemented using 10, 20, and 40 elements. This method of analysis produced good agreement with the experimental results and was noted to be a versatile and detailed analysis, but the approach was deemed inefficient as the increase in computational cost was significant. The modal SDOF analysis was determined to be accurate for both displacement and stress at failure, provided sufficient vibration modes were considered in the member shape function. The method was faster and more direct than the FENTAB model, and was also capable of separating the solution into static and dynamic responses. Using this method, it was determined that the duration of load factor is insufficient to describe the increase in strength at high strain rates and a modal strength ratio can be used to separate the effects of dynamic loading types from the specimen's static strength [22].

Strain rate effects were also studied and reported by Jacques et al. [8], where failure of single 38 mm x 140 mm (2' x 6') wood studs tested statically, using a hydraulic actuator, and dynamically, in the University of Ottawa Shock Tube Test Facility, were compared. A total of 30 specimens were tested statically and dynamically under four-point bending. The average strain rate of the dynamic tests was 0.21 s^{-1}, while the strain rates for static testing ranged from 5.7 x 10^{-6} s^{-1} to 1.9 x 10^{-3} s^{-1}. It was determined that the modulus of rupture was significantly affected by strain rates above 0.1 s^{-1}, with a statistically significant average increase of 41%. Increases in the modulus of elasticity and failure strain were also observed but were not statistically significant. Further research by Lacroix and Doudak [27] indicated a similar increase in the capacity of light-frame walls systems, as well as an 18% increase in wall stiffness. These values were used in a study by Viau and Doudak [28] that aimed to model light-frame walls of various compositions. The resulting models showed good agreement with experimental data when variables such as sheathing tearing were accounted for.

2.3 Behaviour of Mass and Heavy Timber Subjected to Blast Loading

The following section provides a summary of contributions to the characterization of mass and heavy timber elements under simulated blast loads from research using both simulated and field blast testing.

An experimental program by Lacroix and Doudak [9] was carried out to investigate suitable dynamic increase factors (DIF) for glulam members. Specimens were 2,500 mm in length, with three different cross-sections tested: 80 mm x 228 mm, 86 mm x 318 mm, and 137 mm x 222 mm. Two grades of glulam were tested, consisting of grade 20f-ES and grade 24f-ES glulam beams and columns. The glulam members were simply supported and tested under four-point bending both statically using a hydraulic loading system and dynamically using the

University of Ottawa Shock Tube Testing Facility, with dynamic strain rates between 0.14 s^{-1} and 0.51 s^{-1}. It was observed that failure had the potential to initiate at finger joints during the shock tube tests [9]. Specimens which featured continuous or aligned finger joints across the member's width did not experience an increase in flexural strength. In specimens without continuous joints, a statistically significant DIF of 1.14 was determined. No significant trend for stiffness was found when comparing the static and dynamic test results, and the response of all tests was observed as linearly elastic until failure, with little post-peak resistance.

Poulin et al. [10] investigated the static and dynamic out-of-plane behaviour of CLT panels. A total of 18 specimens were tested, 11 of which were 105 mm thick three-ply panels and seven of which were 175 mm thick five-ply panels. Experimental results showed an average DIF of 1.28 for overall capacity with no observable strain rate effect for panel stiffness. Representations of observed flexural and rolling shear failure modes for a three-ply CLT panel are presented in Figure 2.3 [10].

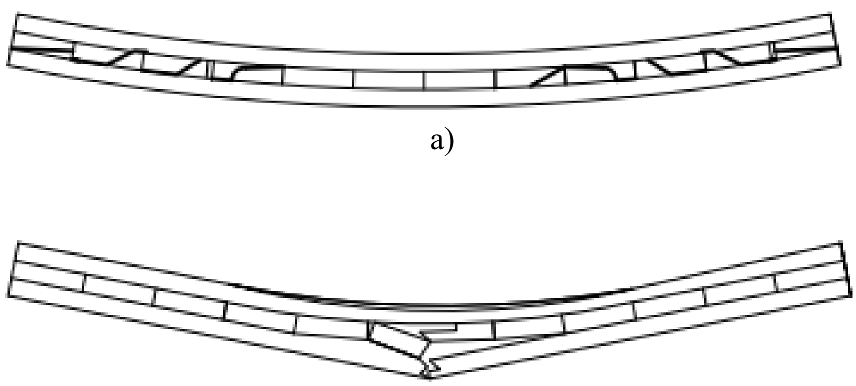

a)

b)

Figure 2.3: Illustration of CLT failure modes in a three-ply CLT panel: a) Rolling shear b) Flexural [10]

In order to characterize the behaviour of the CLT panels for modeling purposes, material predictive models were developed based on the experimental findings. Resistance curves were generated for flexural and rolling shear behaviour. Three-ply flexural behaviour was characterized by a linear-elastic response until ultimate resistance, followed by a sharp drop to a residual strength. Similarly, the resistance curve for five-ply panels was linear until peak resistance, which was then followed by a transition to three-ply behaviour. Accordingly, the resistance dropped to the maximum resistance of the equivalent three-ply panel, which was maintained until the elastic displacement limit of the equivalent three-ply panel was reached. After this limit was exceeded, the resistance was reduced to a residual capacity. This pattern of failure, presented in Figure 2.4 for both three-ply and five-ply panels, was attributed to the sequential flexural fracture of the outermost plies [10]. The resistance curve developed for rolling shear, presented in Figure 2.5 for three-ply panels, consisted of linear behaviour until peak resistance, followed by a residual behaviour according to a reduced stiffness [10]. The models were used in SDOF analyses to predict the mid-span displacements observed during testing and were found to have good agreement with experimental results when the appropriate failure mode was implemented.

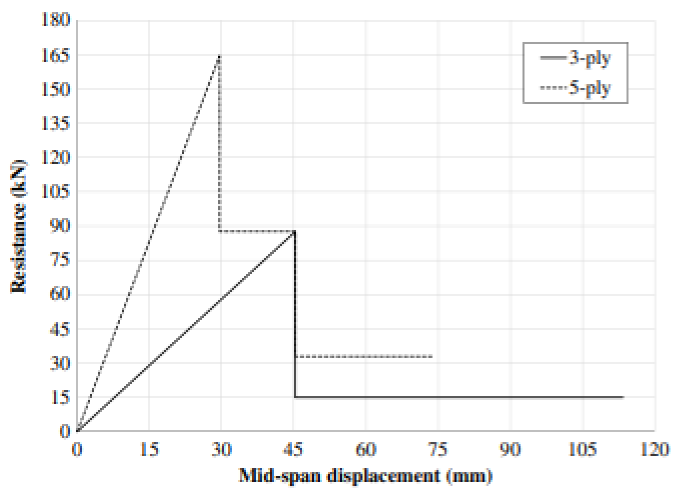

Figure 2.4: Idealized flexural resistance curves for three- and five-ply CLT [10]

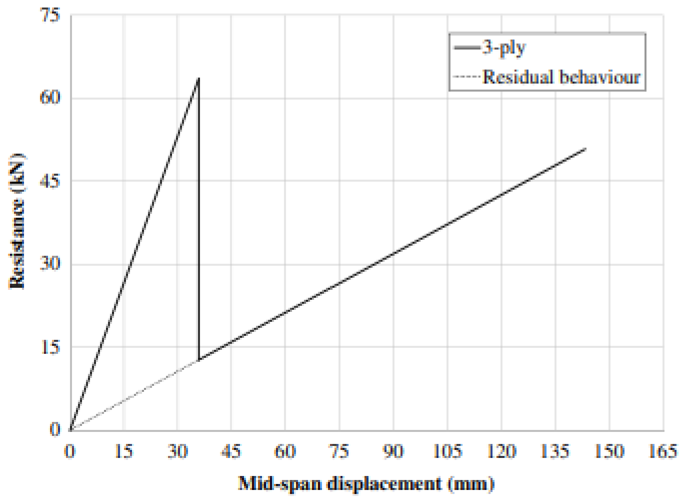

Figure 2.5: Resistance curve for three-ply CLT failing in rolling shear [10]

Research by Weaver et al. [29] [30] further developed the behaviour of CLT elements by subjecting full-scale constructions to live blast loading. Three single room, two-storey CLT structures were tested with varying charge weights at a constant standoff distance. Concrete blocks were used to introduced axial loads on the lower walls, to investigate the effect of significant dead loads on the dynamic response of the first storey wall panels. It was concluded that the addition of axial load reduced damage in the blast-facing panels for the same blast parameters, while altering the displacement behaviour by 10% at most. The authors also conducted individual panel testing, and noted that panel stiffness transitioned from behaviour reminiscent of fixed end conditions to simply-supported behaviour over the course of tests where axial load was applied.

2.4 Blast Analysis of Timber Components

SDOF analysis has been widely used to analyze impact or blast induced behaviour of structural elements. As discussed in section 2.2, the application of a modal variation of SDOF analysis by Jansson [22] led to the conclusion that the apparent increase in capacity at high strain rates in timber was not solely due to load duration effects [22]. Furthermore, Jacques et al. [8] found that SDOF methods were capable of accounting for rate effects and predict the behaviour of single studs subjected to blast loading [8]. Lacroix and Doudak [9] also determined SDOF analysis results agreed with experimental results for simply supported specimens, when given accurate input and dynamic assumptions. Lacroix and Doudak [31] [32] found that creating composite resistance curves using failure mode one or two from Buchanan [20] in a moment-curvature analysis allowed the method to account for variable axial loads in glulam columns and fibre-reinforced polymer reinforcement. Poulin et al. [10] further concluded that SDOF models were suitable for predicting the behaviour of simply supported CLT panels, provided the developed resistance curve used in the method is representative of the failure mode. SDOF methods have also been shown to have reasonable accuracy when modeling traditional timber construction exposed to blast loads; Viau and Doudak [4], for example, found that the behaviour of light-frame stud walls could be described by SDOF analysis by using effective parameters which account for the properties of individual components (e.g. sheathing, fasteners) [4].

SDOF modeling has been shown to be inadequate for certain timber assemblies. Côté and Doudak [33] investigated the blast response of CLT panels with realistic boundary conditions, including typical screw detailing options, steel bracket connections and screw reinforcement. They determined that SDOF analysis was incapable of accounting for the changes in failure mode and energy dissipation of the deforming and yielding connections, and further concluded that more advanced modeling techniques were required to accurately describe dynamic behaviour when realistic end conditions are implemented. Further research on mass timber elements with realistic end connections was conducted by Viau and Doudak, considering both glulam [34] and CLT [35] specimens. It was found that SDOF analysis could not reasonably describe the behaviour of members with non-idealized boundary conditions expect in cases where the connection was substantially stiffer (greater by a factor of ten or more) than the member [36]. A two-degree-of-freedom (TDOF) procedure and software *BlasTDOF* was developed with the capability to account for the blast response of more flexible connections [36]. The method assigned a degree of freedom to the connections as well as the structural member and accepted resistance curves and properties for both. Viau and Doudak [36] successfully predicted the overall resistance and failure behaviour of various combinations of mass timber elements and connections by using experimental results to generate component resistance curves.

2.5 Finite Element Analysis of Timber

The use and application of FEA for timber members and assemblies are very limited, in part due to the complexity of current finite element methods being inefficient for certain applications (e.g. Jansson's discrete beam model for impact loads [22]) that are accurately represented through simpler analytical techniques. Another difficulty of using complex analytical methods for timber materials is the need for material properties that are difficult to isolate and establish experimentally, as discussed in Sandhaas [37]. The author further the suitability of different finite element models to the modeling of timber elements.

Sandhaas [37] noted continuum methods were widely implementable in a variety of commercial software packages, but the analysis relied on averaged values and often had difficulty with convergence towards a solution when non-linear materials were implemented. Furthermore, models with continuum elements often exhibited some degree of mesh dependency. The direct implementation of analytical methods such as fracture mechanics in combination with finite element (FE) codes typically increased computational costs and was unable to account for both brittle and ductile behaviour simultaneously. Hybridized approaches which utilized both continuum and discrete elements were implementable in standard FE software, but commonly had difficulty capturing stress component interactions within timber material and were not suited to matching general behaviour.

Discrete lattice models (e.g. as developed by Reichert [38]) were highly descriptive of material composition and capable of detailed property variation, as all interactions within the material can correspond to sets of linear elements. However, the parameters of the one-dimensional elements were difficult to determine due to the influences of the various scales of material behaviour in wood (e.g. cell walls, fibre behaviour, grain structure, and member shape) and models are required to be calibrated through significant iterations [38]. Furthermore, a lattice model focuses on the internal material structure and the method is poorly suited for simulations involving contact or interaction with other materials, as these complex assemblies significantly increase the model scope. Reichert [38] also noted a high computational cost associated with the technique due to the necessarily small scale of the elements. There was also a noted lack of software packages suitable for the implementation of discrete lattice models, which necessitated the creation of a custom finite element program by Reichert.

Sandhaas et al. [39] developed a static material model for timber in ABAQUS [40] using solid three-dimensional elements with a user material (UMAT) subroutine which implemented a continuum damage approach. This approach to material damage allowed for the detection of both brittle and ductile failure modes and was implementable into the software's ABAQUS/Standard operating mode. The model was incapable of generating permanent deformation and could not generate specific instances of damage such as fibre kinks or tension cracks.

The model used stress-based criteria to initiate the damage process, with different criteria for various failure modes rather than a single failure surface. This follows the theory described by Hashin [41] for use with unidirectional fibre composites, describing separate failure criteria for different modes which can then be identified at the point of fracture. Hashin recommended the use of quadratic interactions to generate the failure surfaces, as higher order approximations were not worthwhile given the scatter within failure data for composites at that time. This order of approximation was maintained within the ABAQUS material model presented by Sandhaas [37], considering wood's inherent distribution of properties and the averaged nature of continuum elements.

The criteria used in the material model presented by Sandhaas et al. [39] consisted of ratios between the stress and elastic capacities, whilst considering the interactions between shear and tension perpendicular to grain components due to the brittle splitting present in both failure modes. Stresses were estimated elastically for use in the failure criteria, and the criteria are presented in Equations [2-1] through [2-5] [39]. The equation for a failure criterion ($F(\sigma)$) relied on the component stress (σ) and capacity (f), and for conciseness the equations including perpendicular to grain components are presented with both orientation subscripts simultaneously.

$$F_{t0}(\sigma) = \frac{\sigma_L}{f_{t0}} \; if \; \sigma_L \geq 0 \quad [2\text{-}1]$$

$$\mathrm{F_{c0}}(\sigma) = \left|\frac{-\sigma_L}{f_{c0}}\right| if \; \sigma_L < 0 \quad [2\text{-}2]$$

$$F_{t90R|T}(\sigma) = \frac{\sigma_{R|T}^2}{f_{t90}^2} + \frac{\sigma_{LT|LR}^2}{f_v^2} + \frac{\sigma_{RT}^2}{f_{roll}^2} \; if \; \sigma_{R|T} \geq 0 \quad [2\text{-}3]$$

$$F_{c90R|T}(\sigma) = \left|\frac{-\sigma_{R|T}}{f_{c90}}\right| if \; \sigma_{R|T} < 0 \quad [2\text{-}4]$$

$$F_{vR|T}(\sigma) = \frac{\sigma_{LT|LR}^2}{f_v^2} + \frac{\sigma_{RT}^2}{f_{roll}^2} \; if \; \sigma_{R|T} < 0 \quad [2\text{-}5]$$

where subscripts are as follows: *t* indicates tension, *c* indicates compression, *0* refers to parallel to grain in the longitudinal *L* direction, *90* refers to perpendicular to grain in either radial *R* or tangential *T* directions, *v* indicates shear and *roll* indicates rolling shear.

Once a failure criterion was exceeded (i.e. evaluated as being greater than unity), damage in the respective mode was initialized. Damage variables were contained between zero and one, and were prevented from decreasing during unloading. The damage then altered the compliance matrix, which was then inverted into the material stiffness matrix. The final stiffness matrix was multiplied by the new strain to calculate the final stress for the increment. The damaged compliance matrix, C^{dam}, is presented in Equation [2-6] and contains various damage terms (*d*), moduli of elasticity (*E*), shear moduli (*G*), and Poisson's ratios (υ) with subscripts indicating respective axes (1, 2, or 3) or respective material orientations as in the failure criteria [39].

$$\mathbf{C}^{dam} = \begin{bmatrix} \frac{1}{(1-d_0)E_{11}} & -\frac{\upsilon_{21}}{E_{22}} & -\frac{\upsilon_{31}}{E_{33}} & 0 & 0 & 0 \\ -\frac{\upsilon_{12}}{E_{11}} & \frac{1}{(1-d_{90R})E_{22}} & -\frac{\upsilon_{32}}{E_{33}} & 0 & 0 & 0 \\ -\frac{\upsilon_{13}}{E_{11}} & -\frac{\upsilon_{23}}{E_{22}} & \frac{1}{(1-d_{90T})E_{33}} & 0 & 0 & 0 \\ 0 & 0 & 0 & \frac{1}{(1-d_{vR})G_{12}} & 0 & 0 \\ 0 & 0 & 0 & 0 & \frac{1}{(1-d_{vT})G_{13}} & 0 \\ 0 & 0 & 0 & 0 & 0 & \frac{1}{(1-d_{roll})G_{23}} \end{bmatrix} \qquad [2\text{-}6]$$

In order to prevent divisions by zero, the damage variables were limited or caused element deletion before reaching a value of one [39]. The effect of damage was differentiated depending on whether the mode was ductile (in compression) or brittle (in tension and shear). Equations [2-7] and [2-8] defined the damage progression for ductile and brittle modes respectively.

$$d = 1 - \frac{1}{\kappa} \qquad [2\text{-}7]$$

$$\mathrm{d} = 1 - \frac{1}{\mathrm{f}_{\mathrm{max}}^2 - 2\mathrm{G}_\mathrm{f}\mathrm{E}}\left(\mathrm{f}_{\mathrm{max}}^2 - \frac{2\mathrm{G}_\mathrm{f}\mathrm{E}}{\kappa}\right) \qquad [2\text{-}8]$$

where κ represents the greatest stress-capacity ratio ($F(\sigma)$ in the damage equations) for the given component since the start of analysis, f_{max} is the capacity of the component, and G_f is the brittle mode's fracture energy. Additionally, shear damage variables were triggered by more than one criterion and are superposed together. Figure 2.6 illustrates the effect of each of these formulations, with a and b representing Equation [2-7] and [2-8] respectively.

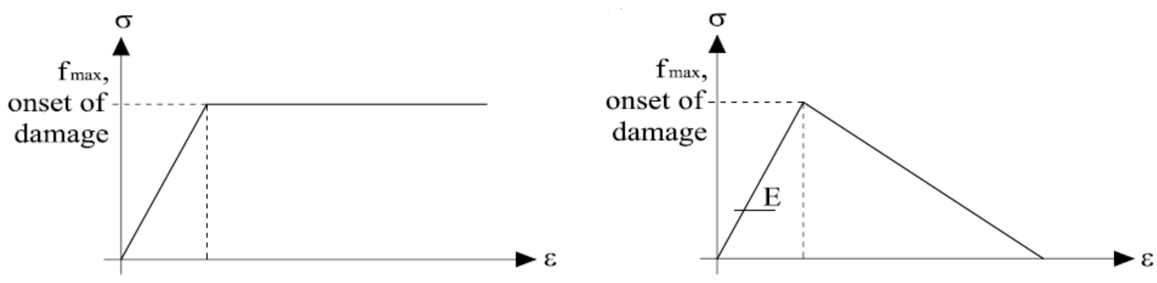

a) b)

Figure 2.6: Effect of damage for a) Ductile modes b) Brittle modes [39]

An artificial viscosity was also implemented for the damage progression in order to stabilize the material damage and improve convergence during nonlinearity. The viscous stabilization was used to control the rate of damage and prevent erroneous solutions at high levels of damage [39]. Mesh dependency was also improved through the use of a crack-band model, which aids in the development of a single localized failure mode regardless of mesh size.

Sandhaas et al. [39] obtained good results in embedment, small-scale specimen, and joint models relative to experimental observations. The material model successfully replicated both ductile and brittle behaviour, and simulations had reasonable accuracy regarding capacity and stiffness using theoretical values in both displacement- and load-controlled scenarios [39]. However, the author noted the lack of literature available for several properties (e.g. shear capacity, fracture energies) and the model was not suited for predicting behaviour dependant on specimen micro-structure. Furthermore, at high levels of damage, stress transfer between nearly collapsed elements and neighbouring elements was compromised. This led to rapid failure not representative of physical behaviour and numerical issues in some models, which were partially alleviated through changes in element and contact formulations [39].

A study by Kaliyanda [42] et al. simulated bolted steel-wood-steel connections in ABAQUS. A set of user-defined field variables (USDFLD) were developed and used to implement progressive failure criteria and the effects of damage. Similar to Sandhaas [43], damage reduced the effective elastic moduli and caused stress redistribution to nearby elements.

Failure modes were developed to be either fibre- or matrix-based, with further designation between tension and compression behaviour. Failure in matrix modes caused damage and degradation in axial properties perpendicular to grain and rolling shear properties, while fibre modes affected properties parallel to the grain and longitudinal shear. Poisson's ratios were also affected following the shear degradation pattern, and if multiple failure modes were initialized all properties were reduced.

In order to reduce computational costs, a displacement-controlled simulation with two planes of symmetry was used, thereby reducing the model domain to a quarter. The model replicated a bolted connection in tension using three-dimensional solid elements for both the steel and timber components, as shown in Figure 2.7. Two joint thicknesses were used, the larger of which was intended to emphasize large three-dimensional deformations and represent large, bolted joints present in mass timber structures.

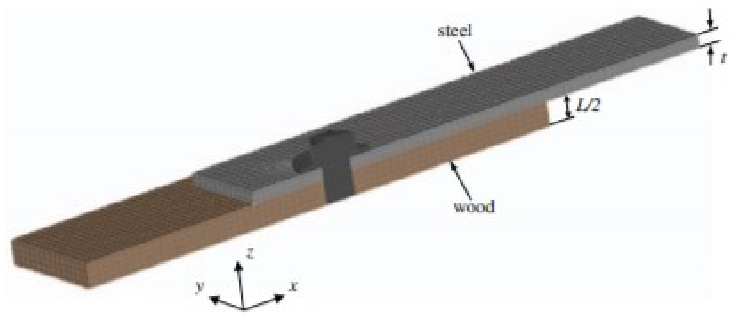

Figure 2.7: Doubly symmetric model of a bolted timber connection [42]

The model was implemented within ABAQUS/Standard, which is commonly used for static applications and used an unconditionally stable implicit formulation which recalculates the global solution matrix at every time-step. Recalculations were necessary during property degradation, which drastically increased runtimes and caused the analysis to prematurely terminate operations due to increment errors despite degradation being limited to 90% [42]. As shown in Figure 2.8, the modeling results showed good correlation with experimental behaviour. Models with shallower timber members captured initial joint stiffness but were unable to match yielding plateaus at higher displacements, while models with thicker depth had better agreement at high displacements but overestimated initial stiffness.

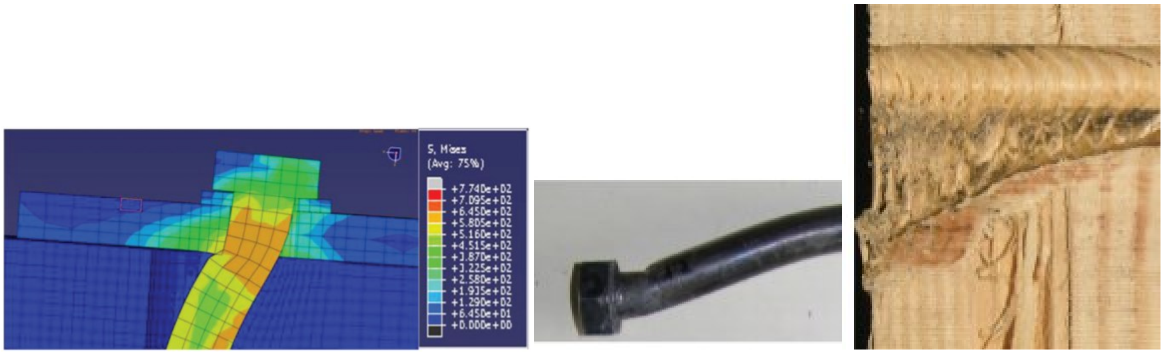

a) b) c)

Figure 2.8: Behaviour comparison images from Kaliyanda et al.: a)ABAQUS joint model b)Deformed bolt head c)Timber crushing damage [42]

Wang et al. [44] utilized a continuum damage approach combined with elastic-plastic damage theory in order to account for permanent deformations caused by compression and bearing loads in timber connections. A subroutine was formulated within ABAQUS/Standard using strain-increments as a basis for calculation. The strain increments were divided into elastic or plastic strain, depending on the evaluation of stress-based failure criteria based on the methodology from Sandhaas [37]. Damage was implemented by Wang et al. [44] using three variables, representing the three axial orientations for wood, which had separate formulations for tensile and compressive behaviour and were combined when considering shear damage. Experimental data was used to calibrate the plastic behaviour and prepare the stiffness and capacity inputs. Viscous regularization and crack-band methods were used to promote convergence and alleviate mesh dependency respectively, and simulations of mortise-and-tenon joints were performed using cyclic displacement-controlled loading. The model could represent the permanent deformation and softening behaviour typical of cyclical compression and joint loadings, but generally overestimated the connection strength and stiffness.

A wood material model was developed by Murray [45] for the LS-DYNA [46] software suite, a finite element environment specifically developed for use in dynamic impact analyses. The model was primarily designed to simulate impacts between motor vehicles and roadside timber elements (e.g. trees, posts). The material model used two failure criteria to initiate damage modified from the Hashin criteria [41] for fibre composites and did not interact with each other. The failure criterion for parallel to grain behaviour considered both axial stress and longitudinal shear stresses, while the failure criterion for perpendicular to grain behaviour considered both radial and tangential representative axes as well as rolling shear. As there is no overlap between the initial criteria, the model generated two entirely separated, but completely and continuously defined, failure surfaces in stress space. These failure surfaces accounted for four failure modes; tension and compression perpendicular and parallel to grain. Shear failures were considered a subset of the respective axial mode, with longitudinal shear contributing to parallel to grain failure and rolling (or perpendicular) shear contributing to perpendicular to grain failure. Damage parallel to grain degraded all stress components, while damage perpendicular to grain only degraded the respective stress components (radial, tangential, rolling shear). This implementation produced catastrophic or complete failure parallel to grain, but localized cracking behaviour perpendicular to grain. This distinction was used to avoid computational issues arising from the low stiffness and strength of timber behaviour perpendicular to grain [45].

The model implemented strain rate effects based on experimental results for some predefined species, with a general adjustment implemented based on material density, impact velocity, and nonlinear parameters for other cases as input by the user. The strain rate effects increase the material capacities used in the modified Hashin criteria [41], and thus expanded the failure surfaces. Greater strain rate effects were implemented perpendicular to grain than parallel to grain. The material model also allowed the user to indicate initial hardening or softening values to modify the constitutive relationships both pre-peak and post-peak.

2.6 Summary

The current state of literature clearly establishes that the wood elements subjected to high strain rates exhibit different behaviours when compared to static loading. Further research has indicated that SDOF modeling can produce reasonably accurate results for the dynamic behaviour of wood but generally cannot account for connection behaviour or multiple failure mechanisms in the same model, which are prevalent in the complex behaviour of mass timber elements such as CLT. More sophisticated finite element methods have been developed, with research efforts focusing on statically loaded wood joints and relatively little contribution to dynamic models. This study intends to contribute to the literature by investigating the viability of full-scale finite element models for simulating wood behaviour at high strain rates.

CHAPTER 3- EXPERIMENTAL PROGRAM

3.1 General

An experimental program was established to evaluate the behaviour of glulam and CLT elements under the effects of simulated far-field blast loads using the University of Ottawa Shock Tube Test Facility. The program included three glulam specimens and three CLT specimens, as presented in Table 3.1.

The CLT and glulam specimens were tested with simply supported boundary conditions in order to characterize their dynamic behaviour. This idealization of the end conditions allowed for direct comparison with existing test results of similar elements and reduced complexity within the analytical methods (discussed in Chapter 5).

For each material, a specimen was subjected to a single blast load as to cause complete failure, in order to establish a baseline for material strength and behaviour as well as compare with analytical methods and other tests. The second approach used in the experimental program includes subjecting a specimen to a blast load corresponding to its elastic limit, and subsequently increasing the blast load to cause failure in the specimen. This procedure was followed in order to investigate possible changes in material behaviour regarding stiffness, strength or both. The third and final approach was to load a specimen in the elastic range and subsequently expose it to increasing blast loads until complete failure is attained. This methodology was intended to evaluate the consistency of member stiffness in dynamic scenarios and help validate the analytical methods for a variety of damage accumulations.

Table 3.1 Specimen Testing Outline

Test Goal	*Glulam Specimen Identifier*	*CLT Specimen Identifier*
Immediate Failure	GL1	CLT1
Elastic Limit	GL2	CLT2
Repeated Flexure	GL3	CLT3

3.2 Specimen Description

All glulam and CLT specimens were produced by Nordic Structures, using spruce-pine-fir (SPF) species group lumber, consisting predominantly of black spruce [47]. The glulam specimens consisted of 86 mm by 178 mm 24F-ES grade members and measured 2.5 m in length.

The CLT specimens consisted of 5 plies, each having a depth of 35 mm, totalling 175 mm panel depth. The panels were cut to a width of 445 mm and a length of 2.5 m, in order to meet the geometrical limitations of the shock tube end-frame. The lay-up consisted of laminates in alternating directions, with the grain running with the major axis of the panel in the outermost and centre plies. The panels were grade E1, with 1950 F_b-1.7E machine stress rated lumber used in the longitudinal plies and No.3/Stud visually graded lumber used in the perpendicular plies [48].

All specimens were stored in humidity-controlled conditions, and the moisture content (MC) was regularly monitored at several locations on each specimen. The specimens were also weighed before testing in order to determine their exact mass, which was used as a modeling input in Chapter 5. The average MC for the CLT specimens was 14.7% with a coefficient of variation (COV) of 0.064. The average mass was determined to be 101.73 kg with a COV of 0.0023. The average MC and mass of the glulam specimens was determined to be 14.0% (COV 0.019) and 20.84 kg (COV 0.0048), respectively.

3.3 Shock Tube Description

All experimental work was performed using the University of Ottawa's Shock Tube Test Facility. The shock tube utilizes pressurized air to generate a variety of uniform reflected pressures and impulses, thereby simulating far-field blast events without the need for explosives.

The shock tube is comprised of three main parts. At the rear of the apparatus, the driver section consists of a cylindrical chamber that is pressurized during testing. This section is comprised of segments, connected with rubber gaskets and heavy hexagonal bolts. The driver pressure determines the peak reflected pressure applied onto the specimen, while the driver length controls the positive reflected impulse. The length can be varied between 305 mm (1 ft) and 5185 mm (17 ft) in increments of 305 mm (1 ft), resulting in a possible maximum positive reflected impulse of 2200 kPa-ms. The maximum reflected pressure that the shock tube is capable of generating is 100 kPa, and the generated blast wave can have a positive phase up to 70 ms. The rear end of the driver is completely sealed and includes a hydraulic retraction system and is pictured in Figure 3.1b, while the front end of the driver uses sets of aluminum foils, collectively referred to as the diaphragm section.

The diaphragm section consists of two separated sets of foils, which together form the diaphragm capacity. The thickness and number of foils vary depending on the combination of pressure and impulse to be applied onto the test specimen. A typical arrangement can be seen in Figure 3.2. The air gap between the foil diaphragms is pressurized concurrently with the driver, such that neither individual diaphragm's capacity is exceeded. Once the desired driver pressure is reached, the section between the foils is promptly drained, resulting in the rupture of both foil sets and thus the release of compressed air as a shockwave. The double-diaphragm firing system allows for better control over the peak pressure and impulse of the wave.

The central section of the shock tube consists of a 6,096 mm long expansion section. This section bridges between the driver section and the end-frame, as shown in Figure 3.1a.

The end-frame assembly includes mounting points, typically used in combination with threaded rods and nuts, as well as twelve release vents (several pictured in Figure 3.3a). The vents are closed prior to the test, and are opened by the shockwave during the test in order to reduce the pressure returning to the driver section. The dimension of the end-frame opening is 2,032 x 2,032 mm (80 x 80 in.) and allows for the testing of large- to full-scale specimens.

While the shock tube can be used for testing wall or slab specimens that fill the entire end-frame opening, a load transfer device (LTD) is required for the testing of beam or column elements with reduced widths, in order to convert the pressure wave from the shock tube into a more suitable applied load. The LTD consists of steel panels reinforced with steel hollow structural sections (HSS) with hinged connections at the top and bottom of the end-frame. In order to cover the openings created by the main panel’s hinges, and thus ensure complete capture of the pressure wave, additional reinforced panels are attached to the transfer device inside the end-frame opening. The load is then transferred to the test specimen through two load-transfer beams, consisting of reinforced steel I-beams bolted to the LTD, as shown in Figure 3.3b. The LTD is capable of freely deflecting up to 200 mm without impairing the transfer of forces to the specimen.

(a) (b)

Figure 3.1: Expansion section (a) and rear view of driver chamber and retraction mechanism (b).

Figure 3.2: Closed diaphragm section, with pressure lines and foils.

(a) (b)

Figure 3.3: View of the end frame side, showing vents and expansion section. (a) View of Load Transfer Device without specimen, with retaining strap. (b)

3.4 Experimental Setup

All specimens were tested dynamically under four-point bending, where two concentrated point loads were applied at the third span points. The clear span between the support points was 2,235 mm, and steel bearing plates were used to prevent crushing at the loading areas.

Eight threaded rods were attached to the shock tube and used to mount various components of the test setup using nuts and washers to prevent horizontal movement, as follows. At both the top and bottom of the test specimen, an HSS with an attached pin was mounted at the end frame, while a larger HSS section was mounted behind the specimen to provide a point of bearing and to house the load cell, as shown in Figure 3.4. The assembly was vertically stabilized using adjustable steel posts and blocking shims, securing the large HSS components between the laboratory floor and ceiling. Overviews of this assembly are shown in Figure 3.4 and Figure 3.5 for glulam and CLT, respectively.

The simply supported end conditions for the glulam elements were provided by using sets of notched plates and pins at the load cell, as shown in Figure 3.6. This permitted rotation at the support point while still transferring reaction forces and preventing localized crushing. For the CLT specimens, the load cell was secured using an HSS section with an additional steel bar welded onto its face as a contact point. Steel bearing plates were nailed into the CLT to prevent localized crushing and, in combination with the round bar, allowed for free end rotation. The mounted load cell is shown in Figure 3.7a, while the CLT specimen with attached bearing plates is shown in Figure 3.7b. For all tests, the assembly was hand tightened in order to prevent vertical movement, while avoiding excessive clamping forces which could cause crushing or partial fixity of the end boundary conditions. Scaled diagrams of the LTD, glulam setup and CLT setup are presented in Figure 3.8 through Figure 3.10.

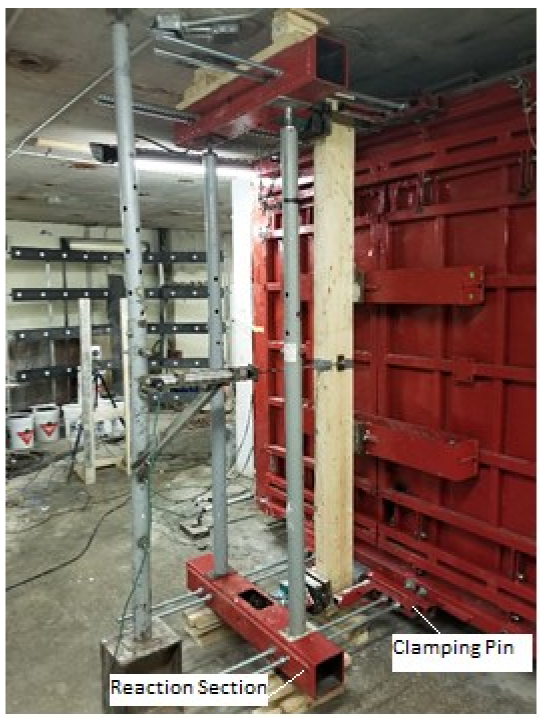

Figure 3.4: Image of experimental setup for glulam, annotated lower components.

Figure 3.5:Image of experimental setup for CLT

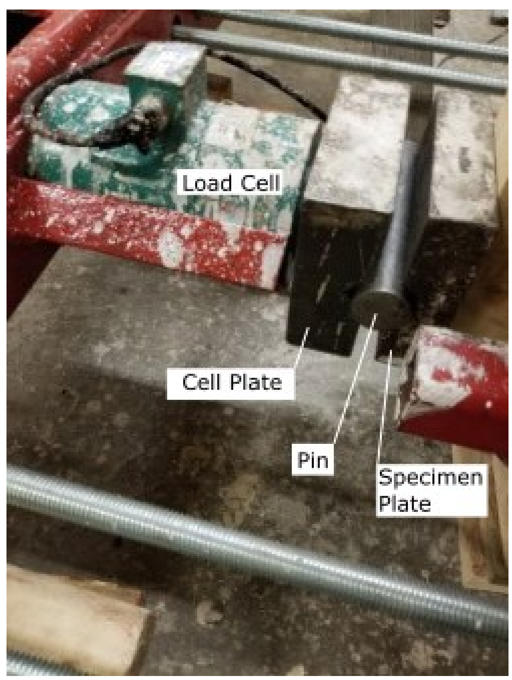

Figure 3.6: Reaction assembly detail for glulam, with mounted load cell and notched plate support system

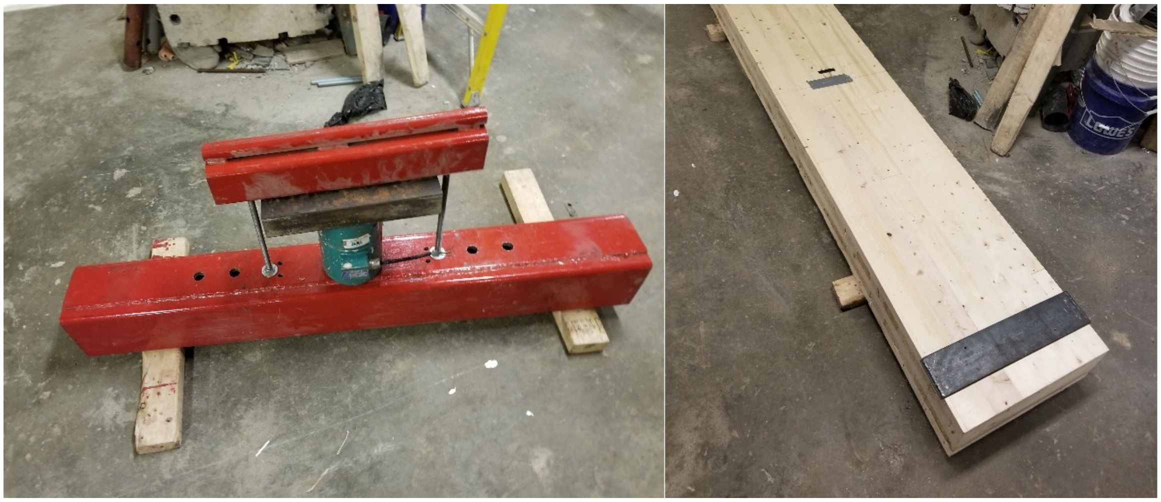

a) CLT reaction assembly b) CLT specimen with bearing plate

Figure 3.7: CLT end details

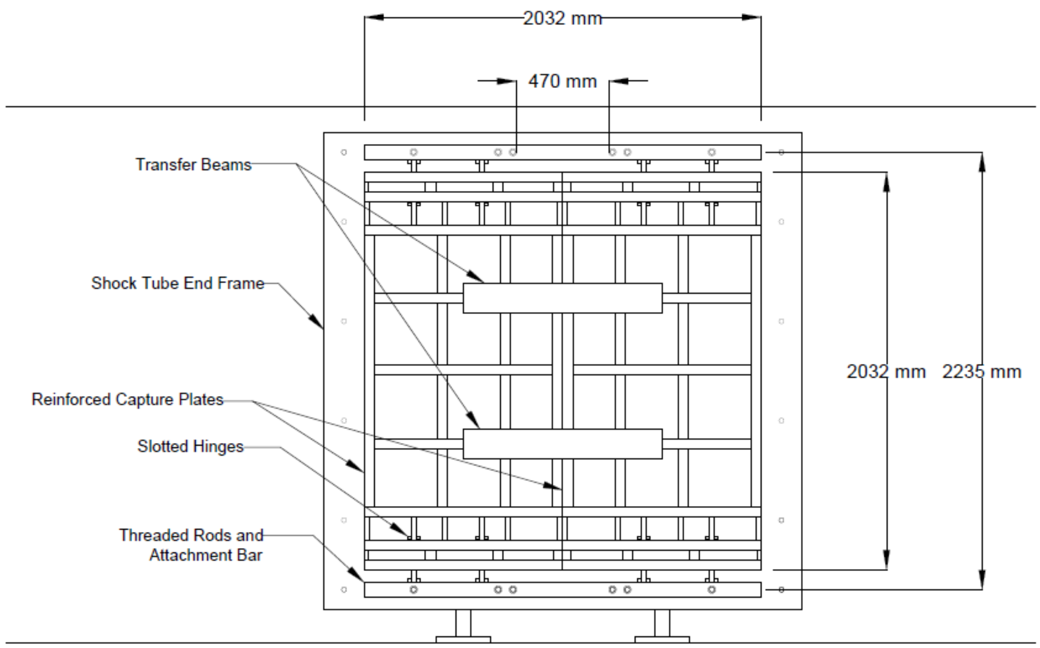

Figure 3.8: Head-on diagram of load transfer device

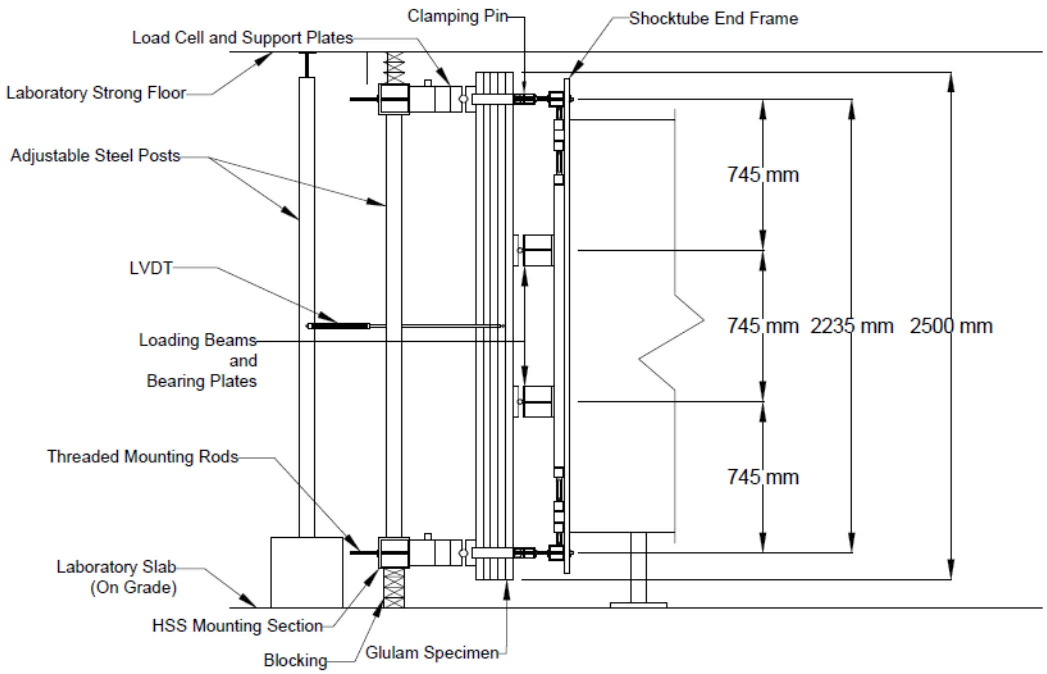

Figure 3.9: Side diagram of experimental setup for glulam

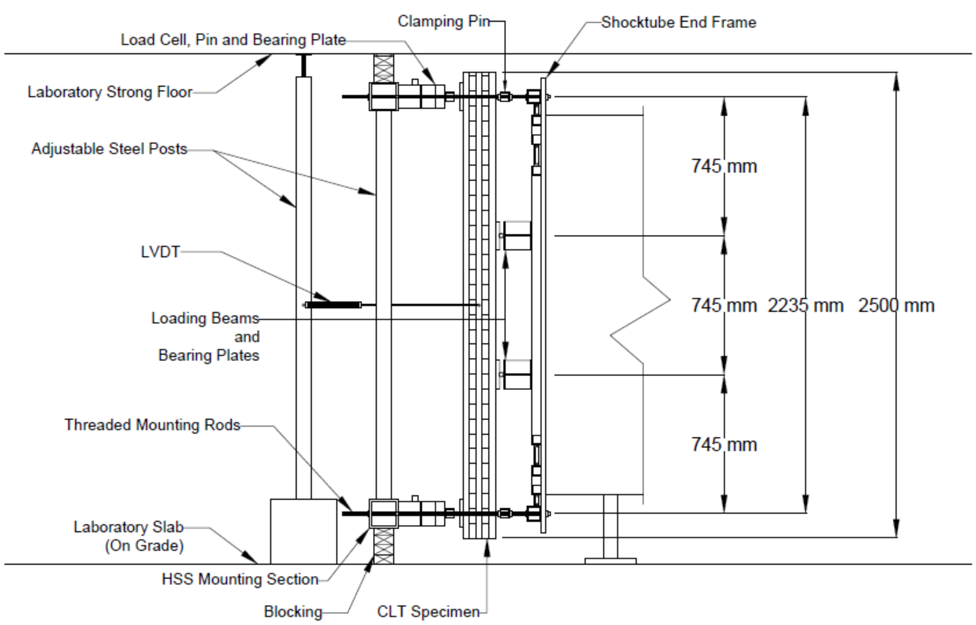

Figure 3.10: Side diagram of experimental setup for cross-laminated timber

3.5 Instrumentation and Methods of Measurement

Two Phantom VEO 410L high-speed cameras were used to capture the overall behaviour of the specimens during the dynamic testing and to allow motion analysis to be conducted, if required. The cameras operated at 2,000 fps, with one aimed along the shock tube opening and another oriented to provide an overview of the tests. Increased lighting, provided using two spotlights, was required for the cameras to record videos at the desired frame rate and clarity. The laboratory layout is presented in Figure 3.11.

Mid-span and end-frame displacements were measured using linear variable differential transducers (LVDTs). An adjustable steel jack post was used to support the LVDT attached to the test specimen. The displacement-time history of the shock tube itself was measured to account for shock tube movement during testing since the deflection of the test specimens was measured relative to the laboratory floor.

Two 350-ohm strain gauges with dimensions of 6.0 mm x 12.5 mm were adhered to the tension and compression faces at mid-span.

Two piezoelectric pressure sensors were installed at the side and base of the shock tube end-frame to record the reflected pressure-time histories of the generated shockwaves, as well as to act as a trigger for the data acquisition system (DAS) and cameras. Finally, two compression load cells (Revere model 92/93) were utilized to capture the reactions (see Figure 3.6 and Figure 3.7a). For all tests, the DAS recorded measurements at a rate of 5,000 readings per second.

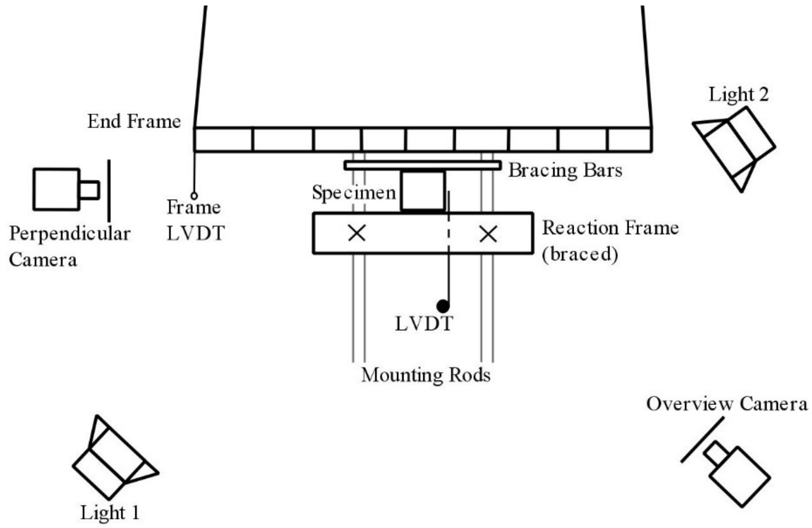

Figure 3.11: Labelled top-view diagram of general testing setup, not scaled.

CHAPTER 4- EXPERIMENTAL RESULTS

4.1 General

The experimental results of the dynamic testing on both glulam and CLT specimens are presented in this chapter. As discussed in Chapter 3, the tests were conducted on full-scale members with idealized simply-supported boundary conditions under four-point bending. All tests were conducted with a driver length of 2,745 mm (9 ft). For each specimen, the mass, moisture content, and the parameters of each blast test (also referred to as a “shot”) are described. These parameters include the driver pressure, peak reflected pressure, positive reflected impulse and maximum displacement. Presented times are measured from the arrival of the blast wave.

The overall member behaviour during the test was documented by images taken either during or after the shot, and the displacement-, resistance- and load-time histories are summarized. For clarity in the figures, wood cracks were outlined using black marker following each shot. A summary of experimental results is presented at the end of the chapter in Table 4.1, with further details presented in Appendix A.

4.2 Nomenclature

Glulam and CLT tests are identified with the prefix GL and CLT, respectively, followed by the specimen number. In order to identify specific shots, a sequential identifier is added thereafter. For example, CLT3.2 refers to the second blast test for the third CLT specimen.

The faces of the specimen are referred to as tension or compression faces when applicable, while the sides are referred to as left and right side as indicted in Figure 4.1.

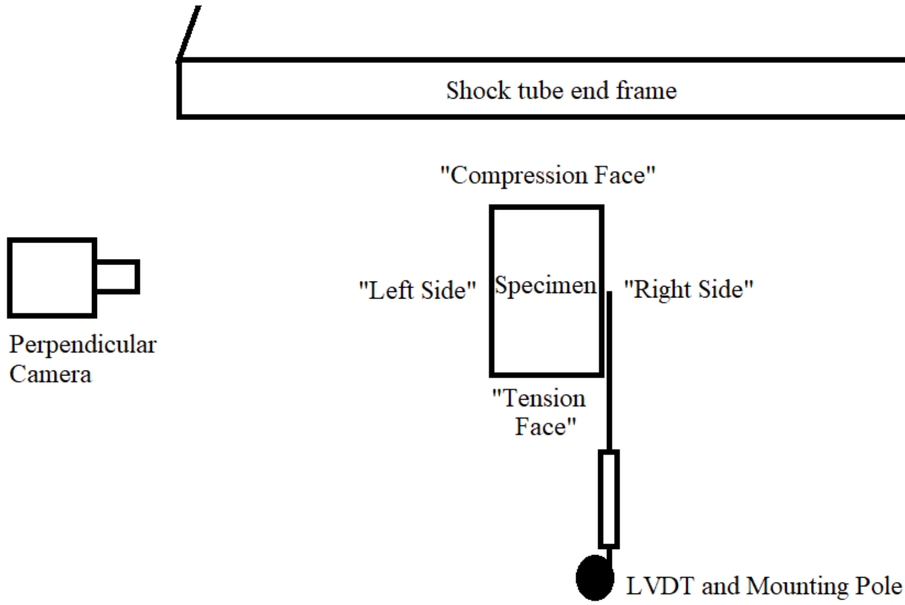

Figure 4.1: Specimen face nomenclature, with reference to experimental setup

The CLT specimens used in the tests consisted of five-ply panels. When referring to a specific ply, a numeric index is used, whereby the plies are counted from the loaded (or compression) face towards the outermost (or tension) face. As shown in Figure 4.2, the ply that is closest to the shock tube is denoted as the first ply, while the fifth ply is the farthest away from the shock tube end frame.

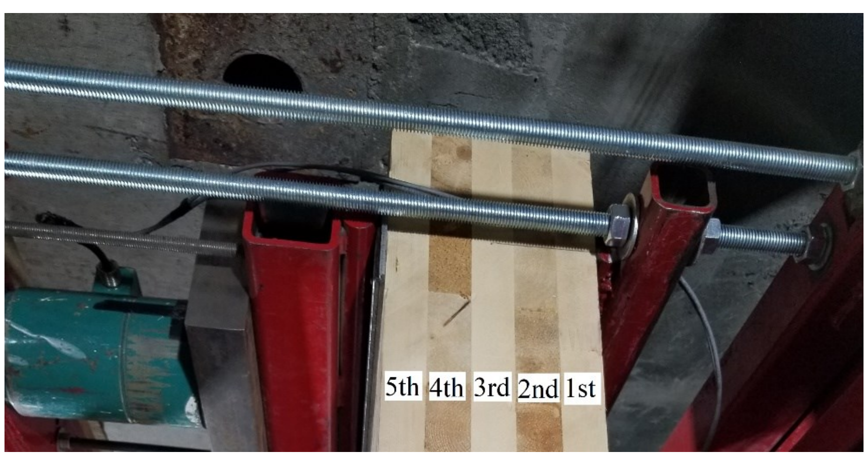

Figure 4.2: CLT specimen end, left side, with annotated ply order

4.3 Glulam Members

A total of six full-scale dynamic tests were performed on three glulam specimens. The first specimen, GL1, was subjected to a single shot, where it was loaded to failure. Specimen GL2 was subjected to two shots, where in the first shot it was loaded to a point near its elastic limit, while it was loaded to failure during the second shot. GL3 was subjected to a total of three increasing dynamic loads until failure was observed during the third shot.

4.3.1 Test GL1.1

Specimen GL1 weighed 20.9 kg and had an average moisture content of 14%. No finger joints were present within the mid-span region. The specimen set up and failure mode is presented in Figure 4.3. The member was tested using a driver pressure of 140.0 kPa, resulting in a peak reflected pressure of 22.3 kPa and a positive reflected impulse of 221.3 kPa-ms over a positive phase duration of 20 ms. The specimen's maximum mid-span displacement was 30.5 mm, which occurred 27 ms into the test. Maximum displacement was reached just after the mid-span failure, which is presented in Figure 4.3b.

a) b) c)

Figure 4.3: a) Specimen GL1 before testing b) Failure during test GL1.1 c) Failure cracks, left side

The significant cracks in the failure region are contained to the middle third of the specimen and extend less than halfway though the member cross-section, as shown in Figure 4.3c. The member experienced rebound after failure, but it sustained significant permanent damage. Fractures initiated at 20.0 ms following the arrival of the blast wave, and crack propagation was observed until 26.0 ms.

4.3.2 Test GL2.1

The moisture content of the second specimen, GL2, was measured to be 14% before testing, while the mass was found to be 20.7 kg. The specimen had no notable defects or damage before testing. It was subjected to a driver pressure of 180 kPa, which resulted in a peak reflected pressure of 30.2 kPa and a positive reflected impulse of 277.0 kPa-ms. The duration of the positive phase was 20.4 ms, and the specimen reached a maximum displacement of 32.7 mm in 23 ms. Some damage was initiated from a finger joint, as shown in Figure 4.4.

Figure 4.4: Minor splitting failure in test GL2.1, post-test

The specimen was able to return to the original position during this shot, and the resulting data is representative of elastic behaviour. The edge damage was therefore considered minor, as it only affected a small portion of the overall section and originated at a finger joint outside of the maximum flexural stress region (i.e. outside of the mid-span region).

4.3.3 Test GL2.2

During the second test of specimen GL2, a driver pressure of 191.7 kPa was used to generate a peak reflected pressure of 34.9 kPa. The positive phase duration was 20.4 ms, and the positive reflected impulse was 295.2 kPa-ms. The specimen failed completely, reaching a maximum displacement of 67.0 mm at 71 ms. The failure initiated at approximately 19.5 ms at mid-span through mid-depth, as shown in Figure 4.5a, and the propagation of cracks continued until approximately 28.5 ms.

a) b) c)

Figure 4.5: a) Initiation cracks during test GL2.2 b) Failure cracks left side c) Failure cracks right side

The specimen failed in flexure, with diagonal cracks extending through the majority of the cross-section as shown in Figure 4.5b and Figure 4.5c. The cracks spread diagonally away from the tension face, extending past the load points and splintering the mid-span tension face. The part of the member that previously split during test GL2.1 broke off the specimen and was thrown as debris.

4.3.4 Test GL3.1

The third specimen, GL3, had a mass of 20.92 kg and an average moisture content of 14% before testing. There were no notable defects on the tension face prior to testing. A driver pressure of 70.3 kPa was used to load the specimen, resulting in a peak reflected pressure of 12.2 kPa and a positive reflected impulse of 115.2 kPa-ms. The duration of the positive phase was 18.2 ms, and the specimen reached a maximum mid-span displacement of 12.7 mm at a time of 23 ms. The specimen remained elastic throughout the test with no observable damage, as shown in Figure 4.6.

Figure 4.6:Specimen after test GL3.1

4.3.5 Test GL3.2

During the second test, specimen GL3 was exposed to a driver pressure of 152.4 kPa. This resulted in a maximum reflected pressure of 25.2 kPa and a positive phase reflected impulse of 239.7 kPa-ms, with a duration of 19.8 ms. A maximum displacement of 28.5 mm was measured at the member's mid-span 23 ms after shock wave arrival. A superficial fracture, shown in Figure 4.7b, occurred during the test: a small section of wood near the beam edge split from the main member, but the member did not have any noticeable permanent deflection.

a) b)

Figure 4.7: a) Location of superficial crack after test GL3.2 b) Close-up of damaged section

4.3.6 Test GL3.3

A driver pressure of 199.3 kPa was used in test GL3.3, which resulted in a peak reflected pressure of 35.5 kPa. The positive reflected impulse was 312.6 kPa-ms and the positive phase duration was 20.4 ms. A maximum displacement of 53.9 mm was reached in 32.6 ms, during flexural failure. The extent of failure is shown in Figure 4.8.

a) b) c)

Figure 4.8: Failure cracks for test GL3.3: a) Left side b)Tension face c)Right side

The specimen splintered in flexure throughout the mid-span. Failure initiated 15.5 ms following the arrival of the shock wave. The failure cracks extended past the loading points and passed knots in the laminations, developing until a tome of 30.0 ms. The vertical extension of the developed cracks prevented the catastrophic fracture of the majority of the mid-span cross-section, as most of the crack tips were no longer able to reverse direction and progress through the cross-section, as developed in GL2.2.

4.4 CLT Members

A total of three full-scale five-ply CLT specimens were tested by six dynamic tests. Panel CLT1 was subjected to a single shot and was loaded to failure. Specimen CLT2 was subjected to three shots. In the first shot, it was brought past its elastic limit, which caused partial failure of the outer laminates. The specimen was then loaded to complete failure in the fourth and fifth plies during the second shot, thereby reducing the effective residual specimen to a three-ply panel. Finally, test CLT2.3 resulted in member failure. CLT3 was subjected to a total of two shots. The first test (CLT3.1) was an elastic shot, which resulted in fully elastic behaviour of the panel, while rolling shear failure was observed during the second test.

4.4.1 Test CLT1.1

Specimen CLT1 had a mass of 101.68 kg and an average moisture content of 14% before testing. No notable defects were observed. The panel was exposed to a driver pressure of 555.0 kPa, resulting in a peak reflected pressure of 78.5 kPa and a positive reflected impulse of 755.0 kPa-ms over a positive phase duration of 25.8 ms. The specimen displaced to a maximum of 275.6 mm over 95.6 ms and failed, as shown in Figure 4.9.

a) b)

Figure 4.9:Failed state overview of specimen CLT1: a) Left side b) Right side

Based on the high-speed recording, splintering flexural failure was initiated in the fifth ply approximately 13 ms following the arrival of the shock wave, and was followed by the development of visible transverse cracks (at approximately 13.5 ms). It is likely that these failure mechanisms developed simultaneously, as cracks in the transverse layers are difficult to identify at initiation. Further analysis of the high-speed footage suggests a third ply failure occurring at approximately 26.5 ms. Large separations between the plies were present in the failed state of the member, due to the combination of fractures in longitudinal layers and separation from the transverse layers. The finger joints between laminates failed in several locations, an example of which is shown in Figure 4.10a. Compressive failure was also present in the compressive face, as shown in Figure 4.10b.

a) b)

Figure 4.10: CLT1.1 failure details: a) Finger joint failure b) Compression wrinkling

4.4.2 Test CLT2.1

The second specimen had notable gaps between lamination in the transverse plies, examples of which are shown in Figure 4.11a. Panel CLT2 weighed 102.04 kg and had an average moisture content of 16%. A driver pressure of 380 kPa was used, which resulted in a peak reflected pressure of 54.7 kPa. The positive phase reflected impulse was 522.6 kPa-ms and the phase duration was 20.8 ms. The specimen sustained minor damage from the blast load, as pictured in Figure 4.11, and reached a maximum displacement of 34.4 mm, which occurred 22.8 ms into the test.

a) b) c)

Figure 4.11: a) Transverse gaps in CLT2 before testing b) Minor damage on tension face c) Rolling shear damage, lower right side

Non-critical fractures occurred in the tension face of the panel, but as shown in Figure 4.11c the primary damage was rolling shear cracks concentrated in the lower half of the panel's transverse plies. The combination of the minor fractures and vertical cracking near the ply edge (especially prevalent in the fourth ply as pictured in Figure 4.12) indicated degradation in panel composition and a shift towards three-ply behaviour.

a) b)

Figure 4.12:a) Vertical crack on right side b) Right side rolling shear cracks

4.4.3 Test CLT2.2

Since the panel was reduced to three-ply following fractures in the fourth and fifth plies, a lower driver pressure was used in test CLT2.2 compared to that used in CLT2.1. The specimen was subjected to a driver pressure 324.1 kPa. This applied a peak reflected pressure of 51.4 kPa onto the panel, with a positive reflected impulse of 458.6 kPa-ms and a positive phase duration of 21 ms. The specimen reached a maximum mid-span displacement of 53.9 mm at a time of 27 ms, before rebounding. Additional damage was observed during the test, largely related to propagation of existing cracks in the transverse plies, as shown in Figure 4.13.

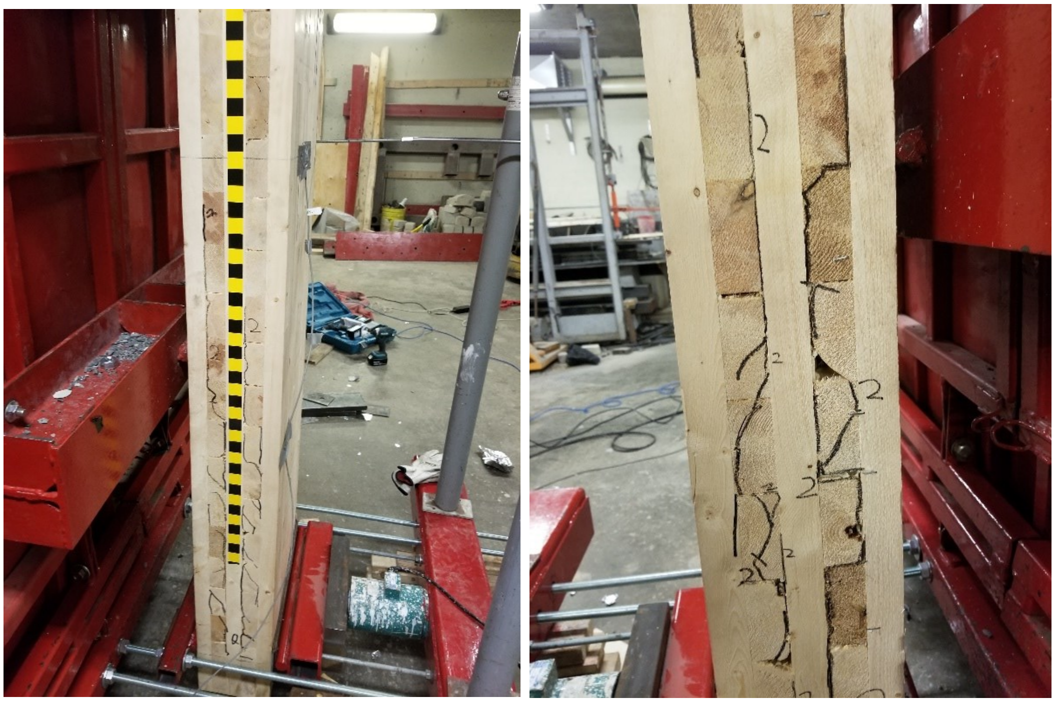

a) b)

Figure 4.13: Propagation of transverse shear cracks: a) Left side b) Right side

The propagation of the rolling shear cracks extended the affected region to the lower support on both the left and right side, as well as connecting the isolated cracks that formed during test CLT2.1. A crack was also started in the second ply on the left side, almost reaching the mid-span of the specimen as pictured in Figure 4.13a. A minor crack in the tension face also formed.

4.4.4 Test CLT2.3

During the third test, a driver pressure of 375.1 kPa was used to generate a peak reflected pressure of 55.8 kPa. The positive phase had a duration of 21 ms and a total impulse of 511.7 kPA-ms. A maximum displacement of 106.2 mm occurred at a time of 41.4 ms. Failure was observed to affect a large portion of the panel, as both the separation of transverse plies in rolling shear action and rupture of the fifth ply in flexure occurred (pictured in Figure 4.14b).

a) b) c)

Figure 4.14: a) Tension face, with flexural fractures b) Point of maximum displacement, illustrating failure behaviour c) Crack extension past support and through end of panel

The failure behaviour in this test consisted of a combination of expansion of earlier rolling shear cracks (16.5 ms) and flexural rupture of the fifth ply caused by the severe curvature of the tension face (17.5 ms). Significant vertical cracking at the joint between the fourth and adjacent plies occurred before the start of the flexural fracture, and a thin lamination was partially detached and thrown as debris. Comparatively minor progression of the previous transverse cracks occurred, most notably extending past the lower support and to the end of the specimen as shown in Figure 4.14c.

4.4.5 Test CLT3.1

Specimen CLT3 had no significant defects. It weighed 101.48 kg and had a moisture content of 14% before testing. The panel was subjected to a driver pressure of 227.5 kPa. The resulting blast wave imparted a peak reflected pressure of 40.3 kPa and a reflected impulse of 359.4 kPa-ms over a positive phase duration of 20.4 ms. A maximum displacement of 22.2 mm was observed 19.2 ms into the test. The panel behaved elastically, with no visible damage present after the test.

4.4.6 Test CLT3.2

A driver pressure of 550.2 kPa was used during test CLT3.2, which resulted in a peak reflected pressure of 40.3 kPa and a positive reflected impulse of 743.4 kPa-ms. The duration of the positive phase was 25.6 ms. The panel exhibited rolling shear failure, as shown in Figure 4.15, and reached a maximum displacement of 105.3 mm over 44.4 ms.

a) b) c)

Figure 4.15: a) Undamaged specimen before testing b) Development of rolling shear cracks during test c) Damaged state of panel, right side

The specimen failed through rolling shear action, with no compressive yielding observed and only minor cracks present on the tension face. The damage was primarily contained to the transverse plies, between the loading points and supports. The cracks initiated 11.0 ms after the arrival of the blast wave and had a consistent trend in the transverse plies, running near the tension face at the supports and the compression face near the load points.

4.5 Experimental Data Analysis

All presented displacements were measured relative to the initial specimen position from the shock tube end-frame. This was done by measuring the displacements of both the specimen's mid-span and the shock tube relative to the laboratory floor to determine the specimen's net movement. Additionally, the signs of the displacement and reaction force readings have been presented such that the positive phase of the blast results in positive displacement and reaction values. A typical pressure-impulse chart is shown in Figure 4.16, alongside graphs representative of general reaction and displacement responses presented in Figure 4.17 and Figure 4.18, respectively. The reaction data from the top and bottom load cells are reasonably similar, as expected with symmetric loading, while the displacement history is characteristic of elastic behaviour. Further graphs and details for all tests are presented in Appendix A.

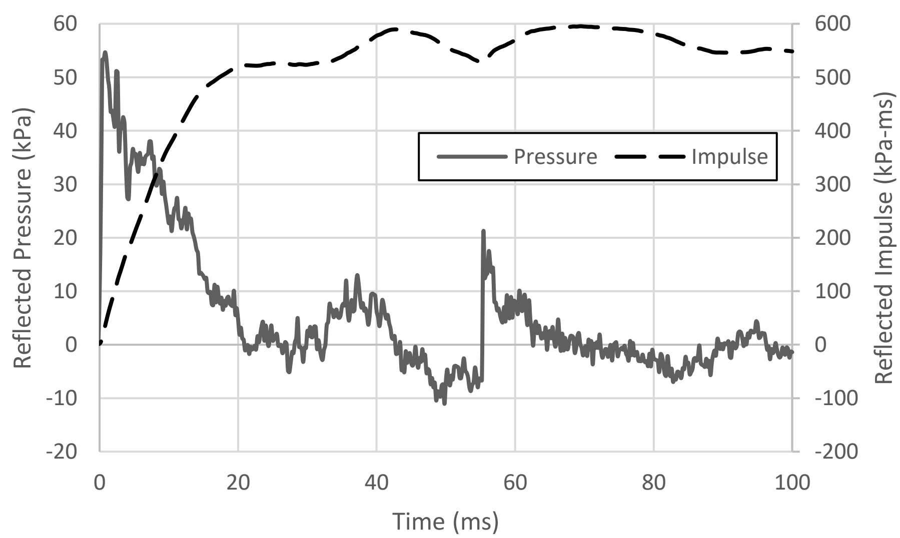

Figure 4.16: Typical pressure- and impulse- time histories, from blast test CLT2.1

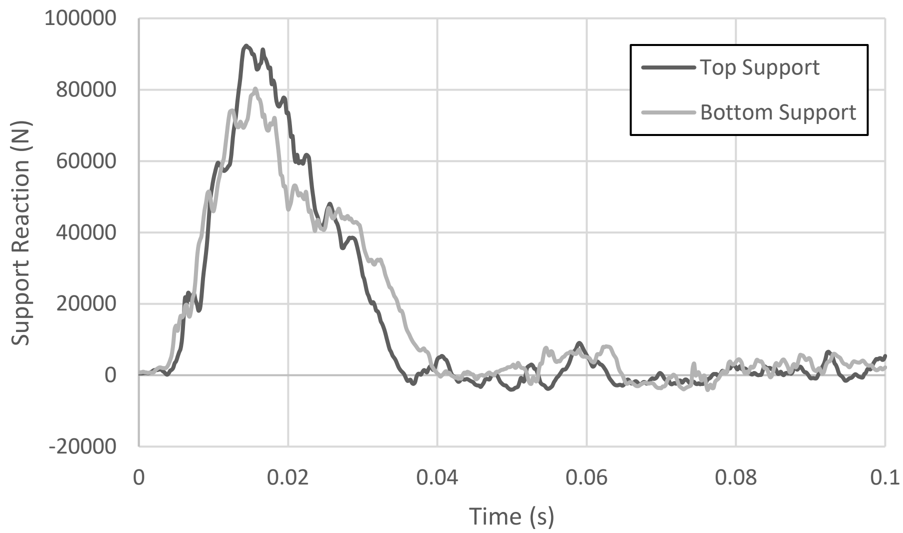

Figure 4.17: Typical reaction-time history, from test CLT2.1

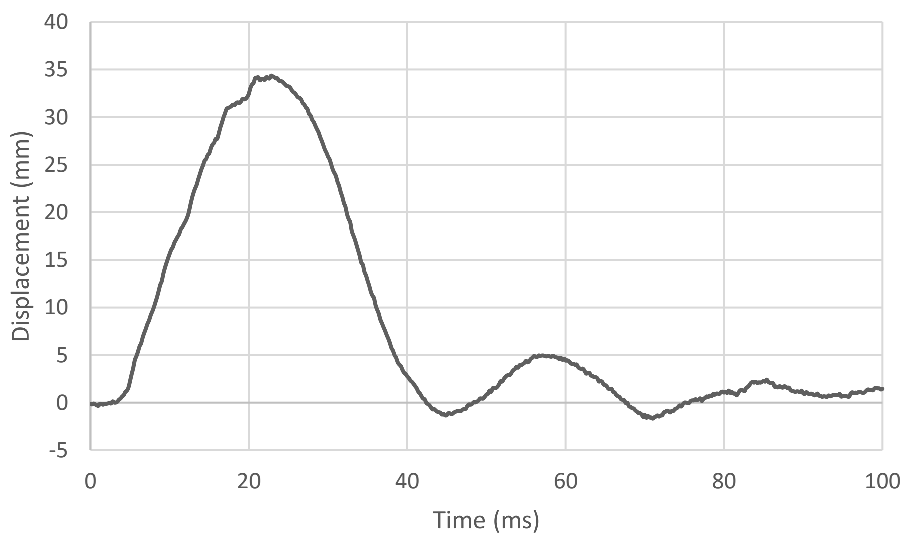

Figure 4.18: Typical (elastic) mid-span displacement-time history, from test CLT2.1

The resistance curve for each specimen was calculated as a function of the experimental pressure-, reaction-, and displacement-time histories. The expression derived by Lacroix [49], which relates the dynamic reactions at the support, *V(t)*, with the applied load, *F(t)*, and the overall resistance *R(t)*, was utilized to obtain the specimen resistance curve. This entails idealizing the LTD's mass as a set of discrete masses at the points of loading. The relationship, presented in Equation [4-1], was derived from moment equilibrium for half the specimen's span taken about the equivalent inertial force vector, whose position from the support is represented by x_{eq} [49]. Figure 4.19 presents the theoretical system the equation represents [49], considering the relationship between moment capacity M_R and ultimate member resistance R_F, as shown in Equation [4-2] [17].

$$R(t) = \left\{\frac{6}{L}\right\}\left\{V(t)x_{eq} + 0.5\left[\frac{L}{3} - x_{eq}\right]F(t)\right\} \qquad [4\text{-}1]$$

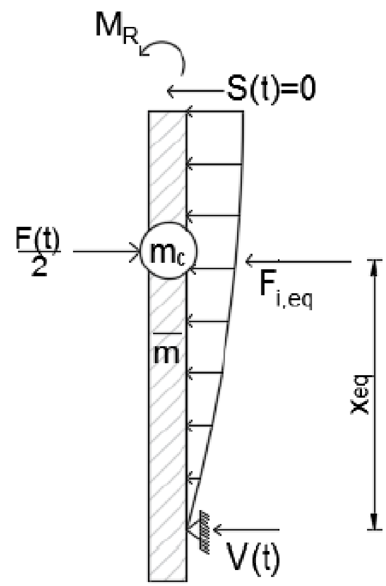

Figure 4.19:Idealized system for the derivation of resistance equations [49]

$$M_R = \frac{R_F \times L}{6} \qquad [4\text{-}2]$$

The position of the resultant inertial force x_{eq} was derived and presented in Equation [4-3], where m_c is the discrete mass at the load point for four-point bending and $\overline{m}$ is the specimen's distributed mass. When considering the behaviour of the LTD and specimen together, a reduced tributary area (equal to 3.55 m^2) on the LTD was considered as the effective load transfer area and the LTD mass was reduced accordingly (to 284 kg) [49]. Therefore, the value of the concentrated mass m_c in Equation [4-3] is half the LTD's effective mass (142 kg in this case).

$$x_{eq} = \frac{0.102\overline{m}L^2 + 0.29m_cL}{0.319\overline{m}L + 0.870m_c} \qquad [4\text{-}3]$$

4.6 Resistance Curves

The experimental dynamic resistance curves for each specimen are presented in Figure 4.20 through Figure 4.25, with all shots for a given specimen plotted simultaneously. Key experimental data is summarized in Table 4.1, including driver and reflected pressures, positive impulse and duration, and maximum displacement and resistance. Further experimental data and individual charts can be found in Appendix A for each test.

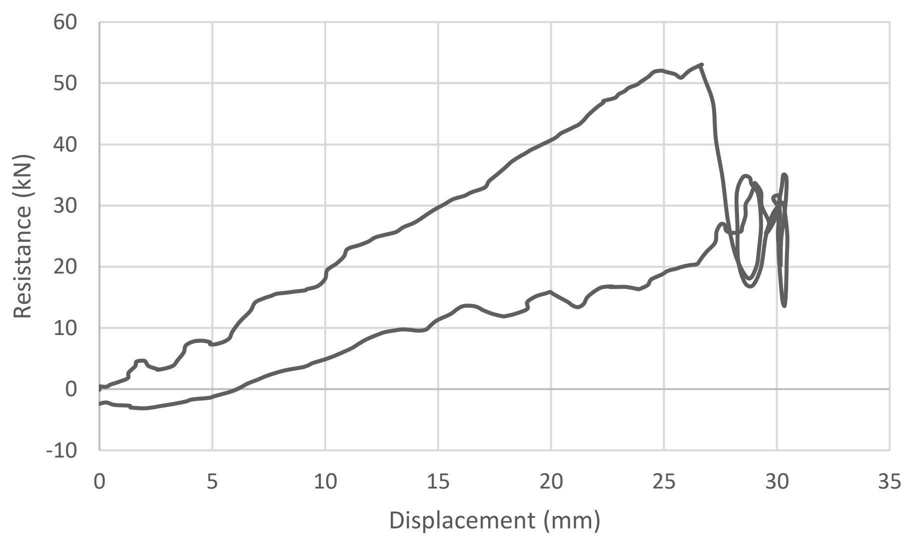

Figure 4.20: Dynamic resistance curve for test GL1.1

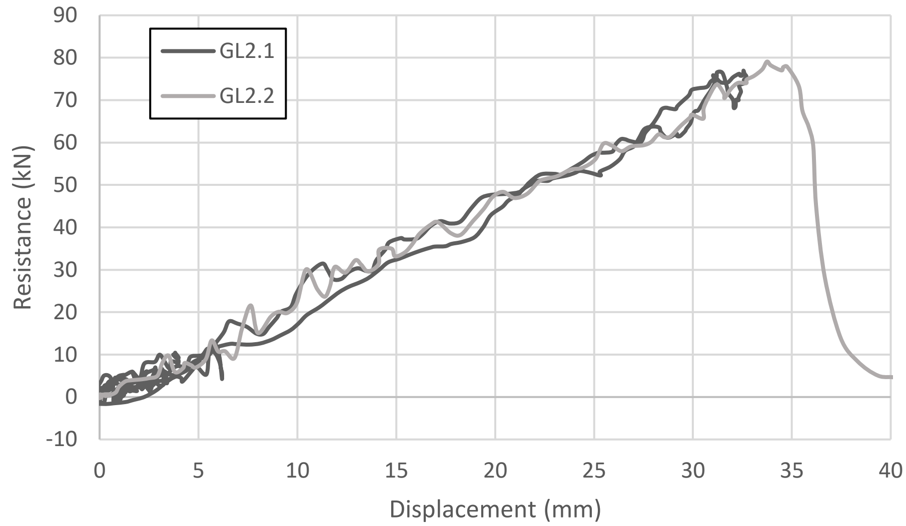

Figure 4.21:Dynamic resistance curves for GL2

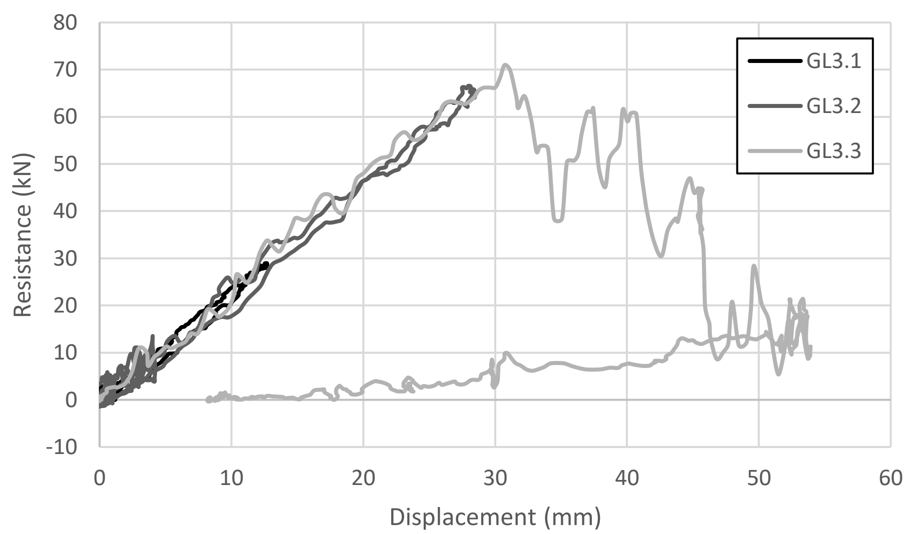

Figure 4.22: Dynamic resistance curves for GL3

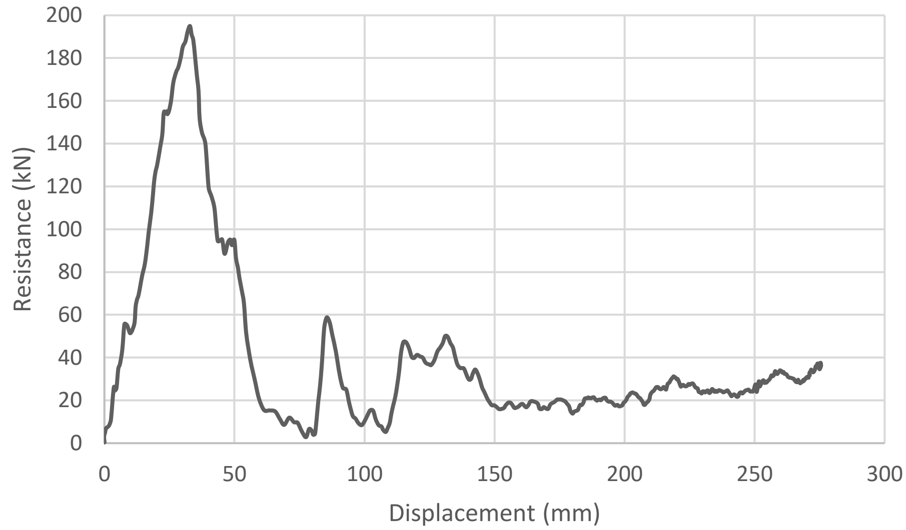

Figure 4.23:Dynamic resistance curve for test CLT1.1

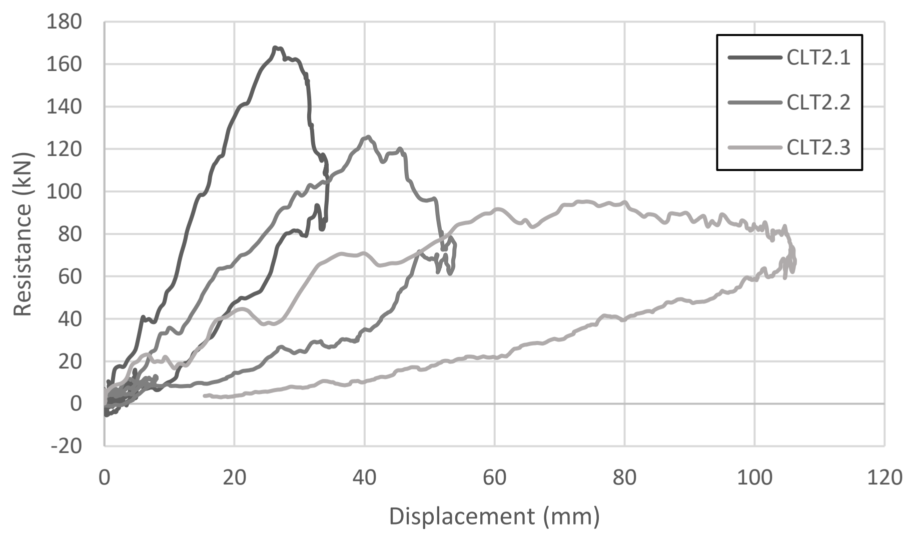

Figure 4.24: Dynamic resistance curves for CLT2

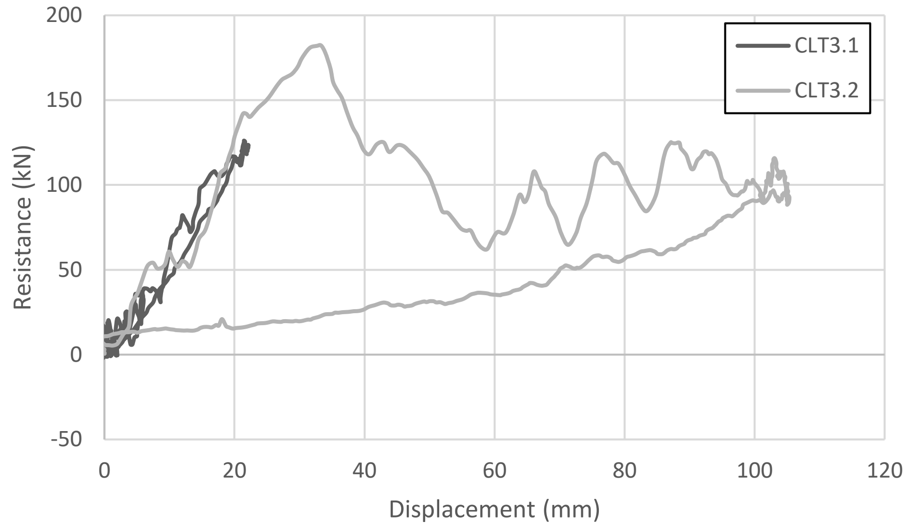

Figure 4.25: Dynamic resistance curves for CLT3

Table 4.1: Summary of Full-Scale Dynamic Test Results

	ID[1]	P_d[2]	P_r[3]	i_s[4]	t_o[5]	Δ_{max}[6]	t_Δ[7]	R_{max}[8]	Δ_{Rmax}[9]	t_{Rmax}[10]
		kPa	kPa	kPa-ms	ms	mm	ms	kN	mm	ms
Glulam	GL1.1	140.0	22.3	221.3	20.0	30.5	27.0	54.5	26.2	21.4
	GL2.1	180.0	30.2	277.0	20.4	32.7	23.0	77.0	32.6	22.6
	GL2.2	191.7	34.9	295.2	20.4	67	71.0	79.1	33.7	20.2
	GL3.1	70.3	12.2	115.2	18.2	12.7	23.0	28.9	12.7	23.8
	GL3.2	152.4	25.2	239.7	19.8	28.5	23.0	66.5	28.0	21.8
	GL3.3	199.3	35.5	312.6	20.4	53.9	32.6	71.0	30.7	16.8
CLT	CLT1.1	555.0	78.5	755.0	25.8	275.6	95.6	195.0	32.9	13.0
	CLT2.1	380.0	54.7	522.6	20.8	34.4	22.8	167.8	26.2	15.0
	CLT2.2	324.1	51.4	458.6	21.0	53.9	27.0	125.7	40.6	19.2
	CLT2.3	375.1	55.8	511.7	21.0	106.2	41.4	95.3	73.5	22.2
	CLT3.1	227.5	40.3	359.4	20.4	22.2	19.2	126.1	21.5	21.4
	CLT3.2	550.2	81.1	743.4	25.6	105.3	44.4	182.2	33.5	13.4

1: Test Identification Code

2: Driver Pressure

3: Peak Reflected Pressure

4: Positive Phase Impulse

5: Positive Phase Duration

6: Maximum Displacement

7: Time of Maximum Displacement

8: Maximum Resistance

9: Displacement at Maximum Resistance

10: Time of maximum resistance

CHAPTER 5- ANALYTICAL METHODS

5.1 General

This chapter presents the methodology used for the analytical prediction of the behaviour of full-scale timber elements subjected to simulated blast loading. SDOF and FEA approaches are discussed, and the results of each methodology are presented. The analytical results will be referenced using the identification nomenclature used throughout the experimental tests.

The inputs and simplifications for the SDOF analysis are summarized, as well as the underlying theories. The discussion of the finite element model includes the model inputs and assumptions, the choice of analytical software, the development of the material model, and the modeling techniques employed in the analyses.

Since flexural bending is the predominant response of timber elements subjected to blast loading, with failure occurring near mid-span, the SDOF analyses were conducted solely based on this failure mode. Contrarily, the finite element model also involved other failure modes, such as longitudinal shear, rolling shear, and tension perpendicular to grain. For both the SDOF and finite element models, damping was neglected due to the lack of influence on the maximum response of actual systems over short timeframes [17].

Additionally, the experimental pressure-time histories were replaced by an equivalent triangular loading (as described in section 1.4) for both analytical approaches. This simplification is implemented due to its common use in SDOF analysis, as well as to reduce the input complexity and file size for the finite element program. Using the same simplified loading across both methods also ensures that the results are comparable. The equivalent pressure-time histories obtained from each test are presented in Table 5.1, and an example of the comparison between an experimental pressure-time history and the idealized pressure used in the analytical approach is presented in Figure 5.1.

Table 5.1: Equivalent Blast Pressure-Time Histories for Analysis

Test ID	Peak Reflected Pressure P_R (kPa)	Positive Impulse i_s (kPa-ms)	Equivalent Phase Duration t_d (ms)
GL1.1	22.3	221.3	19.8
GL2.1	30.2	277.0	18.4
GL2.2	34.9	295.2	16.9
GL3.1	12.2	115.2	18.9
GL3.2	25.2	239.7	19.0
GL3.3	35.5	312.6	17.6
CLT1.1	78.5	755.0	19.2
CLT2.1	54.7	522.6	19.1
CLT2.2	51.4	458.6	17.8
CLT2.3	55.8	511.7	18.3
CLT3.1	40.3	359.4	17.8
CLT3.2	81.1	743.4	18.3

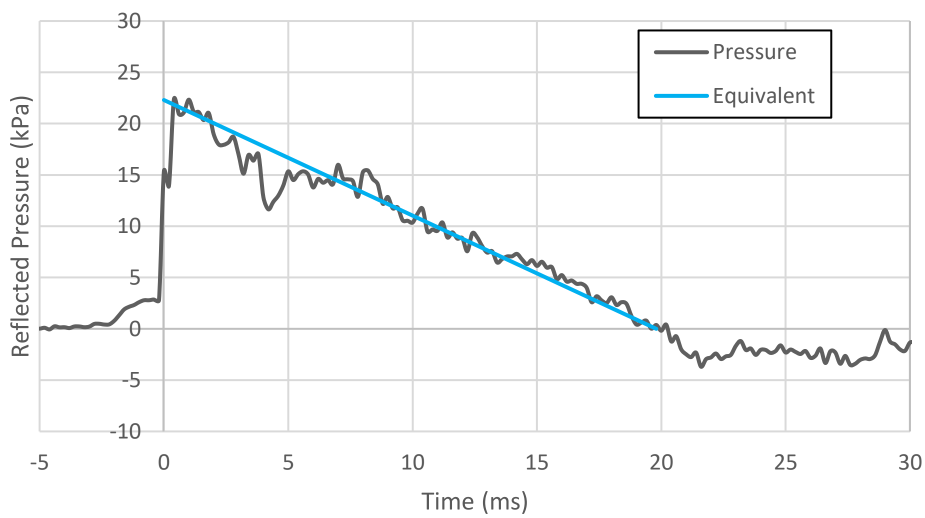

Figure 5.1: Experimental and simplified pressure-time histories for shot GL1.1

The inputs for the analytical methods relied on values sourced from literature (e.g. [10]) or manufacturer data (e.g. [50]). Both models used manufacturer-listed capacities combined with strength and dynamic increase factors from Lacroix and Doudak [9] and Poulin et al. [10] as the basis for the flexural capacities of glulam and CLT, respectively. For example, the use of such average resistance parameters was justified since the glulam beams and CLT panels used in the current study were of identical grade and species and thickness to those used in Lacroix and Doudak [9] and Poulin et al. [10]. In addition to the dynamic increase factors obtained the aforementioned studies, strength increase factors (SIF) were obtained by relating the experimental static results to the design-level properties provided by the manufacturer documentation for the respective product. The increase factors are summarized in Table 5.2, while additional details on the SIF calculation process is presented in Appendix B.

Table 5.2: Analytical Increase Factors for Parallel to Grain Capacities

	DIF	*SIF*	*Total Increase Factor*
Glulam	1.14	1.25	1.43
CLT	1.28	1.23	1.57

5.2 Single-Degree-of-Freedom Model

The SDOF analysis was performed using *RCBlast* version 0.5.1 [51], a SDOF blast analysis software capable of performing equivalent lumped-mass analysis through the numerical integration of the equation of motion. The software implements the average acceleration method, which allows the process to be stable regardless of the time-step. It accepts member resistance in the form of piecewise linear functions and uses load-mass transformation factors to maintain the equivalence of the SDOF analysis [52].

5.2.1 Model Inputs

The equivalent stiffness, K, for the SDOF model was defined using Equation [5-1] [17] and the load-mass transformation factor, K_{LM}, was taken as 0.87 and 1.0 for elastic and plastic behaviour, respectively. These values corresponded to the transformation factors for a system of lumped masses at the load application points and were chosen as such due to the significant mass of the LTD when compared to the relatively light weight of the specimens.

$$K = \frac{56.4EI}{L^3} \quad [5\text{-}1]$$

The resistance curve for the CLT model used average resistance values taken from Poulin et al. [10], with a maximum ductility ratio of 2.5 as proposed by the authors. The resulting curve is presented in Figure 5.2. The elastic region of the resistance curve linearly increased to a peak resistance of 174.2 kN at a displacement of 31 mm. Following this peak, the outer laminate of the five-ply panel was considered to have failed and resistance curve dropped to 83.7 kN. This strength was representative of the capacity of a three-ply panel and continued until a displacement of 41.3 mm where the third ply was observed to reach its elastic limit. The member resistance was subsequently reduced to 34.8 kN as a residual capacity until the ductility limit of 77.5 mm was reached.

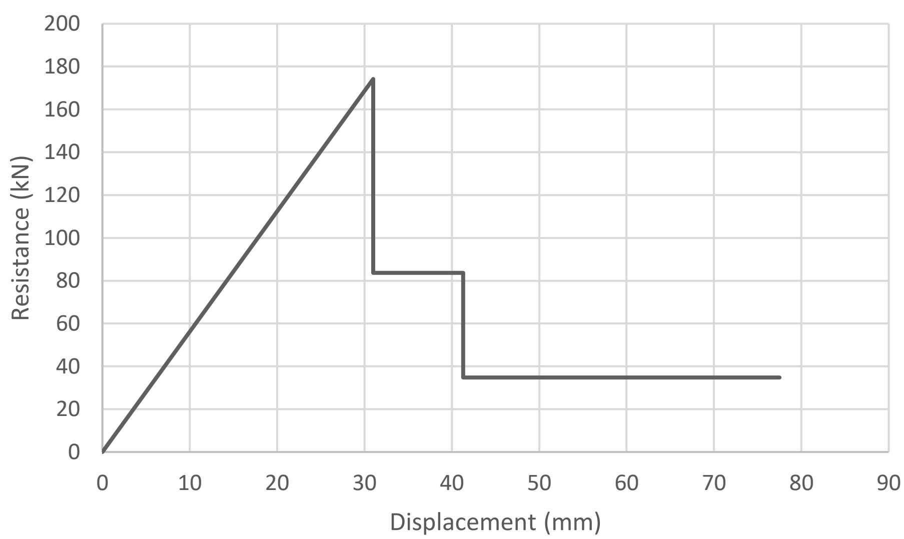

Figure 5.2: Five-ply CLT resistance curve for SDOF analysis

An additional resistance curve was constructed for three-ply behaviour, which also followed the average results from Poulin et al. [10]. The three-ply resistance curve was used to accommodate observations of partial failure in the fourth and fifth plies during tests CLT2.2 and CLT2.3 through additional modeling. The three-ply resistance curve is presented in Figure 5.3, and consisted of linear-elastic behaviour to a limit of 83.7 kN at a displacement of 41.3

mm. The resistance of the member then dropped to 34.8 kN until a maximum displacement of 103.3 mm.

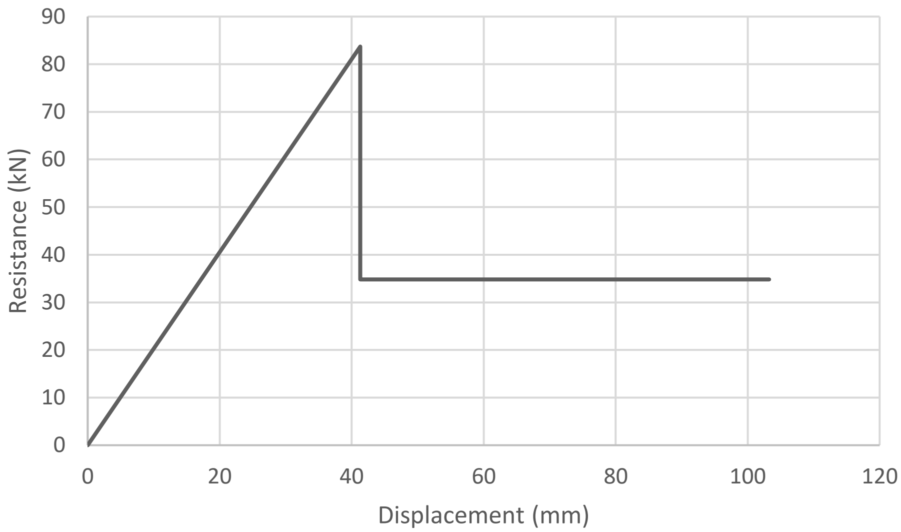

Figure 5.3: Three-ply CLT resistance curve for SDOF analysis

The resistance curve implemented for the glulam model used manufacturer data for bending capacity in combination with the strength and dynamic increase factors based on research by Lacroix and Doudak [31], as shown in Table 5.2. The manufacturer-specified bending strength and modulus of elasticity were 30.7 MPa and 12,400 MPa, respectively [50]. These properties were used to determine the static moment capacity and equivalent stiffness. The static moment capacity was then converted to overall member resistance (as in Equation [4-2]) and increased using the increase factors for glulam. Further details on the calculations are presented in Appendix C. The resulting resistance curve was linear-elastic up to an ultimate resistance of 69.3 kN at a corresponding displacement of 27.4 mm, as shown in Figure 5.4. As there was no post-peak behaviour for glulam members, the load-mass factor remained 0.87.

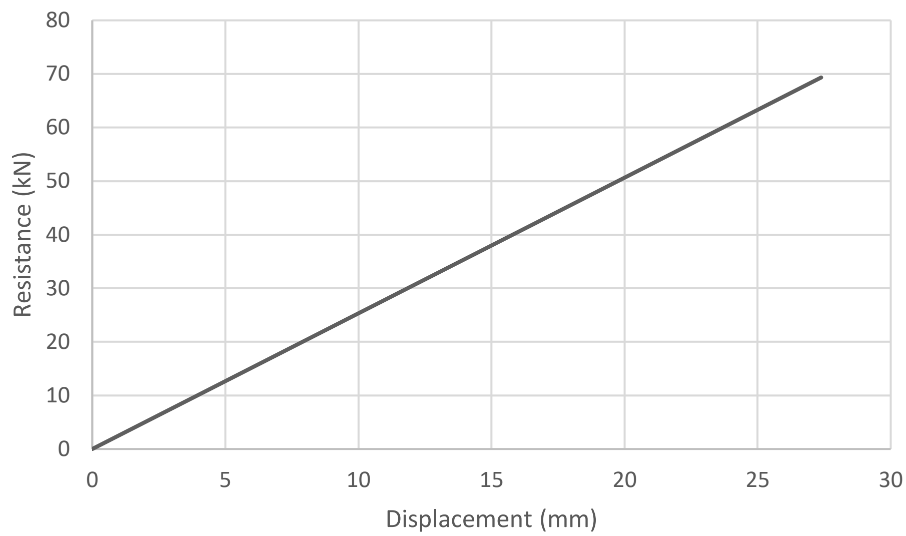

Figure 5.4: Glulam resistance curve for SDOF analysis

5.2.2 Model Results

The output of the SDOF analysis can be separated into two distinct groups differentiated by the presence of model failure. Failure occurs when the model displacement exceeds the bounds of the input resistance curve. Consequently, the program is unable to define the model resistance and the simulation is terminated.

The first group did not exceed the input resistance curve and reached a maximum displacement without failing. For simulations of glulam beams, this indicates that the system remained elastic, while for CLT models this indicates the member had either remained elastic or did not exceed a ductility ratio of 2.5. An example of the output window for CLT, which exceeded the peak resistance without overloading the resistance curve, is presented in Figure 5.5 and shows the utilized portion of the resistance curve (upper left, labelled as the hysteric loop), the applied pressure (upper right), as well as the displacement results (bottom).

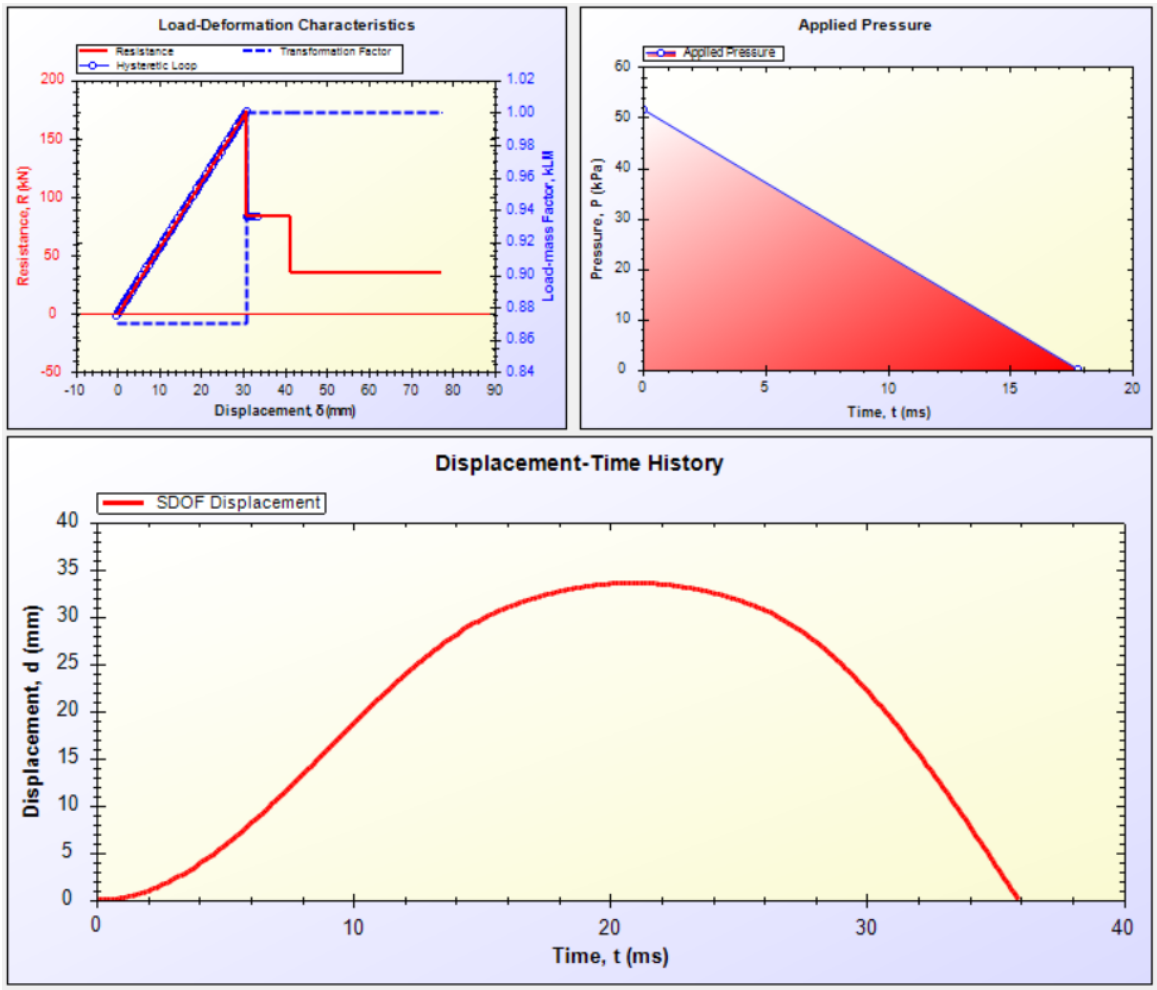

Figure 5.5: RCBlast output window for CLT2.2

The second group of SDOF results consists of cases where the maximum resistance was exceeded for the case of glulam beams, or that the displacement exceeded 2.5 times the elastic limit for the case of CLT panels. An example of this displacement behaviour for CLT is presented in Figure 5.6.

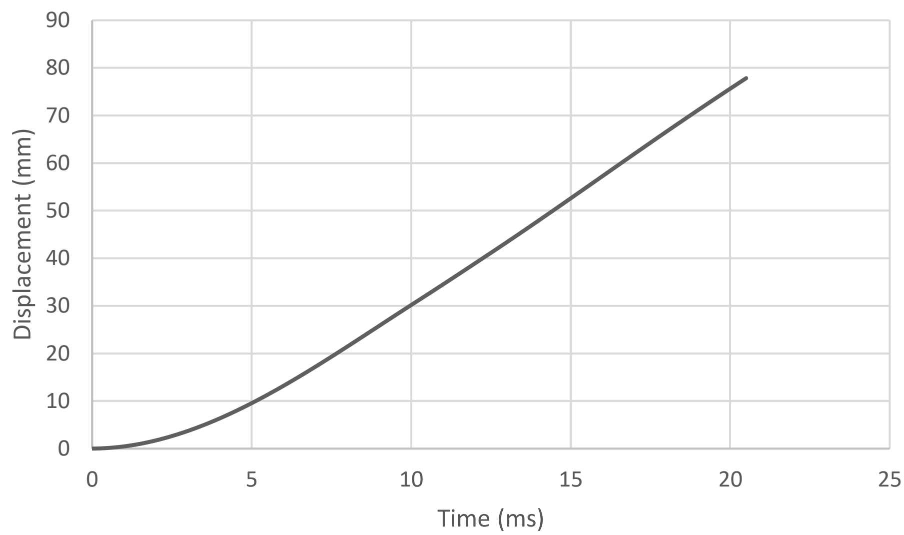

Figure 5.6: Displacement results for CLT3.2

The maximum displacements from the SDOF model are presented in Table 5.3, which also indicates whether failure had occurred or if the member elastically returned to the initial position for glulam simulations. For the CLT models, the behaviour is indicated by the maximum response reached by the simulation, based on the extent of the resistance curve used in calculation. Similar to the glulam models, elastic behaviour signified that the peak resistance was not reached by the CLT model. If the displacement exceeded the elastic region of the curve, the program began to utilize the post-peak region and equivalent damage can be inferred. The model indicated failure in only the fifth ply if the peak resistance was exceeded and it did not extend past the limit for three-ply behaviour, as shown in Figure 5.5. If the simulation entered the residual resistance region of the implemented relationship, then failure up to the third ply was indicated. Complete model failure occurred when the simulation exceeded a ductility ratio of 2.5 before reaching maximum displacement, thereby displacing beyond the definition of the resistance curve and terminating the model.

Tests CLT2.2 and CLT2.3 were modeled using either five-ply or three-ply resistance curves, in order to account for experimentally observed damage to the outer plies. The three-ply variation produced considerably higher maximum displacement results due to a lower initial stiffness, and a comparison of the effects of the different resistance curves on overall model accuracy is presented in Chapter 6. The models which use the three-ply resistance curve are identified by the additional index “-3P” in Table 5.3. The displacement-time histories for all SDOF models are presented in Appendix D, and comparisons between the SDOF analysis and experimental results are discussed in Chapter 6.

Table 5.3: Summary of SDOF Analysis Results

Model ID	Maximum Displacement (mm)	Time of Maximum Displacement (ms)	Damage Level
GL1.1	27.2	22.5	Elastic
GL2.1	27.4	15.3	Complete Failure
GL2.2	27.5	14.0	Complete Failure
GL3.1	14.3	22.2	Elastic
GL3.2	27.5	18.3	Complete Failure
GL3.3	27.5	13.6	Complete Failure
CLT1.1	77.5	20.7	Complete Failure
CLT2.1	47.5	32.1	Third Ply Failure
CLT2.2	33.6	20.8	Fifth Ply Failure
CLT2.2-3P	99.4	51.7	Third Ply Failure
CLT2.3	44.6	29.5	Third Ply Failure
CLT2.3-3P	103.4	35.7	Complete Failure
CLT3.1	25.1	17.9	Elastic
CLT3.2	77.4	20.5	Complete Failure

5.3 Finite Element Analysis

5.3.1 Choice of Software

Two commercially available finite element environments were investigated for this study: ABAQUS [40] and LS-DYNA [46]. Both product suites have supporting research documentation involving wood material models (e.g. Kaliyanda [42] and Murray [45]) and offer a complete environment for the assembly, analysis, and visualization of finite element models.

ABAQUS is a general purpose FEA software, capable of both static and dynamic analyses with a variety of element types and applications. The material analysis program is compartmentalized into ABAQUS/Standard and ABAQUS/Explicit, with other applications dedicated to fields such as electro-magnetic and acoustic modeling. The ABAQUS/Standard component uses an iterative stiffness-based solution based on Newton's method to solve for nodal displacements, which is unconditionally stable and well-suited for static and low-speed dynamic simulations requiring high-definition stress gradients. The ABAQUS/Explicit component uses an advancing time-step solution to determine the kinematic state of the model, which is suited for high-speed dynamic models with nonlinear behaviour. ABAQUS/Explicit often requires more increments to solve a model due to its conditional stability, but the non-iterative nature of the formulation typically results in less memory usage and runtime. Both applications can be accessed through ABAQUS/CAE, which provides a graphical interface for model assembly, file construction and result analysis.

Due to the general-purpose nature of the ABAQUS suite, modular material model templates are implemented which the user can select and assign material properties. The generic material models are unable to describe the complex behaviour of wood, but ABAQUS is capable of implementing user subroutines to expand the application capabilities. The software suite links with a third-party compiler and library in order to insert user programs into the general analysis, allowing for various modifications to the solution process. The user material subroutine (UMAT in ABAQUS/Standard and VUMAT in ABAQUS/Explicit) is used in place of the built-in constitutive relationships.

LS-DYNA is a purpose-built software designed to model dynamic behaviour using a variety of element types. The software uses a specialized solution method with an explicit integration to advance the model variables to the next time-step. The program uses a keyword-based system for user input, with an extensive library of functions, element formulations, and material models implemented into the suite. A graphical interface is available in LS-PRE/POST, which allows for visualization of the model and convenient access to the library of keywords. The program has several capabilities tailored for automotive collisions, including keywords for airbags, seatbelts, and sensors. As discussed in Chapter 2, a material model for wood is implemented into LS-DYNA and includes predefined species as well as options for user input.

Careful considerations and modeling within the two environments led to the decision to use the ABAQUS software for this study. While LS-DYNA already contains a material model for wood, the reliance on the use of a specific keyword structure was deemed detrimental and inappropriate for the current study. ABAQUS allowed for more flexible modeling practices, for example, in terms of model construction. A preliminary investigation into modeling CLT panels in LS-DYNA indicated that the methodology was generally restricted to the definition of individual plies, which could then be assembled into a panel through contact keywords. Conversely, ABAQUS allowed for several approaches for the simulation of a CLT panel, including the partitioning of a single solid into multiple plies (as implemented in section 5.3.7), assembly of discrete parts (as described for LS-DYNA), and direct inclusion of adhesive layers. Furthermore, a higher degree of control was possible in ABAQUS through the development of the material model. As discussed in Chapter 2, the LS-DYNA wood material model does not consider failure interaction between perpendicular and parallel to grain direction as a measure to reduce problematic behaviours [45]. Several other studies (e.g. [39], [42], [44]) include these interactions within the material model, particularly for shear components. The development of a material model in ABAQUS allowed the current study to control the degree of interaction between stress components and draw on a wider pool of research.

5.3.2 Modeling Assumptions

There are several assumptions made, in both the creation of the model and the development of the VUMAT subroutine, relating to the usage and mechanics of the analytical model.

The local cartesian system of reference (i.e. X,Y,Z) is replaced with the terms for the cylindrical axes of wood (longitudinal, radial, and tangential). The behaviour assigned to the perpendicular to grain axes within the material is smeared into a homogenized plane, whereby the local longitudinal (X) axis is assigned parallel to grain properties significantly stronger relative to the perpendicular to grain properties assigned to the identical radial and tangential axes. This facilitates the transition from a cylindrical material definition to the orthogonal material definition used by ABAQUS/Explicit.

It is assumed that the adhesive used for bonding the lamination of engineered wood products is at least as strong as the surrounding wood fibre [12], and thus it is not required to model the bonds between individual laminations. This results in the glulam specimens being considered as a homogenous member, and the plies of the CLT lay-up as homogenous layers attached together. Delamination between the CLT plies is not considered in the model, although failure can still occur at ply interfaces due to the combination of perpendicular and parallel to grain properties.

Due to the limitation that DIFs have not been established for all material strengths in wood, the increase factors are not used as inputs or written into the program. Instead, the user modifies the desired properties before entering them into the VUMAT. This approach allows for the iteration of the model inputs without rewriting the subroutine during development. For the purposes of this study, the dynamic increase factor is only considered to apply to the parallel to grain strengths, as established by the state-of-the-art knowledge (e.g. [8], [9], [28]).

In terms of failure behaviour, it is assumed that the ultimate compressive behaviour of wood does not result in complete material failure via element deletion. This assumption is based on the observed failure patterns of wood under compression, which typically consist of either significant densification (perpendicular to the grain) or fibre kinking (parallel to the grain). Therefore, the implementation of this failure behaviour does not contribute to model failure to the same degree as splitting, for example, which results in a more brittle failure mode. It is also assumed that damage accumulation in tension parallel to grain does not influence damage in other stress components until complete failure [43]. Finally, the deletion of elements in shear only occurs after exposure to additional stresses which would widen the equivalent cracks.

5.3.3 Model Algorithm

The VUMAT material model is initiated by ABAQUS/Explicit following the calculation of the strain increment. The VUMAT subroutine is given information for a set of elements, referred to as a block, and sequentially calculates the stresses and user-defined variables for each element. The input block structure requires the program to repeat the process for each element, which is referred to as a “vectorized” solution structure. Unlike the UMAT material model used in ABAQUS/Standard for static analyses, it is not required to calculate the stiffness matrix and return the results to the main routine. Furthermore, the solution is conditionally stable, and ABAQUS/Explicit decreases the time increment of the solution until stability is reached during calculation.

The overall solution algorithm uses a continuum damage approach based on a program developed by Sandhass [37], and is presented for a single element in Figure 5.7 as a flowchart. After receiving the incremental data, the VUMAT material model estimates the new stress based on an assumption of elastic stress and strain. The predicted stresses are evaluated using the failure criteria, which represent the stress-capacity ratios for the element. The damage process is initiated if a failure criterion is evaluated as greater than unity. The damage algorithm then verifies the criterion output of each component against the respective maximum ratio from the previous time-steps. If the highest stress previously experienced by the element is exceeded, then the current stress-capacity ratio is used as the basis of damage calculation for that component. Otherwise, the previous peak stress information for the component is used. An optional stabilization branch can be enabled by the user, which uses an artificial viscosity to regulate the spread of damage in the model by controlling the rate of damage within the element. The damage reduces the effective moduli in the compliance matrix, which is subsequently inverted to determine the stiffness matrix for the element. The altered stiffness matrix is used with the total strain to calculate the new stress components required by the main ABAQUS/Explicit routine.

The logic for the storage of the peak stress-capacity ratio is not shown in the flowchart for the purpose of conciseness. The historical maximum damage (for both stabilized and base calculations) is stored as a further safety measure to prevent decreases in generated damage, and is also omitted from Figure 5.7 for conciseness.

If a damage parameter is evaluated at a value near to unity (i.e. 0.999995 is used in the VUMAT), the element is flagged as completely failed and marked for deletion. Element deletion is the primary indicator of member failure in the model, and damage results are discussed in terms of percentage towards deletion (i.e. an undamaged component is at 0%, and failure occurs at approximately 100%). Implementing deletion at a value of one is not enacted to avoid divisions by zero and errors in the material matrices, presented in section 5.4.4. It should be noted that the accumulation of damage physically represents material softening through the formation of micro-cracks in the material structure, while element deletion represents the development of complete fractures which split material at the member scale [37].

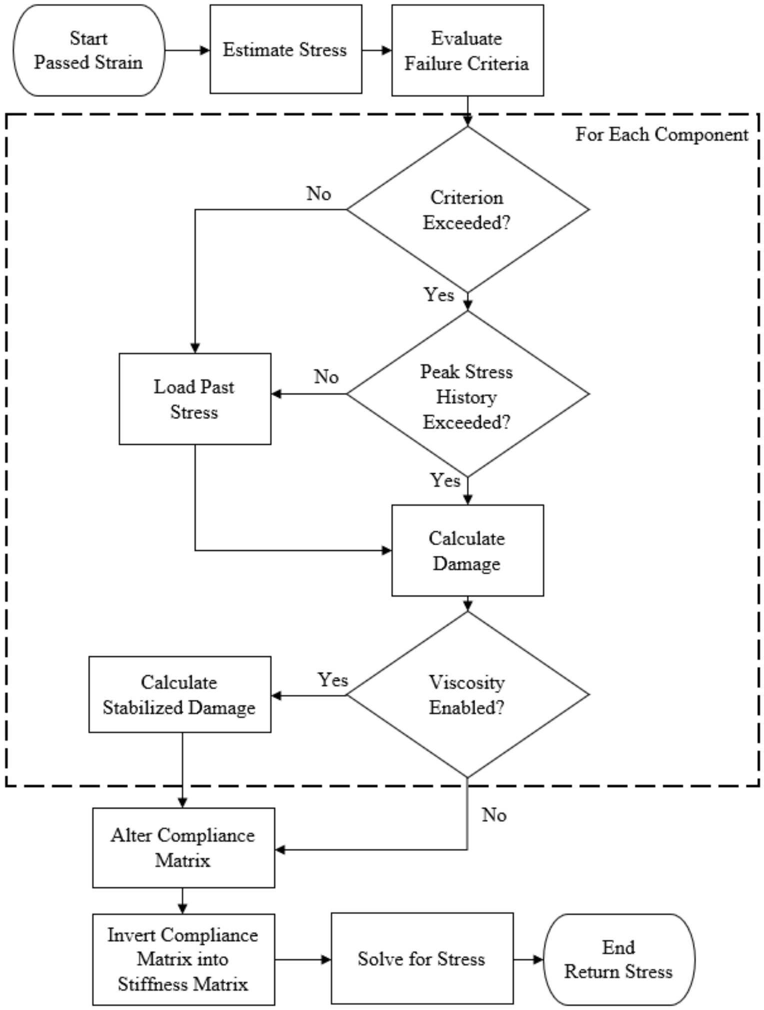

Figure 5.7: Material model flowchart

5.3.4 Model Equations

The equations used in the VUMAT are based on those described by Sandhaas [37], and several of the failure criteria have also been presented in Chapter 2. A more complete set of equations will be presented in this section, including some of the logical statements which control the viscous stabilization.

The elastic stress estimate is performed using Hooke's law. The general equation is written using unique properties for the three cartesian axes, but the terms are simplified as the implemented version assigns identical perpendicular to grain properties to the Y (denoted R) and Z (denoted T) axes and parallel to grain properties to the X (or L) axis. This results in the use of an elastic modulus parallel to grain E_0 and perpendicular to grain E_{90} for the axial components rather than a unique value for each axis, while a longitudinal shear modulus G is implemented for both the LR and LT orientations in combination with a rolling shear modulus G_{roll} for the RT shear component. The reduced terms are presented in Equations [5-2] and [5-3].

$$\sigma = \begin{bmatrix} \sigma_L \\ \sigma_R \\ \sigma_T \\ \sigma_{vR} \\ \sigma_{roll} \\ \sigma_{vT} \end{bmatrix} = D\epsilon = D \begin{bmatrix} \epsilon_L \\ \epsilon_R \\ \epsilon_T \\ \epsilon_{vR} \\ \epsilon_{roll} \\ \epsilon_{vT} \end{bmatrix} \tag{5-2}$$

$$D = \Delta^* \begin{bmatrix} E_0(1-\nu_{RT}\nu_{TR}) & E_0(\nu_{RL}-\nu_{TL}\nu_{RT}) & E_0(\nu_{TL}-\nu_{RL}\nu_{TR}) & 0 & 0 & 0 \\ E_{90}(\nu_{LR}-\nu_{LT}\nu_{TR}) & E_{90}(1-\nu_{TL}\nu_{LT}) & E_{90}(\nu_{TR}-\nu_{TL}\nu_{LR}) & 0 & 0 & 0 \\ E_{90}(\nu_{LT}-\nu_{LR}\nu_{RT}) & E_{90}(\nu_{RT}-\nu_{LT}\nu_{TL}) & E_{90}(1-\nu_{LR}\nu_{RL}) & 0 & 0 & 0 \\ 0 & 0 & 0 & 2G & 0 & 0 \\ 0 & 0 & 0 & 0 & 2G_{roll} & 0 \\ 0 & 0 & 0 & 0 & 0 & 2G \end{bmatrix} \tag{5-3}$$

where D is the stiffness matrix, ϵ is material strain, σ is material stress, υ is Poisson's ratio, and $\Delta^* = (1-\nu_{LR}\nu_{RL}-\nu_{LT}\nu_{TL}-\nu_{RT}\nu_{TR}-2\nu_{LR}\nu_{RT}\nu_{TL})^{-1}$

There are a total of eight failure criteria, each corresponding to a stress component. The respective components are identified by the following subscripts: longitudinal tension ($-_{t0}$), longitudinal compression ($-_{c0}$), radial tension ($-_{t90R}$), radial compression ($-_{c90R}$), tangential tension ($-_{t90T}$), tangential compression ($-_{c90T}$), longitudinal shear with respect to the radial plane ($-_{vR}$), and longitudinal shear with respect to the tangential plane ($-_{vT}$). Each criterion can be considered a ratio of applied stress (σ) to material capacity (*f*) with quadratic interaction where components are combined, as recommended by Hashin [41]. When a criterion is evaluated as greater than unity, it indicates the elastic capacity of the component has been exceeded and damage will accumulate.

Equations [5-4] and [5-5] represent the parallel to grain component in tension ($F_{t0}(\sigma)$) and compression ($F_{c0}(\sigma)$), respectively, and the failure criteria are made up of a single ratio with opposite signs to account for stress conventions.

$$F_{t0}(\sigma) = \frac{\sigma_L}{f_{t0}} \qquad [5\text{-}4]$$

$$F_{c0}(\sigma) = \frac{-\sigma_L}{f_{c0}} \qquad [5\text{-}5]$$

Equations [5-6] and [5-7] are used as the failure criteria for tension ($F_{t90}(\sigma)$) and compression perpendicular to the grain ($F_{c90}(\sigma)$), respectively. The equations are applied to both perpendicular to grain directions and are presented with both indices. The failure criterion for tension perpendicular to grain is contributed to by longitudinal shear as well, due to the splitting modes observed in the shear behaviour of wood [37]. The equation used for compression perpendicular to grain does not interact with other stress components, similar to the that for compression parallel to grain.

$$F_{t90T|R}(\sigma) = \frac{\sigma_{R|T}^2}{f_{t90}^2} + \frac{\sigma_{LT|LR}^2}{f_v^2} \qquad [5\text{-}6]$$

$$F_{c90R|T}(\sigma) = \frac{-\sigma_{R|T}}{f_{c90}} \qquad [5\text{-}7]$$

The failure criterion for longitudinal shear ($F_v(\sigma)$) is similarly repeated for both perpendicular to grain axes, and is presented in Equation [5-8]. It is assumed the rolling shear stress also contributes to the longitudinal shear criterion, as outlined in Sandhaas [37], although the tensile stress perpendicular to grain is not taken to contribute to the criteria following Murray [45].

$$F_{vR|T}(\sigma) = \frac{\sigma_{LT|LR}^2}{f_v^2} + \frac{\sigma_{RT}^2}{f_{roll}^2} \quad [5\text{-}8]$$

Once a failure criterion is evaluated as greater than unity, the value is checked against the highest previous evaluation of that criterion. The greater value is then stored as the peak stress-history variable κ, which is used to calculate damage. Equations [5-9] and [5-10] show expressions to calculate the damage in brittle components, in tensile (d_t) and shear (d_v), respectively, while Equation [5-11] calculates the damage for the ductile compressive components (d). The model does not employ the crack band method for brittle behaviour, which distributes the specific fracture energy throughout the element dimensions and is suitable when a single failure mode is expected during a localized failure [39].

$$d_t = 1 - \frac{1}{f_{max}^2 - 2G_f E}\left(f_{max}^2 - \frac{2G_f E}{\kappa}\right) \quad [5\text{-}9]$$

$$d_v = 1 - \frac{1}{f_{max}^2 - 2G_f G}\left(f_{max}^2 - \frac{2G_f G}{\kappa}\right) \quad [5\text{-}10]$$

$$d = 1 - \frac{1}{\kappa} \quad [5\text{-}11]$$

Rolling shear behaviour does not have a corresponding failure criterion or damage progression. The rolling shear damage variable (d_{roll}) is instead comprised of the longitudinal shear (d_{vR} and d_{vT}) and perpendicular tension (d_{t90R} and d_{t90T}) damage components, according to Equation [5-12].

$$d_{roll} = 1 - (1 - d_{t90R})(1 - d_{t90T})(1 - d_{vR})(1 - d_{vT}) \quad [5\text{-}12]$$

The longitudinal shear damage calculated using Equations [5-8] and [5-10] is further combined with the tensile damage perpendicular to grain to calculate an effective shear variable (d_v^{eff}), as shown with both sets of indices in Equation [5-13], due to the vulnerability of both components to splitting.

$$d_{vR|T}^{eff} = 1 - (1 - d_{t90R|T})(1 - d_{vR|T}) \qquad [5\text{-}13]$$

If the viscous stabilization is enabled by the user, the damage variables are then used in Equation [5-14]. This equation uses an artificial viscosity η obtained from Sandhaas [37] to limit how quickly the damage can develop within the element. The stabilized damage, d_S, is based on the base damage, *d,* calculated at a given time step and the stabilized damage from the previous time step. A maximum condition is included to ensure the level of damage can not decline, and upper indices are used to indicate the time-step of each damage variable.

$$d_S^{(t)} = \max\{0, d_S^{(t-\mathrm{dt})}, \frac{\eta}{\eta+dt} d_S^{(t-\mathrm{dt})} + \frac{dt}{\eta+dt} d^{(t)}\} \qquad [5\text{-}14]$$

where *dt* is the time increment for the analytical step, an index of *(t)* indicates the a given analytical step, and an index of *(t-dt)* indicates the previous analytical step.

Once the damage parameters are calculated, the compliance matrix is built according to Equation [5-15]. A difference between this equation and Equation [2-6] from the UMAT program developed by Sandhaas et al. [39] is the order of the stress and strain tensors. The change is due to the ordering of vectors in the ABAQUS/Explicit syntax and has little effect on the calculation procedure.

$$C^{dam} = \begin{bmatrix} \frac{1}{(1-d_0)E_0} & \frac{-\nu_{RL}}{E_{90}} & \frac{-\nu_{TL}}{E_{90}} & 0 & 0 & 0 \\ \frac{-\nu_{LR}}{E_0} & \frac{1}{(1-d_{90R})E_{90}} & \frac{-\nu_{TR}}{E_{90}} & 0 & 0 & 0 \\ \frac{-\nu_{LT}}{E_0} & \frac{-\nu_{RT}}{E_{90}} & \frac{1}{(1-d_{90R})E_{90}} & 0 & 0 & 0 \\ 0 & 0 & 0 & \frac{1}{(1-d_{vR})2G} & 0 & 0 \\ 0 & 0 & 0 & 0 & \frac{1}{(1-d_{roll})2G_{roll}} & 0 \\ 0 & 0 & 0 & 0 & 0 & \frac{1}{(1-d_{vT})2G} \end{bmatrix} \qquad [5\text{-}15]$$

The matrix is then inverted and used as the damaged stiffness matrix D^{dam} to determine the effective stresses according to Equation [5-16].

$$\sigma^{dam} = \begin{bmatrix} \sigma_L^{dam} \\ \sigma_R^{dam} \\ \sigma_T^{dam} \\ \sigma_{vR}^{dam} \\ \sigma_{roll}^{dam} \\ \sigma_{vT}^{dam} \end{bmatrix} = inv(C^{dam})\epsilon = D^{dam}\epsilon = D^{dam} \begin{bmatrix} \epsilon_L \\ \epsilon_R \\ \epsilon_T \\ \epsilon_{vR} \\ \epsilon_{roll} \\ \epsilon_{vT} \end{bmatrix} \quad [5\text{-}16]$$

5.3.5 Programming Details

The VUMAT subroutine is written in the Fortran programming language and implemented in ABAQUS version 6.13-1. ABAQUS accepts user subroutine code with a .for file extension and syntax matching conventions for Fortran 77. The finite element suite is linked with Intel Parallel Studio XE (2017) and Microsoft Visual Studio (2013) in order to compile and process the user subroutine. The full VUMAT code can be found in Appendix E.

The VUMAT subroutine structure consists of a two-state architecture. In this structure, sets of variables are passed to the program as “old” arrays, and variables are output as part of “new” arrays in order to return to ABAQUS/Explicit. This is clear for solution dependant variables (SDVs), which are used in user subroutines to store values exclusively for the implemented code. SDVs are completely defined within the given subroutine, and updated in every step. For the wood material VUMAT, all damage components, stress histories, and total strain are accounted for through the use of SDVs. An SDV is also used to trigger deletion of the element once the complete failure threshold is exceeded.

The vectorized form of VUMAT subroutines discourages the use of branching code techniques [53]. While a significant section of the code is used for the viscous stabilization section of the subroutine and controlled by an if-statement, the entire section is either enabled or disabled for the entirety of the analysis and does not actively branch the process. Other logical branches in the algorithm are avoided by calculating values for all criteria and variables and using maximum and minimum logical statements to eliminate invalid results.

The inversion of a six-by-six matrix generally requires a relatively long and complex section of code, but due to the make-up of the compliance matrix (Equation [5-15]) the process is optimized to invert the three-by-three section containing the axial components as a matrix and directly calculate the reciprocal of the shear terms. The inversion of a three-by-three matrix increases the overall efficiency of the program by eliminating ineffective operations.

5.3.6 Mesh Sensitivity Analysis

In order to evaluate the consistency of the finite element material model, a sensitivity analysis was conducted for both glulam and CLT models using the parameters for a linear-elastic test. The mesh size, as well as maximum displacements and corresponding times, are presented in Table 5.4 with graphical comparisons presented in Figure 5.8 and Figure 5.9 for glulam and CLT, respectively. For the coarsest CLT mesh the element depth was restricted by the thickness of the plies, resulting in most elements measuring 70 mm x 70 mm x 35 mm. The two coarsest CLT meshes also correlated to a problematic discretization, as the thickness of the CLT ply was modeled with only a single element. The similarity in both displacement and inbound duration indicated that the implemented model was generally not sensitive to mesh size variation in the selected sizes, and images of the meshed members are presented as part of Appendix F.

Table 5.4: Mesh Sensitivity Results

	Mesh Size (mm)	*Maximum Displacement (mm)*	*Time of Maximuim Displacement (ms)*
Glulam	10	15.05	24.5
	20	14.97	25.0
	30	14.95	24.5
	40	15.04	24.5
CLT	9	24.37	18.5
	17.5	24.39	18.5
	35	24.32	18.5
	70	23.90	18.5

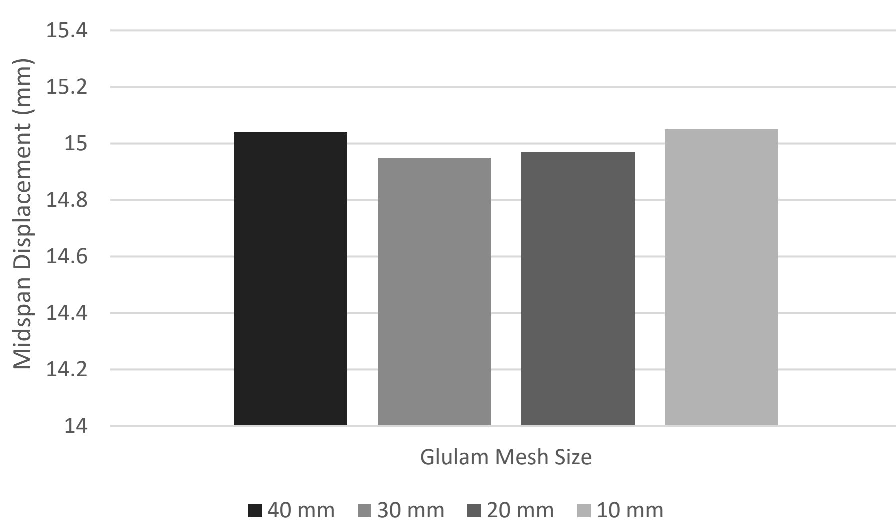

Figure 5.8: Displacement comparison for glulam meshes

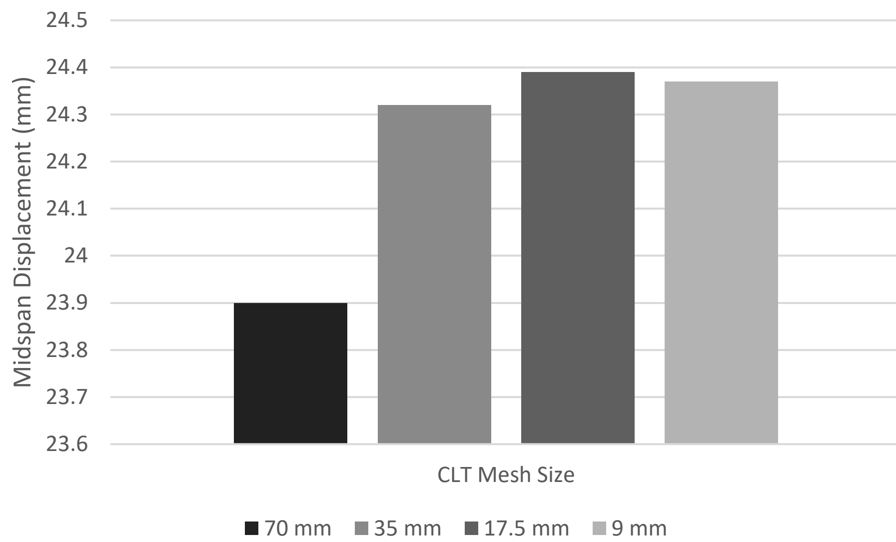

Figure 5.9: Displacement comparison for CLT meshes

As seen in Figure 5.8, the glulam meshes provided similar results across all investigated sizes. The maximum variation in displacement was 0.1 mm, corresponding to a variation of 0.6%, and no clear pattern of convergence was observed as element size decreased. A mesh size of 20 mm was used for the study, as it provided the highest resolution of results without invalid behaviour.

A larger difference with mesh size was observed with the CLT model, as shown in Figure 5.9. There was clear evidence of a trend in the maximum displacement, as the variation reduced as a function of mesh refinement, but the computational cost increase between the 17.5 mm and 9 mm mesh was significant, with the 9 mm mesh increasing the model runtime by an approximate factor of ten. Therefore, the 17.5 mm element size was implemented, as it provided a reasonable balance of result fidelity and runtime.

5.3.7 Modeling Techniques

The models for both glulam and CLT analyses utilize three-dimensional solids without planes of symmetry. Eight-node continuum hexahedral elements were used in all analyses, with full integration (C3D8 elements). A linear element formulation was used over a quadratic element type (C3D20) due to the method ABAQUS uses to allocate mass within an element. Higher-order formulations tend to provide an inferior distribution of inertial forces in dynamic analyses [53]. A reduced formulation (C3D8R element type) was not employed in order to provide a better resolution of results for stress and damage.

The glulam specimens were modeled as a homogenous member, since adhesive failure can be considered negligible as stated earlier, with the parallel to grain direction aligned with the global X-axis. An example of a modeled glulam beam is presented in Figure 5.10a. The plies of the modeled CLT panel were created by portioning sections of the panel geometry, with plies having an assigned orientation, rather than creating each ply separately and attaching them together. This simplified construction significantly reduced the computational cost by reducing contact relationships in the analysis. The plies in the major direction were assigned local material axes, such that the global Y-axis became the longitudinal axis and parallel to grain direction, while the transverse plies were aligned such that the default coordinate system properly aligned the parallel to grain direction with the global X-axis. The general CLT model is presented in Figure 5.10b, which also features the partitioning planes and added material orientation.

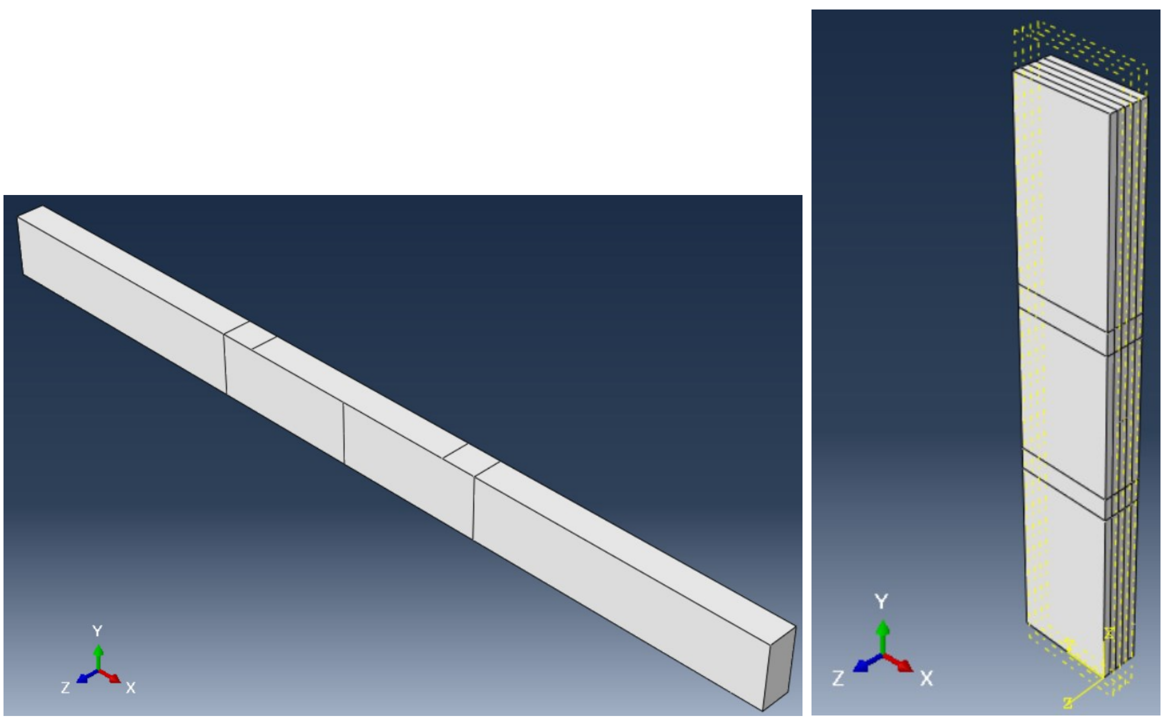

a) b)

Figure 5.10: Main member model and coordinate systems for glulam (a) and CLT (b)

The supports for both models consisted of four cylindrical rigid bodies, acting as pinned supports. The objects were fixed in place, and all forces applied to them were directed through a single point. The curvature of the pin prevented sharp concentrations of stress within the main model. The models were loaded using a pressure applied to two 100 mm wide bands centred at the third span points. This recreated the four-point bending condition used during testing, as well as provided a bearing area to prevent localized crushing similar to the experimental load transfer plates. The model assemblies are presented in Figure 5.11.

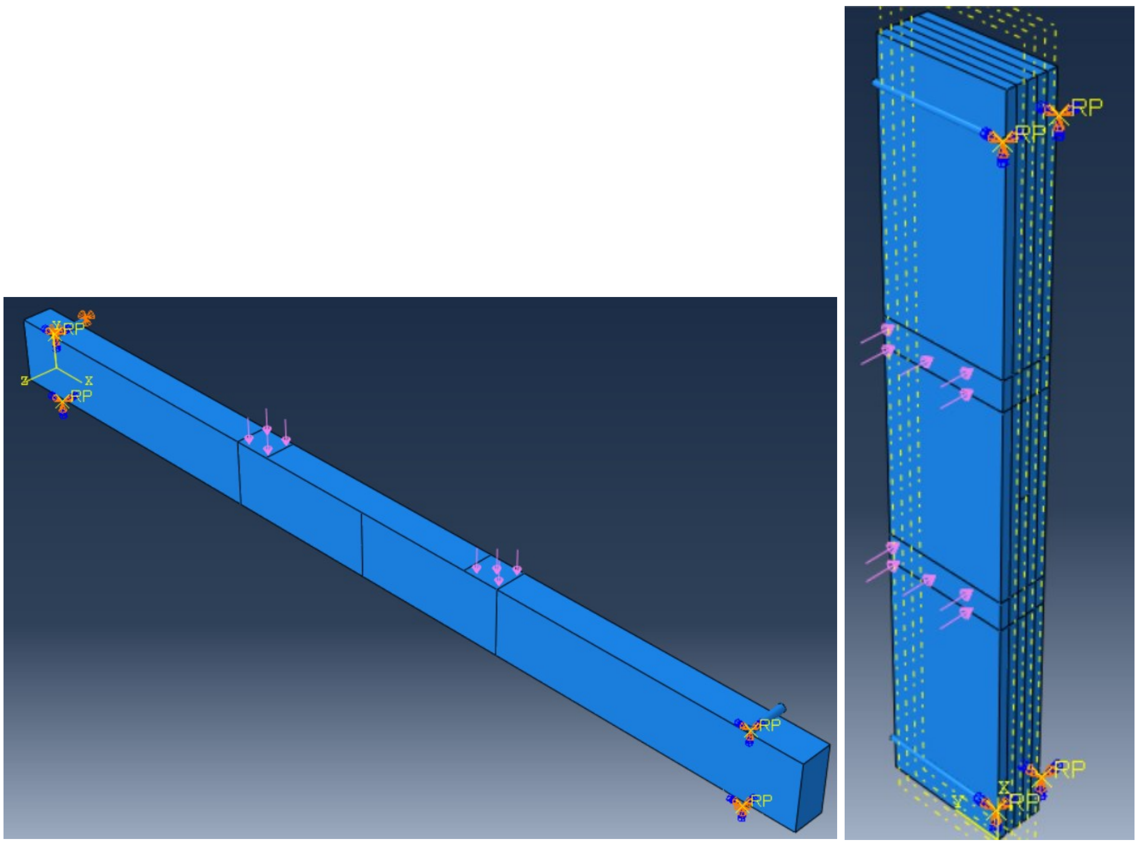

a) b)

Figure 5.11: Model assemblies, with loads and support points, for glulam (a) and CLT (b)

The inertial contribution of the LTD was accounted for by distributing the effective mass of the LTD (284 kg) over the mid-span of the member. This was implemented by increasing the material density in the region between the loading areas.

A summary of the units used in the models is presented in Table 5.5. The input units are particularly important for ABAQUS/Explicit models, as only specific sets of units correctly distribute mass and inertial force within the model.

Table 5.5: Units for Material Model

Property	*Unit*
Length	mm
Force	N
Pressure/Stress	MPa (N/mm^2)
Density	$tonnes/mm^3$ (kg/mm^3 x 10^{-3})
Time	s

5.3.8 Material Inputs

As previously stated, the material model uses inputs derived from manufacturer specifications and literature. The values and sources for these properties are provided in this section, and a summary of all inputs for the VUMAT subroutine is presented in Table 5.6. The density is calculated using the mass of each specimen, and is requested by ABAQUS/Explicit and not the VUMAT subroutine.

The parallel to grain elastic modulus was obtained from design material published by the manufacturer (i.e. Nordic Structures). The listed average modulus for glulam was 12,400 MPa [50], while the moduli for CLT were 11,700 MPa and 9,000 MPa for the longitudinal and transverse layers, respectively [48]. The other moduli were calculated using relationships from the Canadian Standards Association (CSA) O86 standard, presented in Equation [5-17] to [5-19] [7].

$$E_{90} = \frac{E_0}{30} \quad [5\text{-}17]$$

$$G = \frac{E_0}{16} \quad [5\text{-}18]$$

$$G_{roll} = \frac{G}{10} = \frac{E_0}{160} \quad [5\text{-}19]$$

The axial capacities parallel to grain were obtained from the published specifications for glulam [50] and CLT [48] and modified using the appropriate SIF and DIF, as presented in Table 5.2. The tensile strength perpendicular to grain was obtained from a study by Jönsson and Thelandersson [54]. The study examined the perpendicular to grain tensile capacity of glulam beams and found an average strength of 1.37 MPa (COV 0.18). A study by Hoffmeyer et al. [55] examined the behaviour of glulam and timber elements subjected to compression perpendicular to grain and found an average capacity of 2.9 MPa (COV 0.13). However, this capacity was significantly lower than the fifth percentile design value provided by Nordic Structures for both glulam (7.5 MPa [50]) and CLT (5.3 MPa [48]). Therefore, the average value found by the study was deemed inappropriate for the model and the COV was used to adjust the manufacturer values from the fifth percentile to the average strengths presented in Table 5.6.

The longitudinal shear capacity of wood was investigated by Boström [56] while studying fracture behaviour. An average shear capacity of 10.9 MPa in Mode II shear fracture was determined, which generally corresponds to shear cracking. The rolling shear capacity of CLT panels was obtained from a study by Wang et al. [57], where tests were conducted on CLT panels made from Canadian sourced SPF group lumber. An average rolling shear capacity of 1.5 MPa (COV 0.14) was determined for panels without gaps or edge gluing in the transverse layers, which is representative of the specimens used in this study.

The fracture energies were determined from the UMAT inputs provided by Sandhaas [37] for spruce wood. The viscous regularization parameter was also taken from this set of inputs. The Poisson's ratios were obtained from Green et al. [58] and were representative for Sitka spruce.

Table 5.6: Material Properties for Finite Element Subroutine

Property	*Glulam*	*CLT (Major)*	*CLT (Minor)*
Parallel to Grain Elastic Modulus E_0	12400 MPa	11700 MPa	9000 MPa
Perpendicular to Grain Elastic Modulus E_{90}	413 MPa	390 MPa	300 MPa
Shear Modulus G	775 MPa	731 MPa	563 MPa
Rolling Shear Modulus G_{roll}	77.5 MPa	73.1 MPa	56.3 MPa
Parallel to Grain Tensile Capacity f_{t0}	29.1 MPa	23.2 MPa	5.04 MPa
Parallel to Grain Compressive Capacity f_{c0}	47.0 MPa	30.4 MPa	14.2 MPa
Perpendicular to Grain Tensile Capacity f_{t90}	1.37 MPa		
Perpendicular to Grain Compressive Capacity f_{c90}	9.54 MPa	5.30 MPa	
Longitudinal Shear Capacity f_v	10.9 MPa		
Rolling Shear Capacity f_{roll}	1.50 MPa		
Parallel to Grain Fracture Energy G_{f0}	6.0 N/mm		
Perpendicular to Grain Fracture Energy G_{f90}	0.5 N/mm		
Longitudinal Shear Fracture Energy G_{fv}	1.2 N/mm		
Rolling Shear Fracture Energy G_{froll}	0.6 N/mm		
Artificial Viscosity Parameter η	0.0001		
LR Poisson's Ratio υ_{LR}	0.47		
LT Poisson's Ratio υ_{LT}	0.37		
RL Poisson's Ratio υ_{RT}	0.44		

5.3.9 Finite Element Results

The results of the ABAQUS/Explicit analysis were evaluated through the displacement-time history and resistance-displacement relationship, as well as the observed overall damage behaviour. Similar to the method used to obtain the experimental resistance curve, the analytical resistance curves were calculated using Equation [4-1]. The support reactions from the rigid pins in contact with the tension face were used in order to recreate the experimental setup and ensure the comparison between the data sets is appropriate. The displacement-time history was exported from a mid-span node, located at mid-depth of the modeled member. A complete set of mid-span displacements, resistance curves, and model figures is presented in Appendix F.

At time of writing, a method to isolate and transfer the level of damage between models was unable to be implemented. Attempts to implement models consecutively resulted in the transfer of displacements and inertia in addition to the SDV values. Trials which implemented an intermediate step with fixity held the model in the displaced position rather than restoring the original position and generated significant internal forces. The analysis importation feature built into ABAQUS/CAE resulted in the program crashing before analysis.

This setback primarily affected the modeling of the CLT specimens, as glulam were shown to be linear-elastic until failure and does not depend on past damage to accurately define member behaviour. Conversely, CLT panels have a significantly complex post-peak behaviour and accurate simulation of multiple shots requires the transfer of damage and partial failure states.

Model GL1.1 did not result in element deletion, and the model reached a maximum displacement of 29.6 mm at a time of 26.5 ms. Significant damage accumulated during the response parallel to grain, as shown in Figure 5.12, reaching maximums of approximately 80% progress towards element deletion at the mid-span tension face and approximately 65% of deletion at the mid-span compression face.

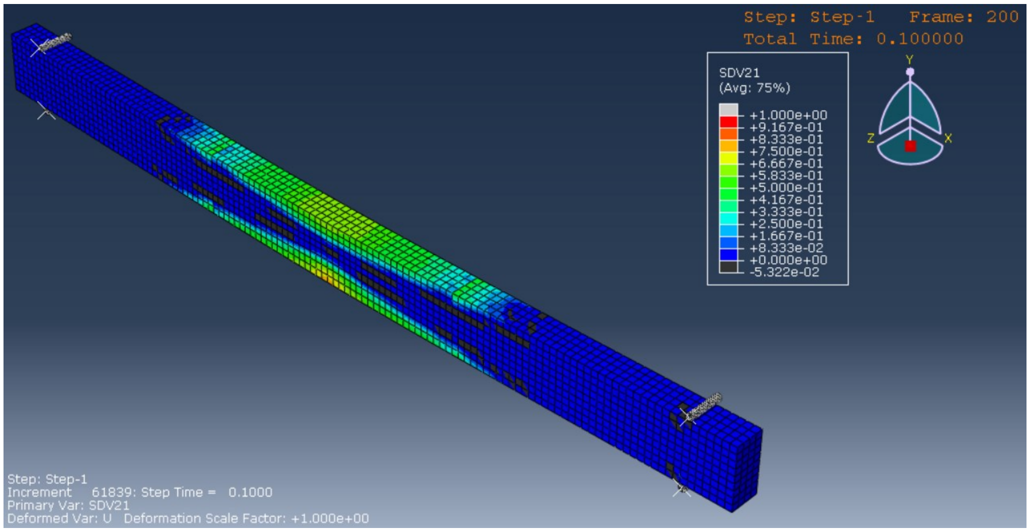

Figure 5.12: Final state of model GL1.1, mapping tensile damage parallel to grain

Model GL2.1 reached a maximum displacement of 38.4 mm after 26.5 ms from initial loading, and exhibited high levels of damage at maximum displacement (up to 94% towards deletion in tension parallel to grain) without element deletion. The presence of significant damage in the perpendicular components near the midspan tension face indicates stress redistribution due to the heavy reduction in the parallel to grain resistance and signifies imminent failure. The damaged state of the member is presented in Figure 5.13.

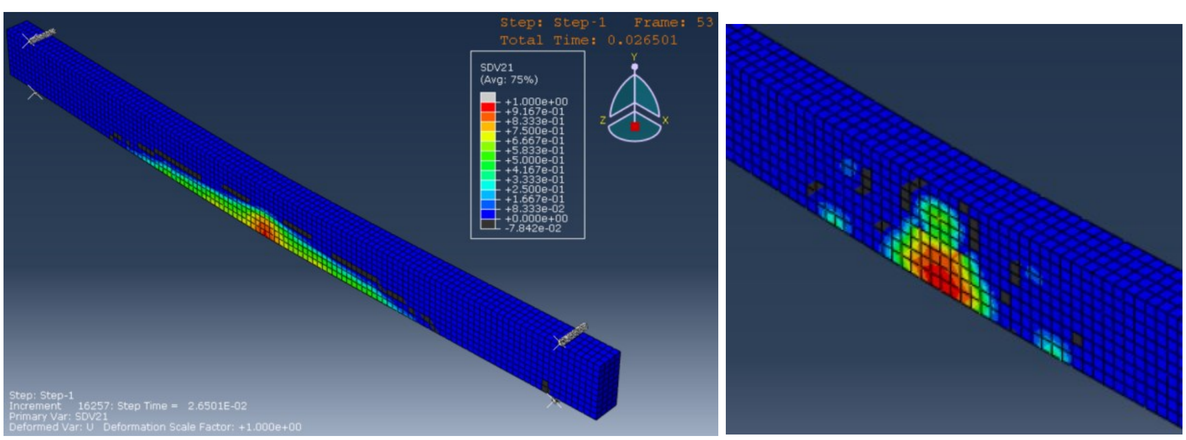

a) b)

Figure 5.13: Damage in model GL2.1: a) Tension parallel to grain b) Tension perpendicular to grain (Global Y), at midspan

Model GL2.2 initiated failure at a time of 29.5 ms at a mid-span displacement of 44.6 mm. The initiation of failure and the failed state of the member are presented in Figure 5.14. The failed state consists of complete failure at mid-span until approximately mid-depth, combined with extended crack development and propagation towards the supports. The cracks developed simultaneously to the mid-span deletion and extended to approximately two thirds of the member.

a)

b)

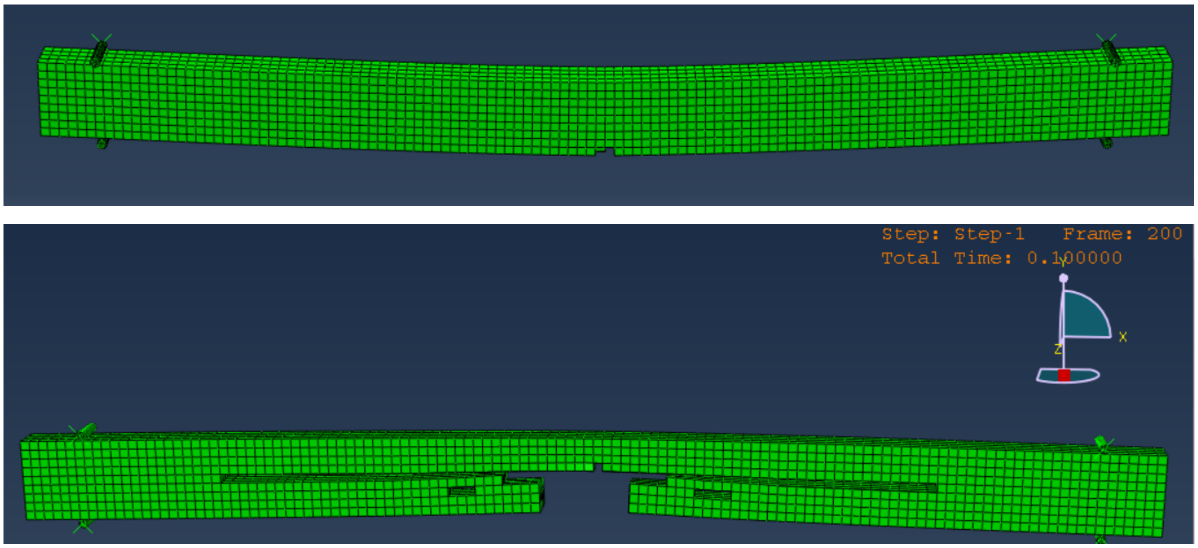

Figure 5.14: Initial mid-span deletion (a) and failed state (b) of model GL2.2

Model GL3.1 reached a maximum displacement of 15 mm at 25 ms after loading and experienced no significant damage in any stress component.

Model GL3.2 did not result in material failure, while a maximum mid-span displacement of 32.9 mm occurred at a time of 26.5 ms. The parallel to grain damage approached 90% at the extreme tension fibre, with tension components perpendicular to grain also displaying localized damage at the mid-span tension face. This behaviour is typical of stress reallocation and approaching flexural failure in the model, as shown in Figure 5.15.

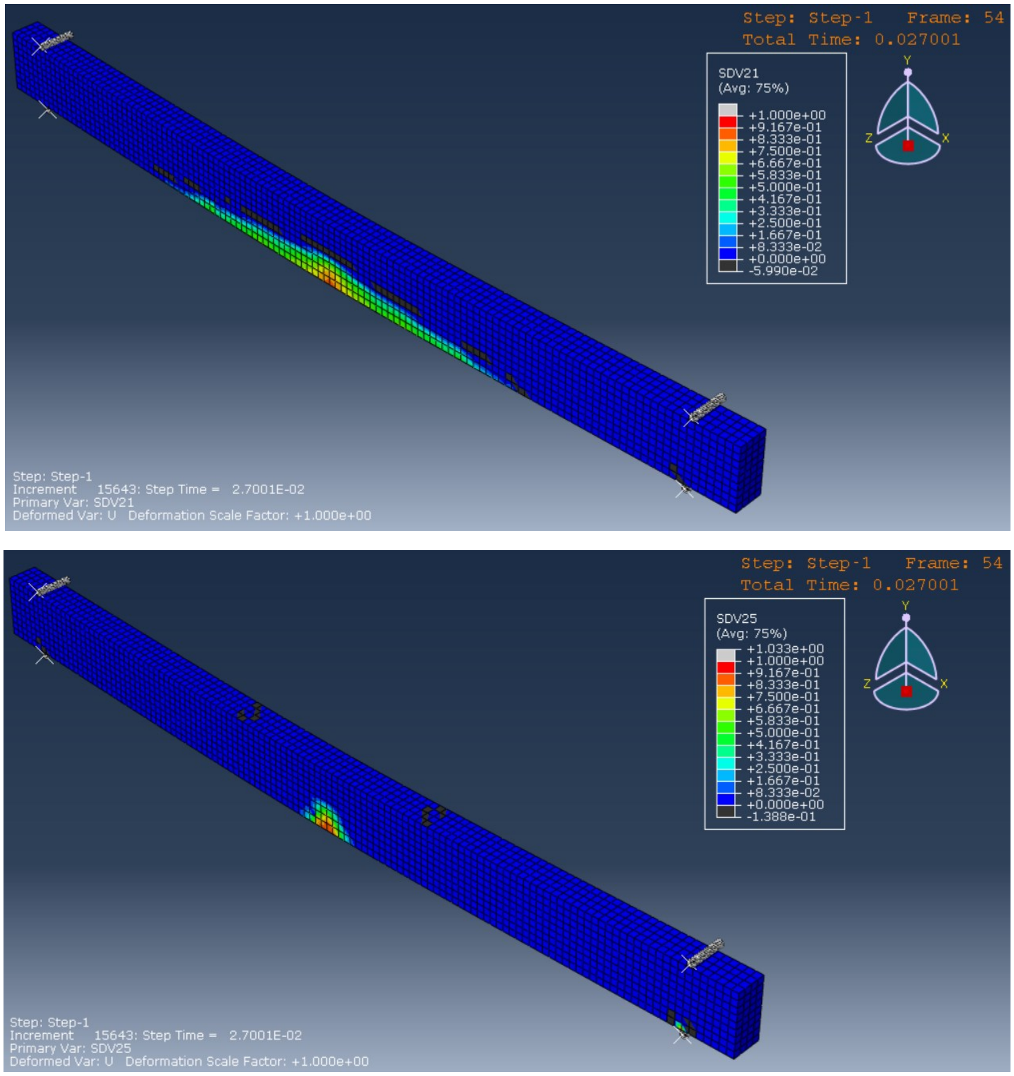

Figure 5.15: Damage development at maximum displacement for GL3.2: a) Tension parallel to grain b) Tension perpendicular to grain (Global Z)

Model GL3.3 resulted in member failure, which initiated at a displacement of 47.3 mm and began at 27 ms. As shown in Figure 5.16, the final state of beam model has significant deletion in the mid-span section as well as cracks propagating towards the supports exhibiting some splintering behaviour.

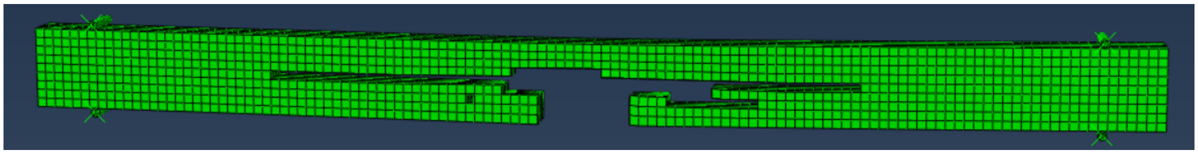

Figure 5.16: Failed state of model GL3.3

Model of CLT1.1 developed rolling shear damage beginning at 12.5 ms and a mid-span displacement of 38.9 mm, as shown in Figure 5.17a, with the first element deletion occurring in the fifth ply at 28 ms and 85.9 mm of displacement. The final state of the member is shown in Figure 5.17b, and consisted of a central break in the fifth ply as well as failure in the fourth ply propagating from the initial break. In addition, the second ply exhibited partial deletion near the supports.

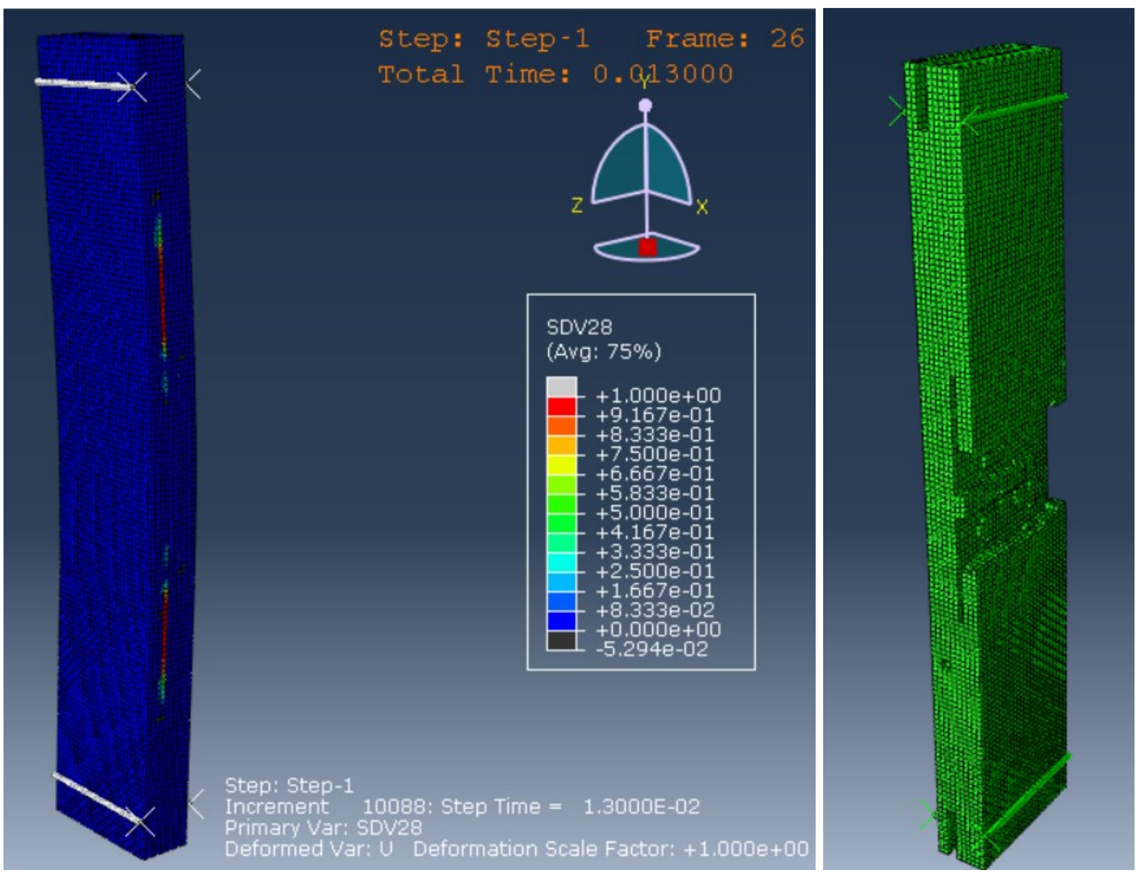

a) b)

Figure 5.17: Failure behaviour of model CLT1.1: a) Initiation of rolling shear damage b)Failed state of panel, with view of tension face

Model CLT2.1 did not result in member failure, and reached a maximum displacement of 37.2 mm in 20 ms. Damage developed predominantly in the outermost plies, up to approximately 87% damage in tension parallel to grain in the fifth ply and 76% damage in compression perpendicular to grain in the first ply. As presented in Figure 5.18, minimal parallel to grain damage was present in the central ply, which indicates flexural behaviour without deterioration of the composite action of the panel through transverse damage.

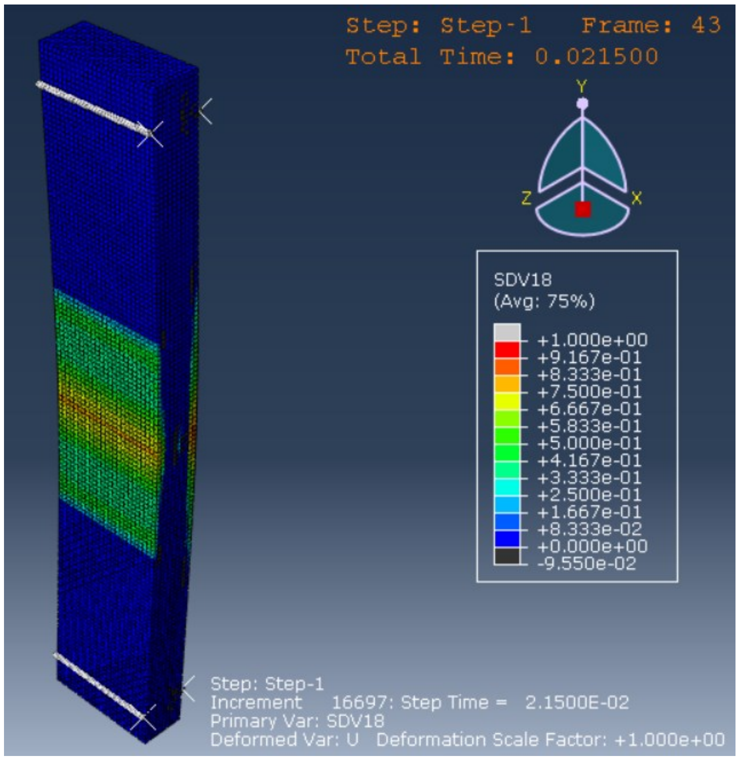

Figure 5.18: Positive phase parallel to grain damage in model CLT2.1

The simulation of test CLT3.1 resulted in only minor damage accumulation, shown in Figure 5.19, with a maximum displacement of 24.4 mm occurring at a time of 18.5 ms.

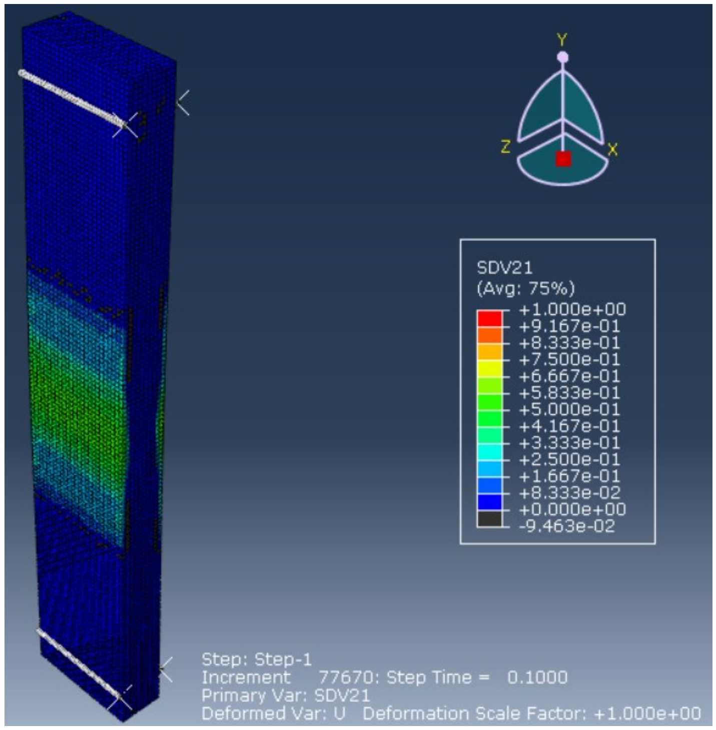

Figure 5.19: Parallel to grain tensile damage in model CLT3.1

An example of the displacement and resistance curve from the finite element models which produced elastic behaviour is shown in Figure 5.20. Fuller details for all models are presented in Appendix F. The resistance curves exhibit numerical scatter due to the solution method used by ABAQUS/Explicit, which does not calculate the global stiffness or equilibrium. This solution method causes the propagation of loads as stress waves within the model and contributes to fluctuations in the resistance curve. A summary of displacement results is presented in Table 5.7, which also indicates whether the given data is for an elastic maximum or initiation of failure, and a typical elastic displacement-time history shown in Figure 5.21. It should be noted that if the members remained elastic following the inbound blast pressure, the modeled members oscillated relatively freely as no damping forces were implemented into the model.

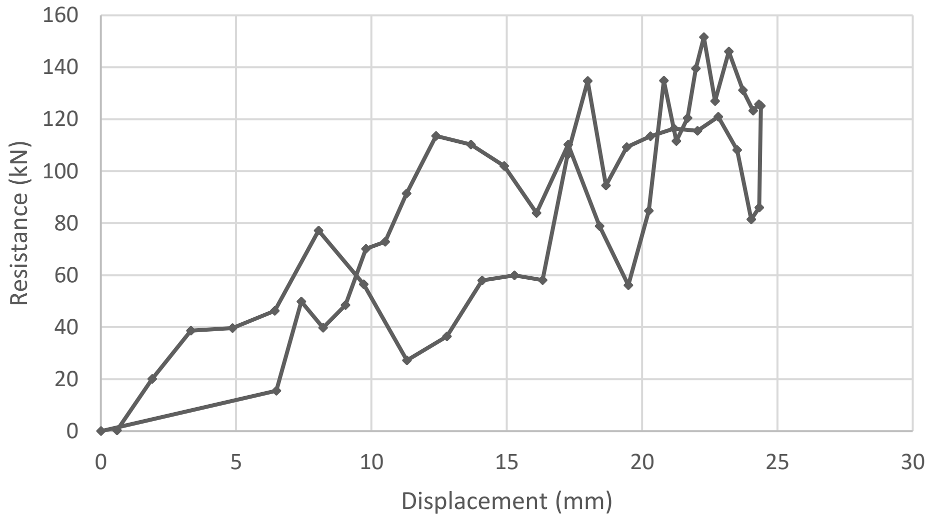

Figure 5.20: Modeled resistance curve for CLT3.1

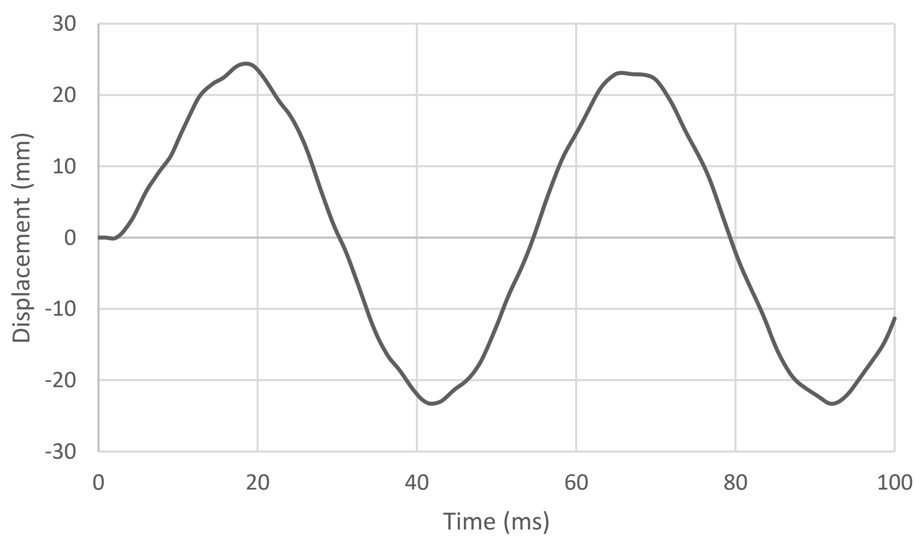

Figure 5.21: Displacement history for model CLT3.1

Table 5.7: Summary of FEA Displacement Results

Model ID	*Displacement (mm)*	*Time (ms)*	*Result Type*
GL1.1	29.6	26.5	Maximum Displacement
GL2.1	38.4	26.5	Maximum Displacement
GL2.2	44.6	29.5	Flexural Initiation
GL3.1	15.0	25.0	Maximum Displacement
GL3.2	32.5	26.5	Maximum Displacement
GL3.3	47.3	27.0	Flexural Initiation
CLT1.1	38.9	12.5	Rolling Shear Initiation
	85.9	28.0	Flexural Initiation
CLT2.1	37.2	20.0	Maximum Displacement
CLT3.1	24.4	18.5	Maximum Displacement

CHAPTER 6- DISCUSSION

6.1 Behaviour of Mass Timber Elements Under Dynamic Loading

6.1.1 Glulam Specimens

The behaviour of the glulam specimens during the dynamic testing was consistently linear-elastic until flexural failure was reached. This was demonstrated in the resistance curves and is consistent with previous findings (e.g.: [31]). When the specimens were loaded within the elastic range, no significant degradation was observed in stiffness even when the same beams were subjected to multiple shots. In addition, specimen behaviour was generally unaffected by superficial damage. An example of this can be seen in Figure 6.1, where it can be observed that no significant change in the dynamic stiffness occurred between tests GL3.2 and GL3.3, despite the formation of minor flexural cracks in test GL3.2 (Figure 6.1a). The failure of each specimen initiated near a knot or other natural defect on the tension face and between the load application points, as shown in Figure 6.2.

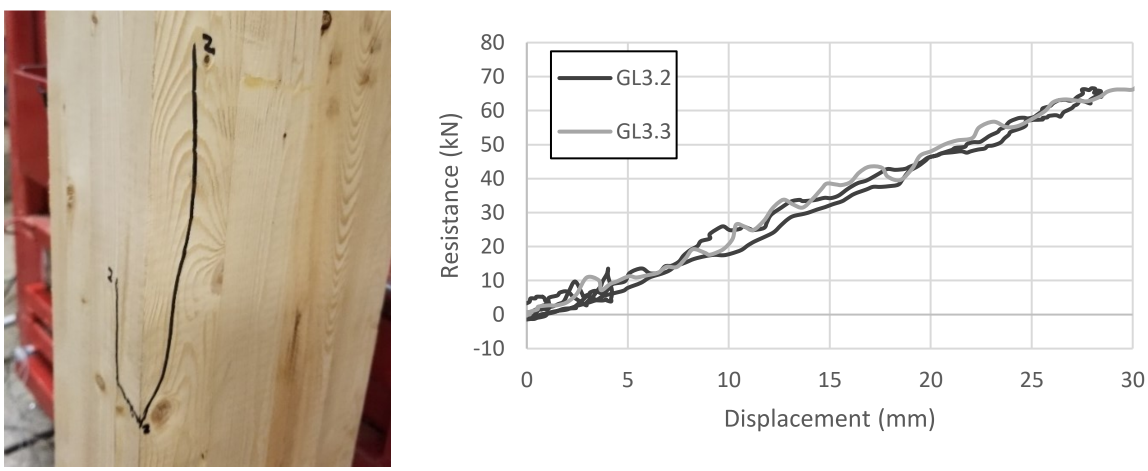

a) b)

Figure 6.1: a) Superficial cracking resulting from test GL3.2 b) Comparison of pre-peak resistance curves for GL3.2 and GL3.3

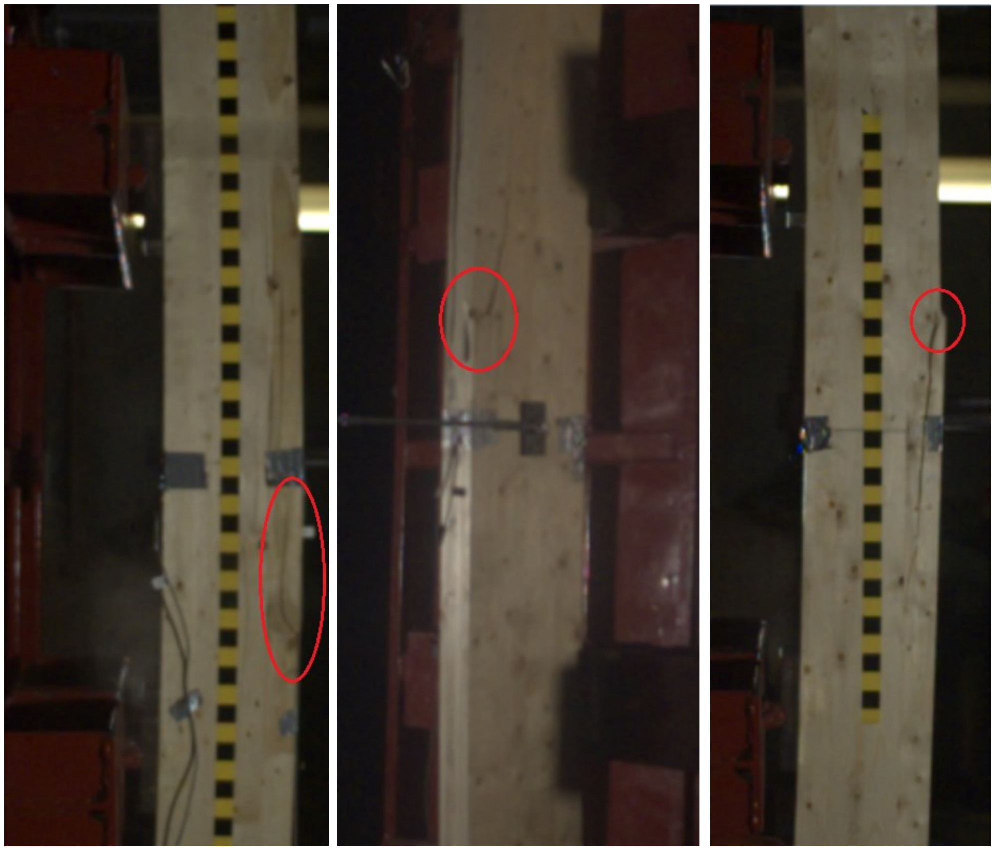

a) b) c)

Figure 6.2: Failure initiation in glulam specimens, with the point of crack origin circled: a) GL1.1 b) GL2.2 c) GL3.3

Specimen GL1 was notably weaker than the other two glulam specimens, with a peak resistance of 54.5 kN at a corresponding mid-span displacement of 26.2 mm. This failure occurred at a lower magnitude compared to the other specimens, both in terms of peak resistance (79.1 kN and 71.0 kN for GL2 and GL3, respectively) and corresponding displacement (33.7 mm and 30.7 mm for GL2 and GL3, respectively). A comparison between the resistance curves corresponding to the failure of each specimen is shown in Figure 6.3, which emphasizes the premature failure in test GL1.1, while demonstrating the consistency in the dynamic stiffness for all glulam specimens tested. It was also noted that a return to original position was observed in test GL1.1 (Figure 6.4b), despite the specimen experiencing substantial flexural cracking (Figure 6.4a). In the case of such crack development, degradation in both stiffness and strength is expected after the shot, however sufficient wood material remained in the cross section for the specimen to rebound back to its initial position.

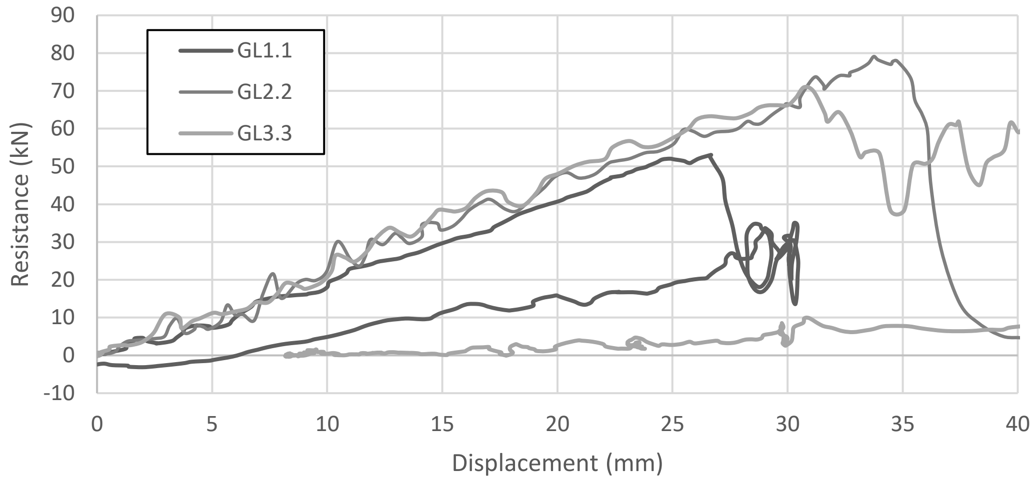

Figure 6.3: Resistance curves for glulam specimen failures

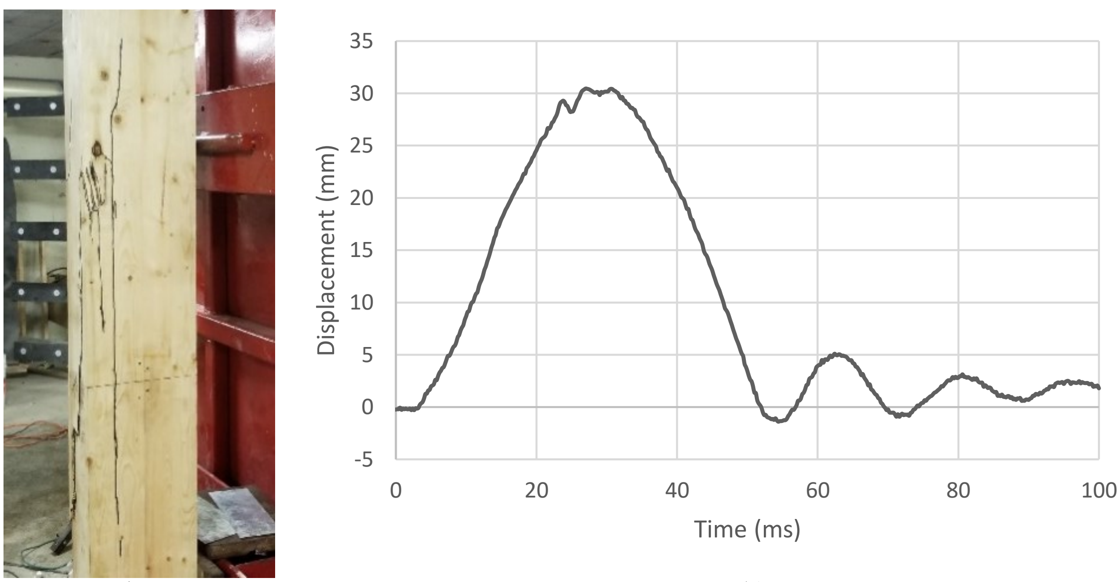

a) b)

Figure 6.4: a) Flexural cracks developed in test GL1.1 b) Displacement-time history for test GL1.1

6.1.2 CLT Specimens

Due to the complex nature of CLT and the potential for different failure mechanisms, it is expected that different failure modes could be observed while testing specimens of similar dimensions and grades. For example, specimen CLT1 failed in flexure, with fractures initiating in the fifth ply and fibre crushing on the compressive face in the first ply. Cracks in the transverse layers (plies 2 and 4) were also observed in the mid-span region near ultimate failure. Panel CLT2 experienced both rolling shear and flexural behaviour, where crack formation occurred in the transverse and longitudinal plies almost simultaneously. The third CLT specimen failed in rolling shear during the second shot (CLT3.2), despite the lack of any observable damage following shot CLT3.1. The rolling shear cracks developed in the transverse plies without the development of significant flexural cracks in any of the three longitudinal plies. The resulting response was characterized by a resistance plateau which maintained a considerable post-peak resistance before returning to the initial position. The experimental resistance curves are compared in Figure 6.5, where it can be observed that the initial dynamic stiffness and peak resistance of the specimens was reasonably consistent regardless of the ultimate behaviour.

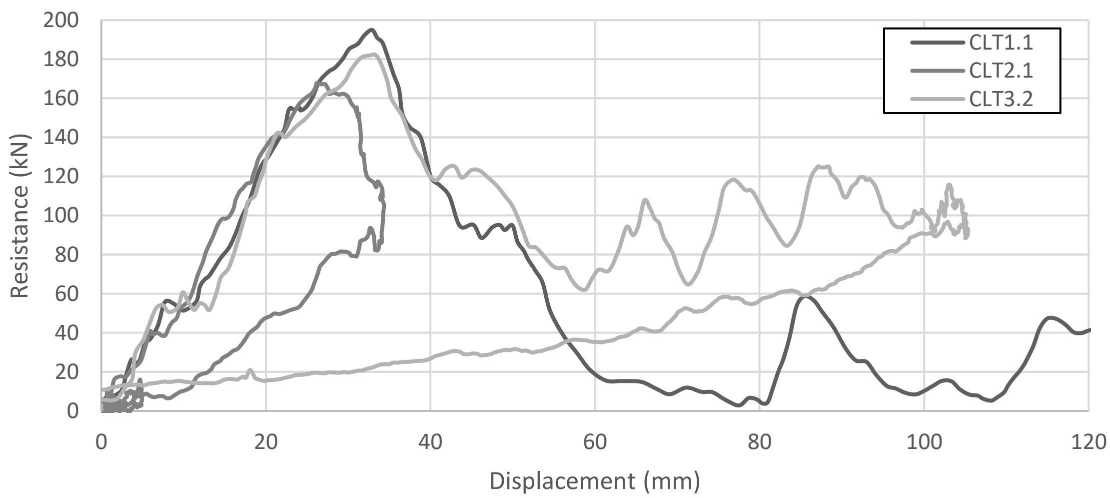

Figure 6.5: Experimental CLT resistance curves displaying both initial stiffness and failure development

6.2 Experimental Comparison with SDOF Analysis

6.2.1 Resistance Curves

The SDOF model used the specimen resistance curves constructed using values from literature, as discussed in Chapter 5. The resulting resistance curves are compared with the experimentally obtained resistance curves in Figure 6.6 and Figure 6.7.

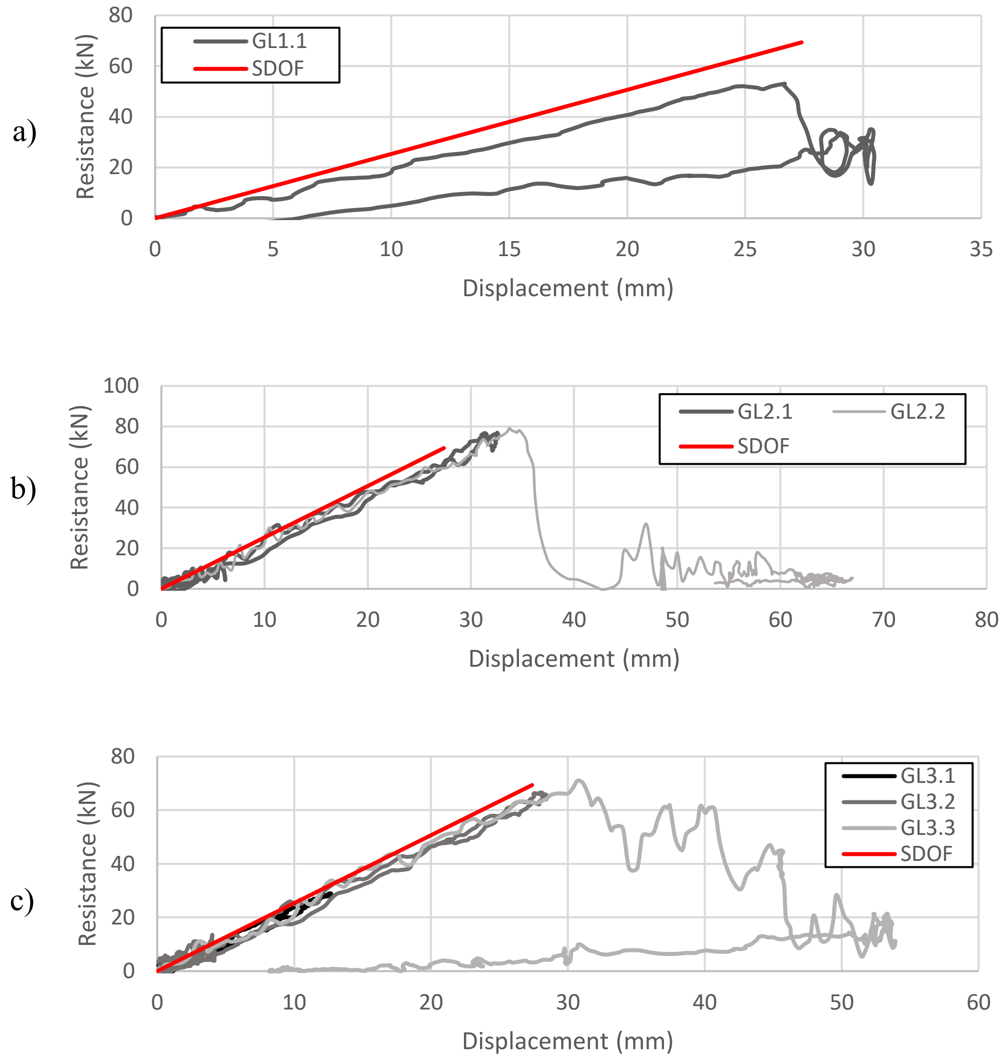

Figure 6.6: SDOF resistance curve comparisons for glulam: a) GL1 b) GL2 c) GL3

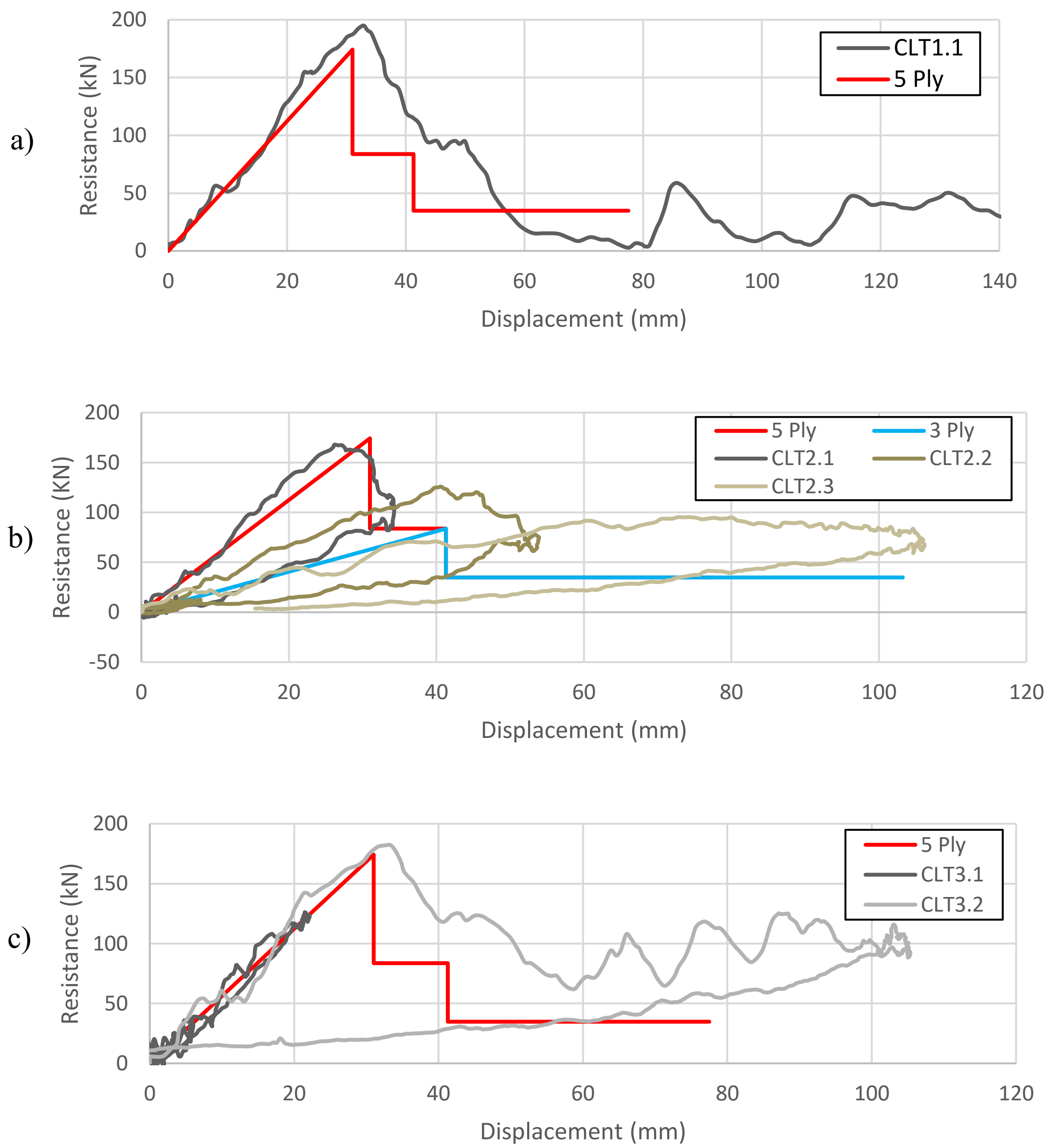

Figure 6.7: SDOF resistance curve comparison for CLT: a) CLT1 b) CLT2 c) CLT3

The analytical glulam resistance curves generally agreed well with the experimental results in terms of stiffness. The most notable difference was for specimen GL1, which was identified as having a somewhat lower stiffness than the other two specimens (Figure 6.6a). Furthermore, it can be observed from the experimental resistance curve for test GL1.1 that failure occurred at a considerably lower level than that obtained by the model, and at a slightly lesser mid-span displacement. The point of failure, as determined in the SDOF resistance curve, aligned reasonably well with that obtained experimentally for specimen GL3 (Figure

6.6c), however the prediction of the ultimate resistance and failure displacement was lower than that observed for specimen GL2 (Figure 6.6b). In general, the theoretical curves compared well with the experimental results, which could be attributed to the relatively simple member behaviour and consistent failure mode (i.e. flexure).

For CLT, the resistance curves implemented in the SDOF model were reasonably accurate to experimentally obtained peak resistance and initial stiffness. The deviations observed in the post-peak behaviour could be attributed to the fact that the model is unable to account for the rolling shear behaviour which developed in specimens CLT2 and CLT3, provided that flexural failure was assumed in the model to govern the panel behaviour. As shown in Figure 6.7b and Figure 6.7c, the post-peak degradation of member strength is not captured well by the theoretical curves. Even when compared to the resistance curve of specimen CLT1 (Figure 6.7a), which failed in flexure, the sudden drops in capacity observed in the SDOF resistance curve also did not match the experimentally observed gradual transitions between panel behaviour (i.e. between five-ply and three-ply resistance, and between three-ply and residual resistance). It can be noted that the behaviour of CLT is more complex and it appears that the use of SDOF modeling provides a reasonable estimate of the behaviour up to peak resistance but fails to describe the post-peak behaviour accurately.

6.2.2 Glulam Displacement and Failure

The SDOF method generally predicted a failure level that was at a lower displacement and time to maximum displacement when compared to the experimental results. The comparisons between the experimentally obtained and SDOF method displacement-time histories are shown in Figure 6.8 to Figure 6.10, which also indicate the points of failure initiation and termination observed during the tests. It is important to note that the results are only compared up to maximum displacement, since after this point where the member begins rebound the LTD may no longer fully contribute to the system's inertia and the modeling assumptions may no longer be valid. Furthermore, the experimental data has been adjusted such that the time of peak pressure corresponds to the origin of the time axis, in order to better compare with the analytical results.

The model for GL1 did not reach failure and predicted a lower maximum displacement (Figure 6.8), which is consistent with the higher stiffness and ultimate displacement in the implemented resistance curve seen in Figure 6.6a. It should be recalled that this specimen exhibited failure at lower displacement and resistance values compared to the other two glulam specimens.

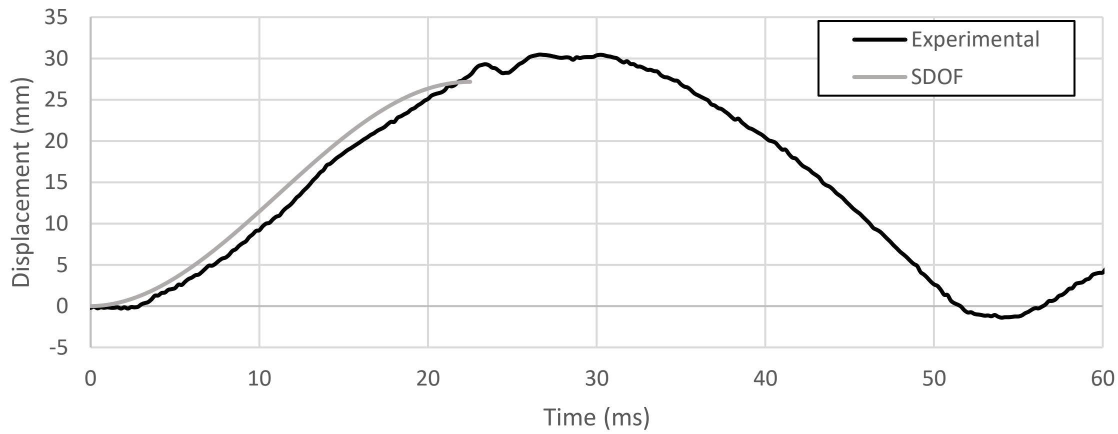

Figure 6.8: Displacement comparison for SDOF model of shot GL1.1

The SDOF analysis for test GL2.1 predicted that the member would fail, as shown in Figure 6.9a, which did not match the experimentally observed elastic behaviour. For similar reasons, the model for shot GL2.2 predicted member failure prior to the initiation of flexural failure observed in the specimen (Figure 6.9b).

a)

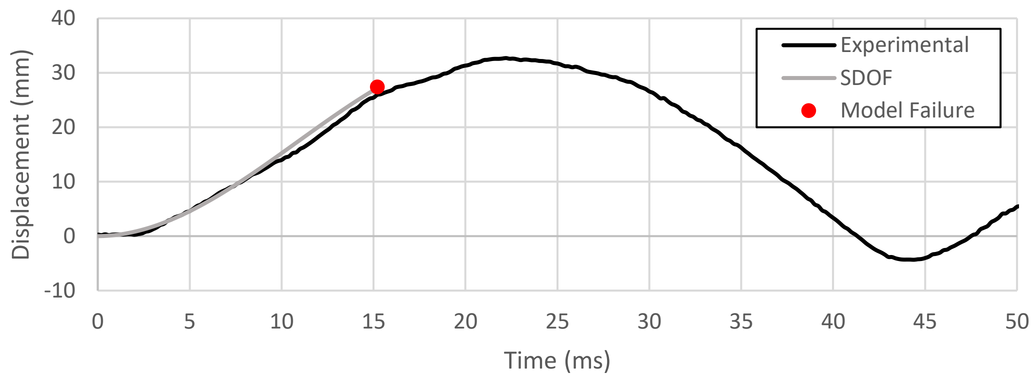

b)

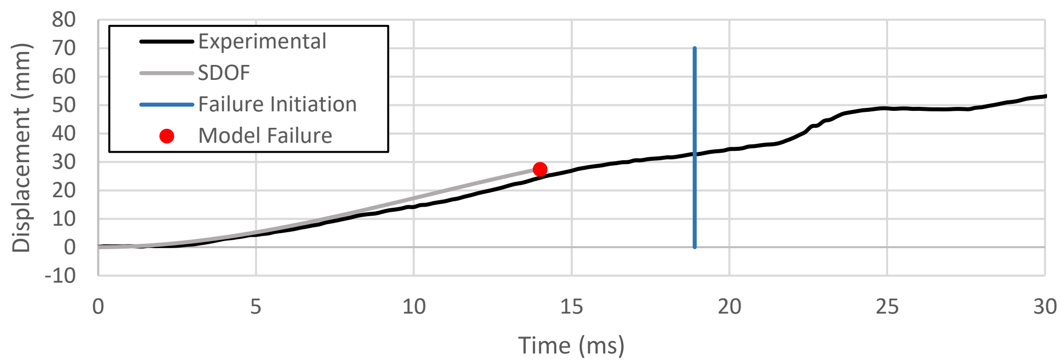

Figure 6.9: Displacement comparison for SDOF model of shots GL2.1 (a) and GL2.2(b) with experimental and analytical time of failure indicated

The model for GL3.1 successfully matched the specimen behavior by remaining in the elastic region of the resistance curve, however it overestimated the maximum mid-span displacement. The model predicted the time to maximum displacement reasonably well, as shown in Figure 6.10a. While the specimen did not fail during test GL3.2, the SDOF model of shot GL3.2 (Figure 6.10b) resulted in failure. The model for test GL3.3 (Figure 6.10c) accurately predicted the displacement of experimental failure, but the prediction occurred slightly before the observed initial cracks during the test. The differences between the analytical results and experimental observations may be attributed to the point of termination for the theoretical resistance curve in Figure 6.6c.

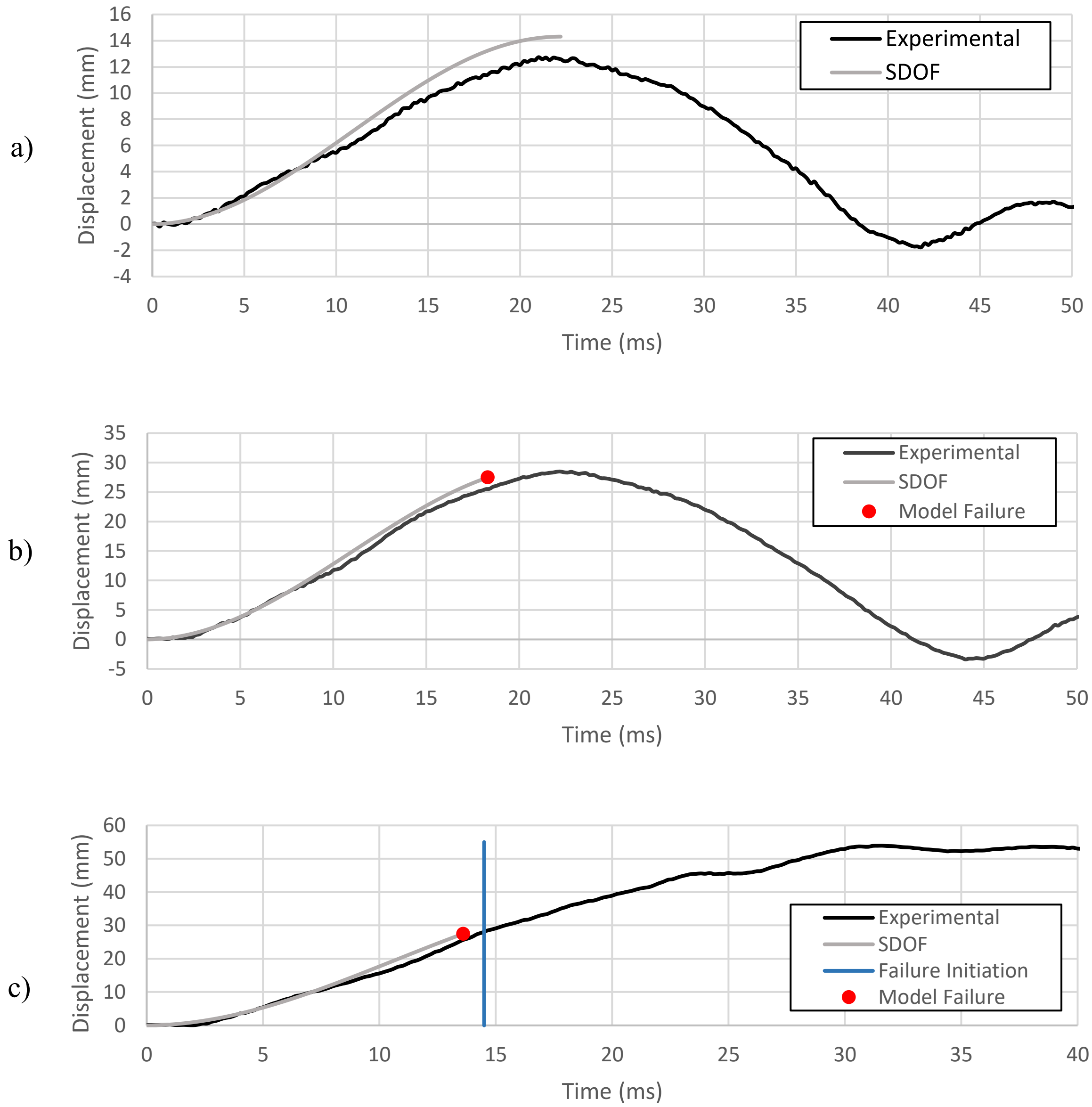

Figure 6.10: Displacement comparison for SDOF model of shots GL3.1 (a), GL3.2 (b), and GL3.3 (c)with experimental and analytical time of failure indicated

6.2.3 CLT Displacement and Failure

The SDOF model was developed in such a way that it is incapable of distinguishing between different failure modes that may occur in CLT (i.e. rolling shear or flexure). As shown in Figure 6.11 to Figure 6.13, the model tended to generally overestimate the mid-span displacement throughout the analysis. Similar to the glulam specimens, the displacement-time histories of the CLT panels are only compared during the inbound phase and the experimental data uses the peak pressure occurrence as a reference time.

While the SDOF model predicted the fifth ply failure of CLT1.1 at a lower time to failure compared to the experimental observations, the corresponding displacement was reasonably accurate. The model results significantly underestimated the post-peak displacement of the CLT panel, as shown in Figure 6.11 where the SDOF model terminates itself before the failure of the third ply was observed during the experiment. These deviations are likely due to the sudden transitions in the theoretical resistance curve used in the SDOF model, which caused the model to indicate damage and termination before the corresponding flexural developments in the specimen. This impaired the model's ability to match post-peak behaviours for the specimen, despite the analytical failure mode matching that of the physical specimen.

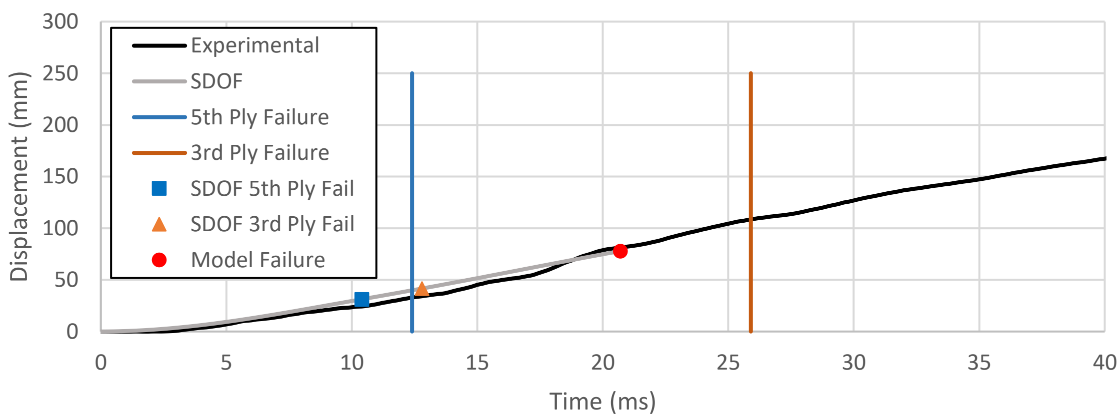

Figure 6.11: Displacement comparison for SDOF model of shot CLT1.1, with times of key experimental and analytical behaviour indicated

Specimen CLT2 displayed combined rolling shear and flexural failure mode throughout the tests, which the SDOF model was unable to completely account for due to the underlying assumption of considering only flexural behaviour. The prediction for shot CLT2.1 resulted in significant overestimation of the maximum displacement and predicted that the fifth and third plies would fail, as can be seen in Figure 6.12a. Considering the specimen behaved mostly elastically during the shot, this is a significant deviation from expected behaviour caused by the sharp reduction in resistance after the peak value was reached. As a consequence of the sudden reduction in resistance (compared to the experimental resistance curves relatively stable degradation), the model displaced considerably more than the specimen in order to dissipate the energy of the equivalent blast load.

In order to account for experimental observations of damage in the outermost plies, both three-ply and five-ply resistance curves were used to model the behaviour of the panel in tests CLT2.2 and CLT2.3 (i.e. where the other ply was already damaged). Both curves produced poor predictions of the maximum displacement observed in test CLT2.2, with the five-ply model analysis producing a slightly more realistic, but underestimated, value. This behaviour can be observed in Figure 6.12b, and stems from transverse ply damage during testing leading to intermediate behaviour between five- and three-ply behaviour, and thus is not adequately described by either implemented resistance curve.

The SDOF model was unable to accurately predict the failure observed in CLT2.3, as the five-ply analysis did not indicate ply failure at displacements near the experimental observation of flexural initiation. This can be attributed to the degraded specimen stiffness differing from the stiffness in the five-ply resistance curve, which was representative of initial panel behaviour. The three-ply implementation indicated failure in the third ply before the experimental observations for flexural failure, although the analysis followed the experimental displacement relatively well, as shown in Figure 6.12c. This is likely due to the increased ductility of the three-ply resistance curve, which agreed reasonably well with the maximum displacement observed in test CLT 2.3 (Figure 6.7c).

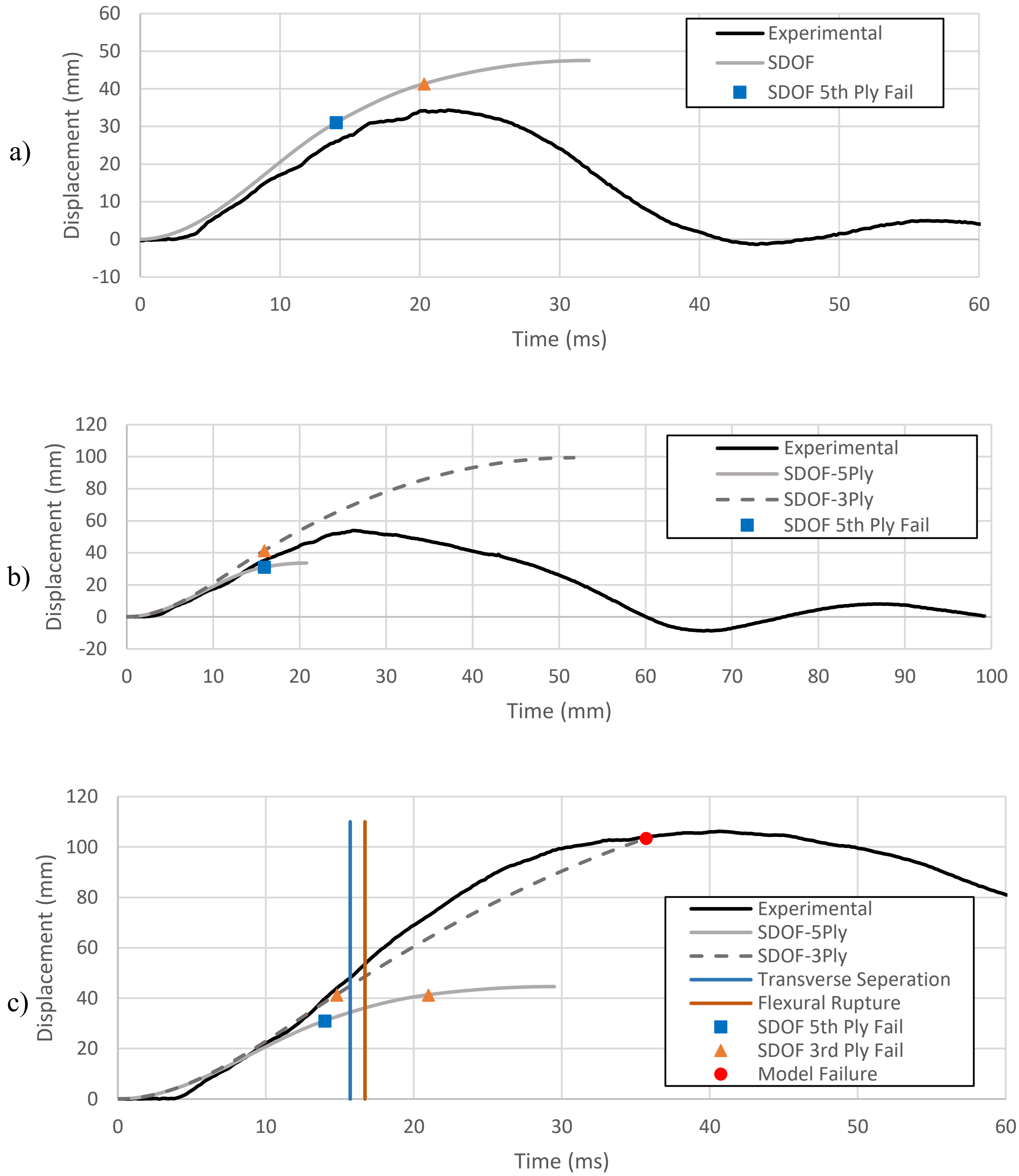

Figure 6.12: Displacement comparison for SDOF model of shots CLT2.1 (a), CLT 2.2 (b), and CLT2.3 (c) with key experimental and analytical behaviour indicated

The experimentally observed behaviour in shot CLT3.1 was predicted by the SDOF model, which remained in the elastic region during the analysis. The SDOF analysis generally produced higher displacements than observed in test CLT3.1, as shown in Figure 6.13a, while the prediction of the time to maximum displacement was reasonable. The model of CLT3.2 (Figure 6.13b) initiated failure at a comparable time to the experimentally observed transverse cracking, despite the difference between the experimental and analytical failure mode. The mid-span displacement for test CLT3.2 was generally overestimated, which could be attributed to this specimen failing in rolling shear rather than flexure.

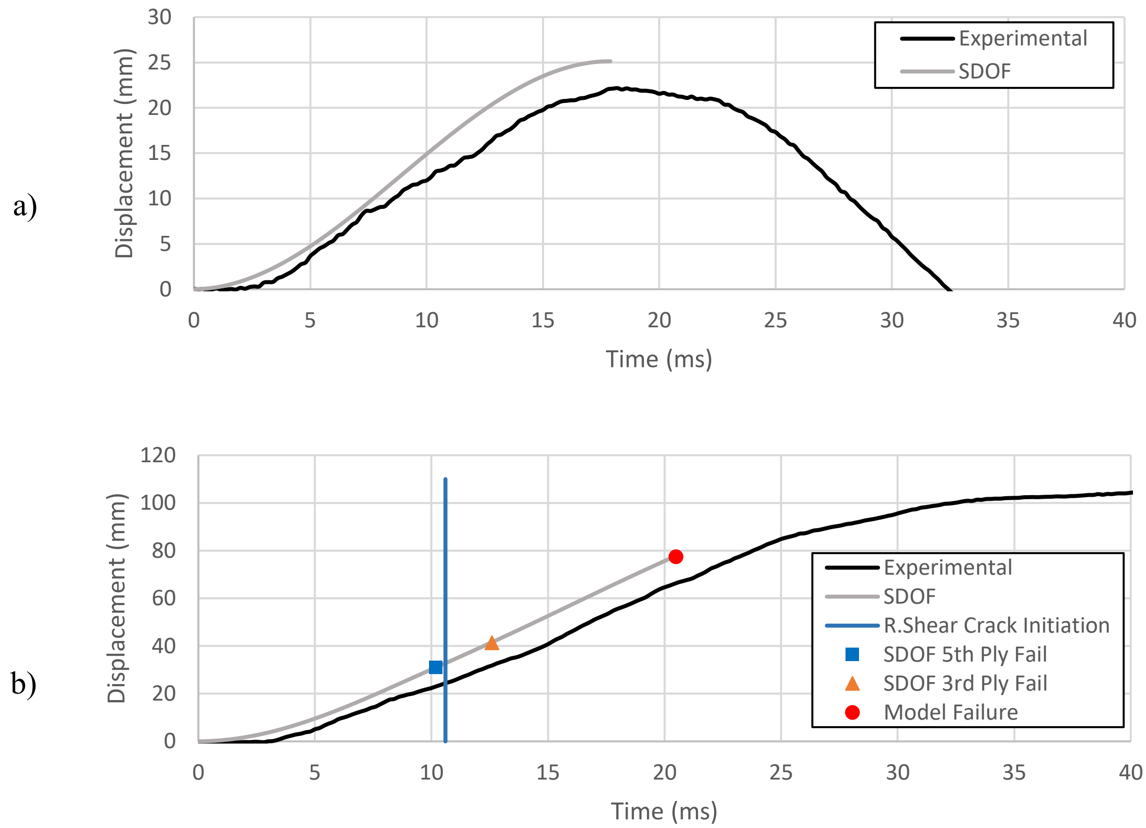

Figure 6.13: Displacement comparison for SDOF model of shots CLT3.1 (a) and CLT3.2 with experimental and analytical behaviour indicated (b)

6.3 Experimental Comparison with FEA

6.3.1 Displacement and Failure Behaviour

In addition to producing a displacement-time history prediction, the ABAQUS/Explicit model allowed for more detailed comparisons with the experimental results in terms of failure progression and the accumulation of damage. Similar to the SDOF results, the comparison only extends to maximum inbound displacement due to the underlying assumptions involving the LTD mass.

The finite element model of shot GL1.1 did not predict the propagation of flexural cracking and failure observed during the dynamic test, but rather only indicated a concentration of damage on the tension face at mid-span. The fact that the model was not able to predict the comparatively weaker behaviour of specimen GL1 is expected and can be attributed to the variability found in the material. Despite the slight discrepancy, it can be seen that the modeled displacement agrees well with the experimental results, as shown in Figure 6.14.

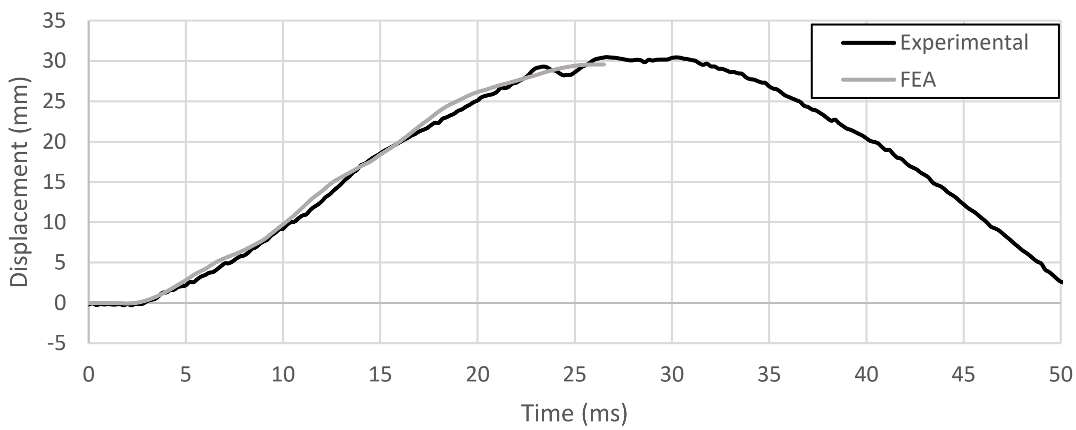

Figure 6.14: Displacement comparison for FEA of shot GL1.1

The simulation results for shot GL2.1 exhibited a high level of damage at maximum displacement but did not exhibit element deletion. Extensive spread of damage between the parallel and perpendicular to grain tension components was observed, which was caused by stress reallocation and is indicative of near material failure within the model. The displacement prediction was reasonably accurate compared to the experimental data but overpredicted the maximum displacement and inbound duration, as presented in Figure 6.15.

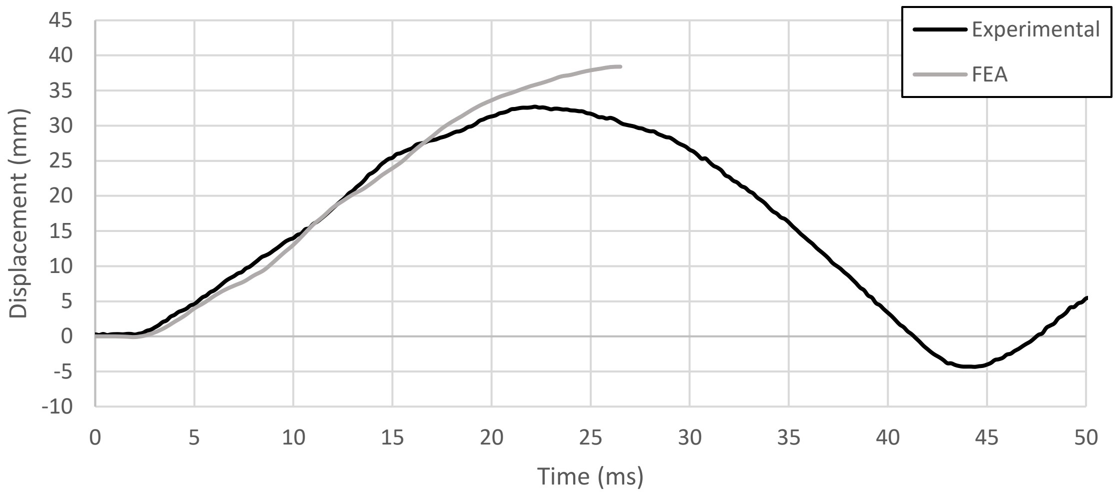

Figure 6.15: Displacement comparison for FEA of shot GL2.1

The predicted failure for shot GL2.2, as defined by the initial element deletion in the model, coincided with the observed maximum propagation of major cracks, as shown in Figure 6.16. It can also be noted that reasonable correlation between the experimental and modeled displacement histories was achieved. Furthermore, it should be noted that damage within the model spreads rapidly, and using the first instance of deletion provides a more reliable indicator of failure. Furthermore, the deletion of an element within the finite element analysis not only leads to local changes in stress distribution, as with physical specimen cracking, but also a reduction to system mass that may introduce further displacement inaccuracy.

The failed states of the analytical and physical specimen are compared in Figure 6.17, where it can be observed that the model produced a satisfactory approximation of flexural failure, with significant central deletion corresponding to the observed flexural cracks which widened at midspan in addition to element failure extending towards the member ends, similar to that observed experimentally.

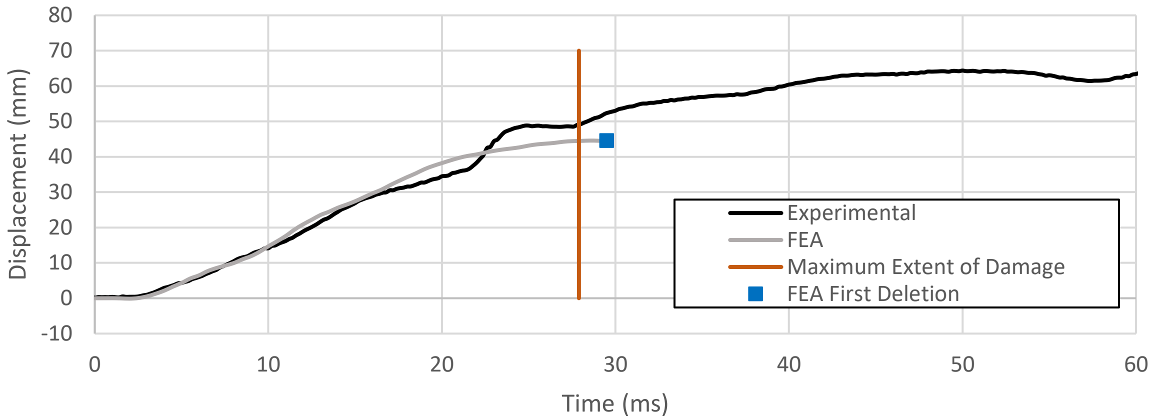

Figure 6.16: Displacement comparison for FEA of shot GL2.2, with experimental and analytical failure observations

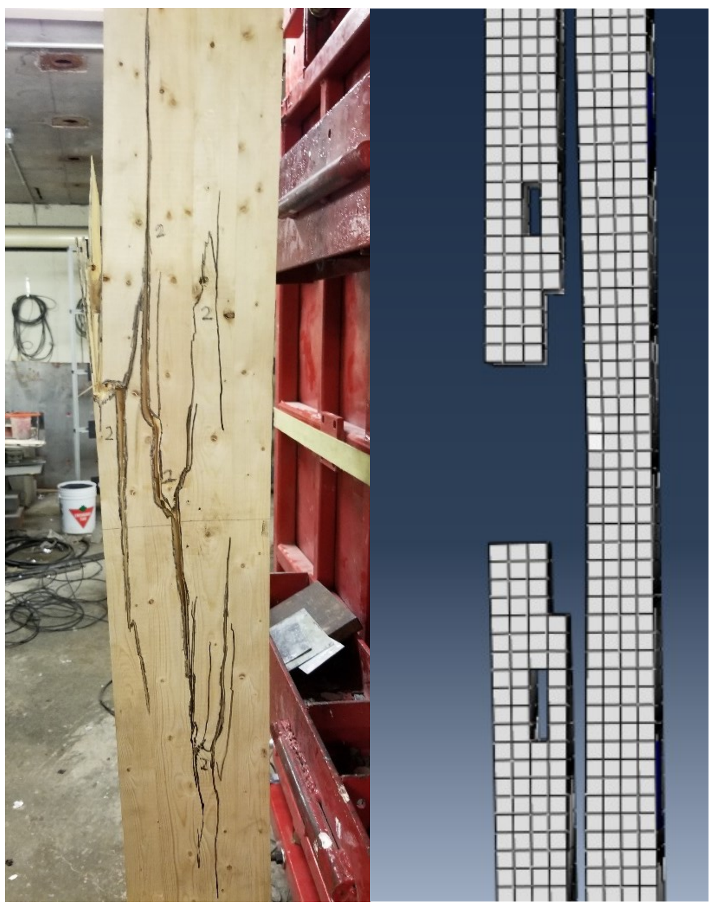

Figure 6.17: Side-by-side comparison between experimental cracking and model deletion for GL2.2

The behaviour generated in the FE model for test GL3.1 corresponded reasonably well to the experimentally observed elastic response, but overestimated the extent and time of maximum displacement compared to the experimental results as shown in Figure 6.18.

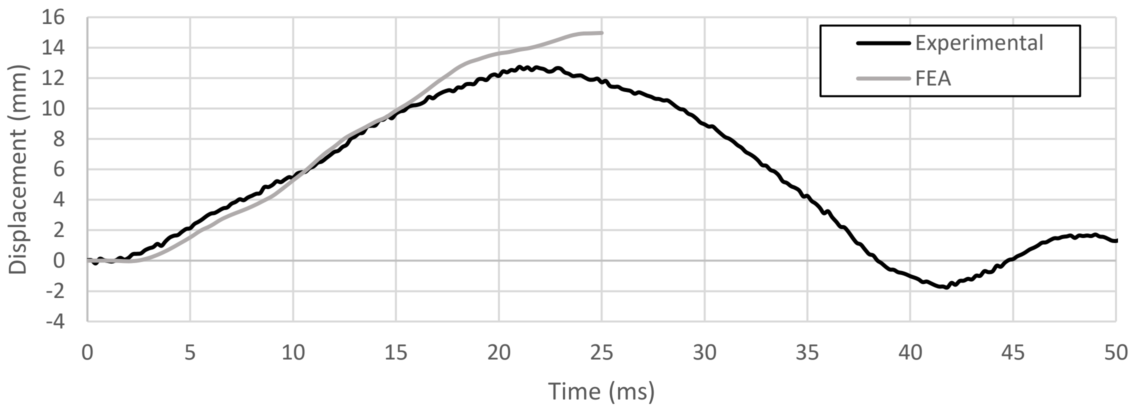

Figure 6.18: Displacement comparison for FEA of shot GL3.1

The finite element model of shot GL3.2 predicted elastic behaviour, as indicated by the absence of element deletion, which was consistent with experimental observations. The maximum displacement was overpredicted by the analysis, as shown in the displacement-time history comparison in Figure 6.19.

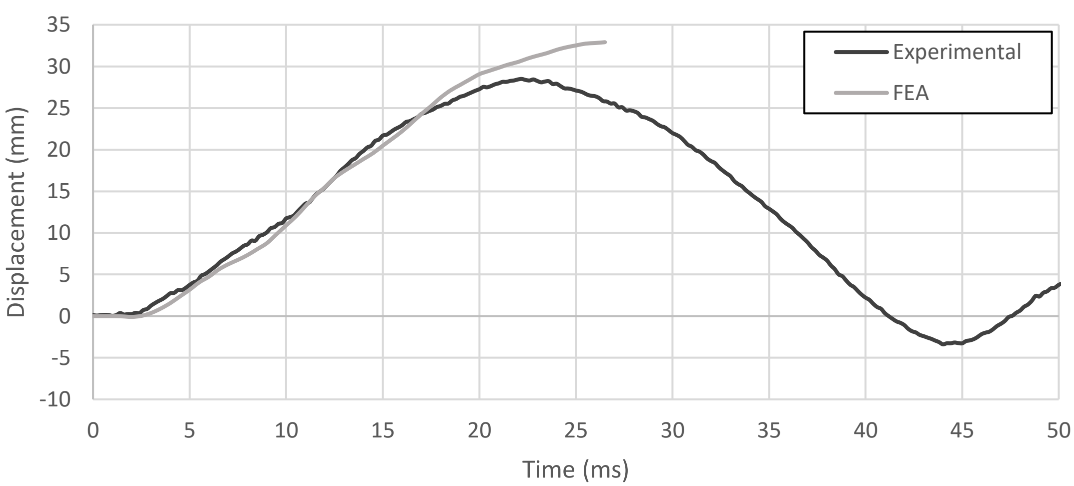

Figure 6.19: Displacement comparison for FEA of shot GL3.2

The model developed for shot GL3.3 resulted in flexural failure with lines of branching element deletion towards the support. This predicted failed state is compared with the experimental results in Figure 6.20, where it can be observed that the model exhibited considerable material failure through the beam depth, extending along the member length. This behaviour resembled the closely spaced cracking along the length of the physical member (Figure 6.20). In particular, the smaller branch of deletion towards the lower support in the model was similar to these parallel cracks, although the model did not propagate these failures to the same extent as that of the observed test results. The initial deletion in the analytical model occurred between the observed times of first and final cracking during the test and reasonably aligned with the end of observed experimental damage, as shown in the displacement comparison in Figure 6.21. The overall displacement prediction agreed well with experimental results.

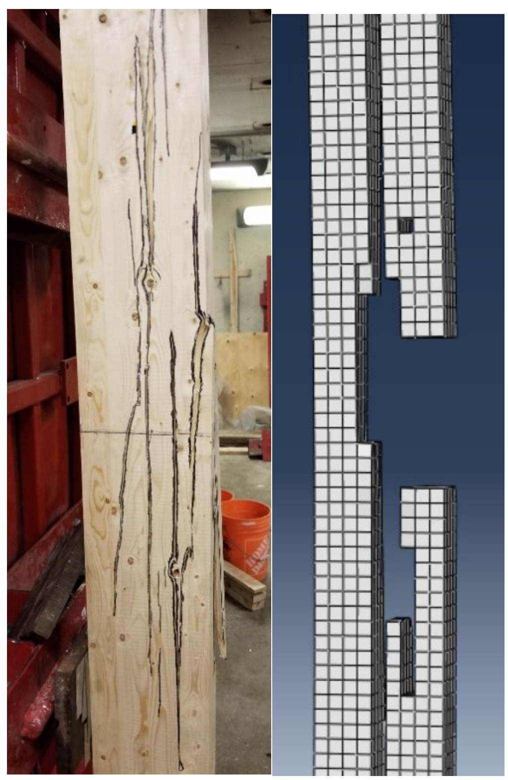

Figure 6.20: Side-by-side comparison between experimental cracking and model deletion for GL3.3

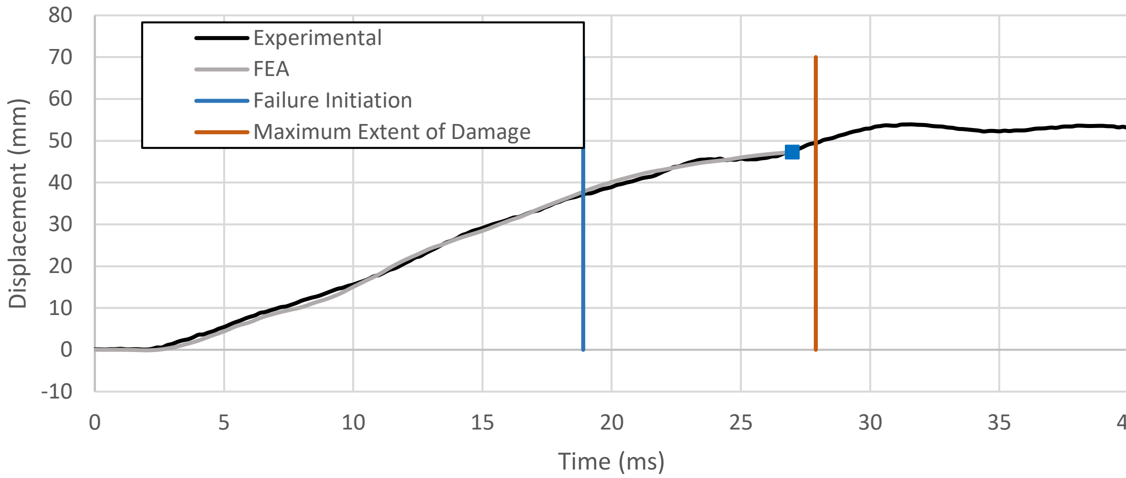

Figure 6.21: Displacement comparison for FEA of shot GL3.3, with key experimental and analytical behaviour indicated

The simulation of test CLT1.1 developed two significant failure mechanisms. The initial behaviour consisted of rolling shear damage near the load application points which propagated throughout the second ply, likely initiated by a high rate of deformation caused by the magnitude of the loading. This would have produced a concentration of shear stresses near the load points, before the internal forces propagated towards the supports, which may have been sufficient to exceed the low rolling shear capacity of the material. The panel continued to deflect and ultimately developed damage parallel to grain in the outer plies until element deletion occurred in the fifth ply, representative of flexural failure. The formation of these patterns aligned with the initial and ultimate failure observations (i.e. initial cracking in the fifth ply and the third ply failure) from high-speed video of the shot and occurred at displacements approximately correlating to the experimental data, as presented in Figure 6.22.

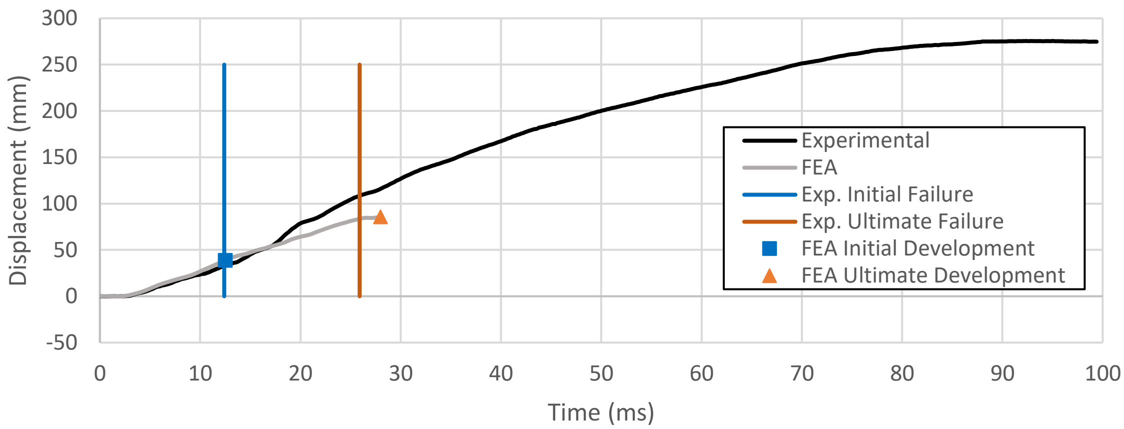

Figure 6.22:Experimental displacement comparison for FEA of shot CLT1.1, including points of initial and ultimate failure

The propagation of deletion within the fourth ply of the model was also consistent with of the cracks in the transverse layers extending behind the ruptured fifth ply, as compared in Figure 6.23. However, the model did not capture the flexural failure in the third ply.

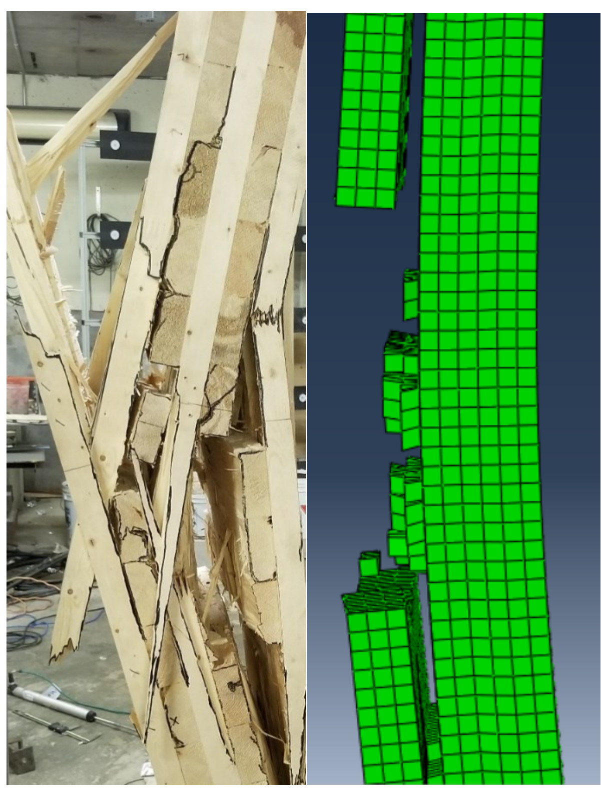

Figure 6.23: Side-by-side comparison of central failure behaviour for CLT1.1

The finite element model for shot CLT2.1 did not predict any rolling shear damage in the transverse layers and primarily predicted tensile damage in the outer plies, consistent with general flexural failure behaviour. The resulting displacement-time history was reasonably similar to the experimental measurements, predicting a higher maximum displacement which occurred before the experimentally observed peak as shown in Figure 6.24.

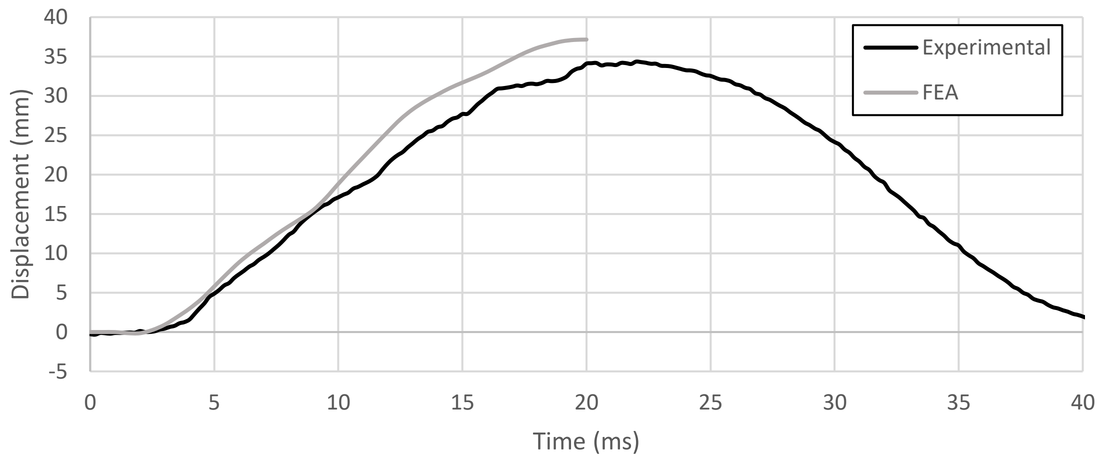

Figure 6.24: Displacement comparison for FEA of shot CLT2.1

The model of test CLT3.1 produced displacement results which were consistent with model CLT2.1 when compared to the experimental results, including overestimation of the maximum displacement, as presented in Figure 6.25. The damage accumulation within the model was limited, similar to the behaviour observed for in physical panel.

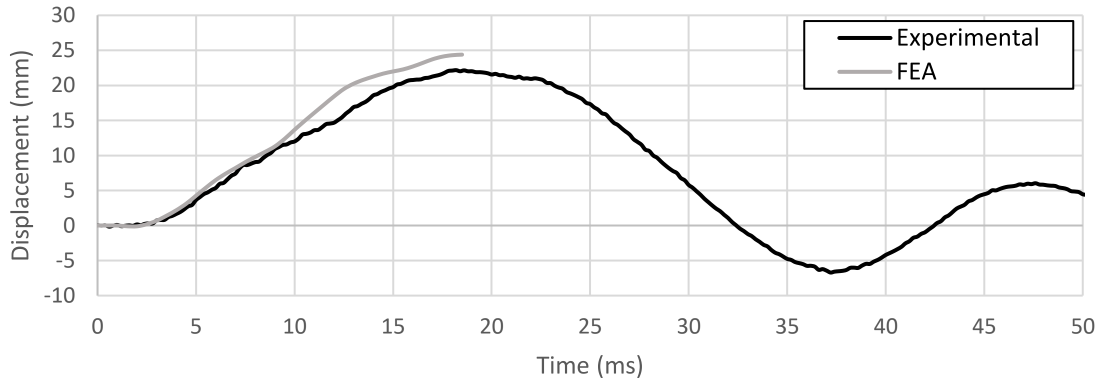

Figure 6.25: Displacement comparison for FEA of shot CLT3.1

6.3.2 Resistance Curves

The resistance curves generated with the output from the ABAQUS model generally exhibited a pattern of oscillation as the model progressed through each time-step. The oscillations can be attributed to the propagation of forces through the member reaching the support points inconsistently across the different time-steps. Another likely source of this could be that the load cells that were used to measure the experimental reactions may not have been sensitive to rapid variations in reaction forces, and thus attenuated the signal and could not capture the variations and oscillations in the reaction forces as the analytical model. While the relative irregularity of the resistance curves prevented a direct numerical comparison, overall consistent trends in the resistance-displacement relationship were observed across both glulam and CLT specimens. The resistance curves are presented in Figure 6.26 to Figure 6.28 for glulam models, and Figure 6.29 for CLT models.

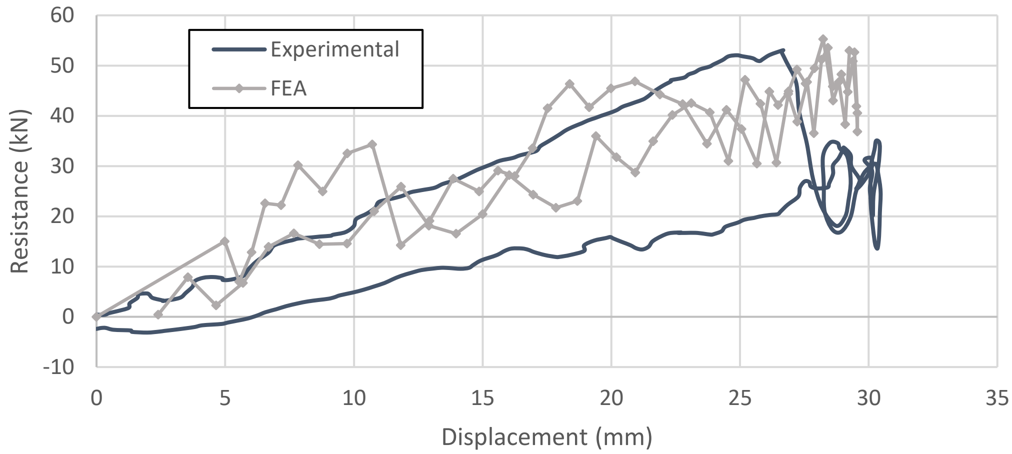

Figure 6.26:Finite element resistance curve comparison for shot GL1.1

a)
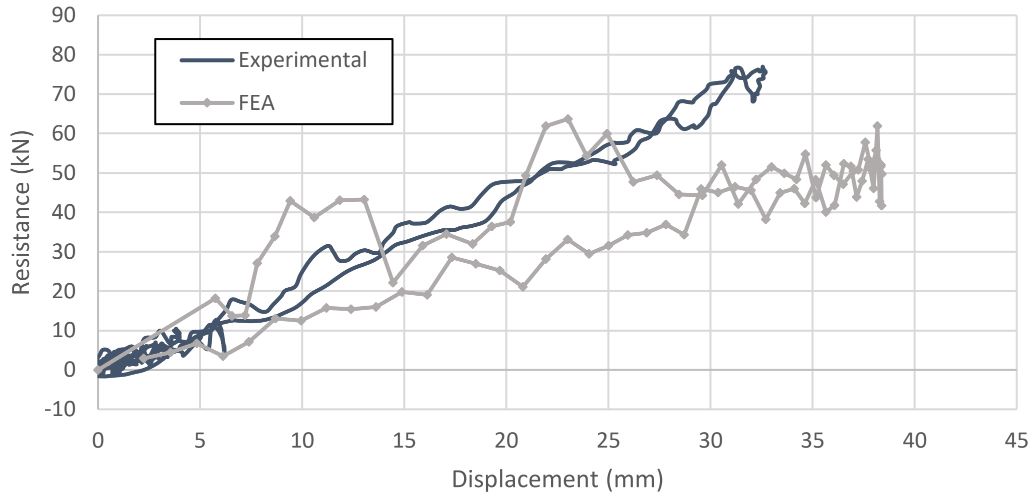

b)
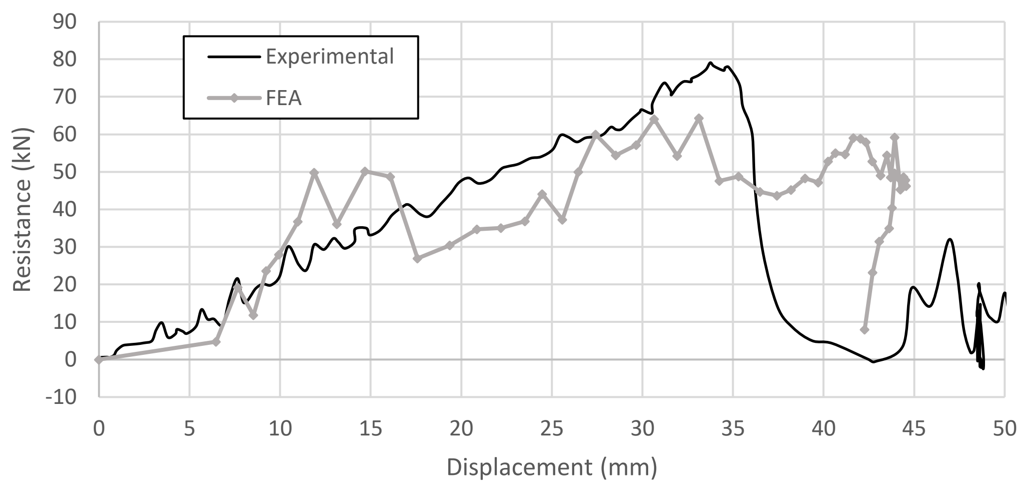

Figure 6.27:Finite element resistance curve comparison for shots GL2.1 (a) and GL2.2 (b)

a)

b)

c)

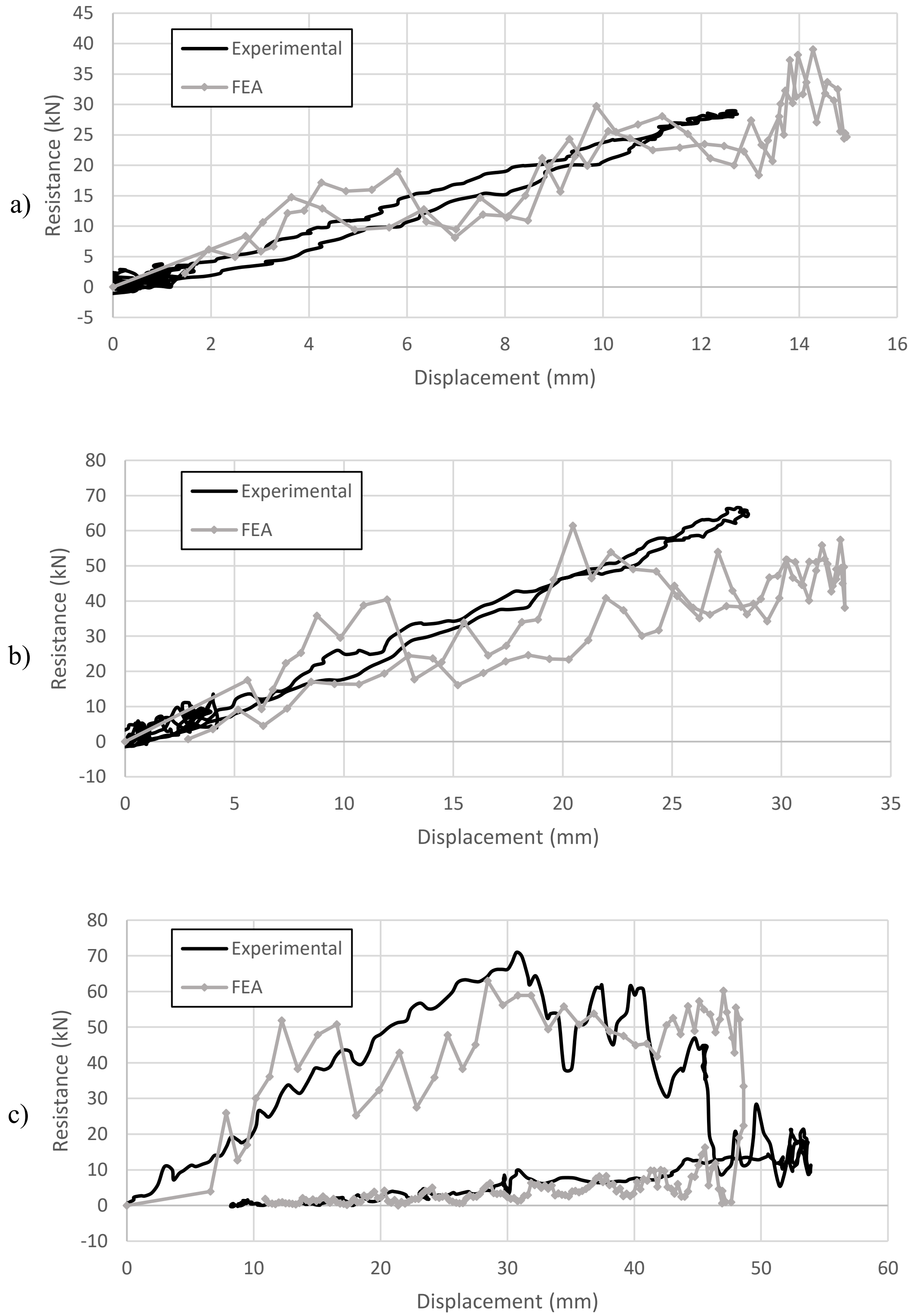

Figure 6.28:Finite element resistance curve comparison for shots GL3.1 (a), GL3.2 (b), and GL3.3 (c)

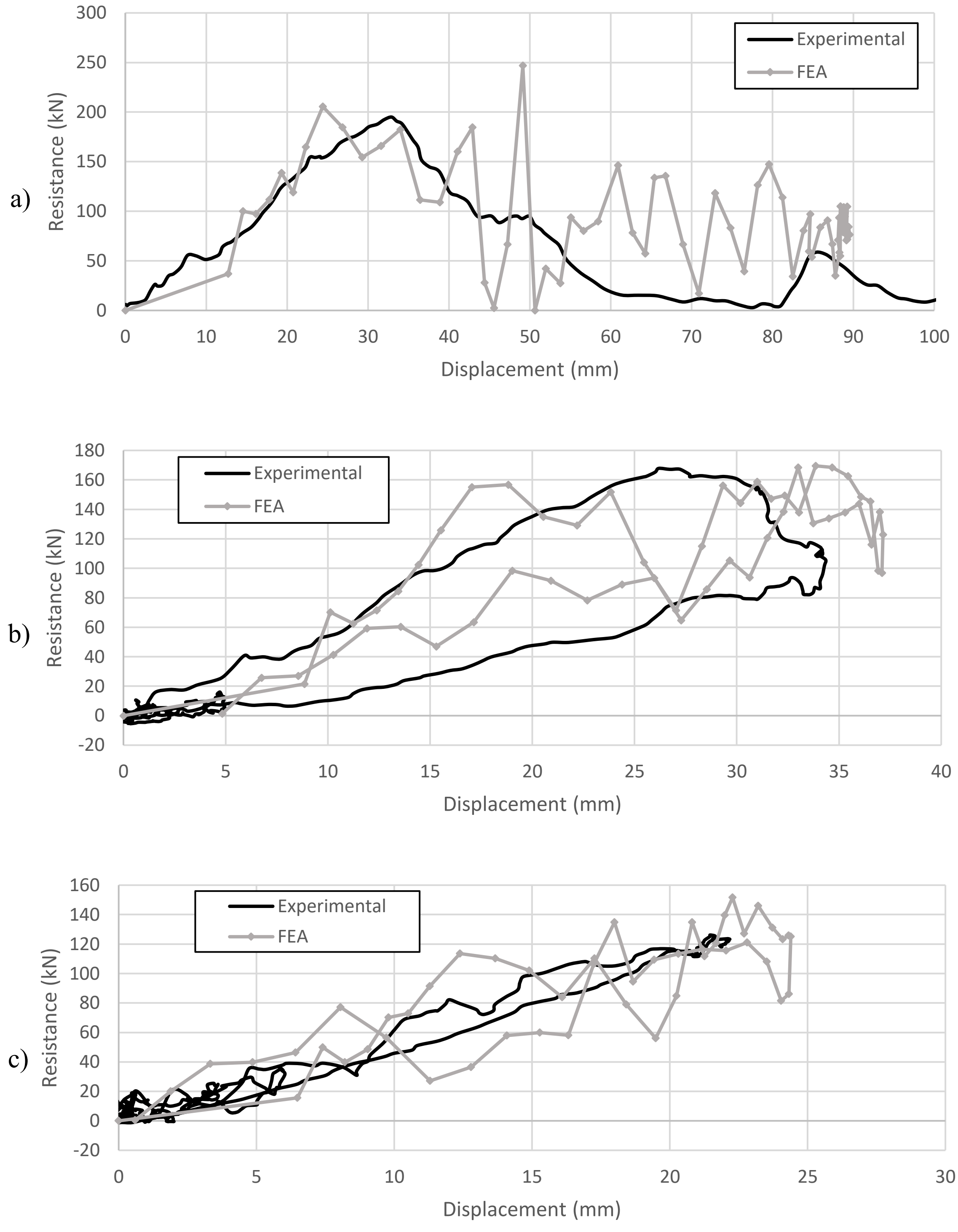

Figure 6.29:Finite element resistance curve comparison for shots CLT1.1 (a), CLT2.1 (b), and CLT3.1(c)

The resistance curves generated from the glulam models agreed reasonably well with the experimentally obtained resistance curves. The predicted curve for test GL1.1 showed good agreement with the initial experimental stiffness but did not match the rebounding stiffness. This discrepancy may be due to the lack of damage in the finite element model, as specimen GL1 reached failure and exhibited stiffness degradation at values where the other glulam specimens behaved elastically. The difference in behaviour may also be attributed to the inclusion of the LTD mass in the FE model, and as mentioned previously, there exists uncertainties related to the contribution of the LTD to specimen behaviour during the rebound phase. The resistance curve output by the model had approximately elastic behaviour as shown in Figure 6.26, which compared well with the experimental stiffness. Similar findings were found for the model of GL3.1, as shown in Figure 6.28a, which produced a reasonable fit to the experimental data. Accordingly, this suggests the LTD may have remained in contact with the glulam specimen during shot GL3.1 and contributed to the inertial forces on the member.

The resistance curves produced by the models for GL2.1 and GL3.2, presented in Figure 6.27a and Figure 6.28b, respectively, initially followed the experimental curves but deviated to a reduced resistance at higher displacements. This was likely caused by the formation of damage in the extreme bending fibres reducing the overall capacity of the analytical member through the softening of the parallel elastic modulus.

The modeled resistance curves for GL2.2 and GL3.3 matched the sudden drop in resistance present in the experimental response, as shown in Figure 6.27b and Figure 6.28c, respectively. The results overpredicted the ultimate displacement, with the model of GL3.3 providing a close fit to the ultimate displacement and residual branch of the experimental curve.

The resistance curve generated by model CLT1.1 followed that of the physical member, although the process of model failure, through rupture of the outer longitudinal ply, increased the erratic behaviour beginning at a displacement of approximately 40 mm, as shown in Figure 6.29a. The modeled resistance curve also fluctuated around a higher average residual strength compared to the experimental results. Model CLT2.1 generated a resistance curve which followed the experimental resistance curve, as shown in Figure 6.29b. The resistance curve obtained from model CLT3.3 followed the general trend of the experimental resistance curve, as shown in Figure 6.29c, and indicated reasonable agreement with the experimental behaviour.

The resistance curves generated by the finite element method generally correlated with experimental results despite the presence of numerical fluctuation, possibly originating from the internal propagation of stresses through the elements or a lack of sensitivity in experimental recording. This is a significant outcome for the potential application of FEA to blast behaviour of timber components, since SDOF models require a resistance curve as input and are unable to predict the force-displacement response of members.

6.4 Comparison Between the Analytical Methods

Both the SDOF and FE models reproduced the experimental results with reasonable accuracy, when considering the effort to develop the models and the input requirements (particularly for the FE model). This consistency in prediction was especially emphasized in cases that did not result in member failure, since the behaviour was sufficiently defined by the maximum displacement and state of the member. Table 6.1 presents a direct comparison between the analytical models and the experimental test data in terms of the accuracy of the predicted displacement. Test GL1.1 was included, despite the significant flexural cracking that was observed during the test, due to its approximately elastic displacement response. The five-ply version for SDOF model CLT2.2 was used in the comparison, as the three-ply resistance curve produced much greater error when implemented.

Table 6.1: Model Comparison Table for Simple Displacement Responses

Test ID	Experimental Results		SDOF Results		FEA Results		Difference SDOF (%)		Difference FEA (%)	
	Δ_{max} [1]	t_{Δ} [2]	Δ_{max} [1]	t_{Δ} [2]	Δ_{max} [1]	t_{Δ} [2]	Δ_{max} [1]	t_{Δ} [2]	Δ_{max} [1]	t_{Δ} [2]
GL1.1	30.5	26.6	27.2	22.5	29.6	26.5	-10.8	+15.4	-3.0	-0.4
GL2.1	32.7	22.2	27.4	15.3	38.4	26.5	-16.2	-31.1	+17.4	+19.4
GL3.1	12.7	21.0	14.3	22.2	15.0	25.0	+12.6	+5.4	+18.1	+19.0
GL3.2	28.5	22.2	27.5	18.3	32.5	26.5	-3.5	-17.6	+14.0	+19.4
Average Absolute Glulam % Difference							10.8	17.4	13.1	14.6
COV							0.43	0.53	0.46	0.56
CLT2.1	34.4	22.0	47.5	32.0	37.2	20.0	+38.1	+45.5	+8.1	-9.1
CLT2.2	53.9	26.2	33.6	20.8	-	-	-37.7	-20.6	-	-
CLT3.1	22.2	18.2	25.1	17.9	24.4	18.5	+13.1	-1.6	+9.9	+1.6
Average Absolute CLT % Difference							29.6	22.6	9.0	5.4
COV							0.39	0.80	0.10	0.69
Overall Average Absolute % Difference							18.9	19.6	11.8	11.5
COV							0.67	0.71	0.45	0.72

1: Maximum Displacement (mm)

2: Time at Maximum Displacement (ms)

As can be observed in Table 6.1, the SDOF method produced more accurate maximum displacements for glulam models in most cases. However, the FE model generally produced more accurate times to maximum displacement. Furthermore, the FE model predicted the maximum displacement of the CLT panels within 10% of experimental values, which was significantly more accurate than the SDOF prediction error of 38.1% and 13.1% for CLT2.1

and CLT3.1, respectively. The average error for the FEA estimation of maximum displacement was 11.8%, with an average error of 11.5% for the estimation of time to maximum displacement. The average error for the SDOF method, excluding values for CLT2.2 for the purposes of direct comparison, was 15.7% and 19.4% for the maximum displacement value and time, respectively. In general, it can be concluded that no significant overall difference can be observed between the two models when considering the estimation of elastic behaviour. This is expected since the behaviour is generally dominated by the stiffness of the member, which can be obtained with reasonable accuracy by both methods. However, the difference in accuracy between the methods for the CLT analyses indicates that the panel behaviour is complex and considerably different to the simpler behaviour of the glulam beams, which was similarly captured by both methods.

As shown in Table 6.2, the FE model was unable to fully account for the behaviour of specimen GL1, which was likely due to variability in the manufacturing (i.e. being weaker than the average of the two other specimens), although the model was more successful in replicating the displacement history from shot GL1.1 than the SDOF analysis (Table 6.1). A finite element model was considered to behave elastically if no element deletion occurred, and the initial failure behaviour was based on the location of primary damage development while the ultimate failure behaviour was based on the location of element deletion. The experimental and FE results generally agreed in terms of failure, although the propagation of failure was reduced for the simulation of test CLT1.1, possibly due to rapid dissipation of energy and inertia caused by element deletion.

Table 6.2: FEA Behavioural Summary and Comparison

Test ID	*Behaviour Development*	*Experimental Behaviour*	*FEA Behaviour*
GL1.1	Initial	Flexural	Elastic
	Ultimate	Flexural	-
GL2.1	Initial	Elastic	Elastic
	Ultimate	-	-
GL2.2	Initial	Flexural	Flexural
	Ultimate	Flexural	Flexural
GL3.1	Initial	Elastic	Elastic
	Ultimate	-	-
GL3.2	Initial	Elastic	Elastic
	Ultimate	-	-
GL3.3	Initial	Flexural	Elastic
	Ultimate	Flexural	-
CLT1.1	Initial	Flexural	R. Shear
	Ultimate	Flexural	Flexural
CLT2.1	Initial	R. Shear	Elastic
	Ultimate	Rebound	-
CLT3.1	Initial	Elastic	Elastic
	Ultimate	-	-

The SDOF models did not consistently predict the failure behaviour of glulam and CLT specimens and tended to fail prior to the corresponding observations. This was particularly the case for models of CLT specimens, where the fit to experimental results was generally worse for the SDOF model due to its limitation of only being capable of predicting flexural behaviour. As such, it was unable to account for the rolling shear behaviour in models CLT2.3 and CLT3.2.

The overall accuracy of the methods is compared in Figure 6.30 and Figure 6.31 for displacement and time to maximum displacement, respectively. It can be observed that both methods produced reasonable approximations of experimental displacements, considering inputs were not adjusted for individual test or specimen observations. The FEA results were within approximately 15% of experimental values. A greater discrepancy was observed in values predicted by the SDOF model, with the least accurate values within 50%. The comparison shows that the finite element model more accurately captured the time to maximum displacement and failure, which is indicative of the accuracy of the approximation throughout the response, and produced a slightly better fit in terms of maximum displacement. It should be noted that Figure 6.30 and Figure 6.31 used maximum displacement or displacement at failure for the comparison.

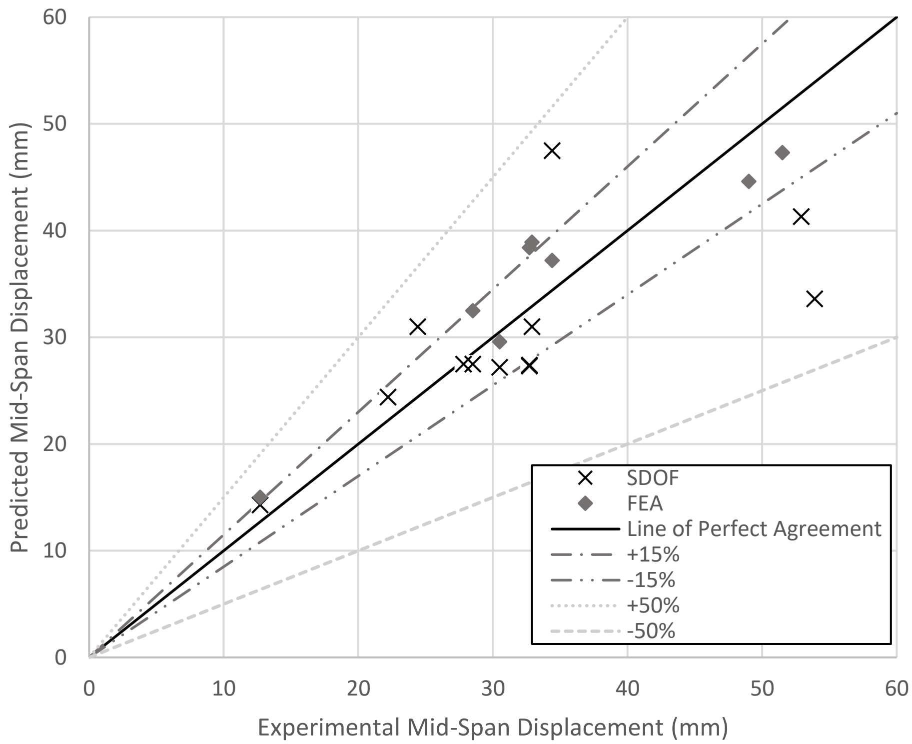

Figure 6.30:Experimental displacements versus analytical predictions

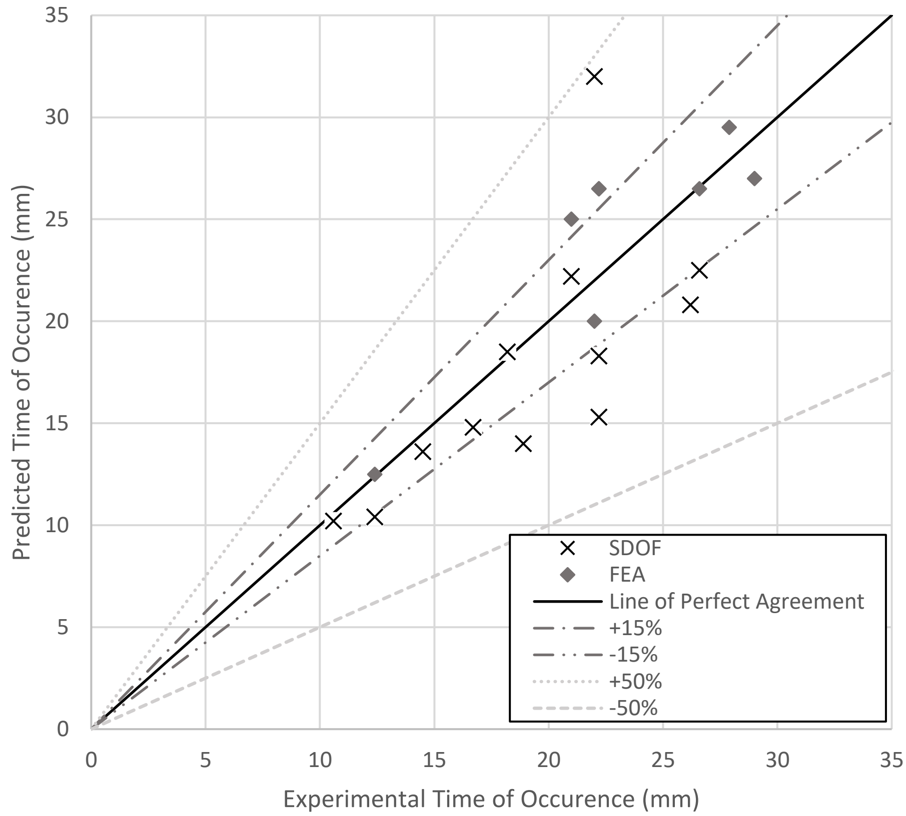

Figure 6.31:Experimental versus predicted times for key behaviours

The FE method generally produced more accurate ultimate behaviour, with the model developing failures that closely resemble those observed in the experimental results. For example, the finite element model for GL2.2 developed element deletion at approximately the same time as ultimate failure in the physical specimen. Also, the model of CLT1.1 developed multiple failure modes that aligned well with experimental observations obtained from the high-speed recording. The finite element model of GL3.3 did not initialize deletion at times corresponding to the experimental observations, but still indicated material failure within the appropriate timeframe.

In summary, both analytical models predicted the elastic behaviour with comparable accuracy, however the FE model was able to predict specimen failure and post-peak behaviour with more detail and better accuracy compared to the SDOF model. It could be concluded that. from a design perspective, the SDOF model sufficiently described member behaviour (i.e.

stiffness and maximum displacement), especially when considering its ease of use and general accuracy.

CHAPTER 7- CONCLUSIONS

7.1 General

In the present study, three glue-laminated timber (glulam) beams and three cross-laminated timber (CLT) panels were subjected to repeated simulated blast loads. The main objective of the experimental study was to evaluate the accuracy of single-degree-of-freedom (SDOF) and finite element analysis (FEA) methodologies to predict the behaviour in terms of displacement-time histories and failure modes. This chapter summarizes the key findings and conclusions drawn from the current study, and proposes possible ideas for future research.

7.2 Conclusions

The following conclusions can be drawn from the current study:

- The failure behaviour of glulam beams subjected to blast loads was found to be highly consistent. Specimens subjected to multiple shots did not experience any stiffness or strength degradation and remained linear-elastic until failure. Failure in glulam specimens was consistently initiated in the midspan region at the tension face. Conversely, the failure behaviour of CLT panels was more complex and differed significantly between the three specimens. The observed behaviours included flexural failure, rolling shear failure, and a combined behaviour where both modes developed simultaneously.
- SDOF analysis was shown to effectively predict the maximum mid-span displacement of glulam members subjected to blast loads, within a 20% error margin. However, the model was found to be incapable of consistently predicting the displacement and time of failure, especially for CLT panels. Generally, the predictions of failure by the SDOF analysis method were premature for both specimen types, including cases where failure was predicted for specimens which remained elastic during the experimental tests. It was also found that SDOF analysis was inconsistent when predicting the maximum mid-span displacement of the CLT panels subjected to blast loads, with up to a 50% error margin. This degree of error was attributed to the model's inability for to account for multiple failure modes, namely rolling shear and flexural failure in the CLT panels.

- A material model for wood was implemented into ABAQUS/Explicit through a dynamic user subroutine (VUMAT). The model used continuum damage mechanics to alter the material stiffness matrix once the elastic strengths were exceeded and was shown to be effective in capturing the dynamic response of timber elements. Reasonably accurate analytical predictions were obtained for both maximum mid-span displacements and the corresponding times, with an average error in elastic models of 11.8% and 9.5% respectively. The finite element models reasonably simulated specimen ultimate behaviour, with good agreement with the experimental observations. However, computational issues with damage transfer prevented the modeling of repeated tests on CLT panels.
- The FE model was capable of producing resistance-displacement relationships which correlated well to experimental results. While the analytical resistance curves displayed considerable fluctuations compared to the experimental data, the overall trends generally followed specimen behaviour. The resistance curves implemented in the SDOF models generally agreed well with experimental results, particularly with regard to initial stiffness, and were deemed sufficiently accurate from the perspective of design use.

7.3 Recommendations for Future Work

Based on observations and results detailed in previous chapters, the following topics have been identified for future work:

- Developing a method to isolate and transfer damage from one model to another, possibly through additional user subroutines, to expand the capability for sequential analysis.
- Investigating the potential of finite element models to be used with more complex boundary conditions, such as realistic end connections and simultaneous axial loading.
- Further refining the modeling techniques to reduce result fluctuation and model assumptions, such as mass distribution techniques and loading methods, which would help broaden the applicability of the model.

- Developing an updated version of the wood material model which accounts for local strength variation, to better account for the presence of defects within timber members and the natural scatter of wood properties, ideally through a stochastic component of the analysis.
- Conducting additional testing on wood components and specimens in order to obtain critical material parameters which are not well established in the literature, such as specific fracture energy according to grain direction. This would ultimately provide better definition for model input variables and reduce the uncertainty in the analysis.

REFERENCES

[1] I. Kuzmanovska, E. Gasoarri, D. T. Monne and M. Aitchison, "Tall Timber Buildings: Emerging Trends and Typologies," in *2018 World Conference on Timber Engineering*, Seoul, South Korea, 2018.

[2] M. Klippel and A. Frangi, "Fire Safety of Glued-Laminated Timber Beams in Bending," *Journal of Structural Engineering,* vol. 143, no. 7, p. 4017052, 2017.

[3] M. A. H. Mirdad, Y. H. Chui and D. Tomlinson, "Capacity and Failure-Mode Prediction of Mass Timber," *Journal of Structural Engineering,* vol. 147, no. 2, p. 4020338, 2021.

[4] C. Viau and G. Doudak, "Investigating the Behaviour of Typical and Designed Wall-to-Floor Connections in Light-Frame Wood Stud Wall Structures Subjected to Blast Loading," *Canadian Journal of Civil Engineering,* vol. 43, no. 6, pp. 562-572, 2016.

[5] A. Lopez-Molina, "The Effect of Steel Strapping Tensioning Technique and Fibre-Reinforced Polymer on the Performance of Cross-Laminated Timber Slabs Subjected to Blast Loads," University of Ottawa, Ottawa, ON, 2018.

[6] Canadian Wood Council, "Structure and Properties of Wood - CWC Educator's Kit," March 2019. [Online]. Available: https://cwc.ca/wp-content/uploads/2019/03/Structure-and-Properties-of-Wood.ppt. [Accessed March 2021].

[7] Canadian Standards Association, CSA O86: Engineering Design in Wood, Mississauga, ON: CSA Group, 2017.

[8] E. Jacques, A. Lloyd, A. Braimah, M. Saatcioglu, G. Doudak and O. Abdelalim, "Influence of high strain-rates on the dynamic flexural material properties of spruce-

pine-fir wood studs," *Canadian Journal of Civil Engineering,* vol. 41, no. 1, pp. 56-64, 2014.

[9] D. N. Lacroix and G. Doudak, "Determining the Dynamic Increase Factor for Glued-Laminated Timber Beams," *Journal of Structural Engineering,* vol. 144, no. 9, p. 4018160, 2018.

[10] M. Poulin, C. Viau, D. N. Lacroix and G. Doudak, "Experimental and Analytical Investigation of Cross-Laminated Timber Panels Subjected to Out-of-Plane Blast Loads," *Journal of Structural Engineering,* vol. 144, no. 2, p. 4017197, 2018.

[11] C. Viau, "Investigation and Optimization of Connections in Timber Assemblies Subjected to Blast Loading," University of Ottawa, Ottawa, ON, 2020.

[12] FP Innovations, CLT Handbook: Cross Laminated Timber, Quebec City, QC: Author, 2011.

[13] D. Dusenberry, Handbook for Blast-Resistance Design of Buildings, Hoboken, N.J.: Wiley & Sona, 2010.

[14] D. Cormie, G. Mays and P. Smith, Blast effects on buildings, London, UK: Thomas Telford Limited, 2009.

[15] US Army Corps of Engineers, "UFC 3-340-02 Structures To Resist The Effects Of Accidental Explosions, With Change 2," 5 December 2008. [Online]. Available: https://www.wbdg.org/ffc/dod/unified-facilities-criteria-ufc/ufc-3-340-02. [Accessed 14 April 2021].

[16] F. G. Friedlander, "The diffraction of sound pulses I. Diffraction by a semi-infinite plane," *Proceedings of the Royal Society of London, Series A,* vol. 186, no. 1006, pp. 322-344, 1946.

[17] J. M. Biggs, Introduction to Structural Dynamics, New York, NY: McGraw-Hill, 1964.

[18] D. L. Logan, A First Course in the Finite Element Method, Toronto, ON: Nelson/Thomson Canada, 2007.

[19] J. Dinwoodie, Timber, its nature and behaviour, London, UK: CRC Press, 2000.

[20] A. H. Buchanan, "Bending Strength of Lumber," *Journal of Structural Engineering,* vol. 116, no. 5, pp. 1213-1229, 1990.

[21] I. Bazan, "Ultimate Bending Strength of Timber Beams," Nova Scotia Technical College, Halifax, NS, 1980.

[22] B. Jansson, "Impact Loading of Timber Beams," University of British Columbia, Vancouver, BC, 1992.

[23] J. Barrett and W. Lau, "Canadian Lumber Properties," Canadian Wood Council, Ottaw, ON, 1994.

[24] J. Liska, "Effect of rapid loading on the compressive and flexural strength of wood," United States Deptartment of Agriculture, Forest Service, Forest Products Laboratory, Madison, WI, 1950.

[25] J. S. Nadeau and R. Bennett, "An explanation for the rate-of-loading and duration-of-load effects in wood in terms of fracture mechanics," *Journal of Materials Science,* vol. 17, no. 10, pp. 2831-2840, 1982.

[26] R. Spencer, "Rate of loading effect in bending for Douglas-Fir lumber," in *1st International Conference on Wood Fracture*, Banff, AB, 1978.

[27] D. N. Lacroix and G. Doudak, "Investigation of Dynamic Increase Factors in Light-Frame Wood Stud Walls Subjected to Out-of-Plane Blast Loading," *Journal of Structural Engineering,* vol. 141, no. 6, p. 4014159, 2015.

[28] C. Viau and G. Doudak, "Investigating the Behaviour of Light-Frame Wood Stud Walls Subjected to Severe Blast Loading," *Journal of Structural Engineering,* vol. 142, no. 12, p. 4016138, 2016.

[29] M. Weaver, C. O'Laughlin and C. Newberry, "Blast Resistance of Cross-Laminated Timber Construction," in *17th International Symposium on the Interactions of the Effects of Munitions with Structures*, Bad Neuenahr, DE, 2017.

[30] M. Weaver, C. Newberry, L. Podesto and C. O'Laughlin, "Blast Testing of Loaded Cross-Laminated Timber Structures," in *SEI Structures Congress 2018*, Fort Worth, TX, 2018.

[31] D. N. Lacroix and G. Doudak, "Effects of High Strain Rates on the Response of Glulam Beams and Columns," *Journal of Structural Engineering,* vol. 144, no. 5, p. 4018029, 2018.

[32] D. N. Lacroix and G. Doudak, "Experimental and Analytical Investigation of FRP Retrofitted Glued-Laminated Beams Subjected to Simulated Blast Loading," *Journal of Structural Engineering,* vol. 144, no. 7, p. 4018089, 2018.

[33] D. Côté and G. Doudak, "Experimental investigation og cross-laminated timber panels with realistic boundary conditions subjected to simulated blast loads," *Engineering Structures,* vol. 187, pp. 444-456, 2019.

[34] C. Viau and G. Doudak, "Behaviour and Modeling of Glulam Beams with Bolted Connections Subjected to Shock Tube-Simulated Blast Loads," *Journal of Structural Engineering,* vol. 147, no. 1, p. 4020305, 2021.

[35] C. Viau and G. Doudak, "Behaviour and modelling of cross-laminated timber panels with boundary connections subjected to blast loads," *Engineering Structures,* vol. 197, p. 109404, 2019.

[36] C. Viau and G. Doudak, "Dynamic analysis methods for modelling timber assemblies subjected to blast loading," *Engineering Sturctures,* vol. 233, p. 111945, 2021.

[37] C. Sandhaas, "Mechanical Behaviour of Timber Joints with Slotted-In Steel Plates," Delft University of Technology, Delft, Netherlands, 2012.

[38] T. Reichert, Development of 3D Lattice Models for Predicting Nonlinear Timber Joint Behaviour, Edinburgh, UK: Edinburgh Napier University, 2009.

[39] C. Sandhaas, A. K. Sarnaghi and J.-W. v. d. Kuilen, "Numerical modeling of timber and timber joints: computational aspects," *Wood Science and Technology,* vol. 54, no. 1, pp. 31-61, 2019.

[40] Dassault Systèmes, *ABAQUS FEA,* Software: Simulia, 2020.

[41] Z. Hashin, "Failure Criteria for Unidirection Fiber Composites," *Journal of Applied Mathematics,* vol. 47, pp. 329-334, 1980.

[42] A. Kaliyanda, D. Rammer and R. Rowlands, "Three-Dimensional Nonlinear Finite-Element Analysis of Wood-Steel Bolted Joints Subjected to Large Deformations," *Journal of Structural Engineering,* vol. 145, no. 10, p. 4019108, 2019.

[43] C. Sandhaas, J.-W. v. d. Kuilen and H. J. Blass, "Constitutive Model for Wood Based on Continuum Damage Mechanics," in *World Conference on Timber Engineering*, Auckland, New Zealand, 2012.

[44] M. Wang, X. Song and X. Gu, "Three-Dimensional Combined Elastic-Plastic and Damage Model for Nonlinear Analysis of Wood," *Journal of Structural Engineering,* vol. 144, no. 8, p. 4018103, 2018.

[45] Y. D. Murray, Manual for LS-DYNA Wood Material Model 143, McLean, VA: Federal Highway Administration, 2007.

[46] LSTC, LS-DYNA, Software: Livermore Software Technology Corp., 2020.

[47] Nordic Structures, "Nordic-Lam Glued Laminated Timber," 2020. [Online]. Available: https://www.nordic.ca/en/products/nordic-lam-glued-laminated-timber-glulam. [Accessed 15 February 2020].

[48] Nordic Structures, Nordic X-Lam Technical Guide NS-GT6, Montreal, QC: Author, 2020.

[49] D. N. Lacroix, "Investigating the Behaviour of Glulam Beams and Columns Subjected to Simulated Blast Loads," University of Ottawa, Ottawa, ON, 2017.

[50] Nordic Structures, "Technical Note S01," Author, Montreal, QC, 2015.

[51] E. Jacques, *RCBlast [Version 0.5.1],* Retrieved from www.rcblast.ca, 2014.

[52] E. Jacques, "Blast Retrofit of Concrete Walls and Slabs," University of Ottawa, Ottawa, ON, 2011.

[53] Dassault Systèmes, *ABAQUS 6.13 Documentation,* 2013.

[54] J. Jönsson and S. Thelandersson, "The effect of moisture gradients on tensile strength perpendicular to grain in glulam," *Holz als Roh- und Werkstoff,* vol. 61, no. 5, pp. 342-348, 2003.

[55] P. Hoffmeyer, L. Damkilde and T. Pedersen, "Structural timber and glulam in compression perpendicular to grain," *Holz Als Roh- Und Werkstoff,* vol. 58, no. 1-2, pp. 73-80, 2000.

[56] L. Boström, "Method for determination of the softening behaviour of wood and the applicability of a nonlinear fracture mechanics model," Lund University, Lund, SE, 1992.

[57] Z. Wang, J. Zhou, W. Dong, Y. Yao and M. Gong, "Influence of technical characteristics on the rolling shear properties of cross laminated timber by modified planar shear tests," *Maderas,* vol. 20, pp. 469-478, 2018.

[58] D. W. Green, J. E. Winandy and D. E. Kretschmann, "Chapter 4: Mechanical Properties of Wood," in *Wood Handbook: Wood as an Engineering Material*, Madison, WI, USDA Forest Service, Forest Products Laboratory, 1999, pp. 4.1-4.45.

[59] Canadian Standards Association, CSA S850: Design and Assessment of Buildings Subjected to Blast Loads, Mississauga, ON: CSA Group, 2012.

APPENDIX A: DYANMIC TESTING RESULTS

A.1 Specimen GL1

Specimen GL1 weighed 20.9 kg and had a moisture content of approximately 14%. The specimen failed in flexure during the first shot, with cracks developing over roughly a third of the cross-section.

A.1.1 Test GL1.1

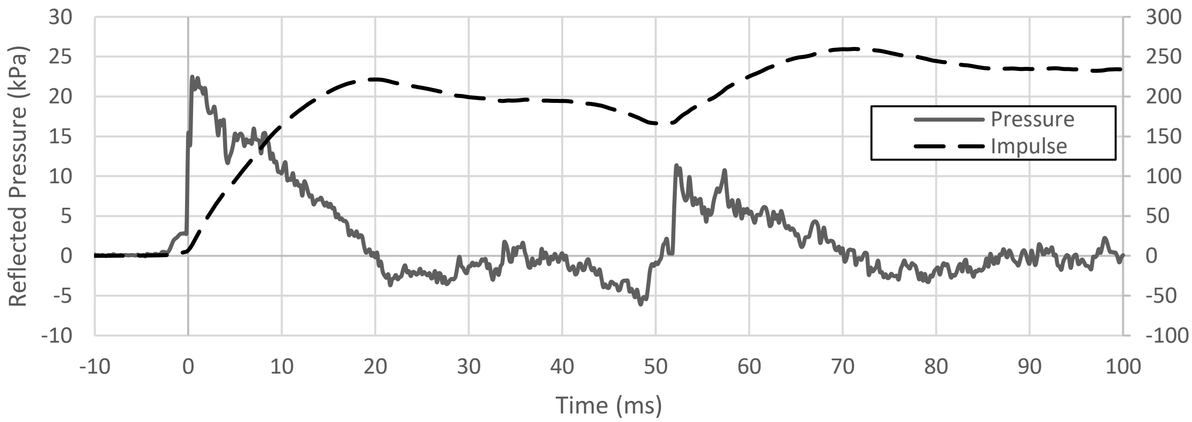

Figure A.1: Pressure-time history and cumulative impulse for GL1.1

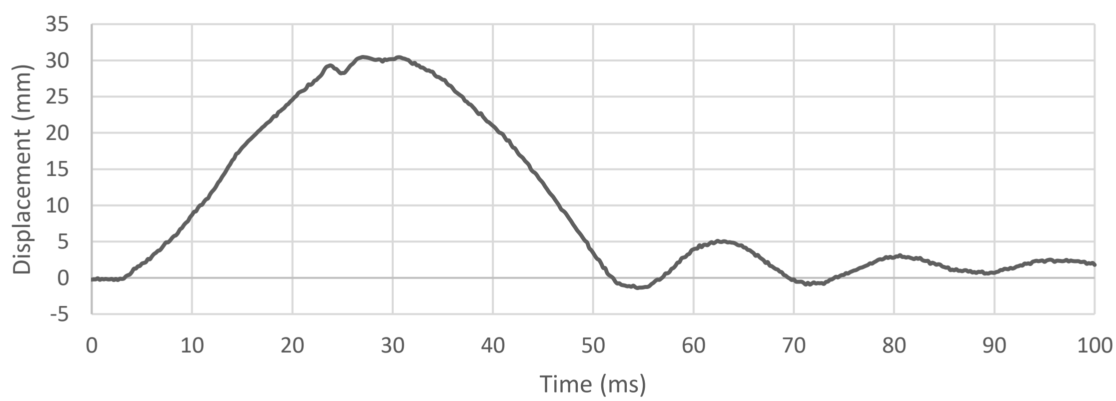

Figure A.2: Displacement-time history for GL1.1

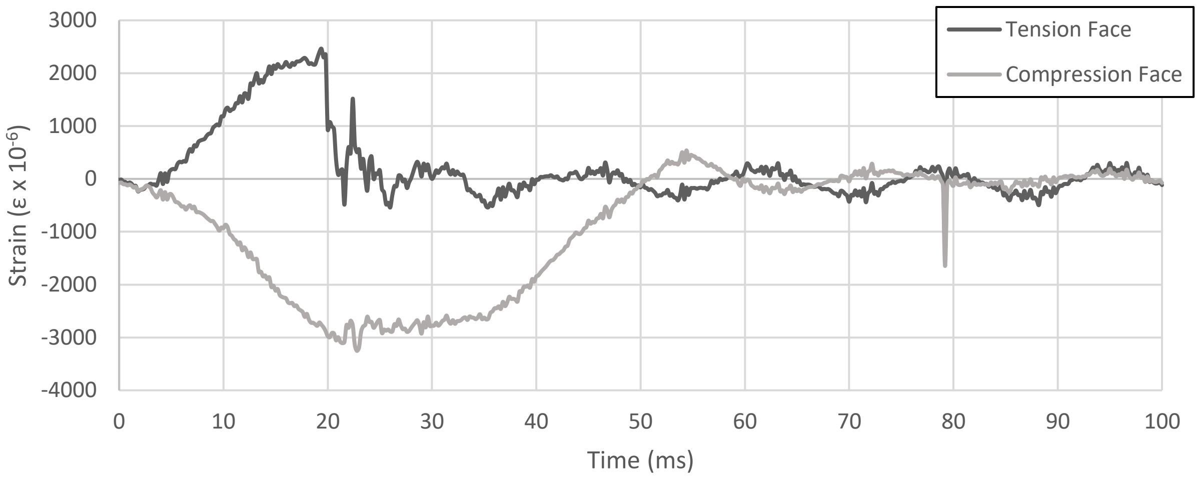

Figure A.3: Mid-span strain measurements for GL1.1

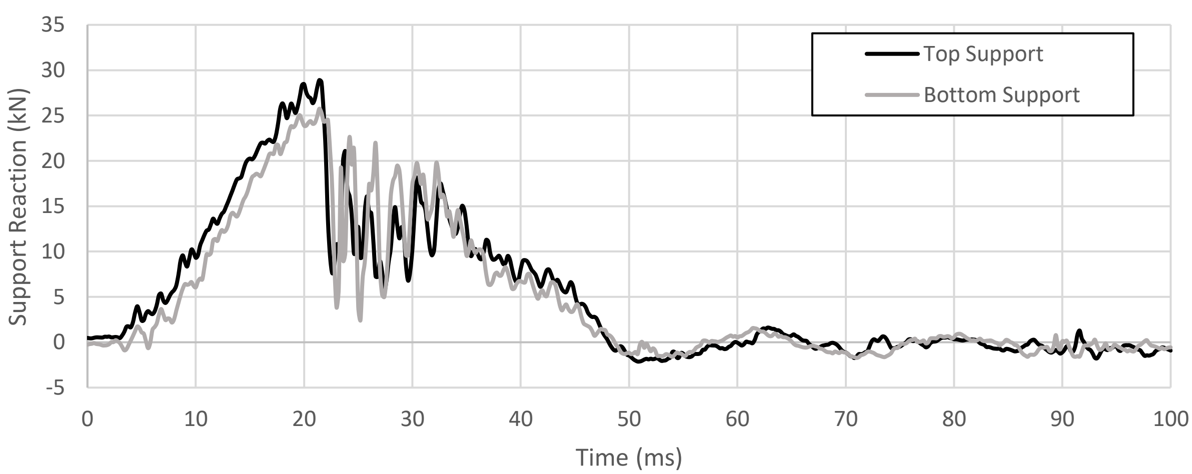

Figure A.4: Reaction-time histories for GL1.1

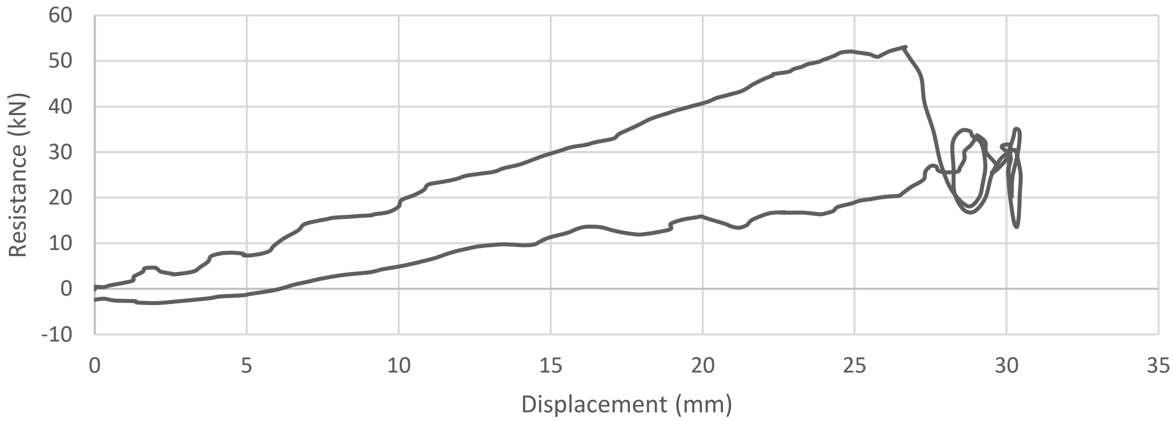

Figure A.5: Experimental resistance curve for GL1.1

a) b) c) d)

Figure A.5: Initial (a) and failed state (b, left side; c, tension face; d, right side) for test GL1.1

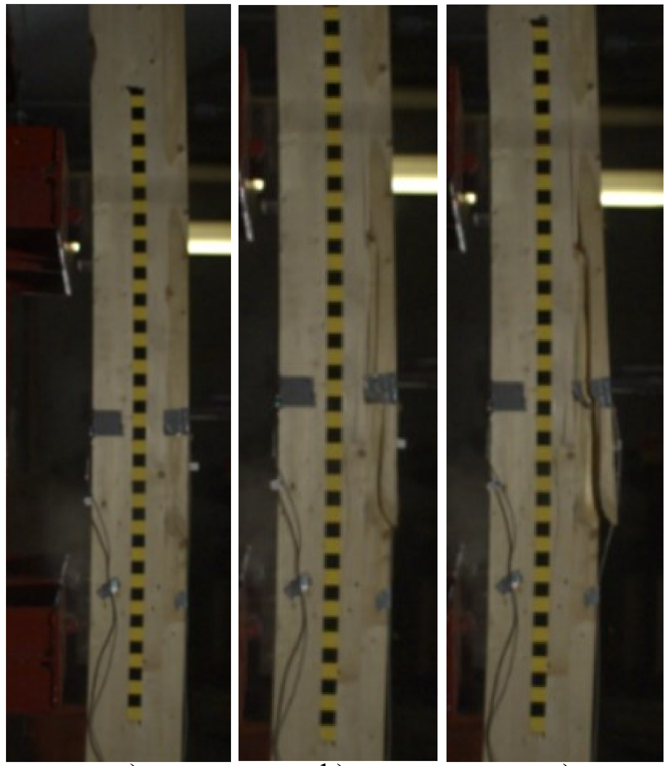
a) b) c)

Figure A.6: Progression of failure during test GL1.1: a) 21 ms b) 22.5 ms c) 25.5 ms

A.2 Specimen GL2

Specimen GL2 weighed 20.7 kg and had a moisture content of approximately 14%. The first test on the specimen resulted in minor damage due to a finger-joint failure in an edge lamination. The second test caused specimen failure, with widespread cracking throughout the mid-span region.

A.2.1 Test GL2.1

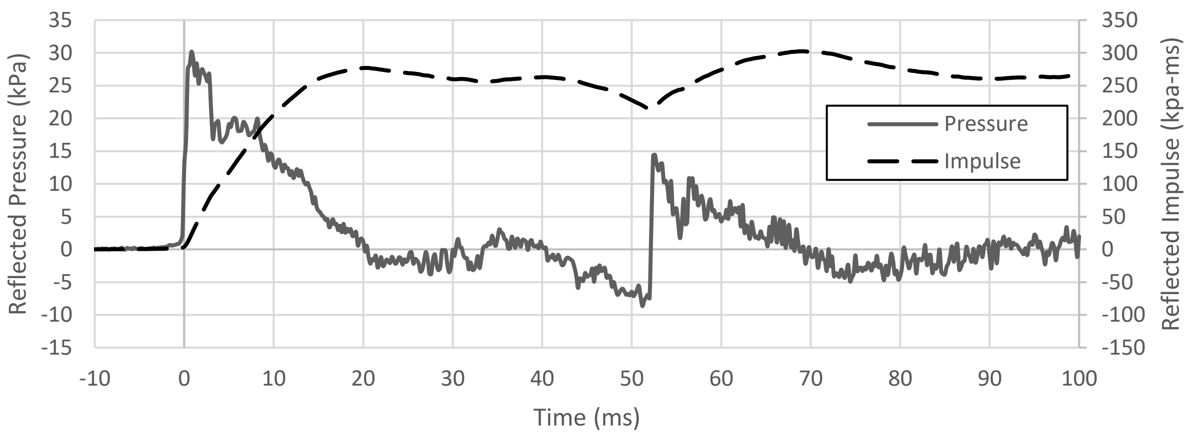

Figure A.7: Pressure-time history and cumulative impulse for GL2.1

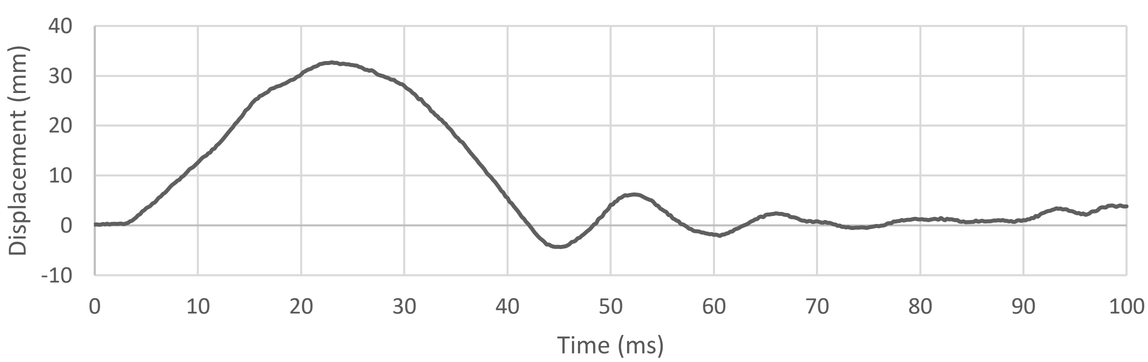

Figure A.8: Displacement-time history for GL2.1

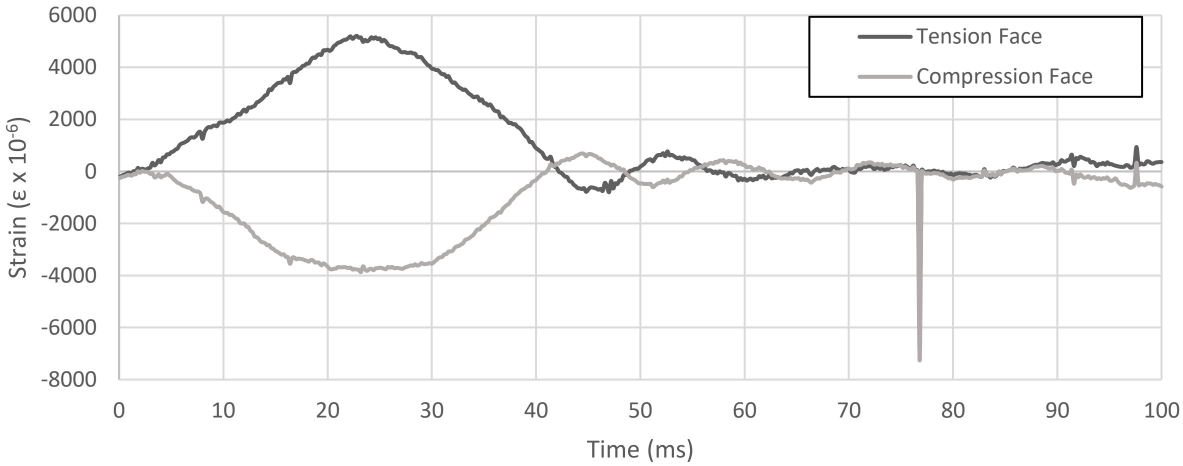

Figure A.9: Mid-span strain measurements for GL2.1

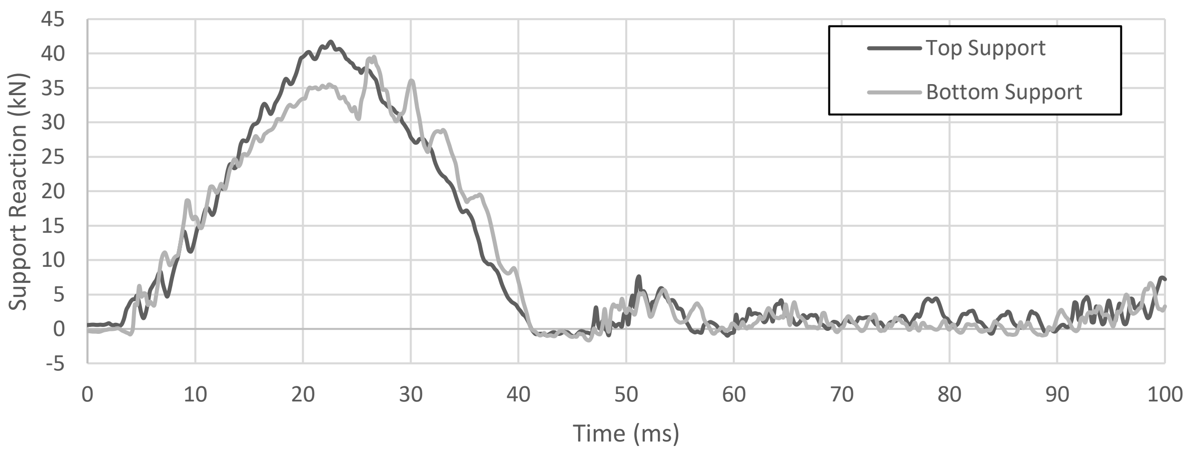

Figure A.10: Reaction-time histories for GL2.1

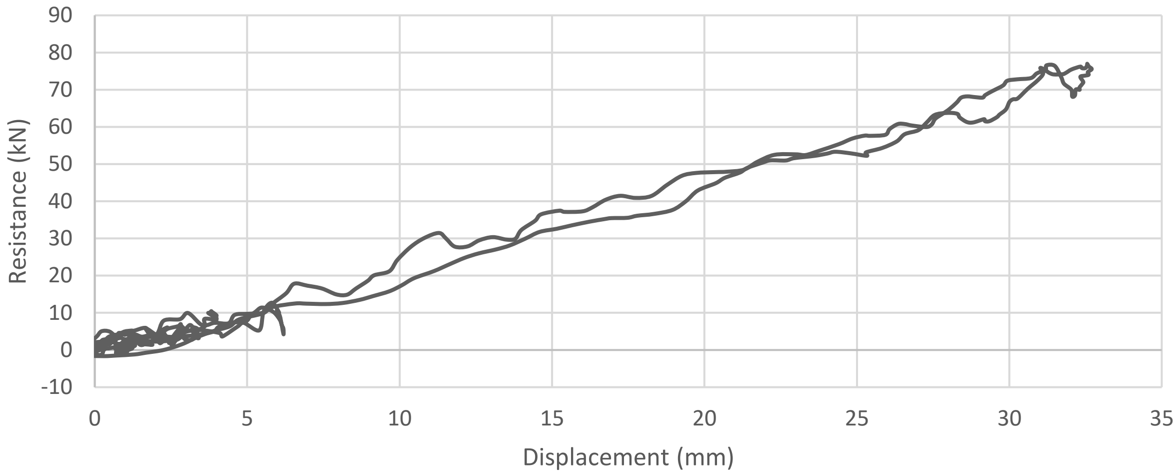

Figure A.11: Experimental resistance curve for GL2.1

Figure A.12: a) Specimen before test GL2.1 b) Undamaged right side, after test c) Cracking and minor laminate failure d) Detail image of finger-joint failure

A.2.2 Test GL2.2

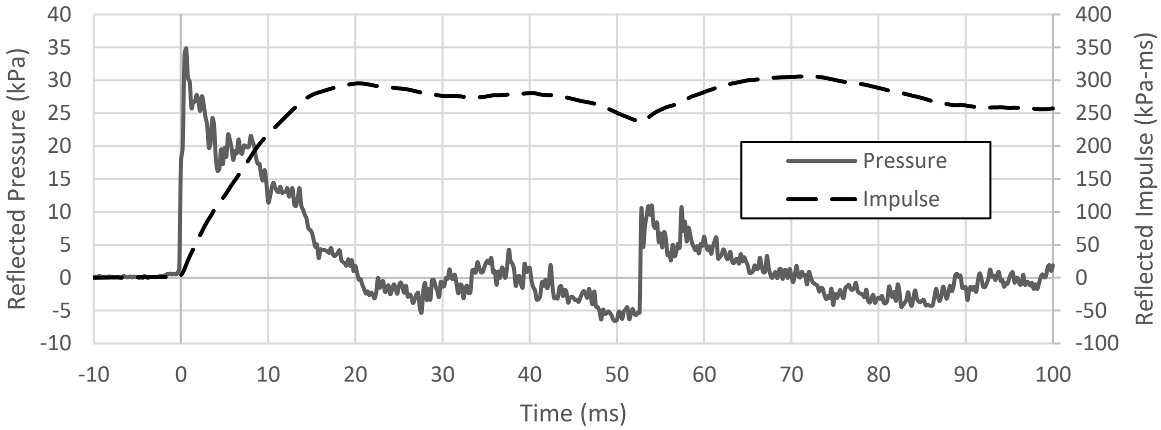

Figure A.13: Pressure-time history and cumulative impulse for GL2.2

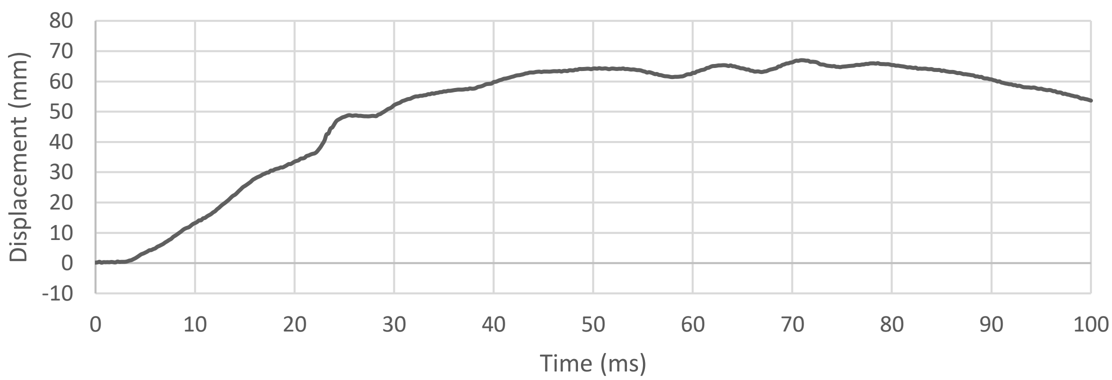

Figure A.14: Displacement-time history for GL2.2

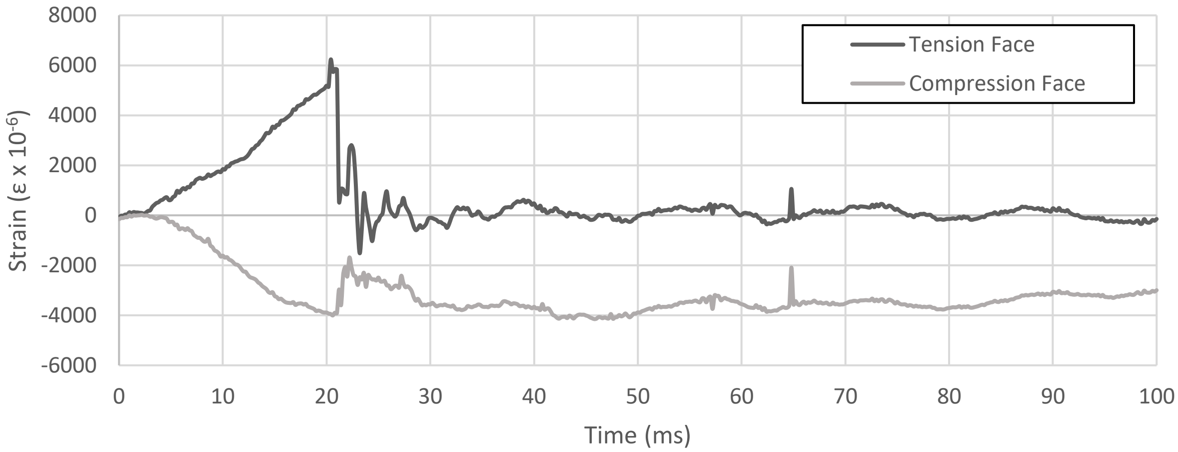

Figure A.15: Mid-span strain measurements for GL2.2

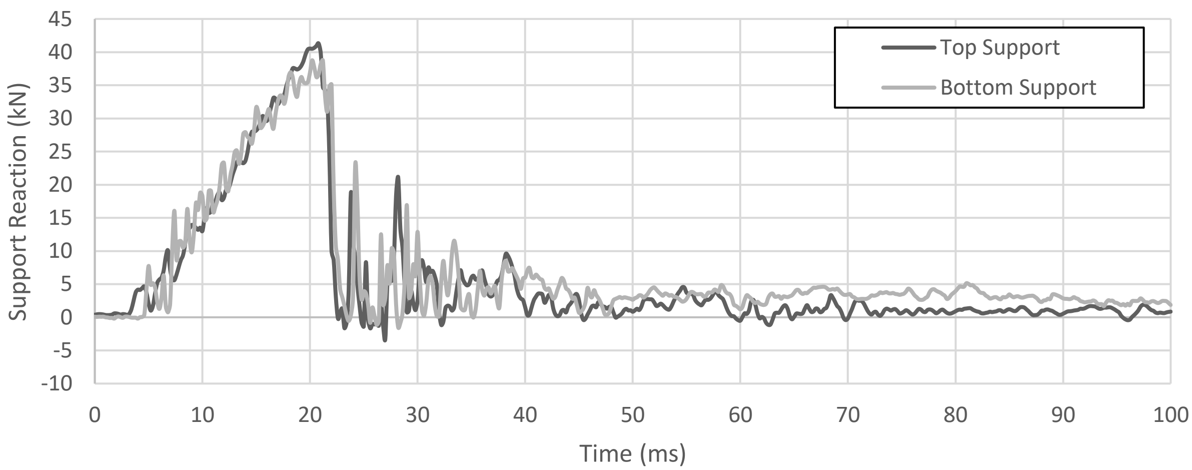

Figure A.16: Reaction-time histories for GL2.2

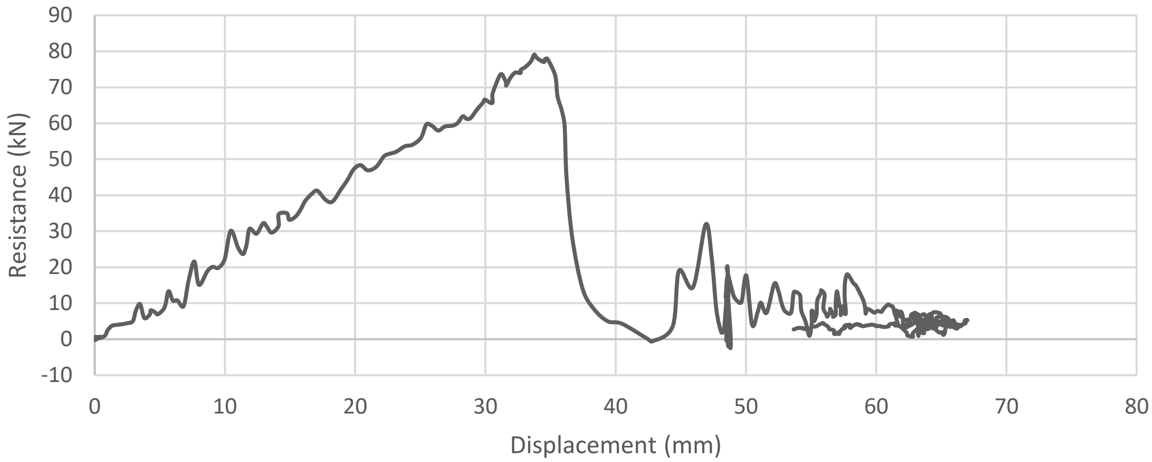

Figure A.17: Experimental resistance curve for GL2.2

a) b) c) d)

Figure A.18: Final state for shot GL2.2: a) Left side b) Tension face c) Right side d) Reversing crack details

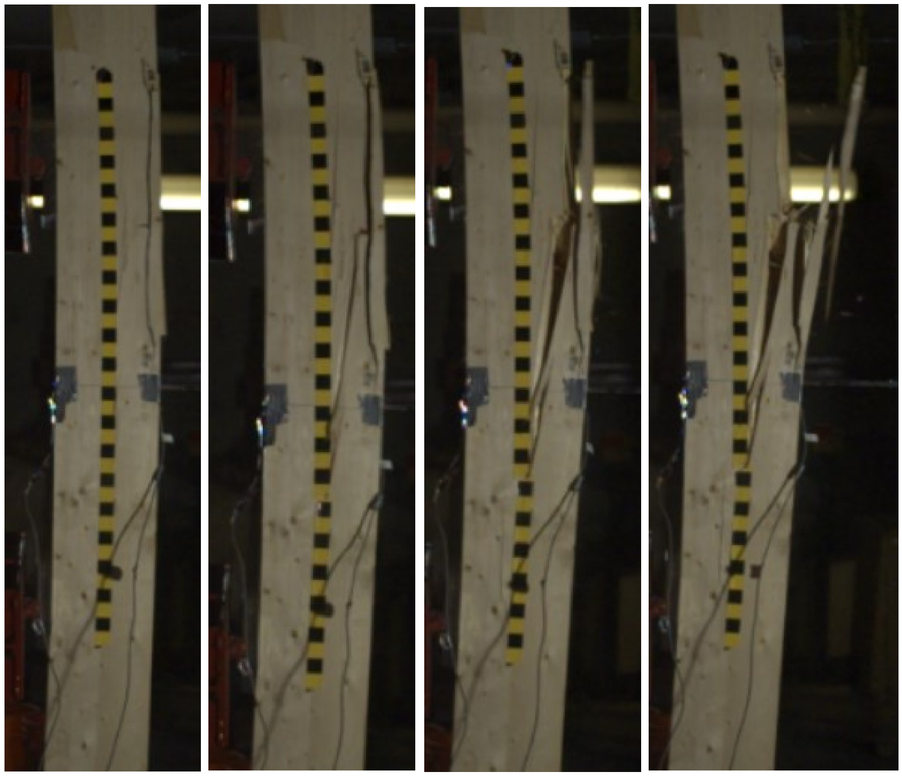

a) b) c) d)

Figure A.19: Progression of failure during test GL2.2: a) 20.5 ms b) 21.5 ms c) 23.5 ms d) 28.5 ms

A.3 Specimen GL3

Specimen GL3 weighed 20.92 kg and had a moisture content of approximately 14%. The member remained elastic during the first shot, and exhibited superficial damage along one edge during the second shot. The third shot resulted in flexural failure, with cracks developing along the length of the member and through the majority of the mid-span cross-section. The strain gauge on the tension face did not function properly during the tests, and the strain gauge on the compression face failed after the second test

A.3.1 Test GL3.1

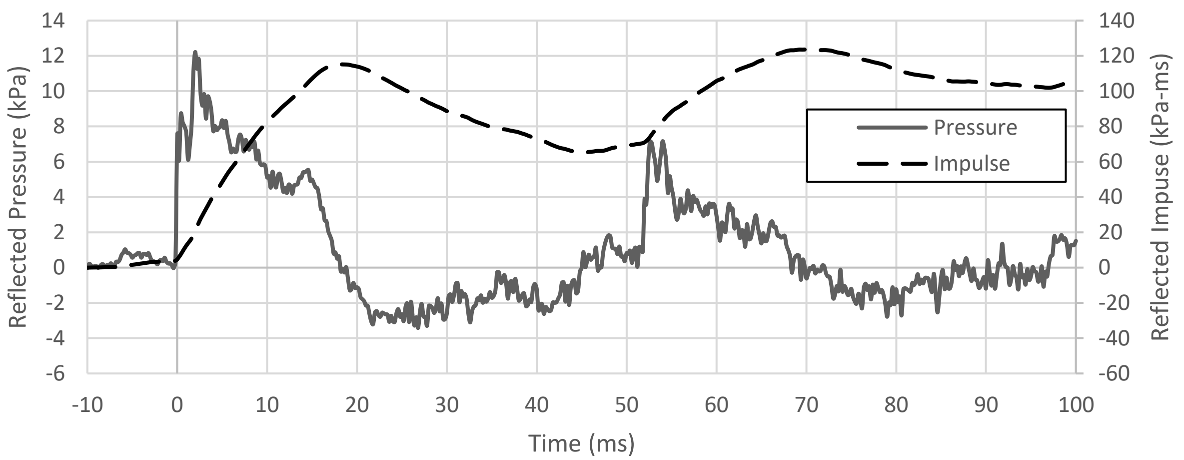

Figure A.20: Pressure-time history and cumulative impulse for GL3.1

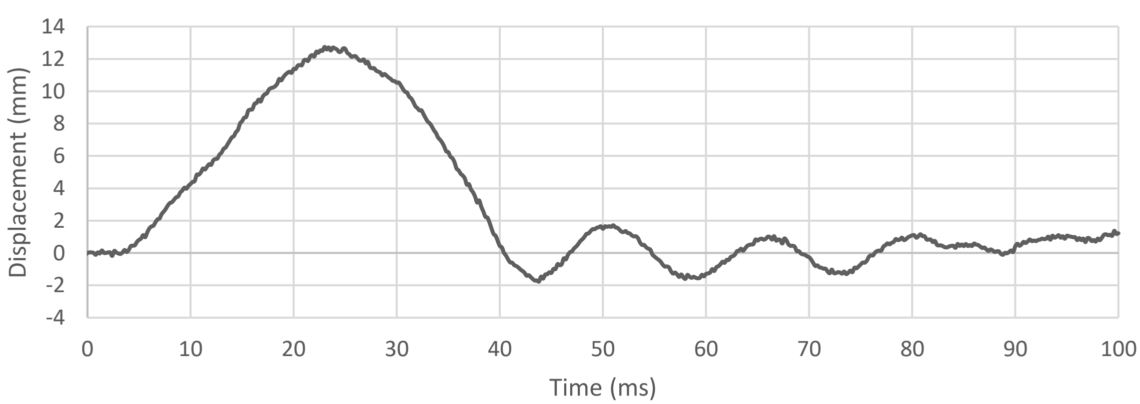

Figure A.21: Displacement-time history for GL3.1

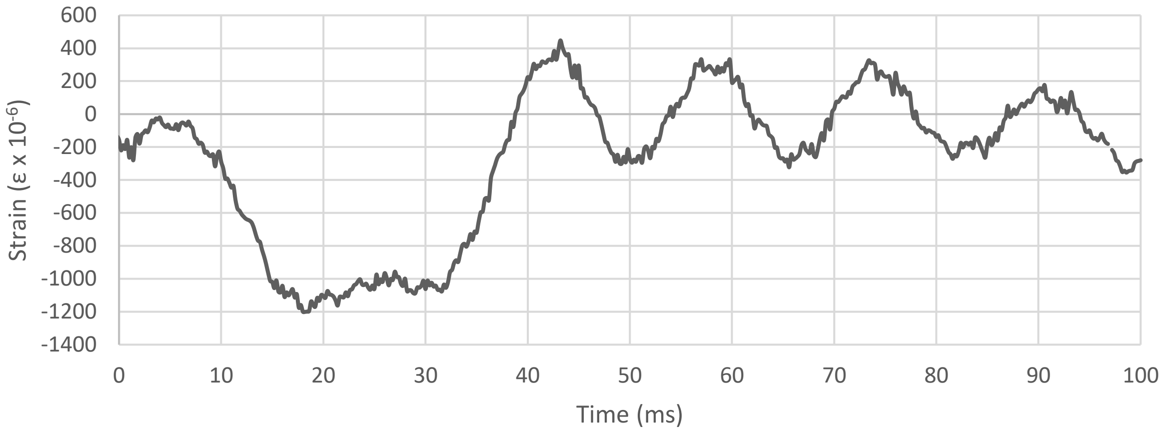

Figure A.22: Mid-span compressive strain history for GL3.1

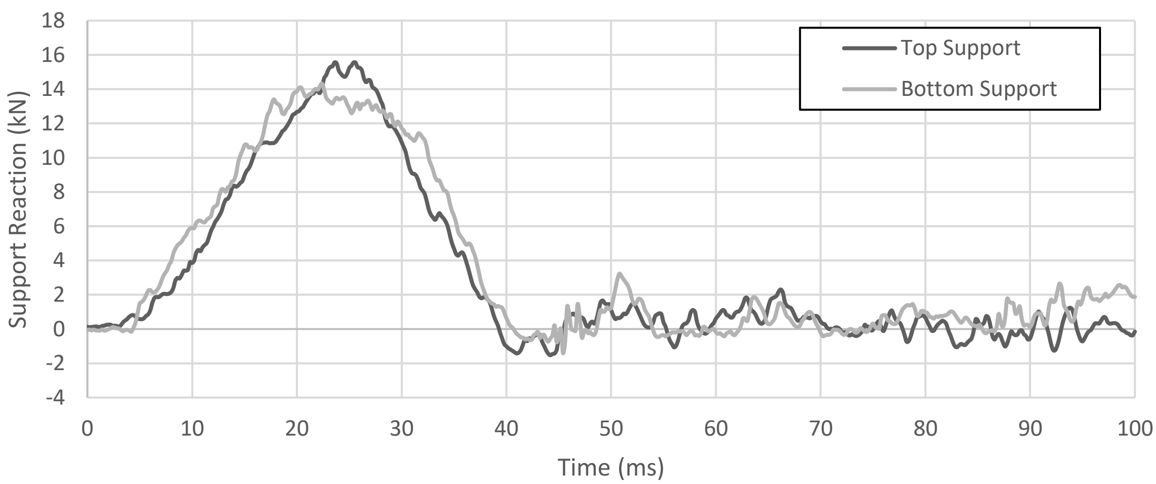

Figure A.23: Reaction-time histories for GL3.1

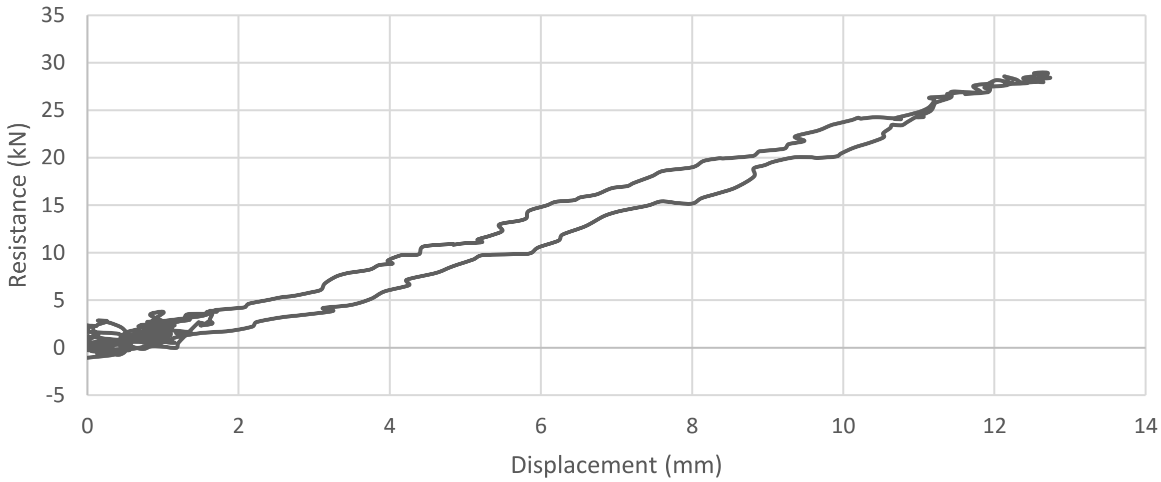

Figure A.24: Experimental resistance curve for GL3.1

a) b)

Figure A.25: Undamaged specimen after test GL3.1: a) Left side b) Right side

A.3.2 Test GL3.2

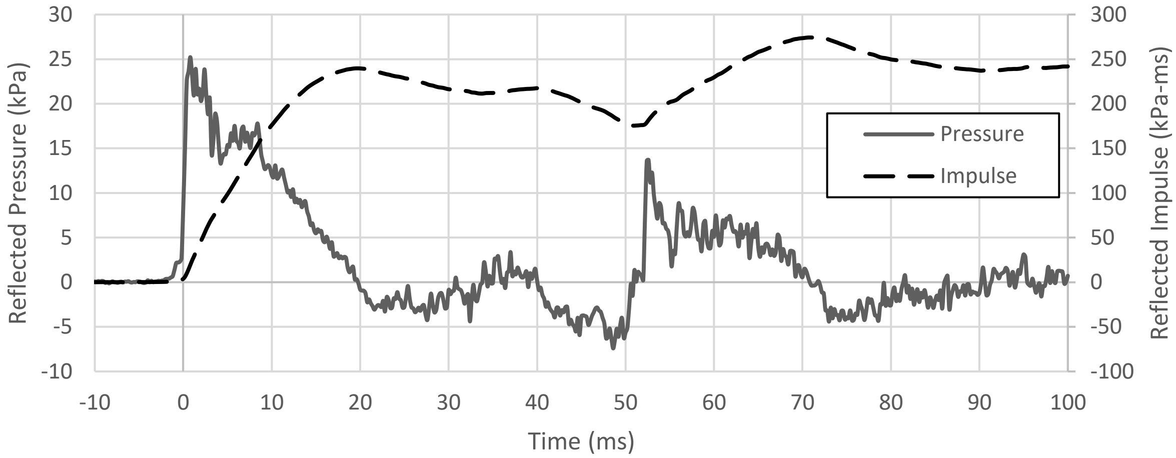

Figure A.26: Pressure-time history and cumulative impulse for GL3.2

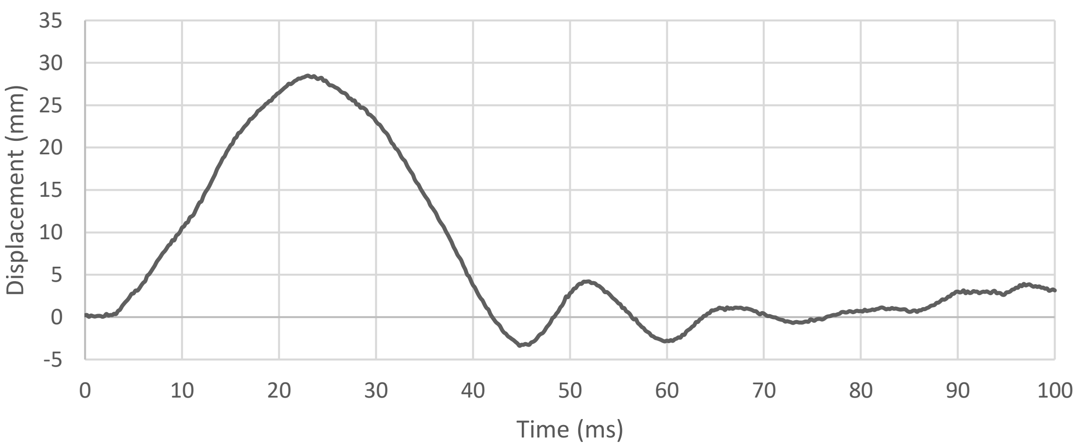

Figure A.27: Displacement-time history for GL3.2

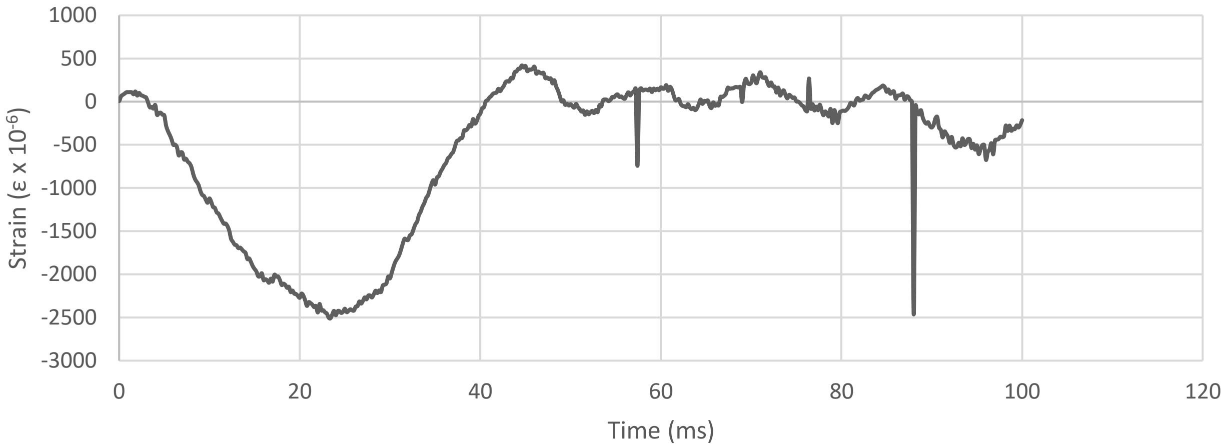

Figure A.28: Mid-span compressive strain history for GL3.2

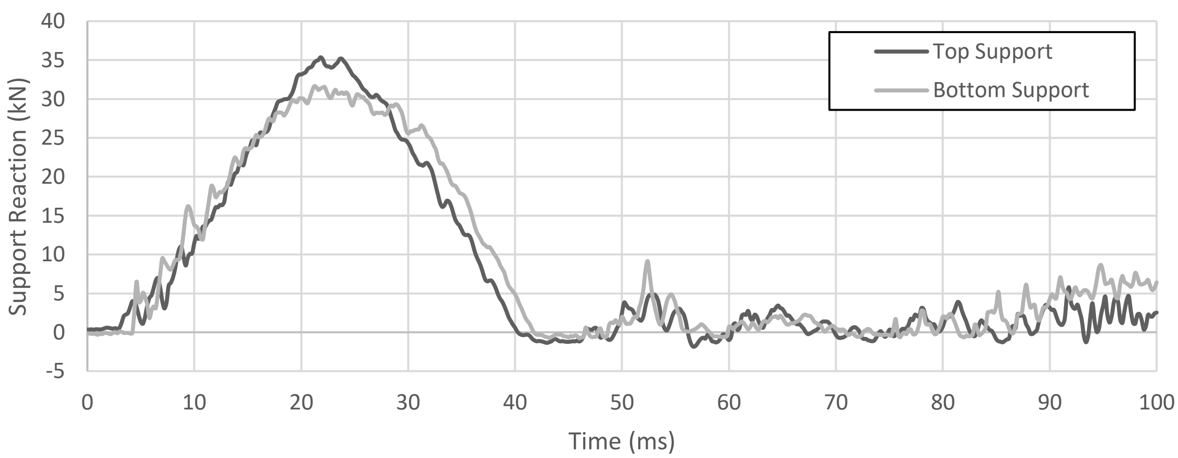

Figure A.29: Reaction-time histories for GL3.2

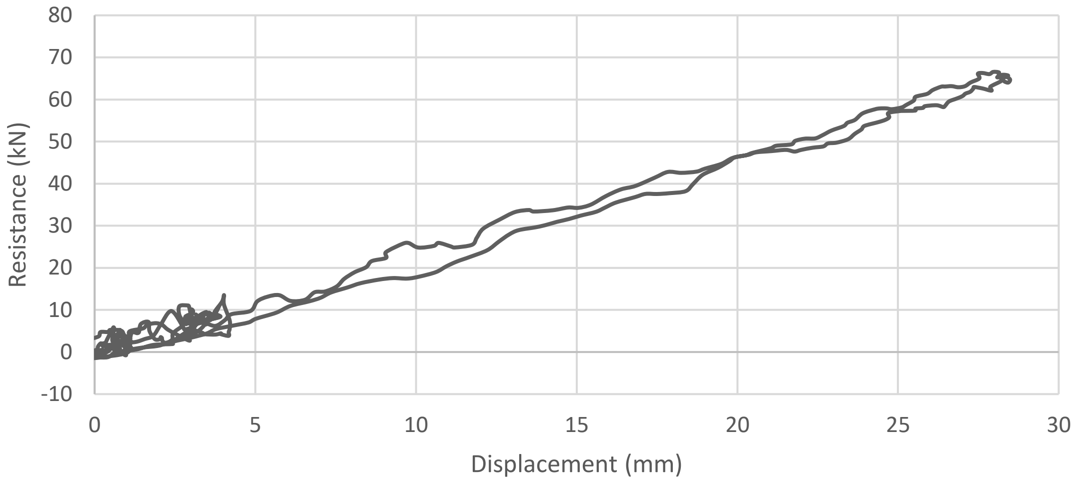

Figure A.30: Experimental resistance curve for GL3.2

a) b)

Figure A.31: a) Superficial damage after shot GL3.2 b) Superficial crack detail

A.3.3 Test GL3.3

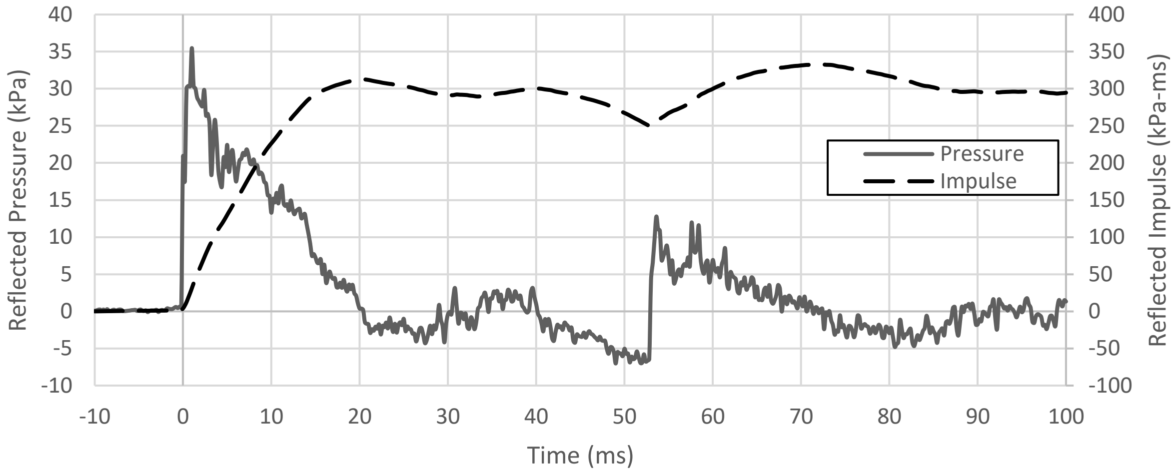

Figure A.32: Pressure-time history and cumulative impulse for GL3.3

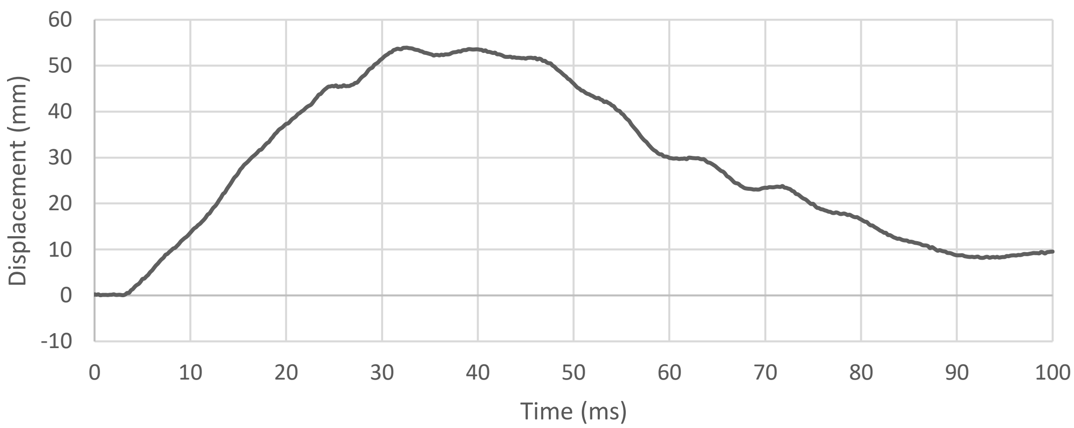

Figure A.33: Displacement-time history for GL3.3

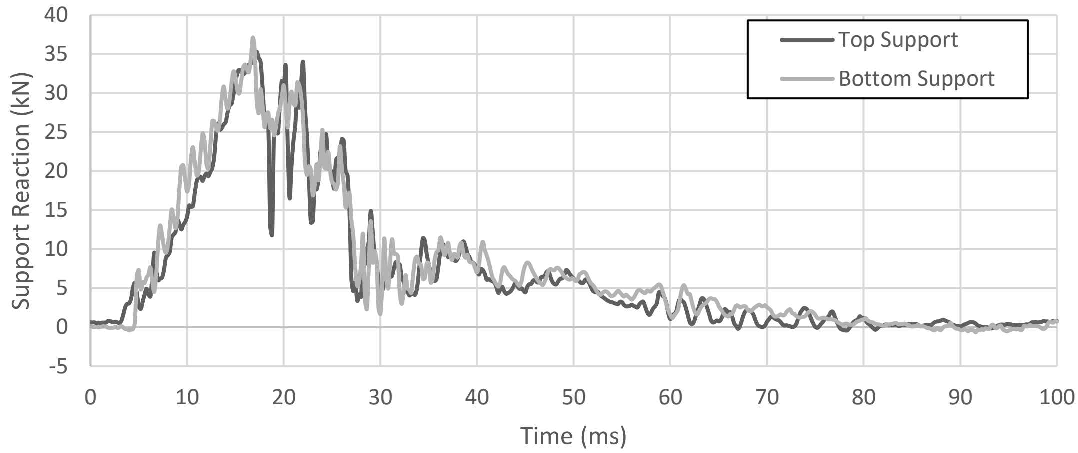

Figure A.34: Reaction-time histories for GL3.3

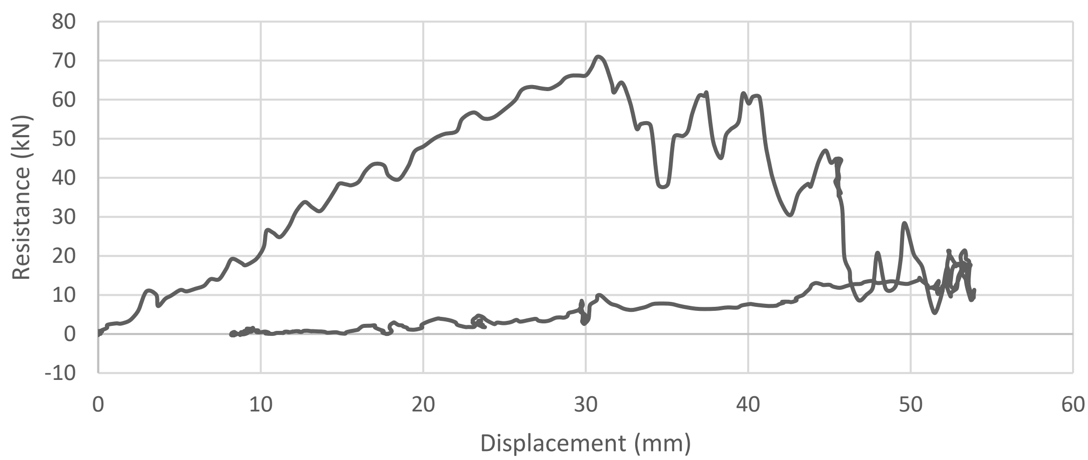

Figure A.35: Experimental Resistance curve for GL3.3

a) b) c)

Figure A.36: Failed specimen after test GL3.3: a) Left side b) Tension face c) Right side

a) b) c)

Figure A.37: Progression of failure during test GL3.3: a) 15.5 ms b) 21 ms c) 28 ms

A.4 Specimen CLT1

Specimen CLT1 weighed 101.68 kg and had a moisture content of approximately 14%. The specimen failed during its first test, with damage indicative of flexural behaviour generally confined to the mid-span section.

A.4.1 Test CLT1.1

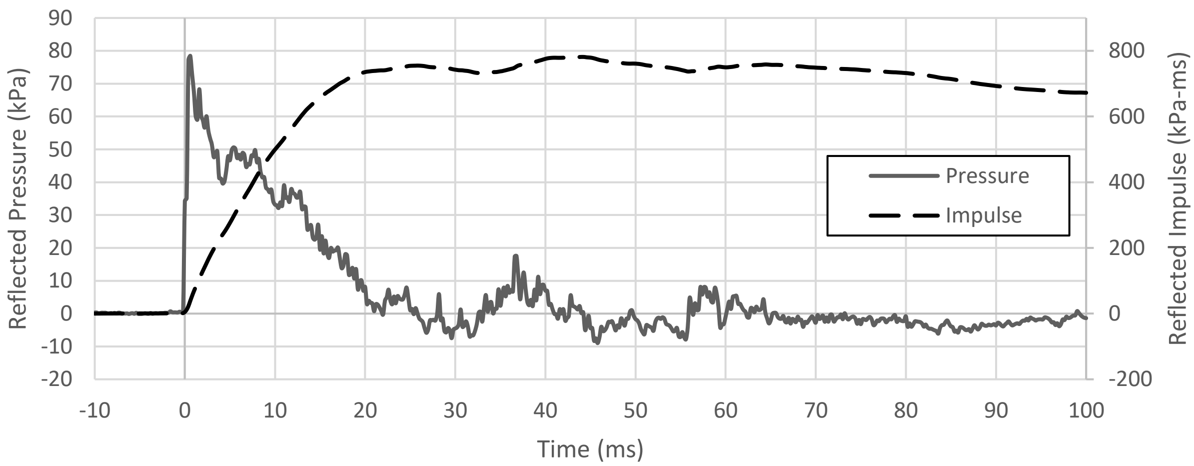

Figure A.38: Pressure-time history and cumulative impulse for CLT1.1

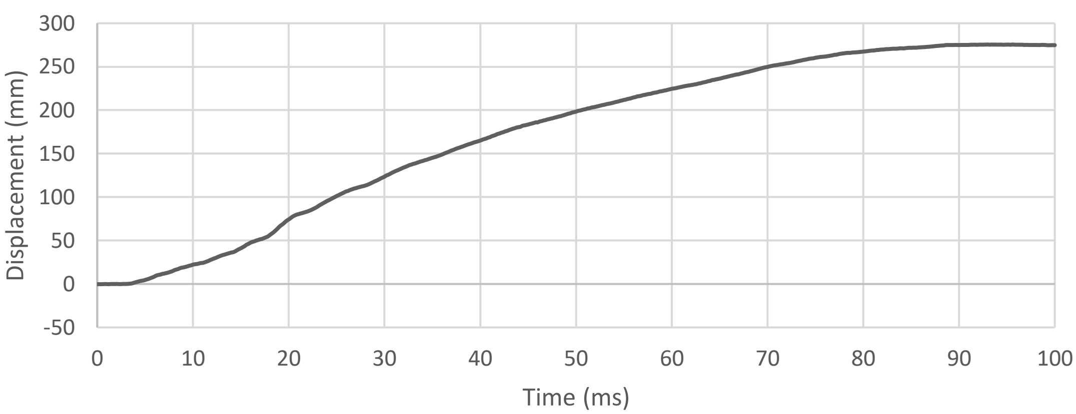

Figure A.39: Displacement-time history for CLT1.1

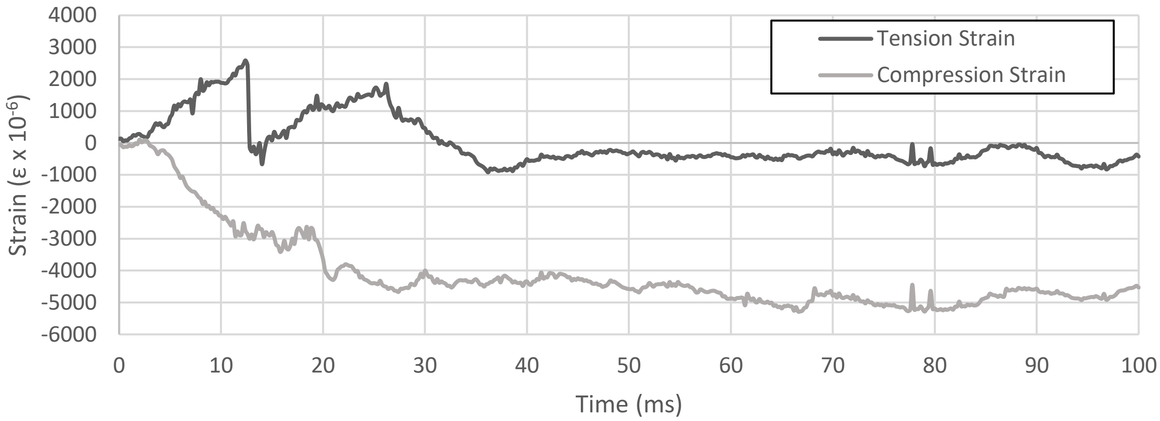

Figure A.40: Mid-span strain measurements got CLT1.1

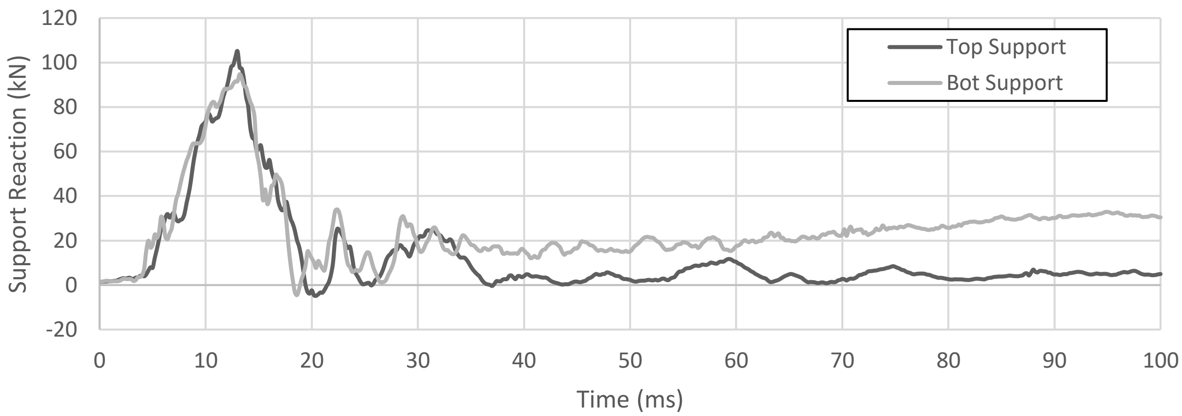

Figure A.41: Reaction-time histories for CLT1.1

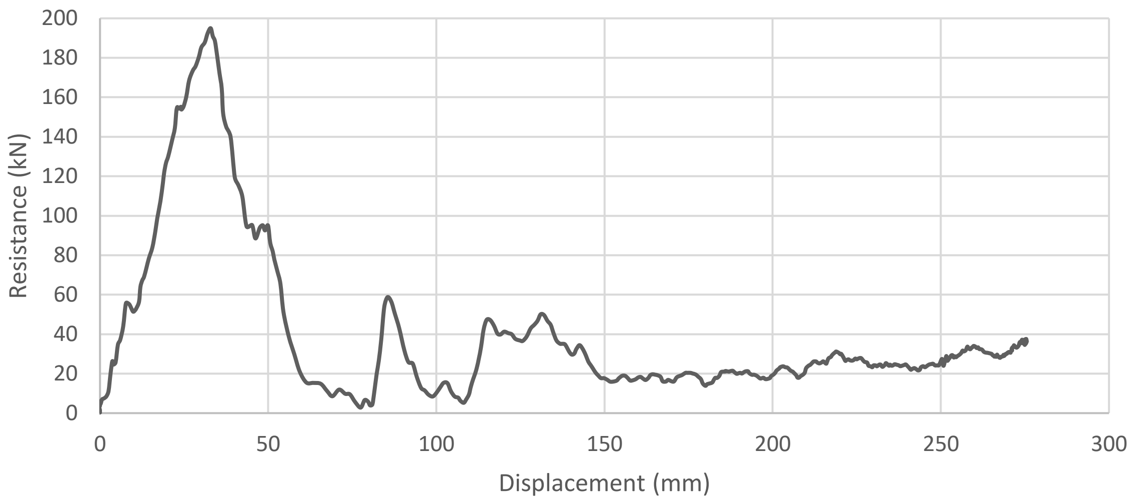

Figure A.42: Experimental resistance curve for CLT1.1

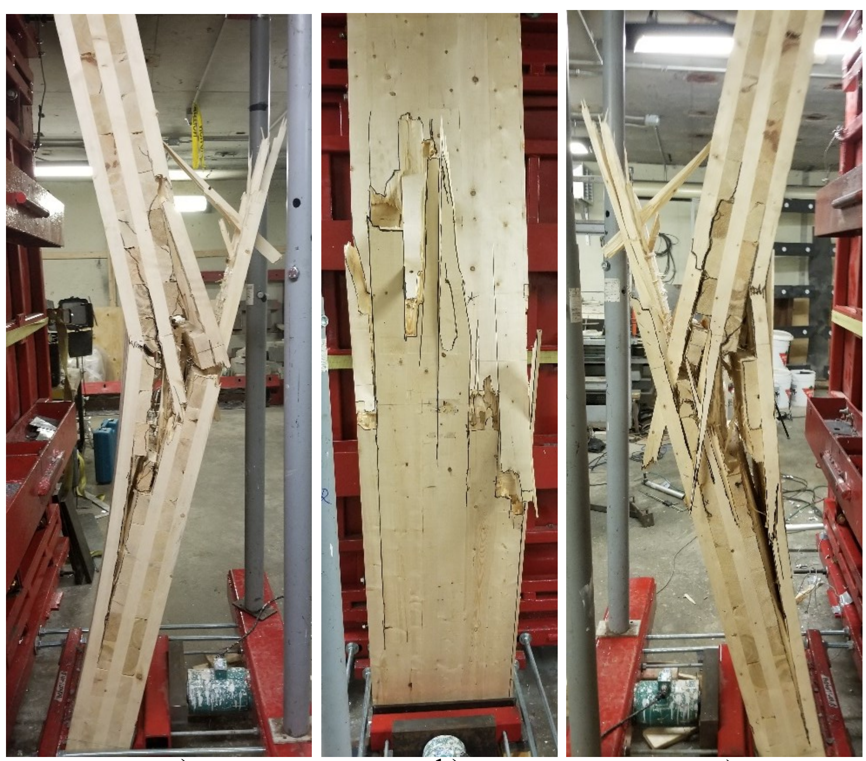

a) b) c)

Figure A.43: Overview of final state for shot CLT1.1: a) Left side b) Tension face c) Right side

Figure A.44: CLT1.1 Finger joint failures: a) Left tension face b) Lower tension face c) Left side, fifth ply d) Right side, first ply e) Inner lamination f) Right side, fifth ply

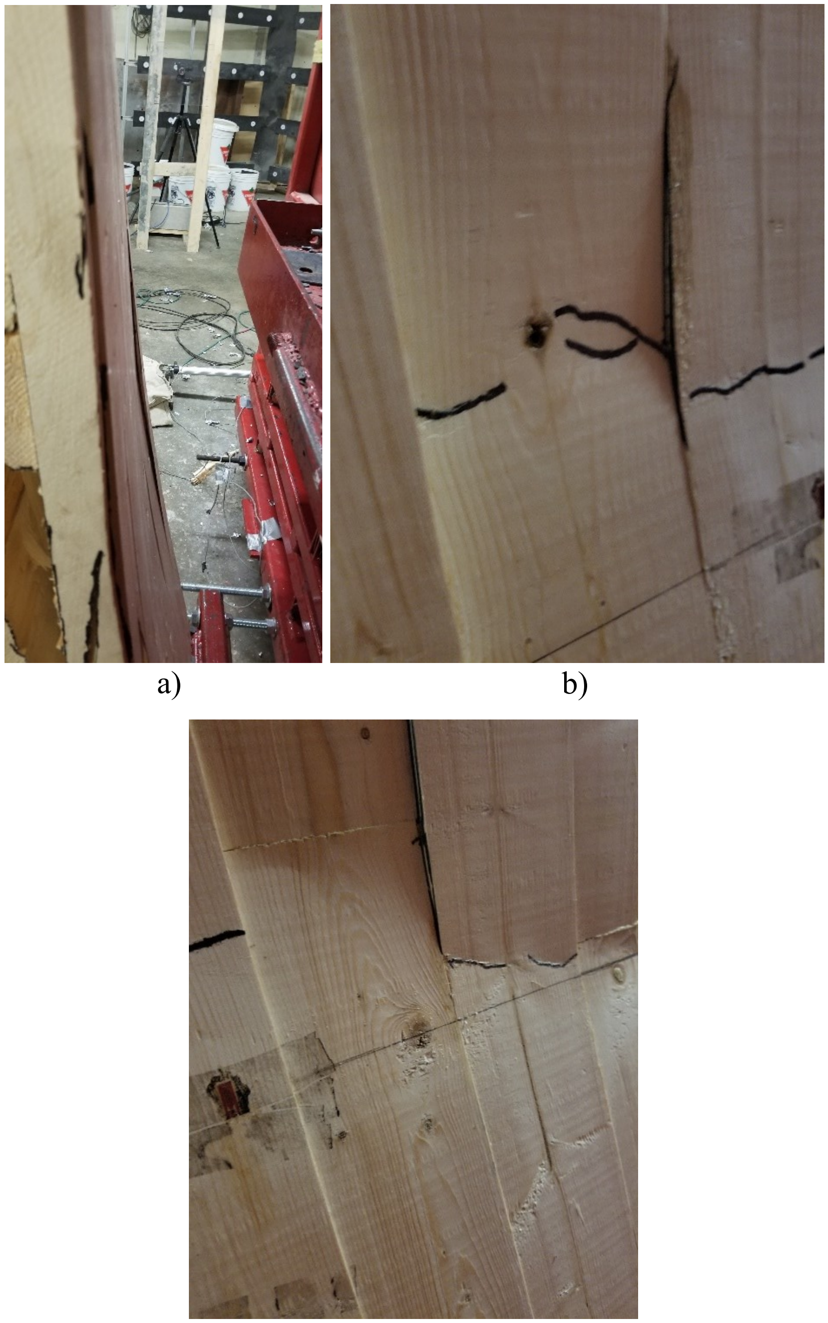

a) b)

c)

Figure A.45: Compressive damage development in first ply from shot CLT1.1: a) Curvature near lower loading beam b) Wrinkling and offset of individual laminates c) Plastic hinge formation

a) b) c) d)

Figure A.46: Progression of failure during shot CLT1.1, overview: a) 13 ms b) 19.5 ms c) 25 ms d) 37.5 ms

a) b) c) d)

Figure A.47: Progression of failure during shot CLT1.1, side view: a) 13 ms b) 18.5 ms c) 26.5 ms d) 39.5 ms

A.5 Specimen CLT2

Specimen CLT2 weighed 102.04 kg and had a moisture content of approximately 16%. Both the first and second tests resulted in damage to both the outermost and transverse plies. The third test caused member failure, and observed behaviour consisted of separation in the transverse plies followed by flexural failure of the tension face. The strain gauge for the compression face failed after the first test, and the strain gauge for the tension face reported invalid results for the third test.

A.5.1 Test CLT2.1

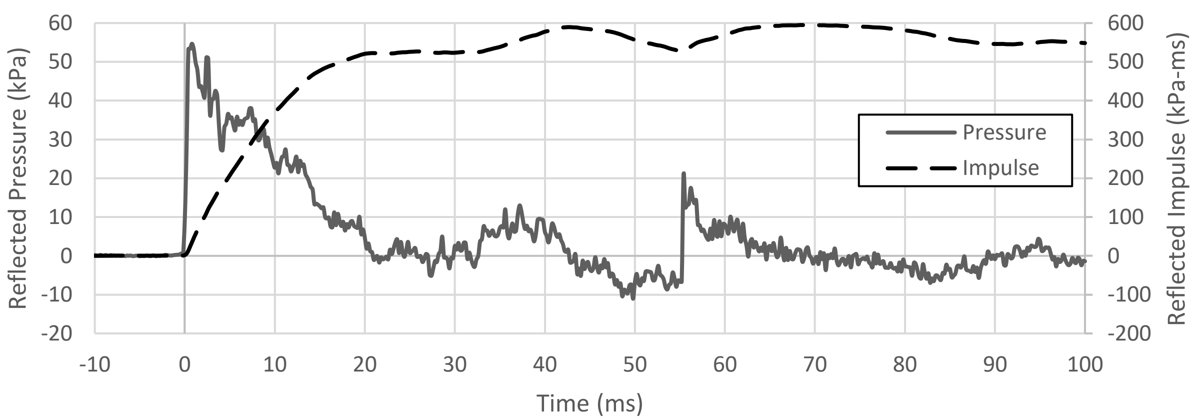

Figure A.48: Pressure-time history and cumulative impulse for CLT2.1

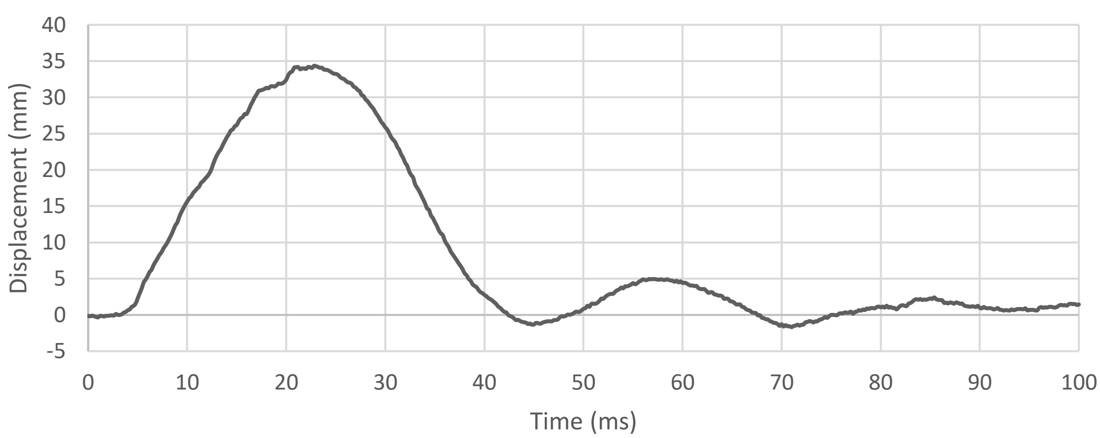

Figure A.49: Displacement-time history for CLT2.1

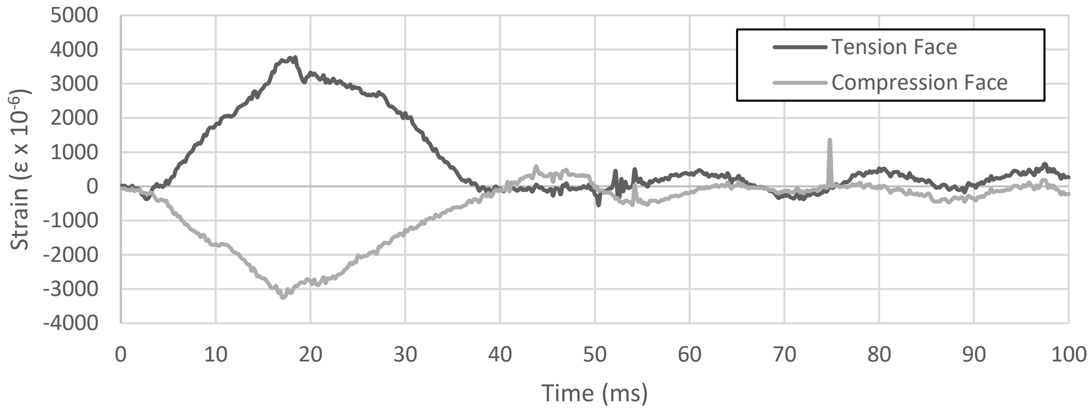

Figure A.50: Mid-span strain measurements for CLT2.1

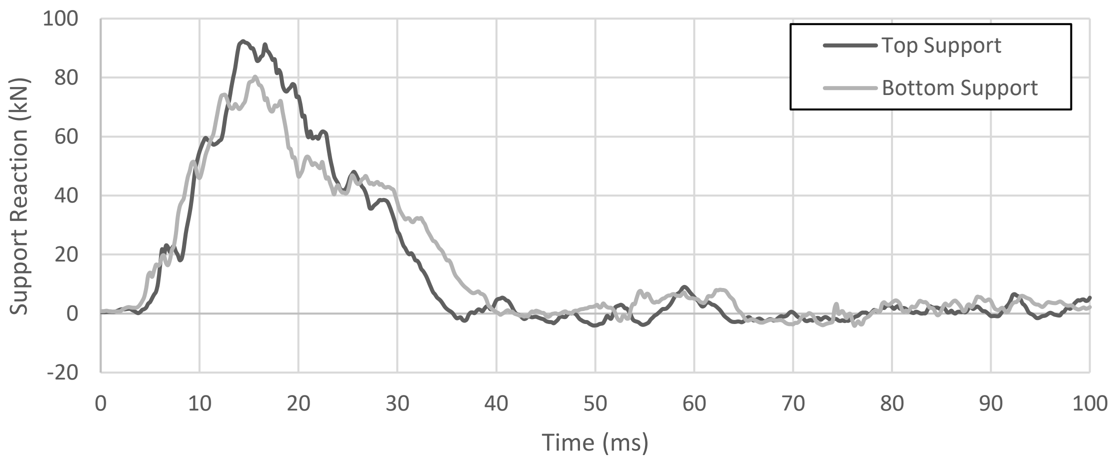

Figure A.51: Reaction-time histories for CLT2.1

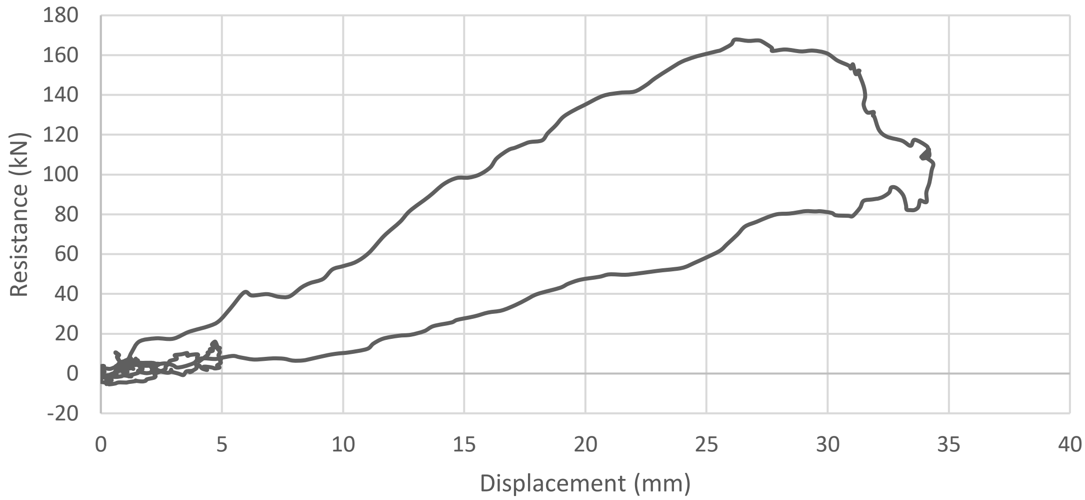

Figure A.52: Experimental resistance curve for CLT2.1

Figure A.53: Pre-existing transverse gaps in specimen CLT2 a) Right side, top b) Right side, bottom c) Left side, top

a) b) c)

Figure A.54: Specimen after shot CLT2.1: a) Left side b) Tension face c) Right side

a) b) c)

Figure A.55: Transverse cracking details for shot CLT2.1: a) Left side, bottom b) Right side, bottom c) Right side, top

Figure A.56: Formation of rolling shear cracks during test CLT2.1, 24 ms

A.5.2 Test CLT2.2

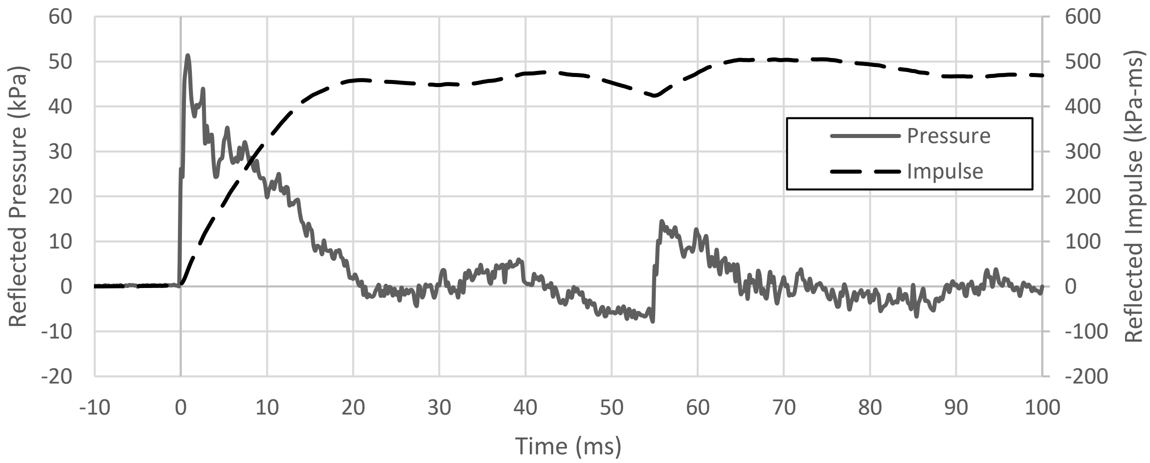

Figure A.57: Pressure-time history and cumulative impulse for CLT2.2

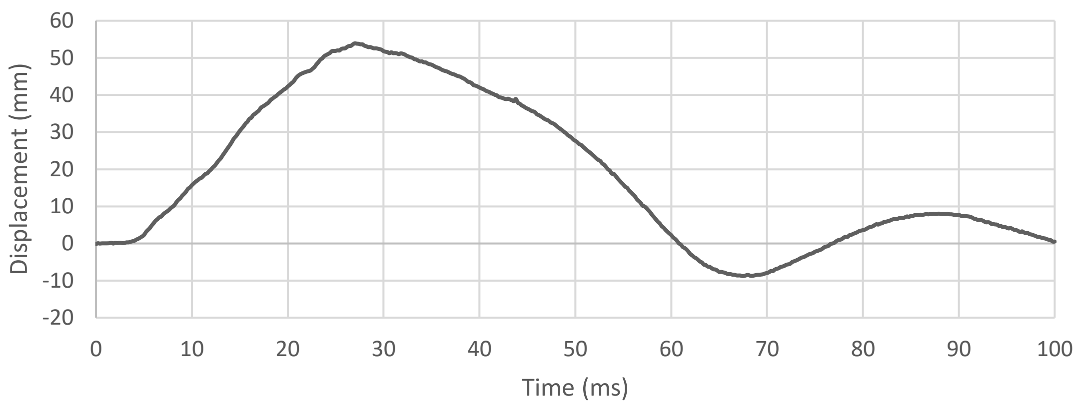

Figure A.58: Displacement-time history for CLT2.2

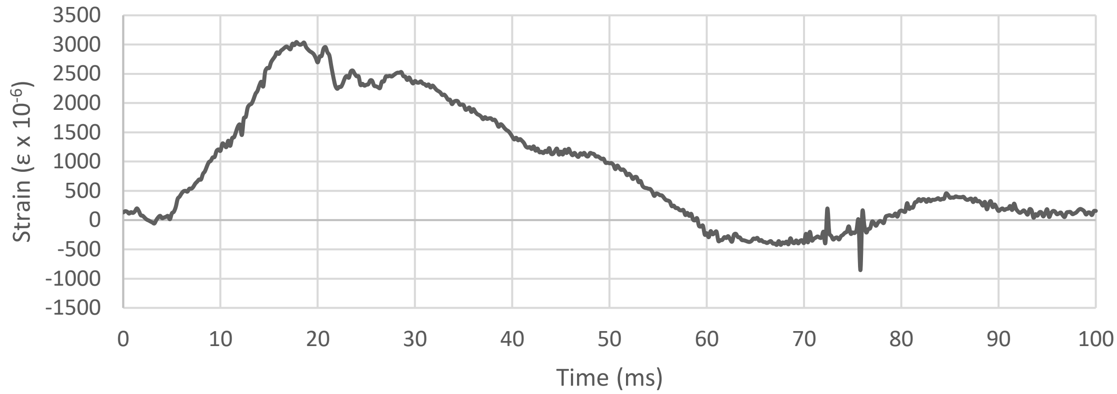

Figure A.59: Mid-span tensile strain history for CLT2.2

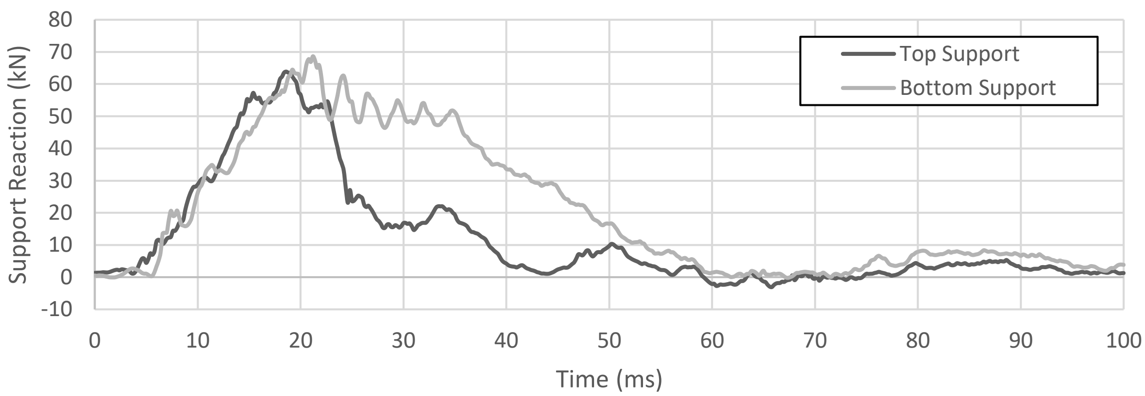

Figure A.60: Reaction-time histories for CLT2.2

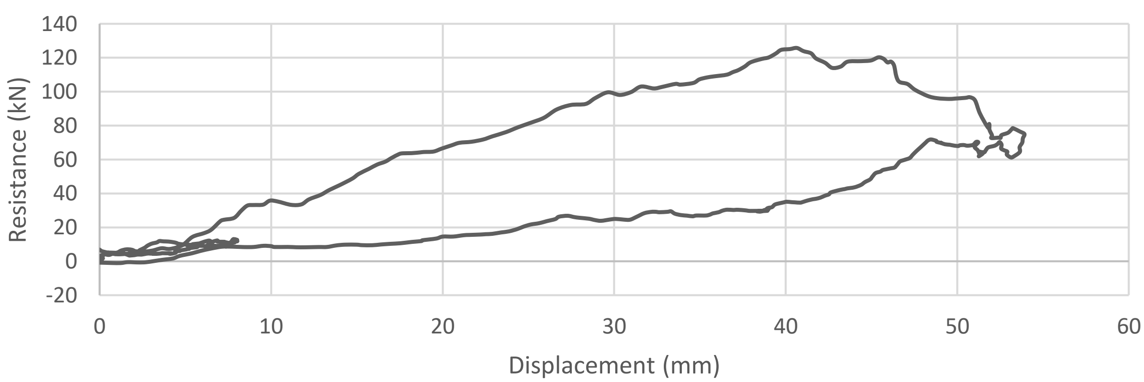

Figure A.61: Experimental resistance curve for CLT2.2

a)

b)

c)

d)

Figure A.62: State of specimen damage after shot CLT2.2: a) Left side b) Tension face c) Right side, support d) Right side, lower half

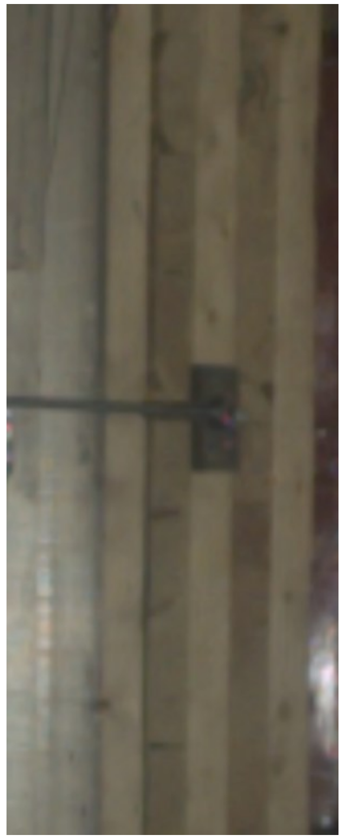

Figure A.63: Partial separation of fifth ply on the right side during test CLT2.2, 16 ms

A.5.3 Test CLT2.3

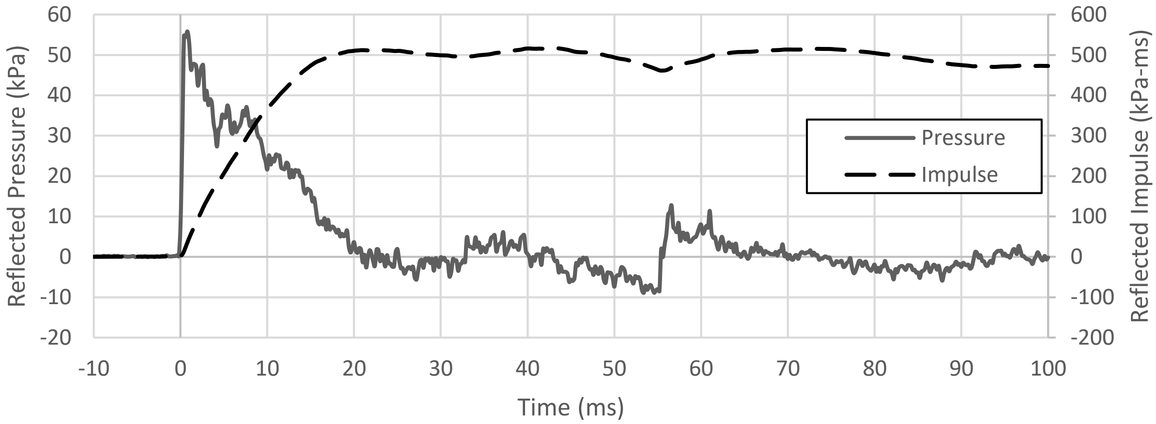

Figure A.64: Pressure-time history and cumulative impulse for CLT2.3

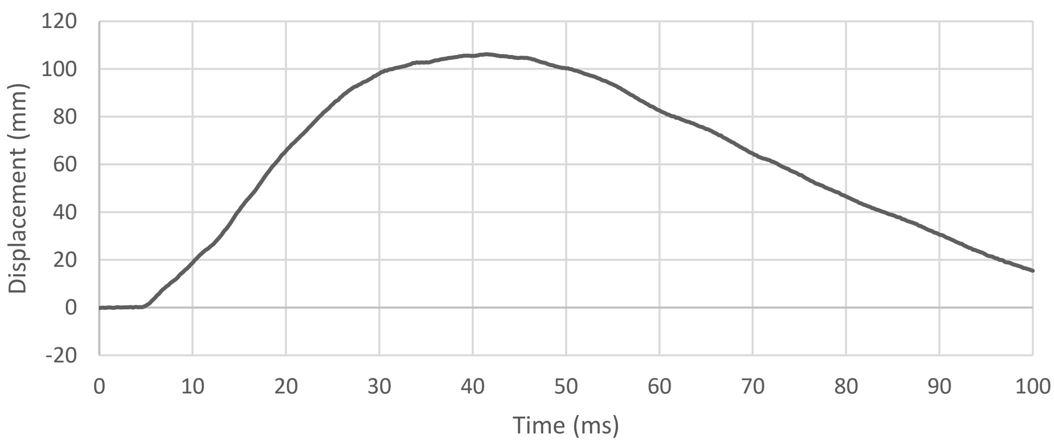

Figure A.65: Displacement-time history for CLT2.3

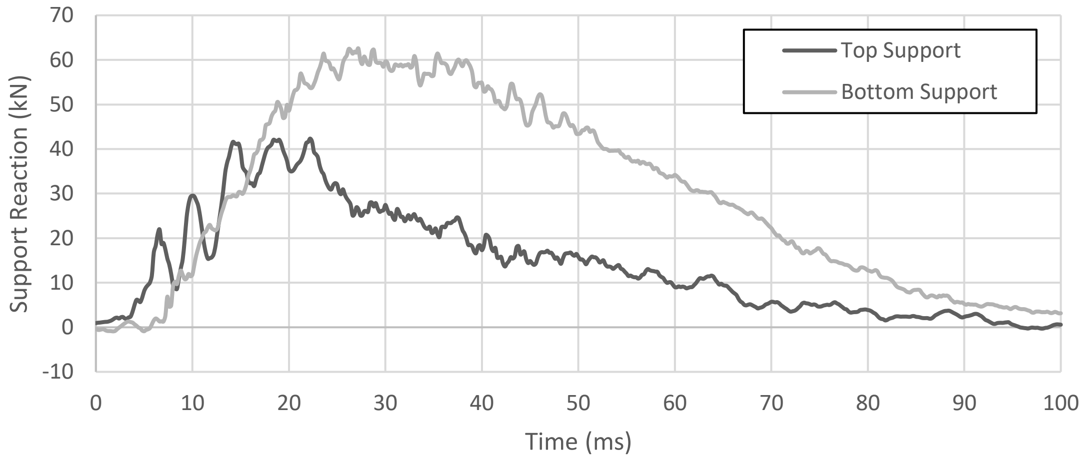

Figure A.66: Reaction-time histories for CLT2.3

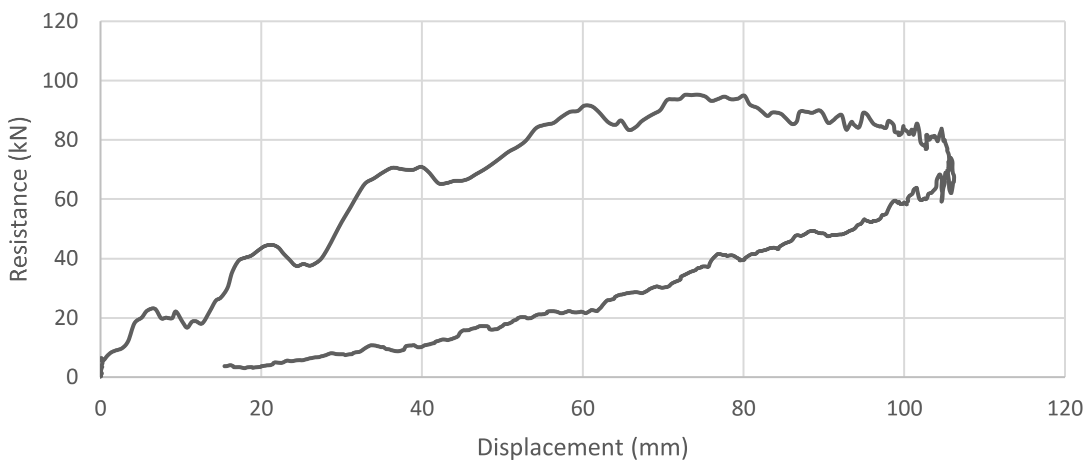

Figure A.67: Experimental resistance curve for CLT2.3

a) b) c)

Figure A.68: Final state of specimen after shot CLT2.3: a) Left side b) Tension face c) Right side

a) b) c)

Figure A.69: Details of specimen failure: a) Finger joint failure on tension face b) Propagation of cracks past supports c) Right side transverse cracking

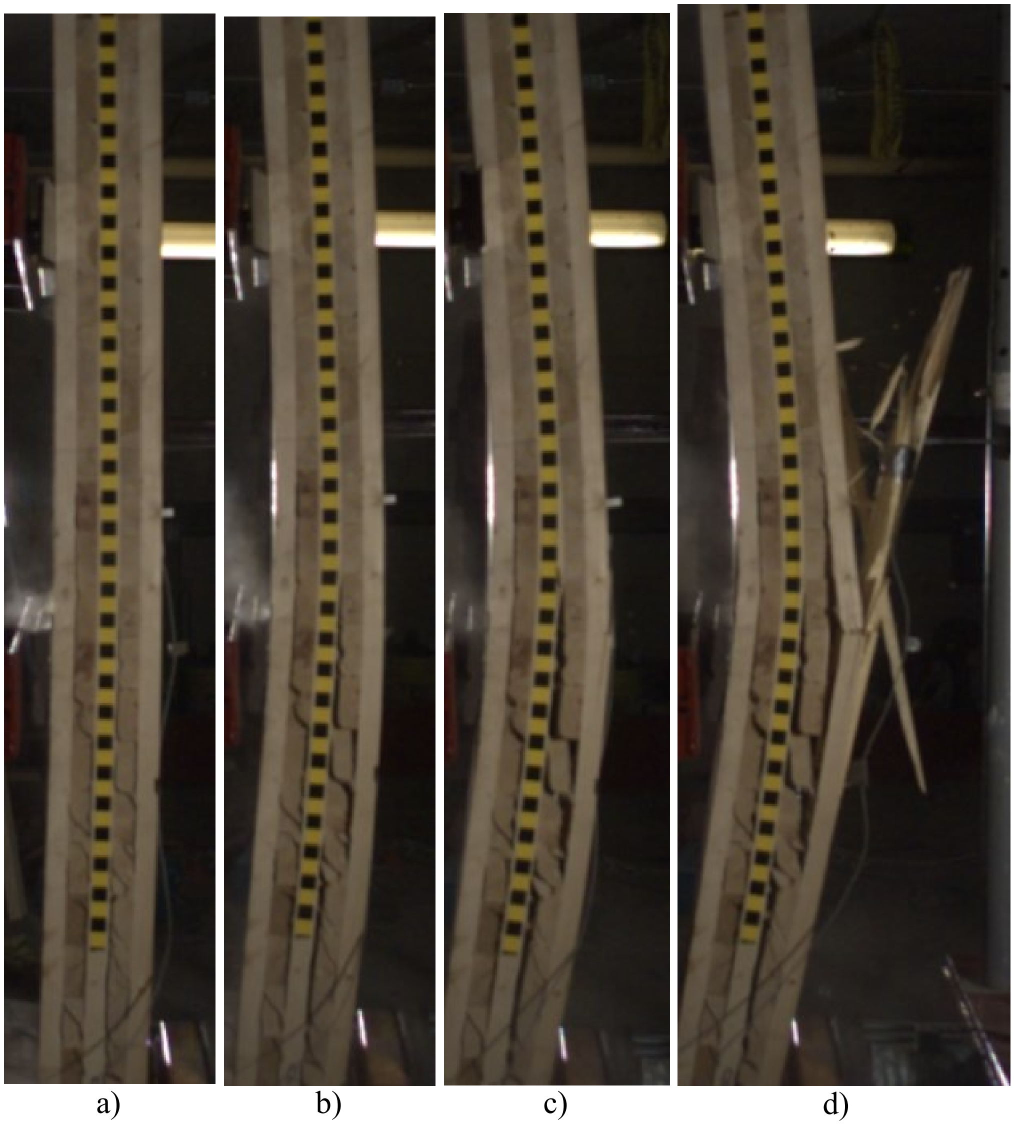

Figure A.70: Progression of failure during test CLT2.3: a) 7.5 ms b) 16.5 ms c) 24.5 ms d) 50 ms

A.6 Specimen CLT3

Specimen CLT3 weighed 101.48 kg and had a moisture content of approximately 14%. The specimen behaved elastically during the first test, with no observable damage after the test. The panel failed in rolling shear during the second test, with superficial damage to the longitudinal plies and significant cracking and separation in the transverse plies.

A.6.1 Test CLT3.1

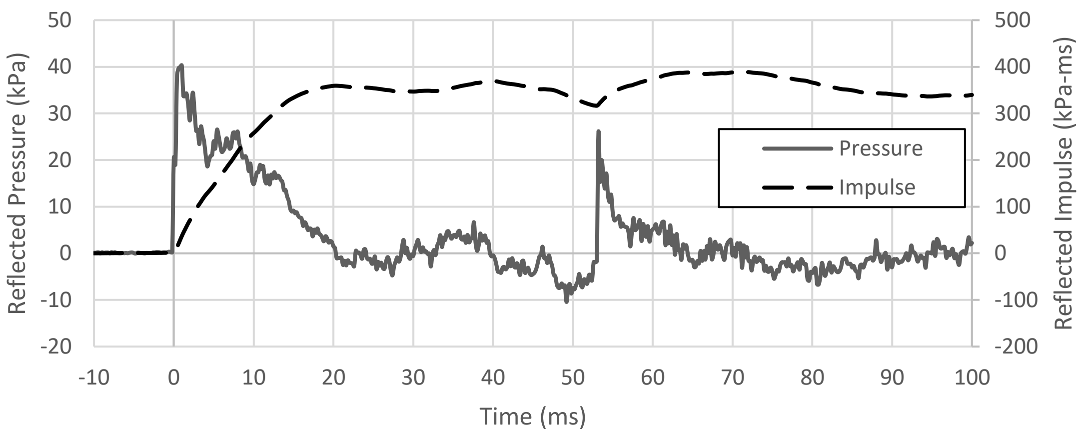

Figure A.71: Pressure-time history and cumulative impulse for CLT3.1

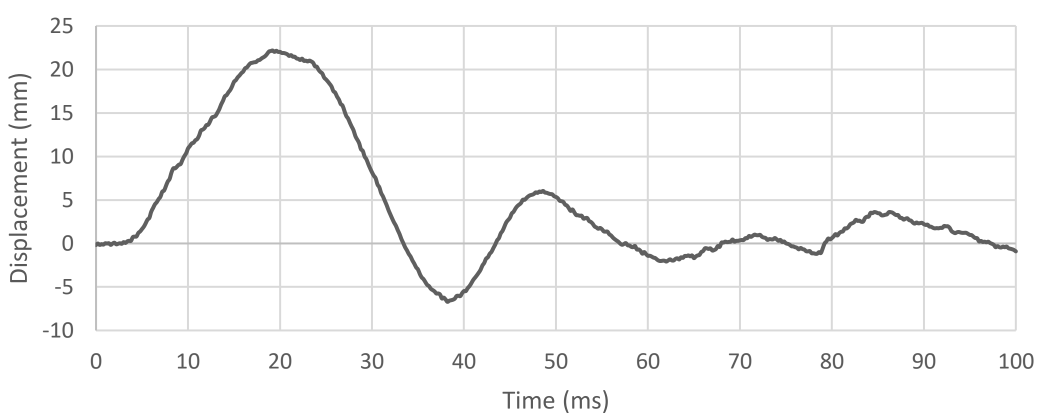

Figure A.72: Displacement-time history for CLT3.1

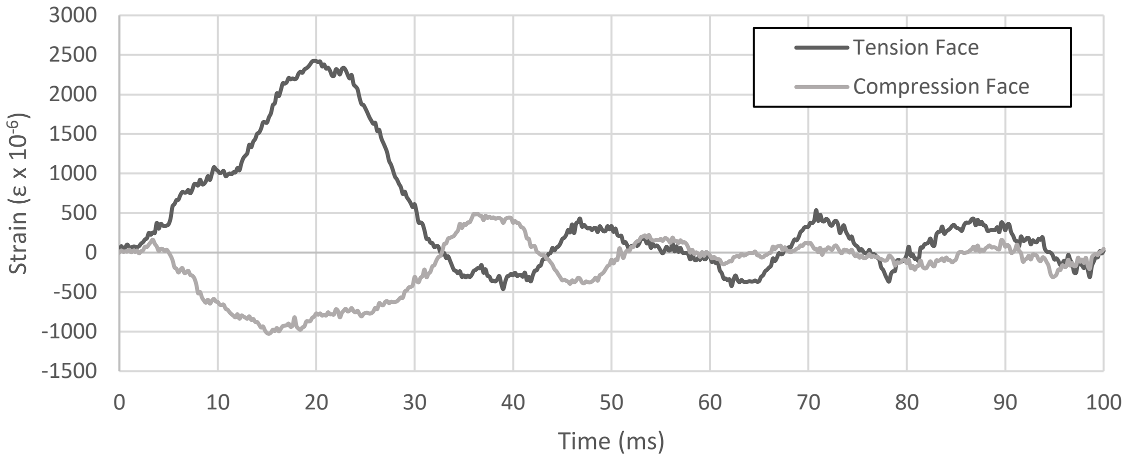

Figure A.73: Mid-span strain measurements for CLT3.1

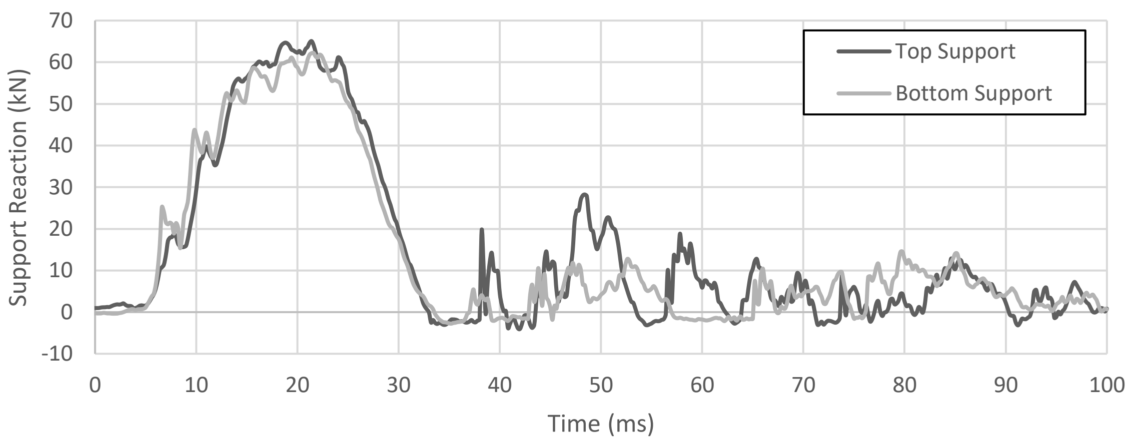

Figure A.74: Reaction-time histories for CLT3.1

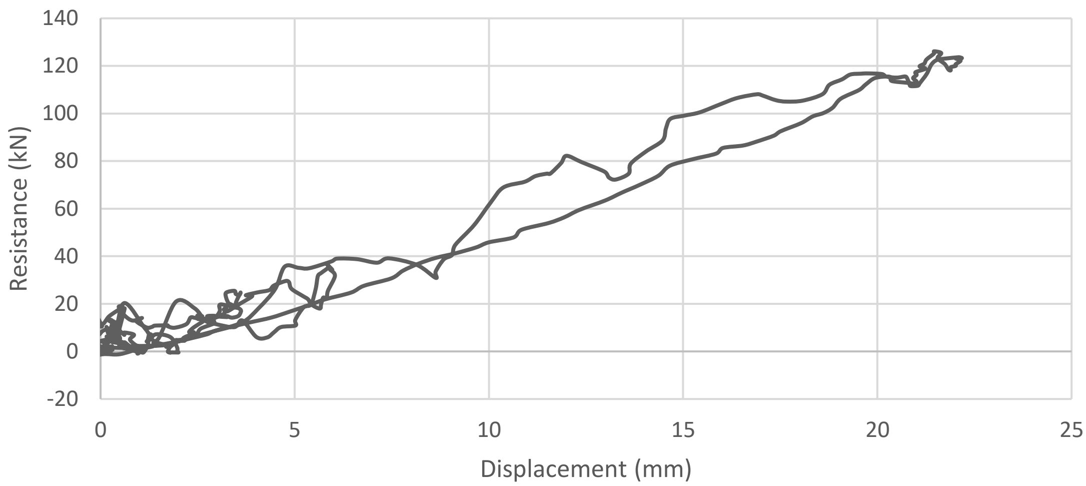

Figure A.75: Experimental resistance curve for CLT3.1

a) b)

Figure A.76: Undamaged specimen after test CLT3.1: a) Left side b) Right side and tension face

A.6.2 Test CLT3.2

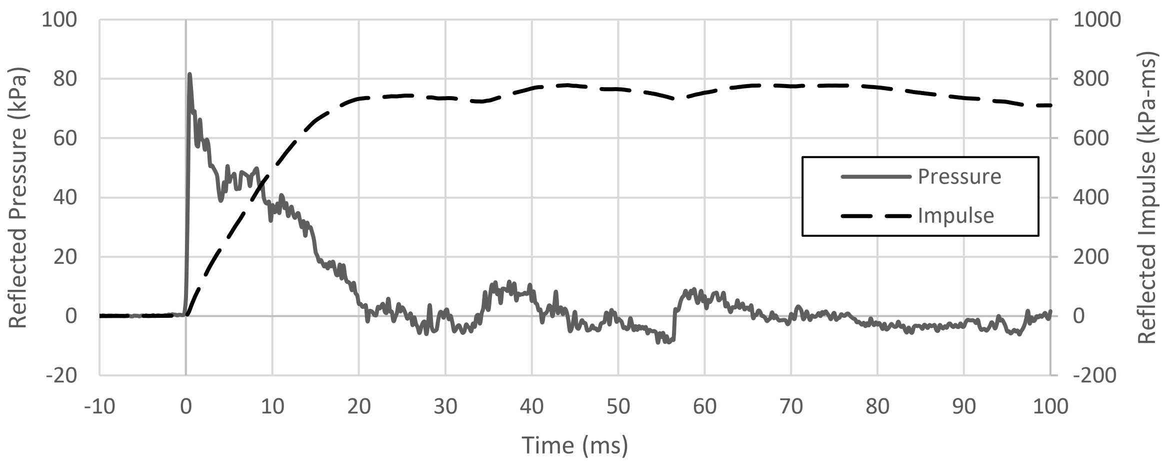

Figure A.77: Pressure-time history and cumulative impulse for CLT3.2

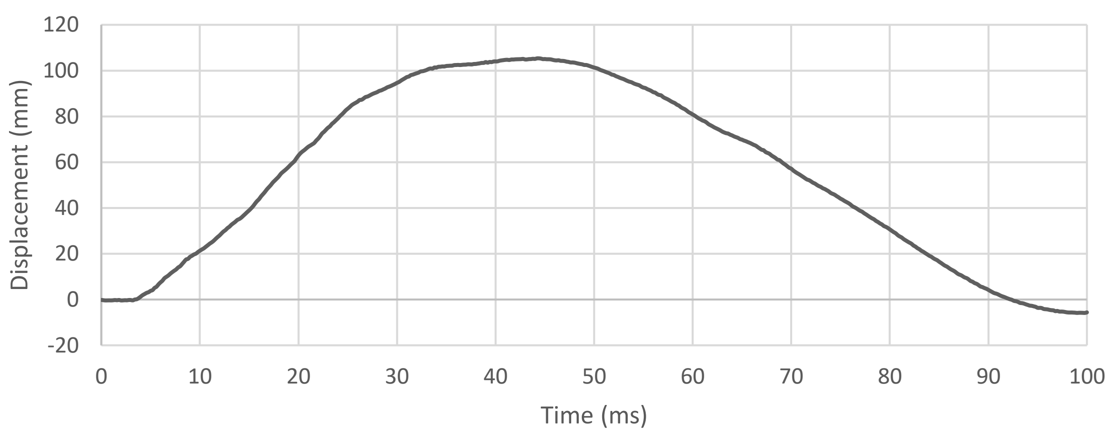

Figure A.78: Displacement-time history for CLT3.2

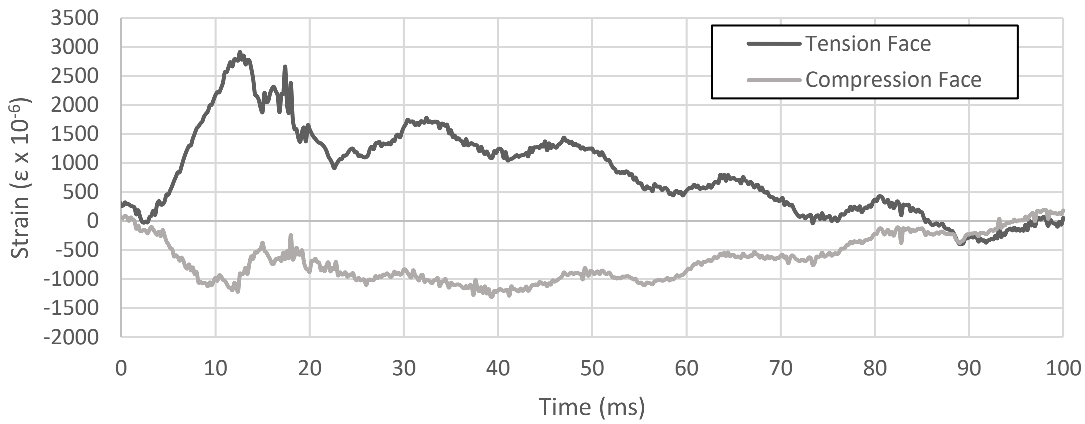

Figure A.79: Mid-span strain measurements for CLT3.2

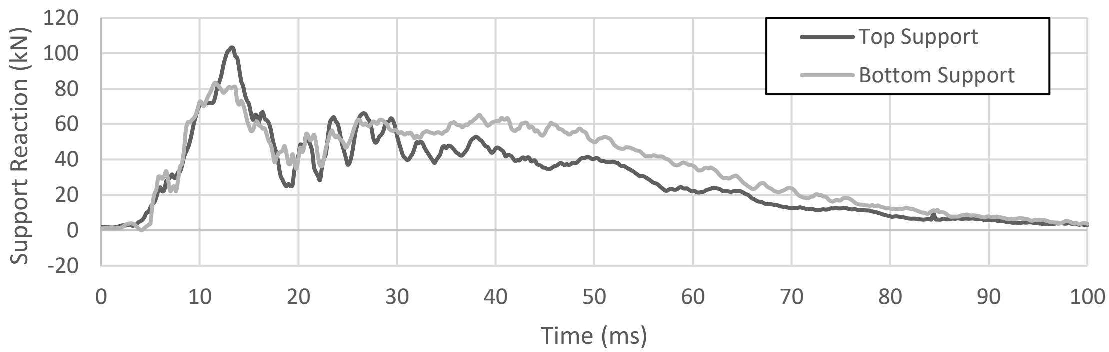

Figure A.80: Reaction-time histories for CLT3.2

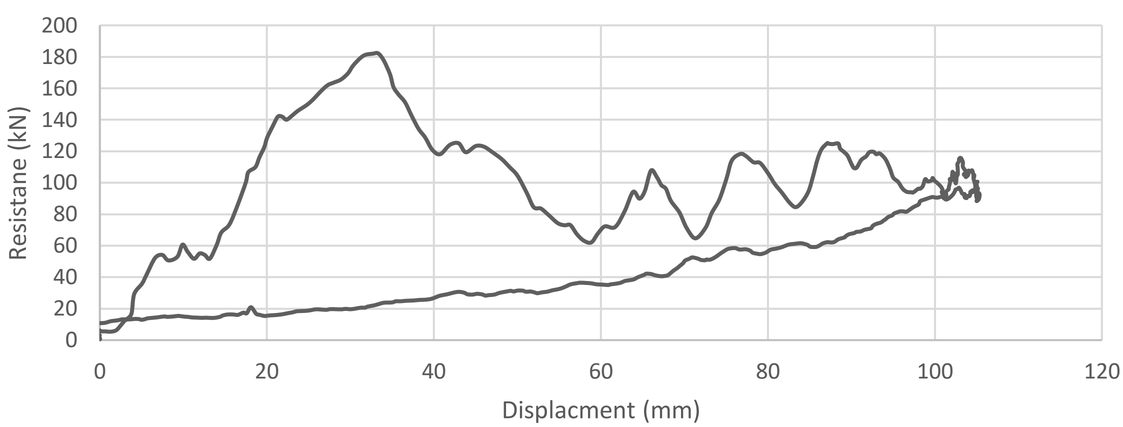

Figure A.81: Experimental resistance curve for CLT3.2

a) b) c)

Figure A.82: State of specimen after test CLT3.2: a) Left side b) Tension face c) Right side

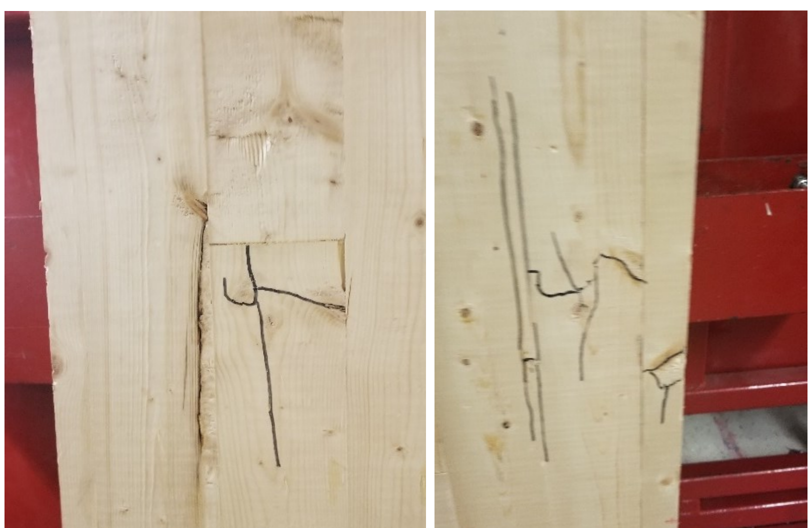

a) b)

Figure A.83: Superficial flexural cracking details on tension face: a) Upper left b) Lower right

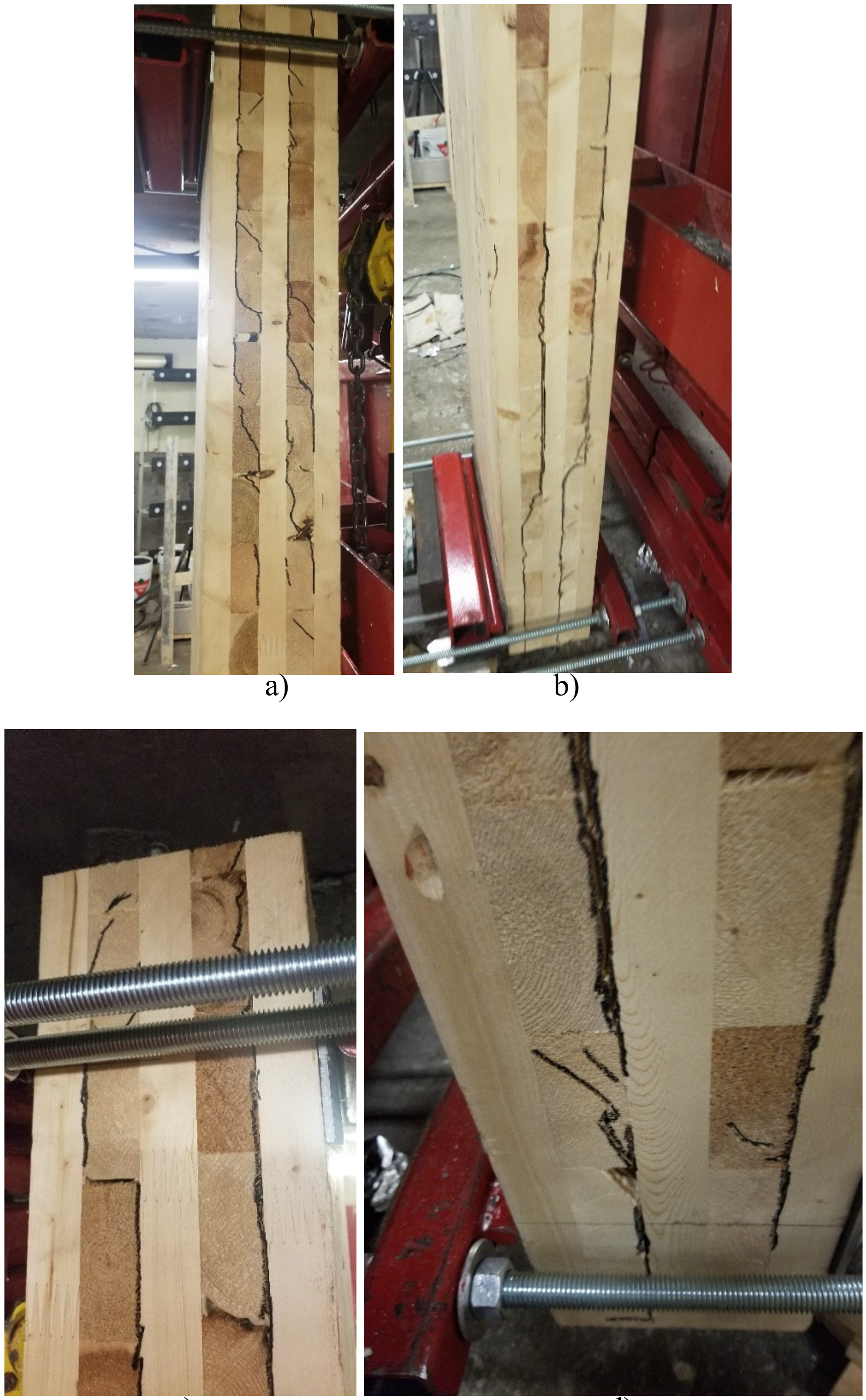

a) b)

c) d)

Figure A.84: Transverse cracking details at supports: a) Top right b) Bottom right c)Top left d) Bottom Left

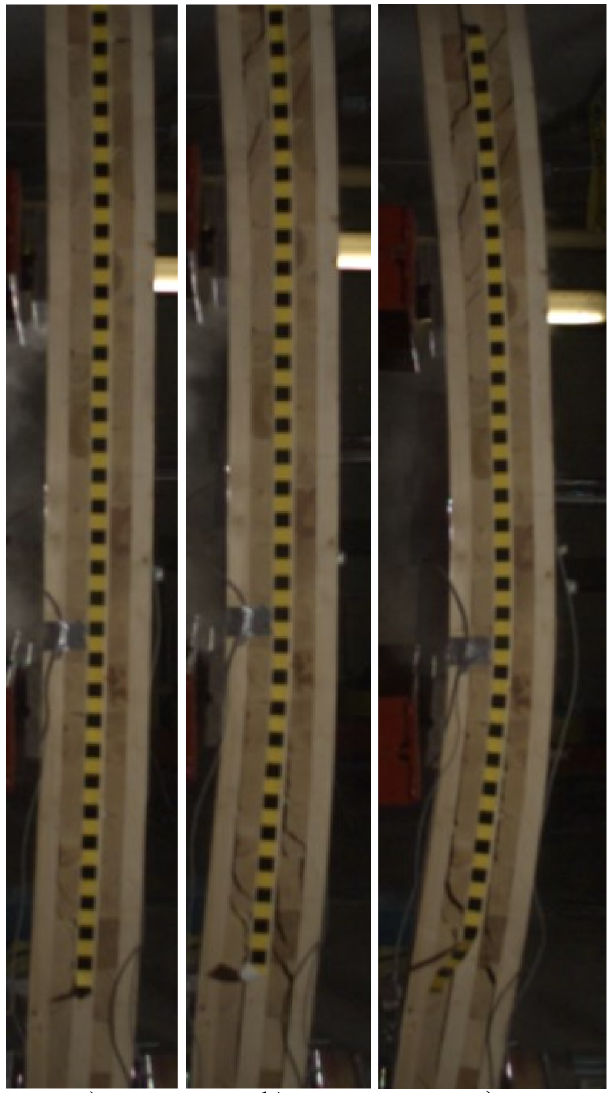

a) b) c)

Figure A.85: Progression of failure during test CLT3.2: a) 12 ms b) 18.5 ms c) 37 ms

APPENDIX B: STRENGTH INCREASE FACTOR DETERMINATION

The strength increase factors (SIF) for glulam and CLT were calculated by comparing theoretical resistances calculated using equations from CSA O86 [7] with average static test results from Lacroix and Doudak [9] and Poulin et al. [10], respectively.

Lacroix and Doudak [9] performed destructive static testing on glulam beams of grade 20f-ES with cross-sectional dimensions of 80 mm x 228 mm, as well as beams of grade 24f-ES with dimensions of 86 mm x 318 mm and 137 mm x 222 mm. All beams were 2,500 mm long, and tested under four-point bending with a clear span of 2,235 mm. The average of the reported static resistances was 105.79 kN (COV 0.091), 165.65 kN (COV 0.033), and 141.88 kN (COV 0.089) for the 80 mm, 86 mm, and 137 mm wide beams, respectively.

Poulin et al. [10] investigated the static resistance of three- and five-ply grade E1 CLT panels, which measured 105 mm and 175 mm thick respectively. All panels were 445 mm wide and 2,500 mm long, and were tested under four-bending with a span of 2,235 mm. The average static resistance for the three-ply specimens was 68.4 kN (COV 0.08), while the five-ply specimens had an average static resistance of 128.6 kN (COV 0.03).

The resistance equation used to calculate the design-level bending moment resistance (M_r) for glulam is presented in Equation [B-1] [7]. An additional calculation is typically required by CSA O86 to account for the beam's lateral stability, but considering the consistency of material failure during simulated blast test (e.g. [49]) and the rapid nature of blast loading it was considered that lateral buckling behaviour would not develop. The specified material bending strength (f_b) was obtained from manufacturer specifications [50], and was equal to 25.6 MPa and 30.7 MPa for grade 20f-ES and 24f-ES, respectively.

$$M_r = \phi(f_b K_D K_H K_{Sb} K_T)\frac{bd}{6}\,K_x K_{Zbg} \qquad \text{[B-1]}$$

where:
ϕ is the glulam strength reduction factor, equal to 1 for nominal capacity

K_D is the load duration factor, equal to 1 for blast applications [59]

K_H is the structural system factor, equal to 1 for single members

K_{Sb} is the service condition factor for bending, equal to 1 for dry conditions

K_T is the chemical treatment factor, equal to 1 for untreated timber

b is the width of the cross-section, *d* is the depth of the cross section

K_x is the glulam curvature factor, equal to 1 for uncurved members

K_{Zbg} is the size factor, calculated according to $K_{Zbg} = \left(\frac{130}{b}\right)^{0.1}\left(\frac{610}{d}\right)^{0.1}\left(\frac{9100}{L}\right)^{0.1} \leq 1.3$ where L is the length between points of zero moment (i.e. the span length in four-point bending)

The bending capacity in the major axis ($M_{r,y}$) for the CLT panels was similarly calculated using Equations [B-2] and [B-3] from CSA O86 [7]. The material bending strength (f_b), longitudinal elastic modulus (E) and effective bending stiffness ($(EI)_{eff}$) were obtained from the manufacturer documentation [48]. The bending strength and modulus of elasticity for longitudinal plies of grade EI CLT panels was 28.2 MPa and 11,700 MPa, respectively. The three-ply panel had an effective bending stiffness of 481.1 x 10^9 Nmm^2, while the effective bending stiffness for the five-ply panels was 1,842.3 x 10^9 Nmm^2.

$$M_{r,y} = \phi(f_b K_D K_H K_{Sb} K_T) S_{eff,y} K_{rb,y} \qquad \text{[B-2]}$$

where:

ϕ is the CLT strength reduction factor, equal to 1 for n

K_D is the load duration factor, equal to 1 for blast applications [59]

K_H is the structural system factor, equal to 1 for single members

K_{Sb} is the service condition factor for bending, equal to 1 for dry conditions

K_T is the chemical treatment factor, equal to 1 for untreated timber

$S_{eff,y}$ is the width of the cross-section

$K_{rb,y}$ is the CLT adjustment factor, equal to 0.85 for the primary direction

$$S_{eff,y} = \frac{(EI)_{eff}}{E}\frac{2}{h} \qquad \text{[B-3]}$$

where:

h is the thickness of the CLT panel

The moment resistances were then converted to an overall member resistance (R) using Equation [B-4] in order to be directly comparable with the experimental results.

$$R = \frac{M_r 6}{L} \quad \text{[B-4]}$$

where:
L is the span length

The design-level resistance for the glulam sizes tested by Lacroix and Doudak [9] were determined to 73.0 kN, 152.9 kN, and 117.5 kN for the 80 mm, 86 mm, and 137 mm wide members, respectively. The panel capacities for the three-ply and five-ply panels were calculated to be 50.5 kN and115.8 kN, respectively. Comparing the experimental and design-level capacities resulted in an overall SIF of 1.25 for glulam and 1.23 for CLT.

APPENDIX C: GLULAM RESISTANCE CURVE FOR SINGLE-DEGREE-OF-FREEDOM ANALYSIS

The behaviour of glulam beams was observed by Lacroix and Doudak [9] to be linearly elastic until flexural failure with no notable post-peak resistance. Therefore, the resistance curve for single-degree-of-freedom analysis can be defined by a single failure point. The midspan displacement is used for the characteristic displacement under four-point bending, and the design-level material bending capacity is determined from Equation [C-1] [7]. The moment resistance is then converted to the overall static member resistance using Equation [C-2]. The ultimate dynamic resistance is obtained by applying the strength increase factor (SIF) and dynamic increase factor (DIF) obtained from Lacroix and Doudak [9] to the design-level capacity, and the displacement at failure is found by dividing the dynamic resistance by the equivalent stiffness for four point bending determined in Equation [C-3] [17].

$$M_r = \phi(f_b K_D K_H K_{Sb} K_T)\frac{bd}{6}\,K_x K_{Zbg} \qquad \text{[C-1]}$$

where:
M_r is the bending moment capacity

ϕ is the glulam strength reduction factor, equal to 1 for blast applications [59]

f_b is the specified material bending strength

K_D is the load duration factor, equal to 1 for blast applications [59]

K_H is the structural system factor, equal to 1 for single members

K_{Sb} is the service condition factor for bending, equal to 1 for dry conditions

K_T is the chemical treatment factor, equal to 1 for untreated timber

b is the width of the cross-section, d is the depth of the cross section

K_x is the glulam curvature factor, equal to 1 for uncurved members

K_{Zbg} is the size factor, calculated according to $K_{Zbg} = \left(\frac{130}{b}\right)^{0.1}\left(\frac{610}{d}\right)^{0.1}\left(\frac{9100}{L}\right)^{0.1} \leq 1.3$ where L is the length between points of zero moment (i.e. the span length in four-point bending)

$$R = \frac{M_r 6}{L} \qquad \text{[C-2]}$$

where:
R is total member resistance

L is the span length

$$K = \frac{56.4EI}{L^3} \qquad \text{[C-3]}$$

where:
K is the equivalent stiffness for the midspan of a member under four-point bending

E is the elastic modulus of the beam

I is the moment of inertia of the beam cross-section, equal to $\frac{bd^3}{12}$

The glulam specimens in this study had an 86 mm x 178 mm cross-section, and were tested with a span length of 2,235 mm. The elastic modulus and bending strength were equal to 12,400 MPa and 30.7 MPa, respectively, and were obtained from manufacturer specifications [50]. The size factor was calculated to be 1.36 for the specimen dimensions, therefore the value was limit to 1.3 as prescribed in CSA O86 [7]. The design level moment resistance was determined to be 18.1 kNm, which corresponded to an overall static resistance of 48.7 kN. After applying the SIF and DIF of 1.25 and 1.14, respectively, based on results from Lacroix and Doudak [9], a dynamic resistance of 69.3 kN was determined. The moment of inertia for the beam cross-section was determined to be approximately 40.4 x 10^6 mm^4, and the equivalent stiffness was determined to be 2.53 kN/mm. This results in an ultimate displacement of 27.4 mm for the resistance curve.

APPENDIX D: SINGLE-DEGREE-OF-FREEDOM RESULTS

D.1 Glulam Analysis Results

<u>Model GL1.1:</u> System mass: 304.9 kg

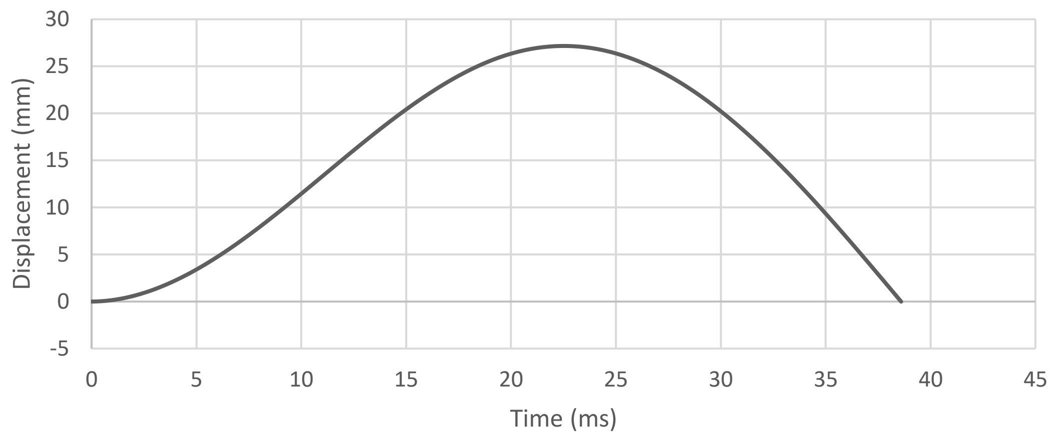

Figure D.1: Displacement results for SDOF model GL1.1

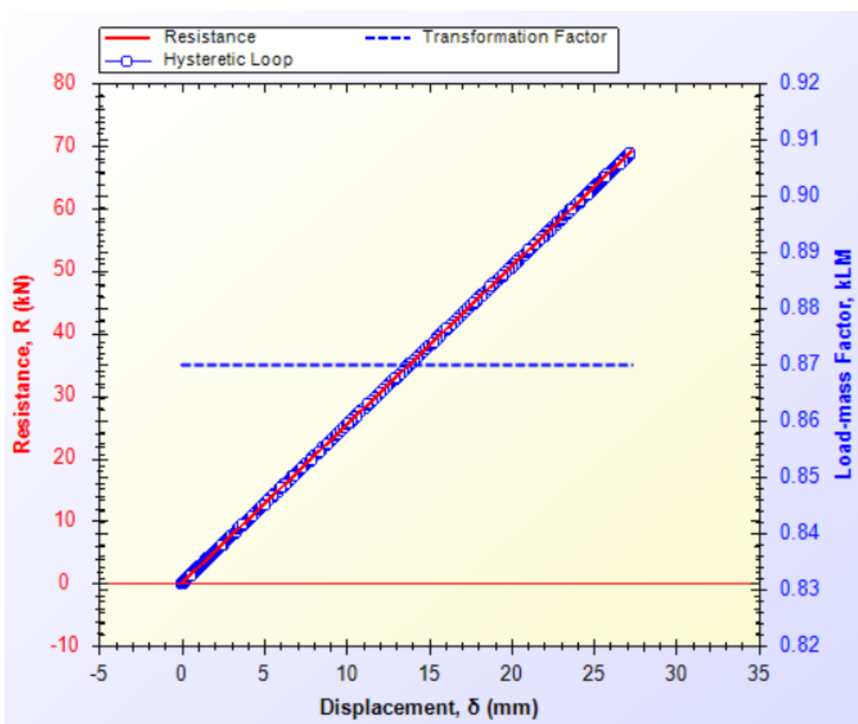

Figure D.2: Resistance history for SDOF model GL1.1

Model GL2.1: System mass: 304.7 kg

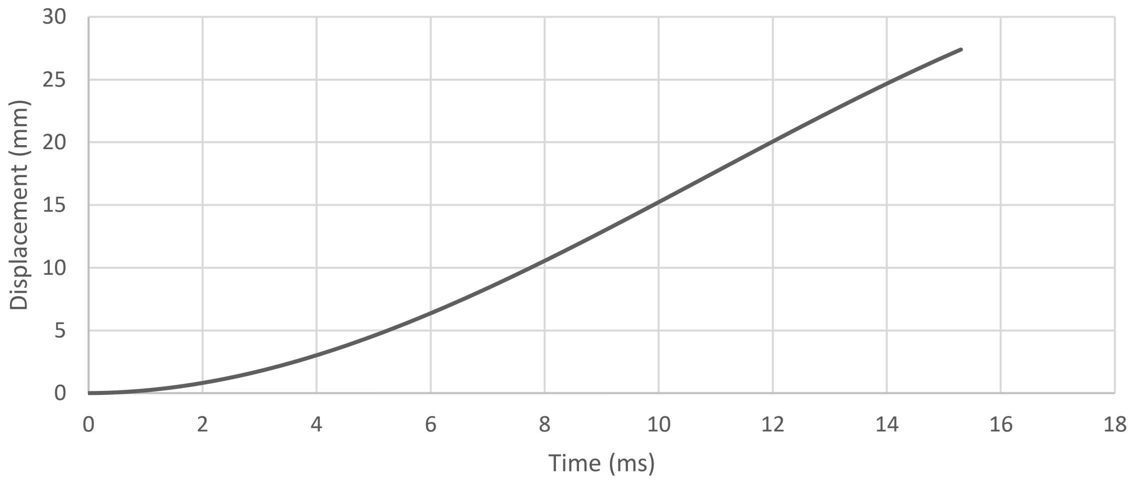

Figure D.3: Displacement results for SDOF model GL2.1

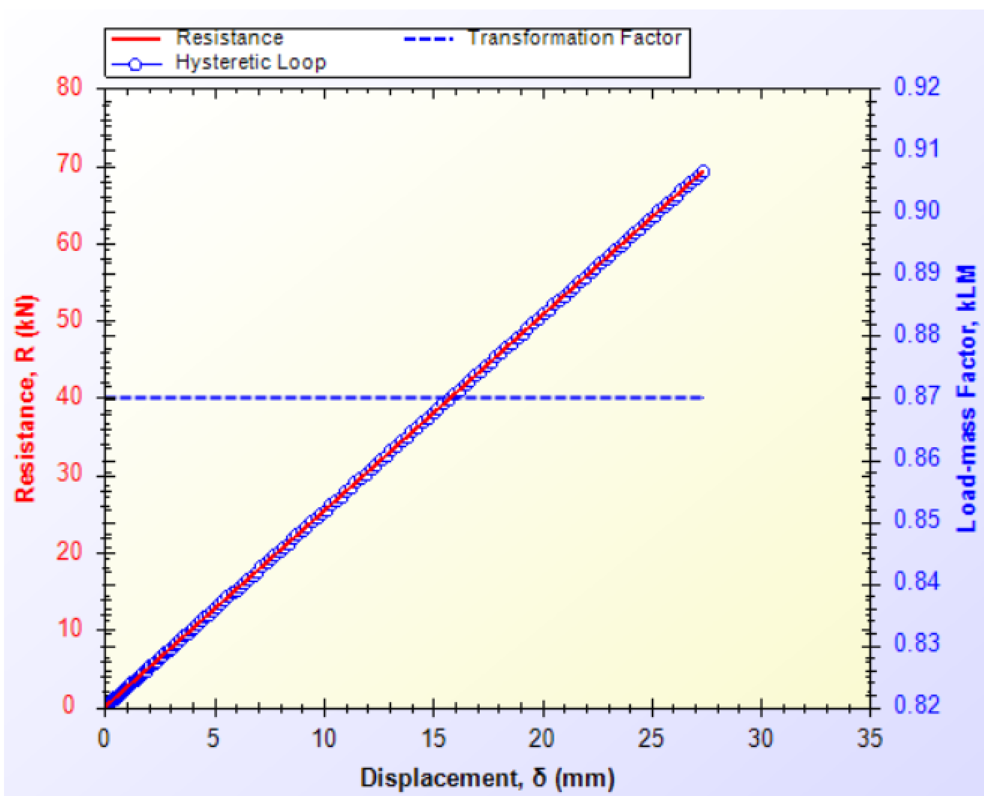

Figure D.4: Resistance history for SDOF model GL2.1

Model GL2.2: System mass: 304.7 kg

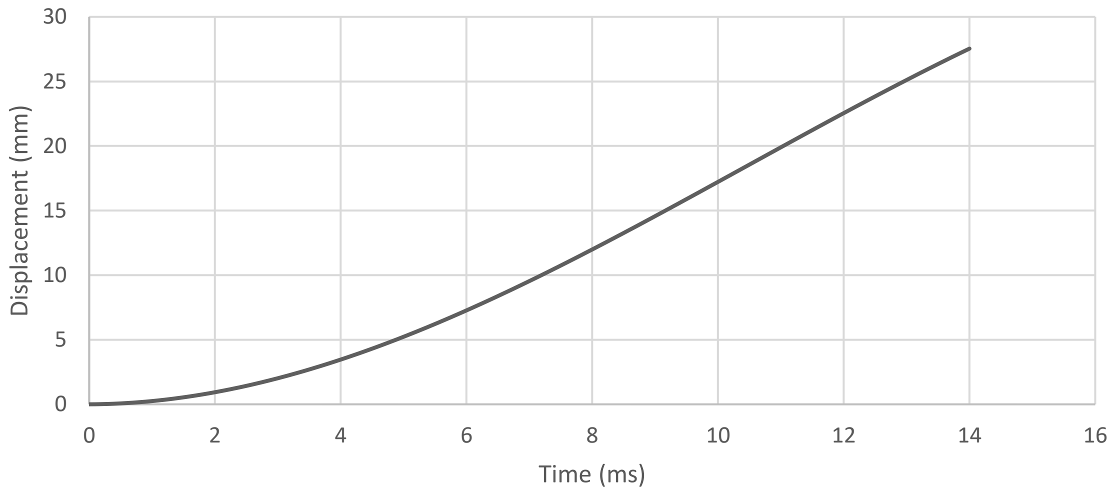

Figure D.5: Displacement results for SDOF model GL2.2

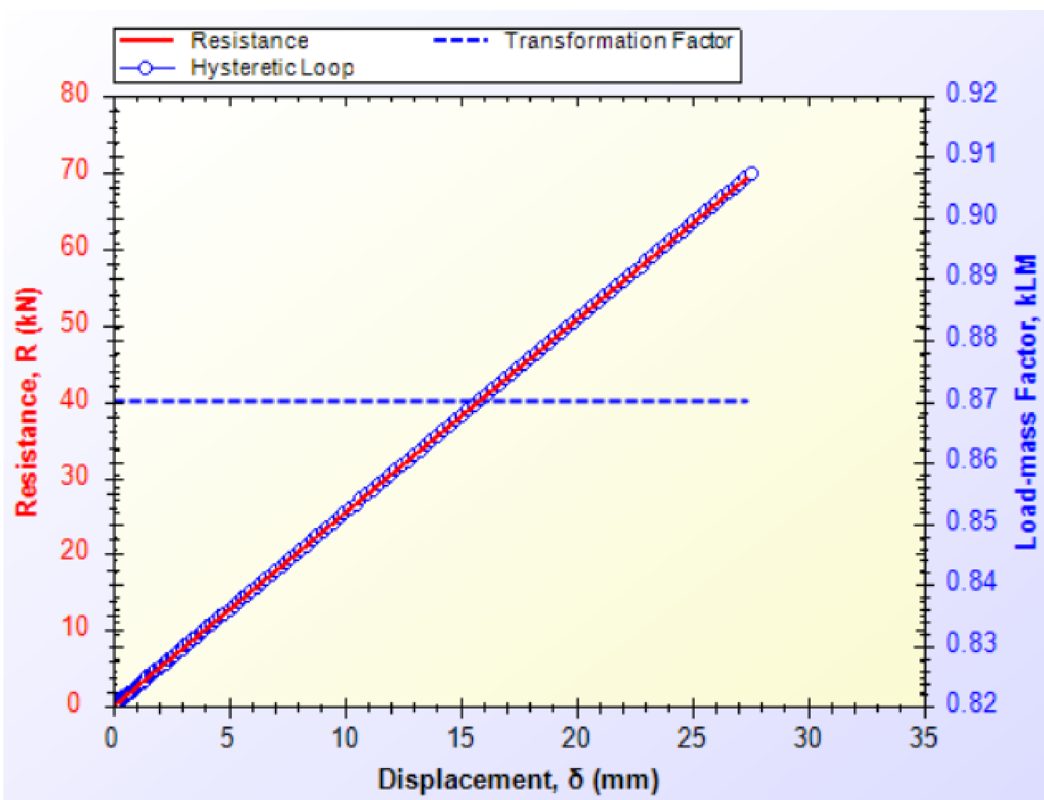

Figure D.6: Resistance history for SDOF model GL2.2

<u>Model GL3.1:</u> System mass: 304.92 kg

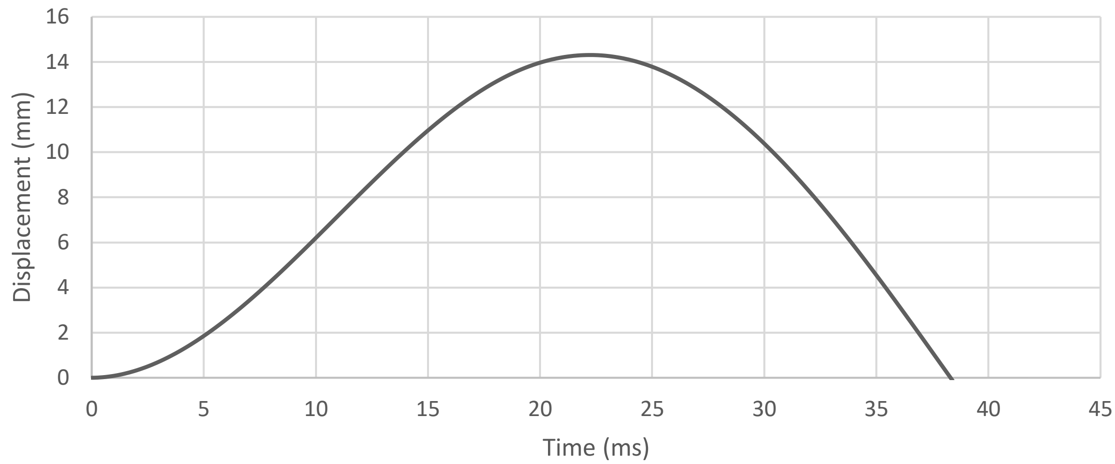

Figure D.7: Displacement results for SDOF model GL3.1

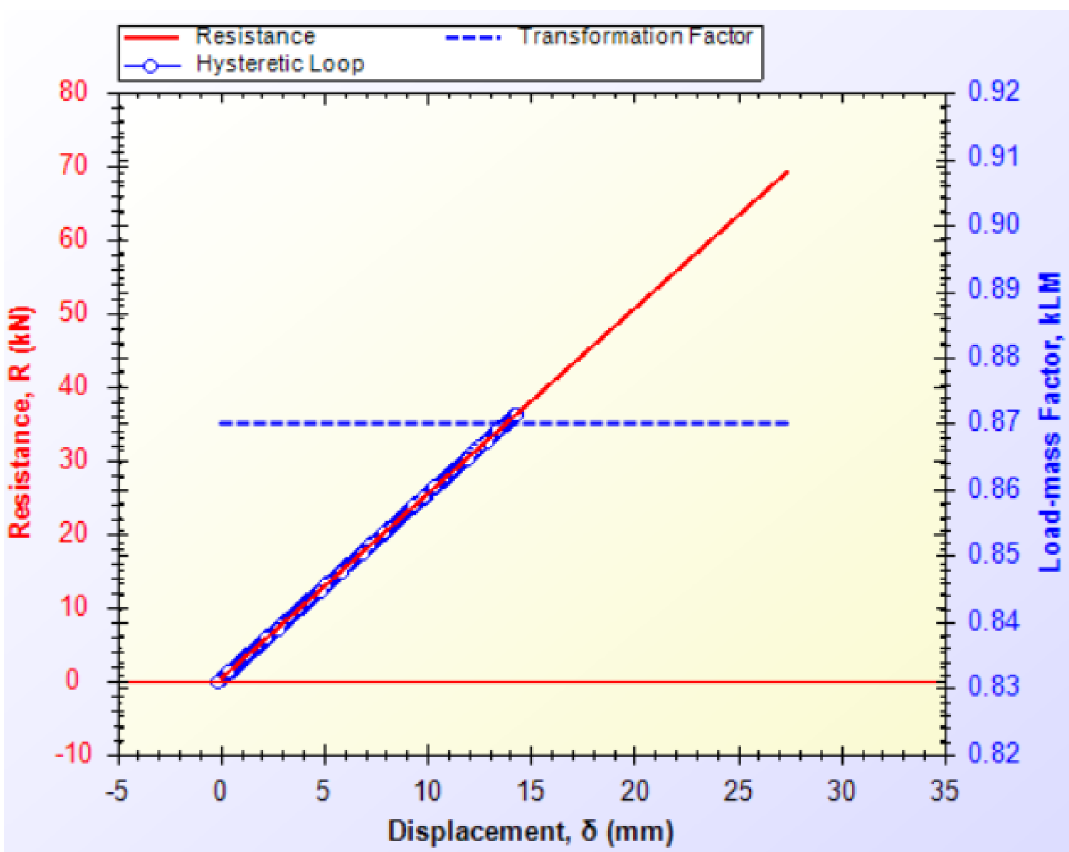

Figure D.8: Resistance history for SDOF model GL3.1

<u>Model GL3.2:</u> System mass: 304.92 kg

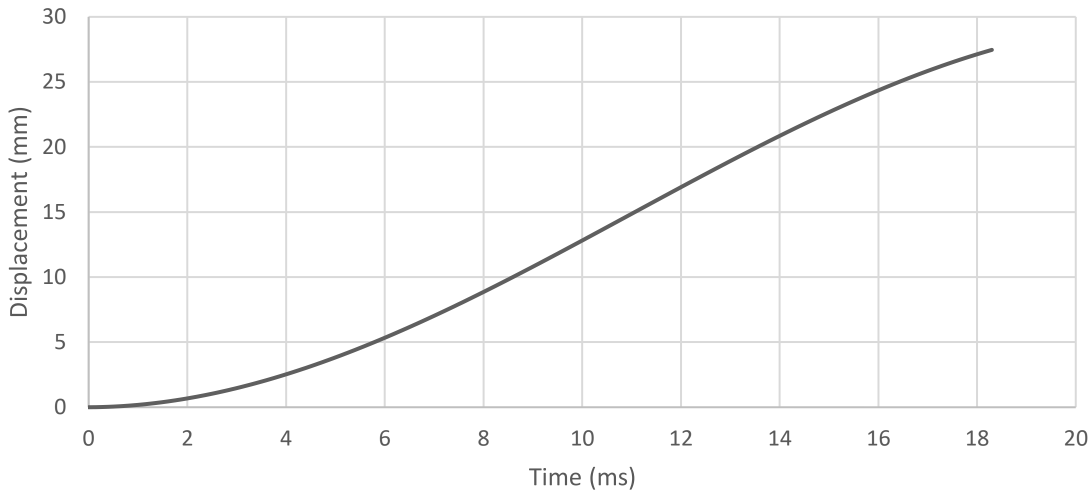

Figure D.9: Displacement results for SDOF model GL3.2

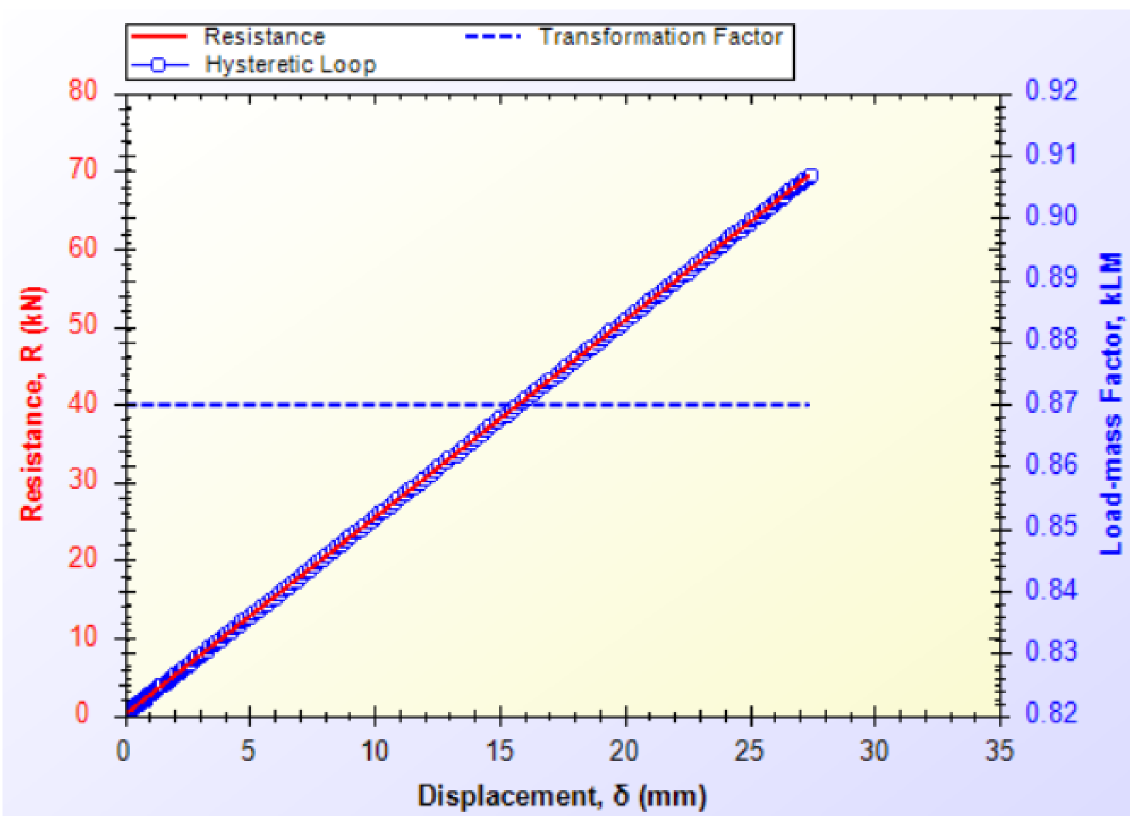

Figure D.10: Resistance history for SDOF model GL3.2

<u>Model GL3.3:</u> System mass: 304.92 kg

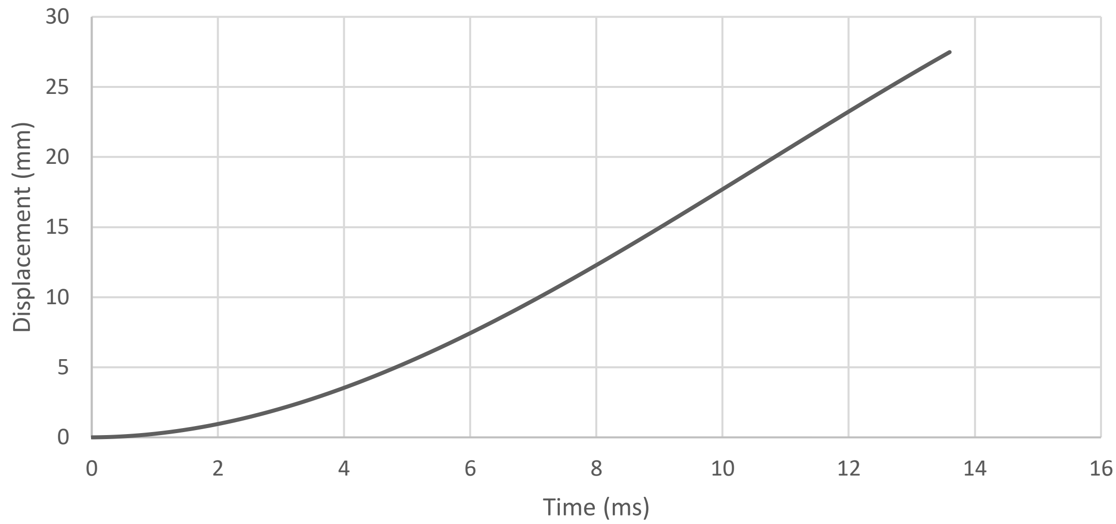

Figure D.11: Displacement results for SDOF model GL3.3

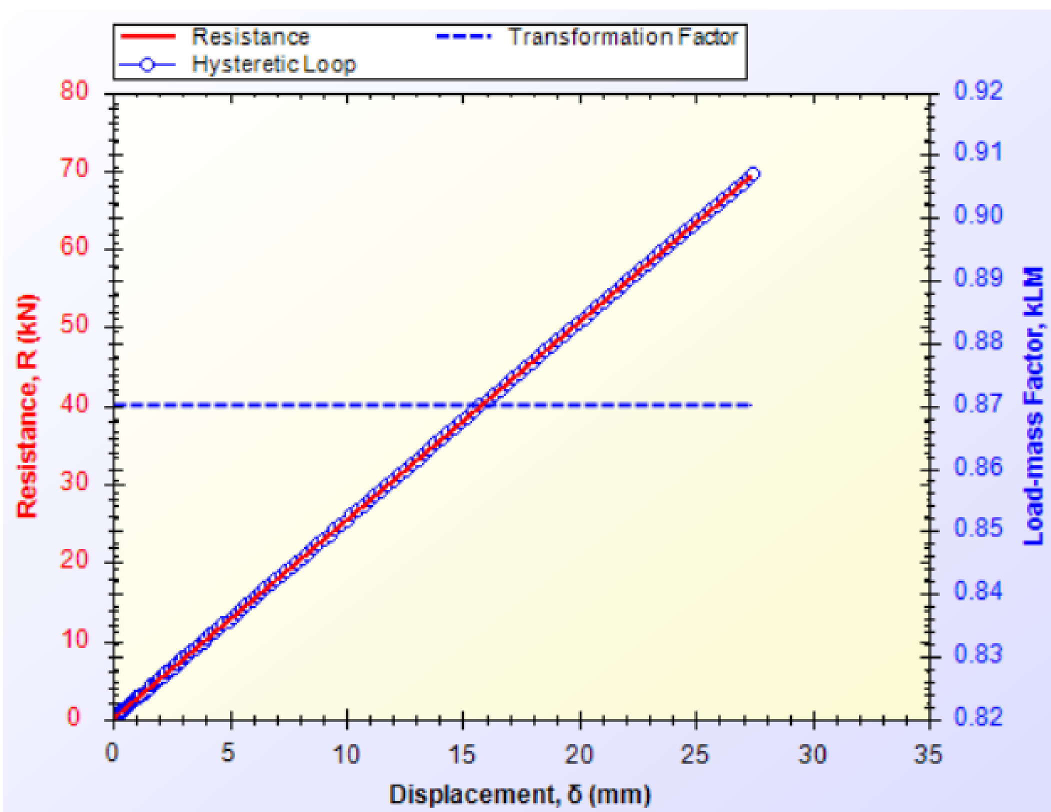

Figure D.12: Resistance history for SDOF model GL3.3

Model CLT1.1: System mass: 385.68 kg

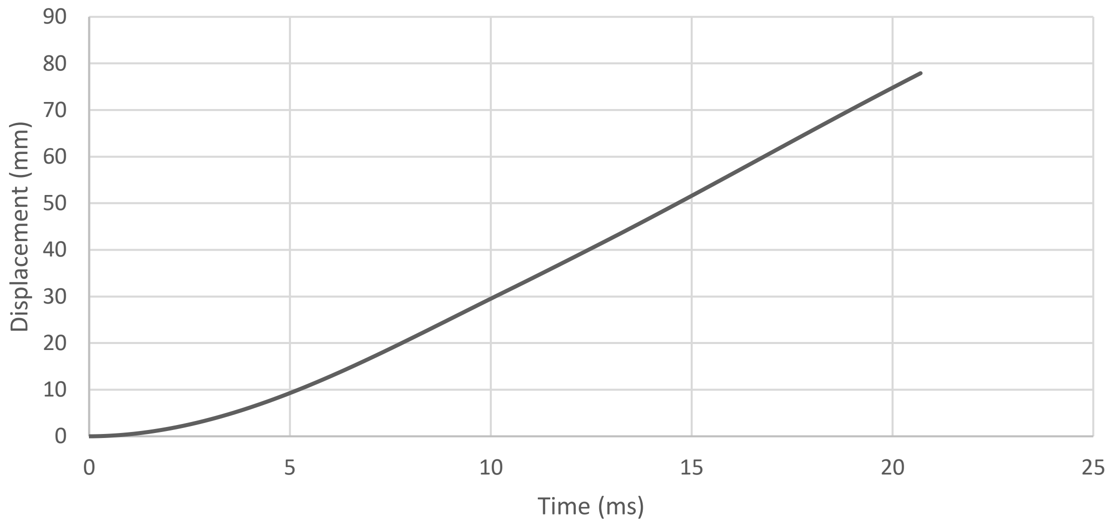

Figure D.13: Displacement results for SDOF model CLT1.1

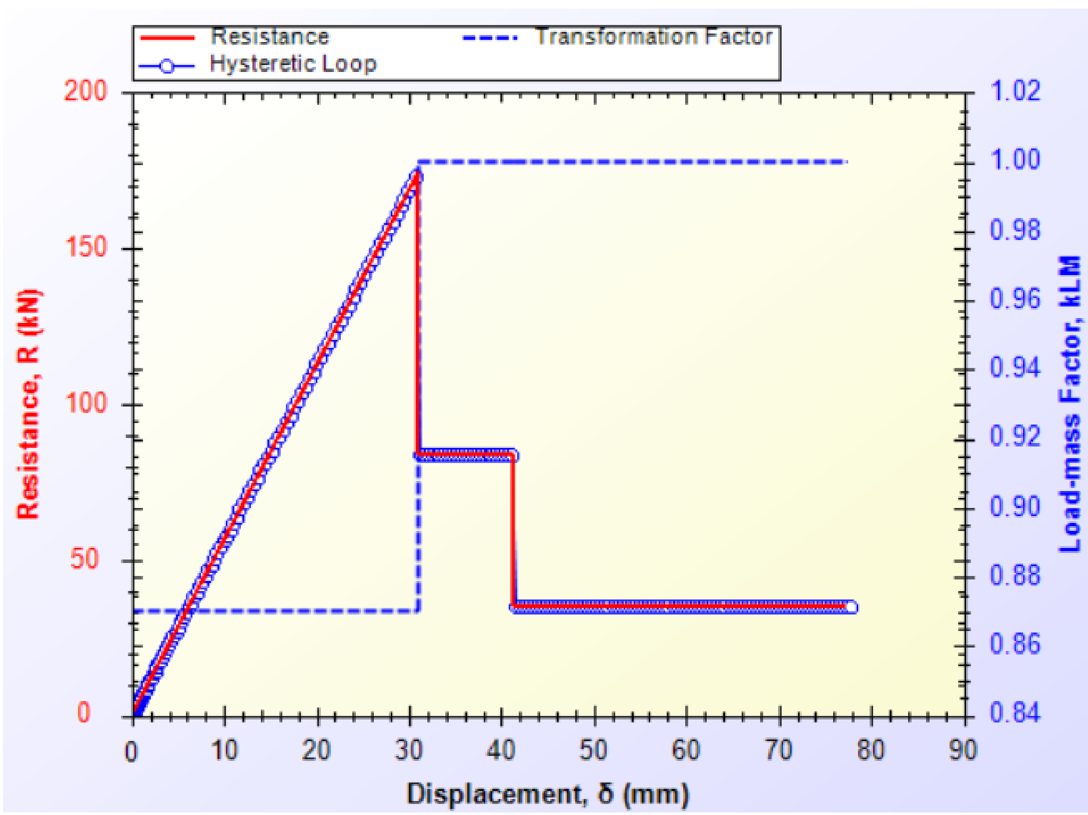

Figure D.14: Resistance history for SDOF model CLT1.1

Model CLT2.1: System mass: 386.04 kg

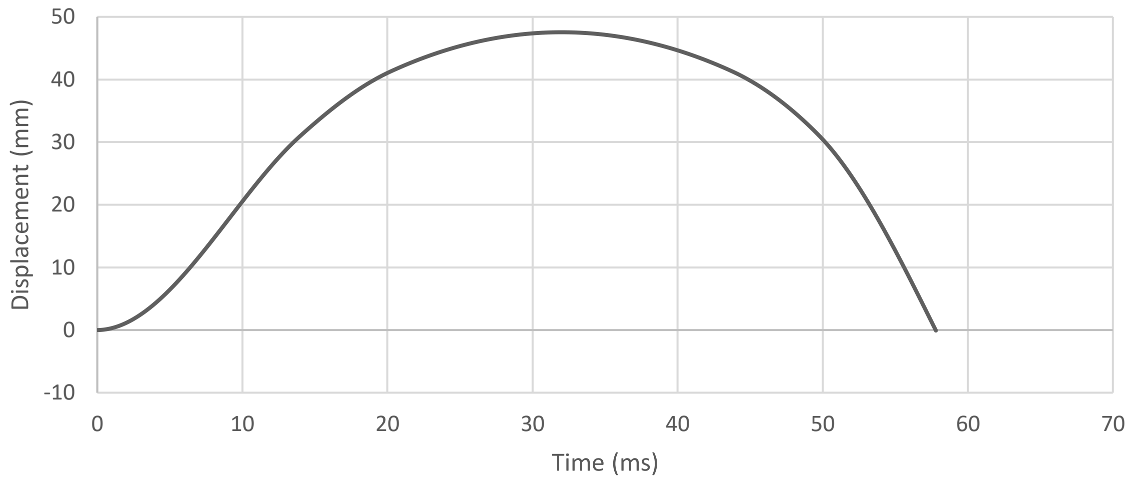

Figure D.15: Displacement results for SDOF model CLT2.1

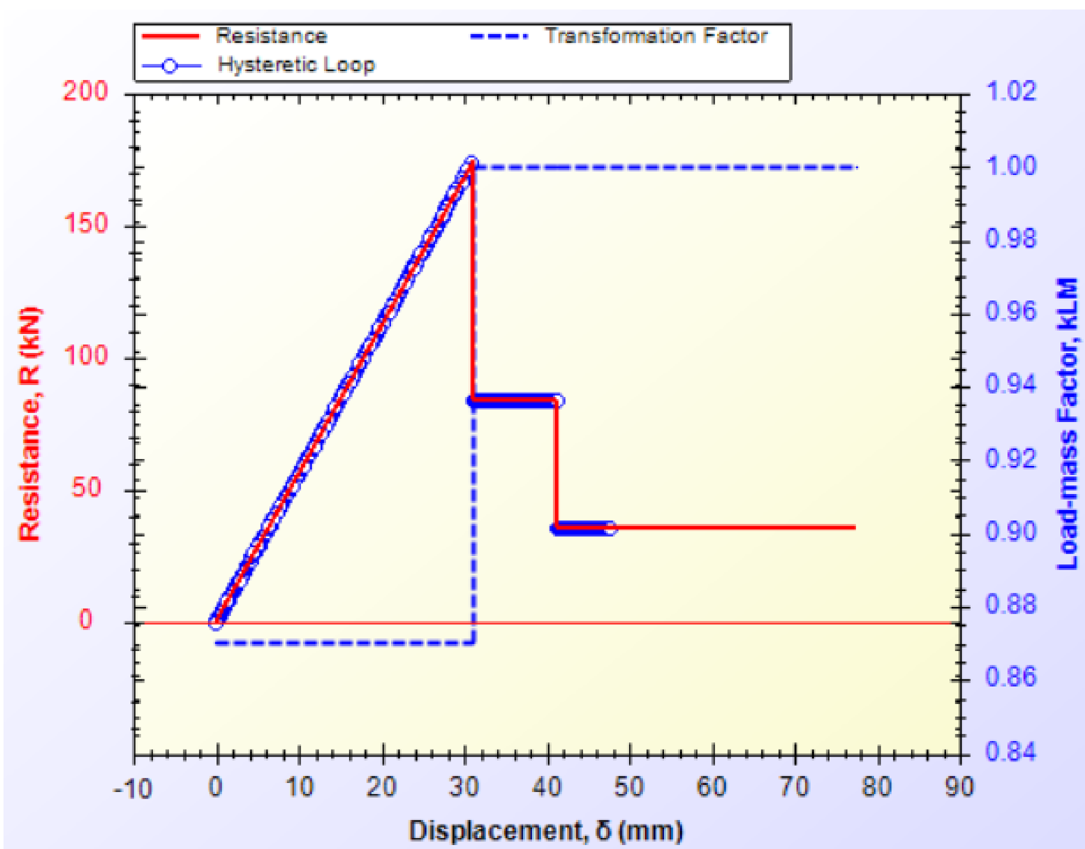

Figure D.16: Resistance history for SDOF model CLT2.1

<u>Model CLT2.2:</u> System mass: 386.04 kg

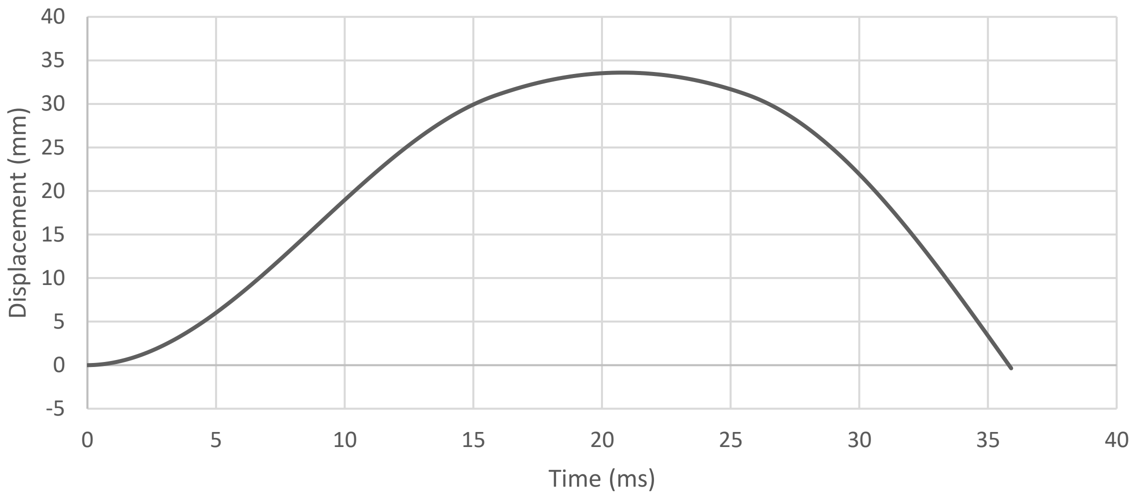

Figure D.17: Displacement results for SDOF model CLT2.2

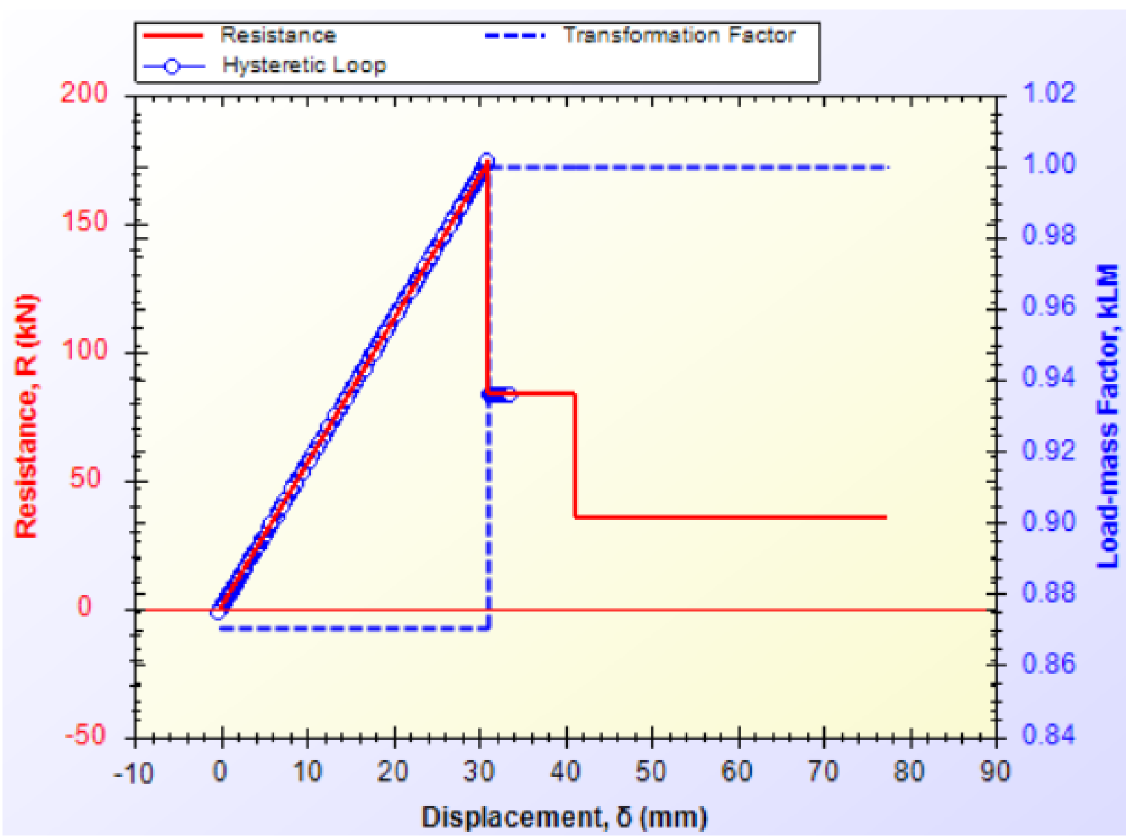

Figure D.18: Resistance history for SDOF model CLT2.2

Model CLT2.2-3P: System mass: 386.04 kg

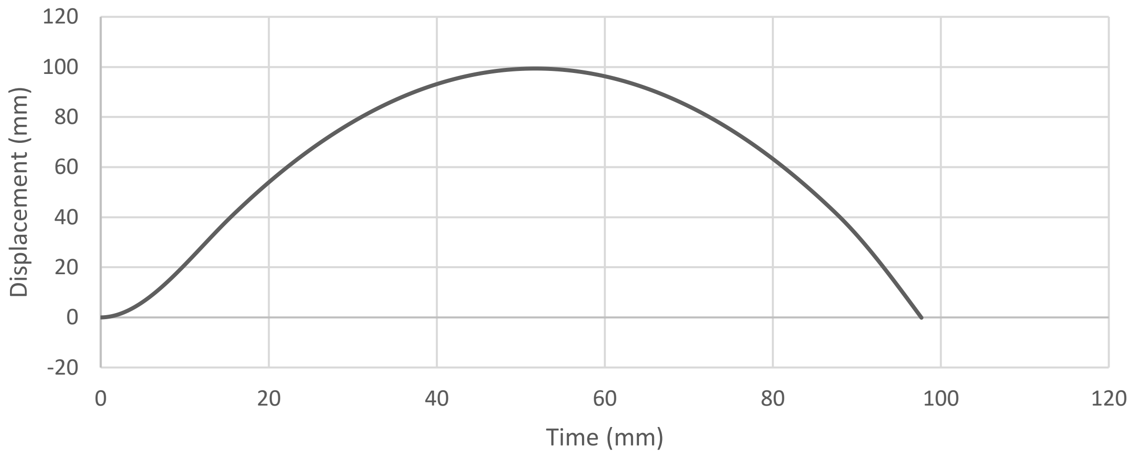

Figure D.19: Displacement results for SDOF model CLT2.2-3P

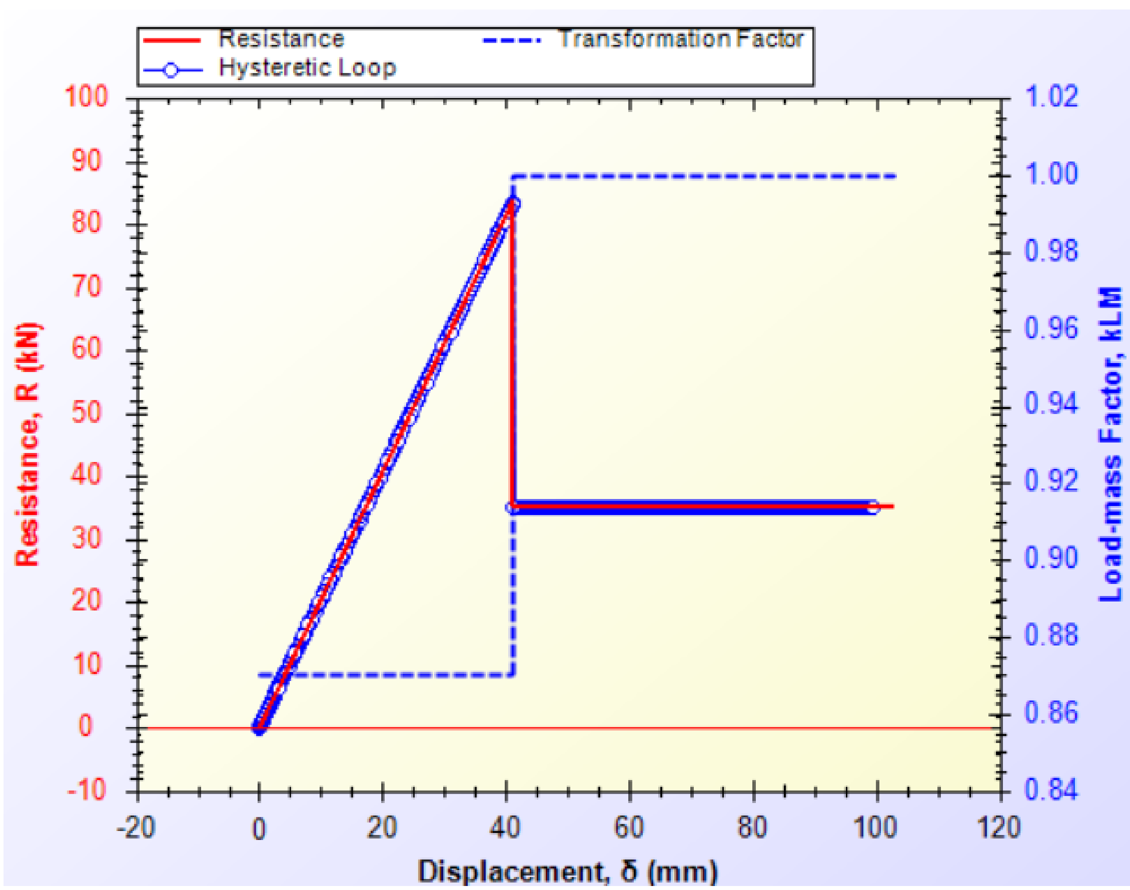

Figure D.20: Resistance history for SDOF model CLT2.2-3P

Model CLT2.3: System mass: 386.04 kg

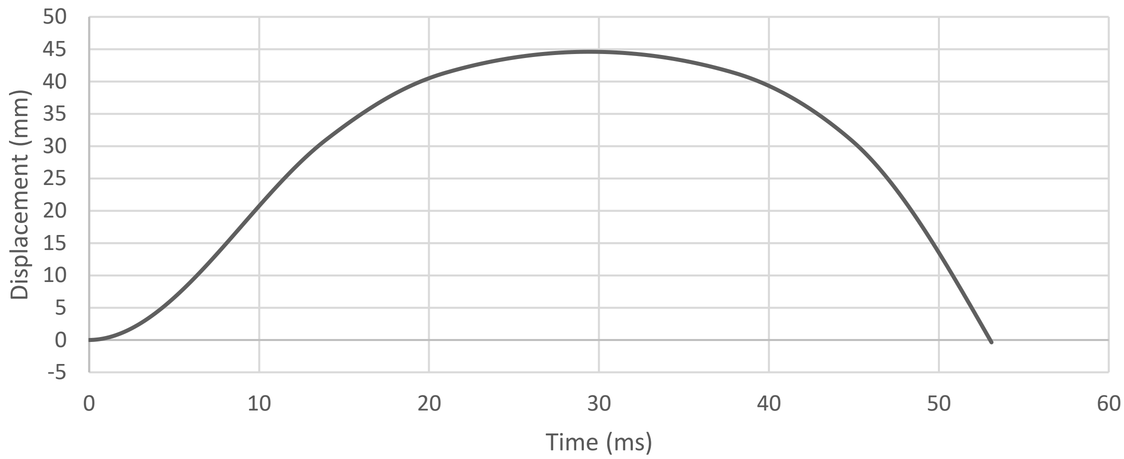

Figure D.21: Displacement results for SDOF model CLT2.3

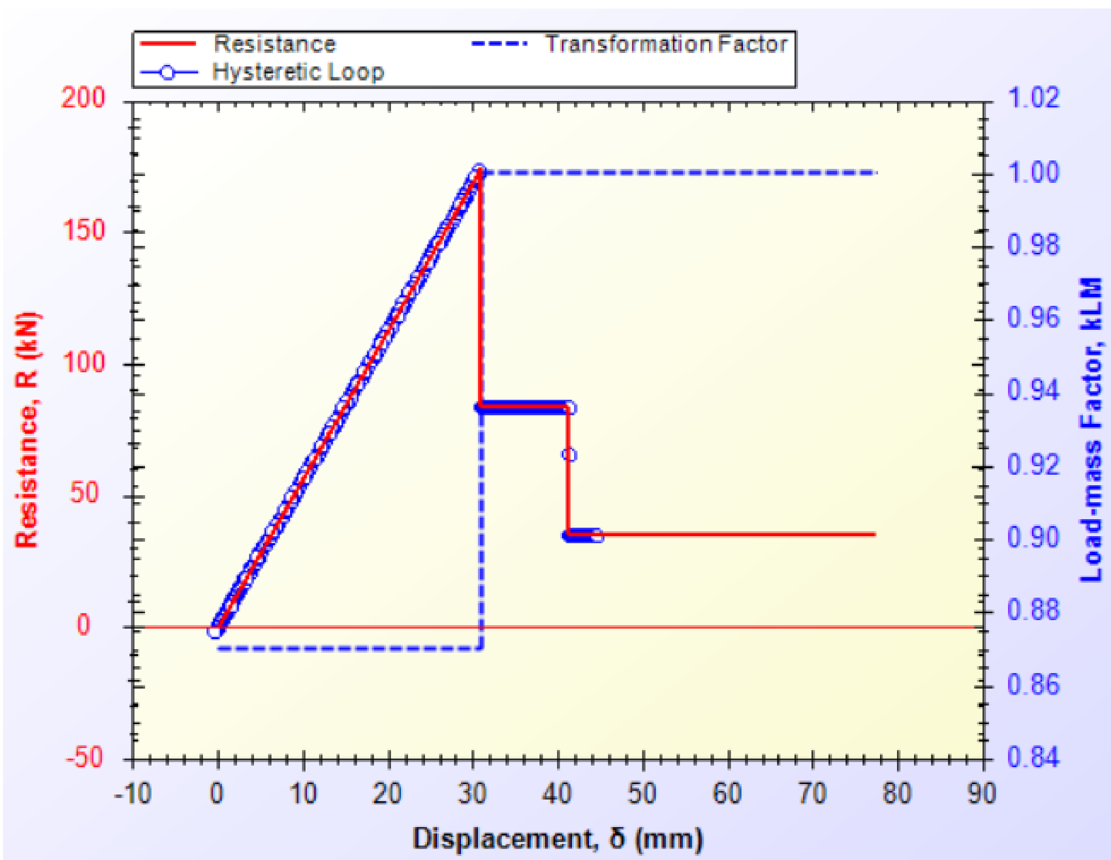

Figure D.22: Resistance history for SDOF model CLT2.3

Model CLT2.3-3P: System mass: 386.04 kg

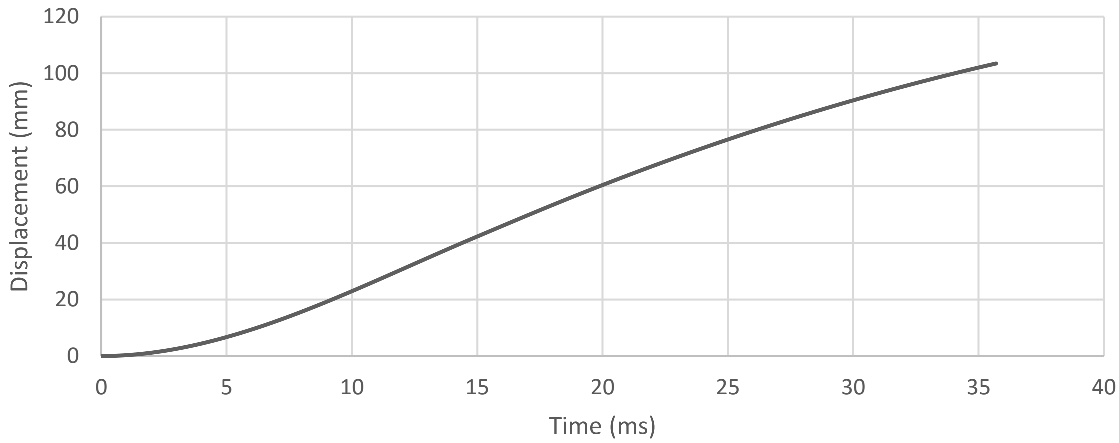

Figure D.23: Displacement results for SDOF model CLT2.3-3P

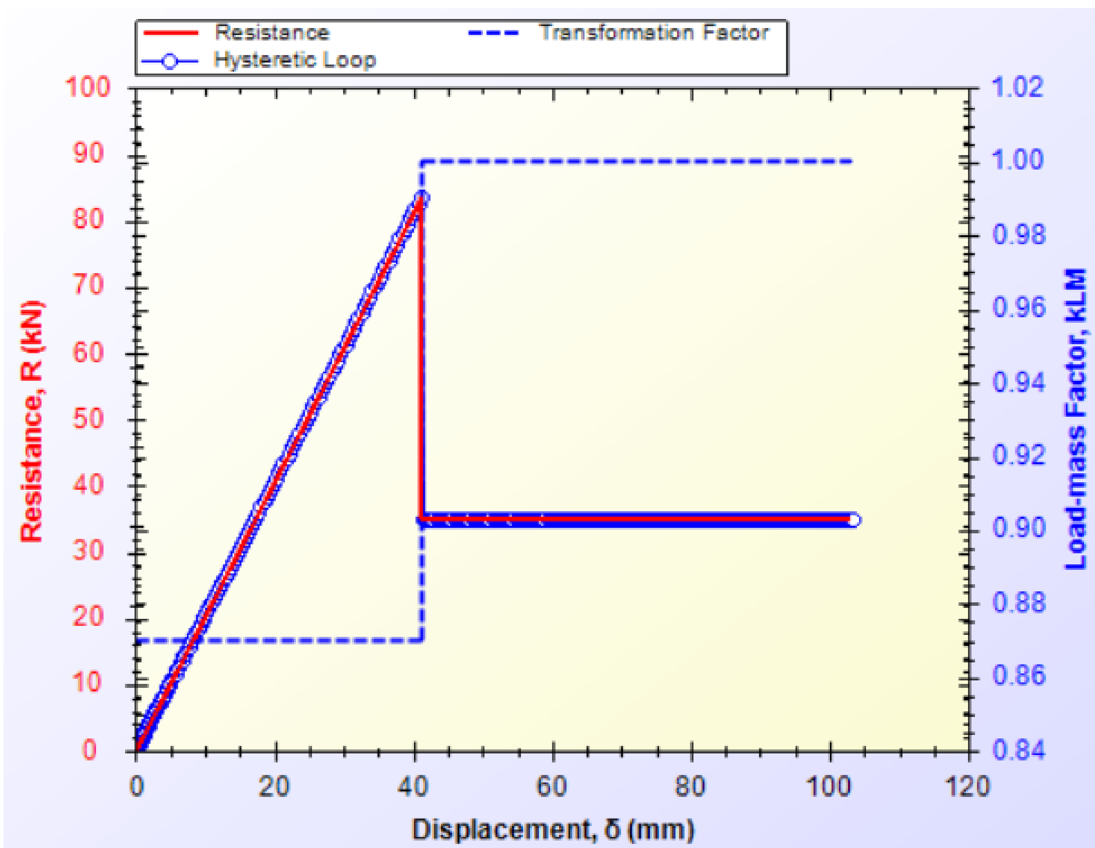

Figure D.24: Resistance history for SDOF model CLT2.3-3P

Model CLT3.1: System mass: 385.48 kg

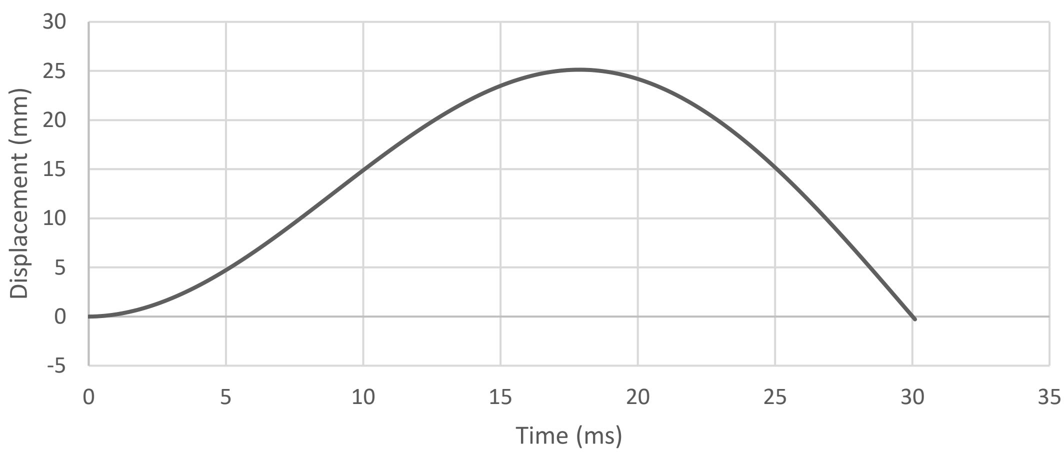

Figure D.25: Displacement results for SDOF model CLT3.1

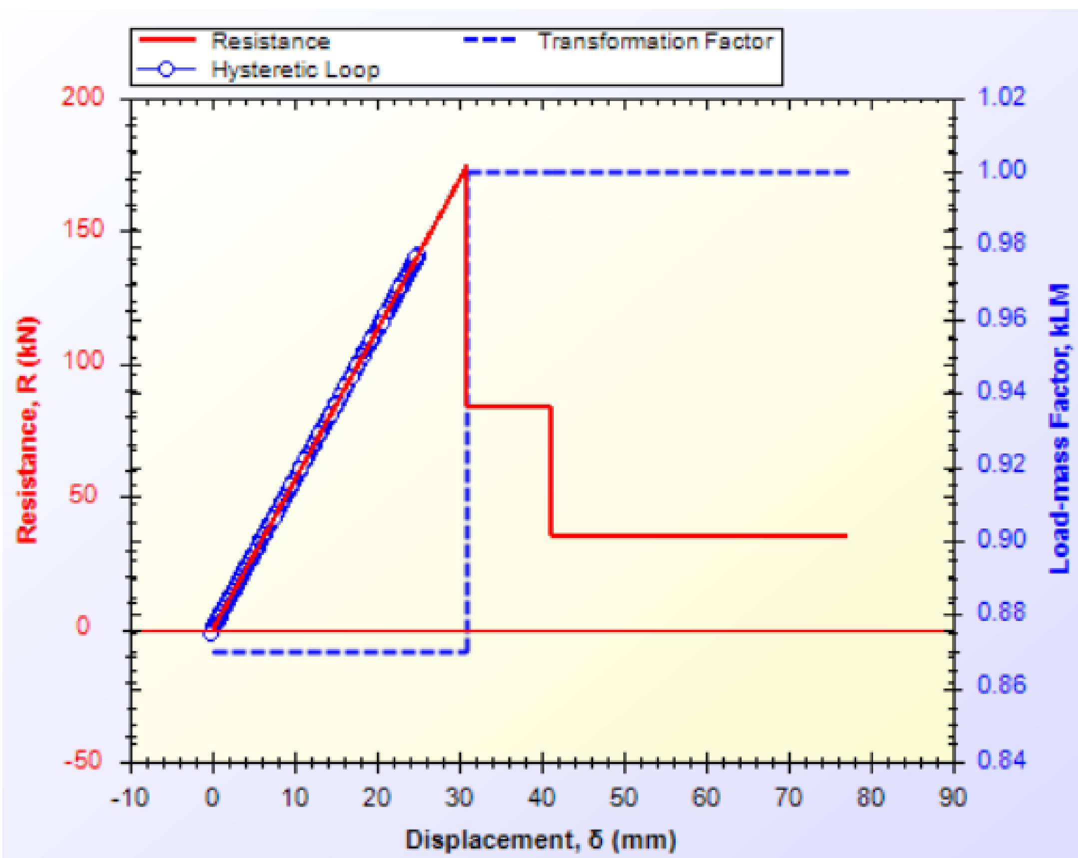

Figure D.26: Resistance history for SDOF model CLT3.1

Model CLT3.2: System mass: 385.48 kg

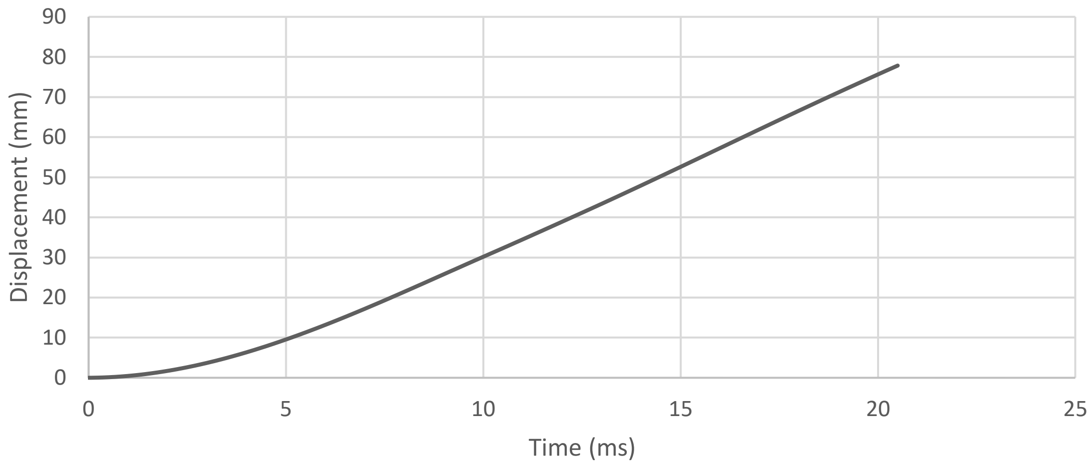

Figure D.27: Displacement results for SDOF model CLT3.2

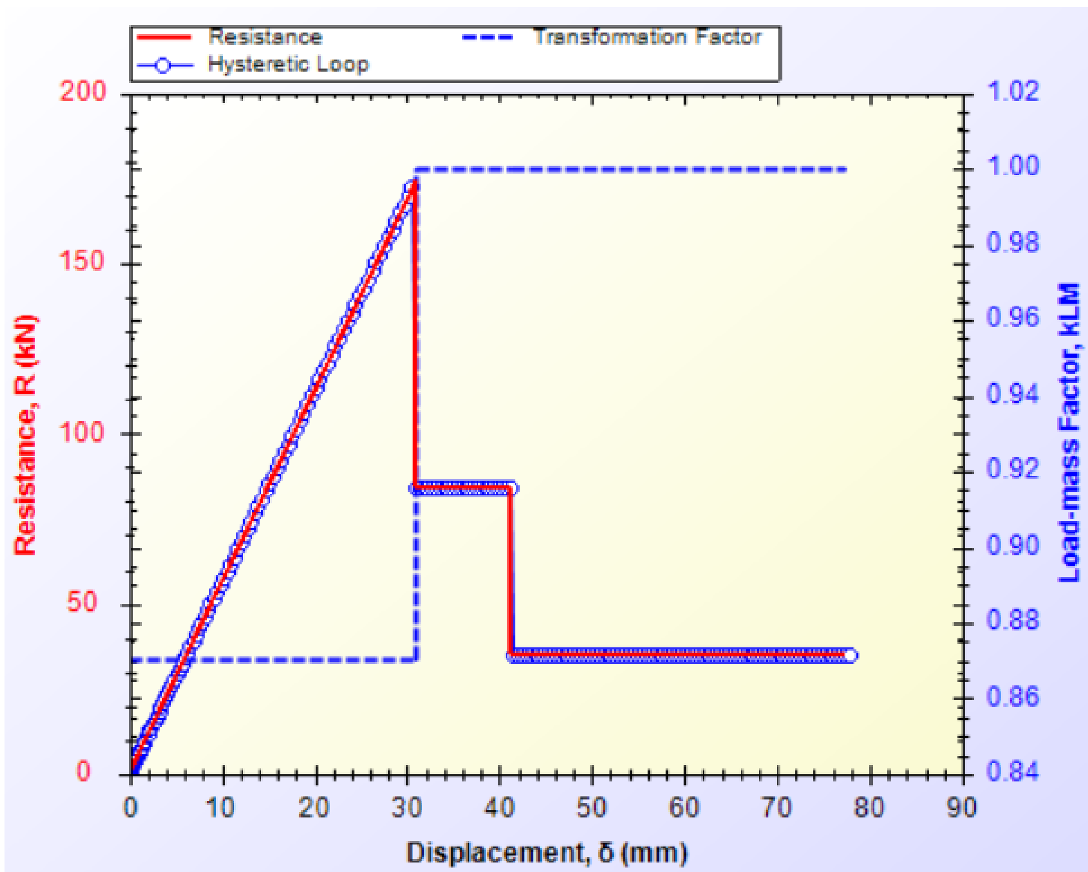

Figure D.28: Resistance history for SDOF model CLT3.2

APPENDIX E: ABAQUS VUMAT CODE

```
      subroutine vumat(
C Read only (unmodifiable)variables -
     1  nblock, ndir, nshr, nstatev, nfieldv, nprops, lanneal,
     2  stepTime, totalTime, dt, cmname, coordMp, charLength,
     3  props, density, strainInc, relSpinInc,
     4  tempOld, stretchOld, defgradOld, fieldOld,
     5  stressOld, stateOld, enerInternOld, enerInelasOld,
     6  tempNew, stretchNew, defgradNew, fieldNew,
C Write only (modifiable) variables -
     7  stressNew, stateNew, enerInternNew, enerInelasNew)
C
      include 'vaba_param.inc'
C
      dimension props(nprops), density(nblock), coordMp(nblock,*),
     1  charLength(nblock), strainInc(nblock,ndir+nshr),
     2  relSpinInc(nblock,nshr), tempOld(nblock),
     3  stretchOld(nblock,ndir+nshr),
     4  defgradOld(nblock,ndir+nshr+nshr),
     5  fieldOld(nblock,nfieldv), stressOld(nblock,ndir+nshr),
     6  stateOld(nblock,nstatev), enerInternOld(nblock),
     7  enerInelasOld(nblock), tempNew(nblock),
     8  stretchNew(nblock,ndir+nshr),
     9  defgradNew(nblock,ndir+nshr+nshr),
     1  fieldNew(nblock,nfieldv),
     2  stressNew(nblock,ndir+nshr), stateNew(nblock,nstatev),
     3  enerInternNew(nblock), enerInelasNew(nblock)
C
      character*80 cmname
C
        REAL*8  ExpectedStrain, ExpectedStress, ComM, detinv, E_11,
     1    E_perp, G, Groll, f_t0, f_c0, f_t90, f_c90, f_v, f_roll,
     2   G_f90, G_fv, G_froll, viNU, PoiRatio_12, PoiRatio_13,
     3   PoiRatio_23, PoiRatio_21, PoiRatio_31, PoiRatio_32, CapDelta,
     4   Ft0, Fc0, Ft90R, Fc90R, FvR, Ft90T, Fc90T, FvT, K_t0,
     5   K_c0, K_t90R, K_c90R, K_t90T, K_c90T, K_vR, K_vT, d_t0, d_c0,
     6   d_t90R, d_c90R, d_t90T, d_c90T, d_vR1, d_vT1, d_vR, d_vT,
     7   d_roll, d_0, d_90R, d_90T, ZERO, ONE, TWO, dv_t0, dv_c0,
     8   dv_t90R, dv_c90R, dv_t90T, dv_c90T, dv_vR1, dv_vT1, dv_roll,
     9   dv_vR, dv_vT, dv_0, dv_90R, dv_90T, Stiffness
        INTEGER  i, j, km, Deletion
        DIMENSION ExpectedStrain(ndir+nshr), ExpectedStress(ndir+nshr),
     1    ComM(ndir+nshr,ndir+nshr),Stiffness(ndir+nshr,ndir+nshr)
C
C     WOOD MATERIAL MODEL
```

```
C     Input material properties:
C     props(1): E11- parallel to grain modulus
C     PROPS(2): Perpendicular to grain modulus
C     PROPS(3): Longitudinal shear modulus
C     PROPS(4): G23- Rolling shear modulus
C     PROPS(5): ft0- parallel tension strength
C     PROPS(6): fc0- parallel compression strength
C     PROPS(7): ft90- perpendicular tension strength
C     PROPS(8): fc90- perpendicular compression strength
C     PROPS(9): fv- longitudinal shear strength
C     PROPS(10): froll- rolling shear strength
C     PROPS(11): Gf0- Parallel fracture energy
C     PROPS(12): Gf90- perpendicular fracture energy
C     PROPS(13): Gfv- shear fracture energy
C     PROPS(14): Gfroll- rolling fracture energy
C     PROPS(15): Nu- artificial viscosity. To deactivate stabilization, =0
C     PROPS(16): 1-2 Poisson ratio
C     PROPS(17): 1-3 Poisson ratio
C     PROPS(18): 2-3 Poisson ratio
C
C     State dependent vairables:
C   1 through 8:Kappa-force history
C   9 through 17: d- damage tracking/max. Order t0,c0,t90R,c90R,t90T, c90T, vR, vT, roll
C   18 through 20: Effective d- damage tracking/visualization. Order 0, 90R, 90T
C   21 through 29: Stabilized dv- stabilized damage control. Order as d
C   30: Deletion trigger
C   31-36: Strain
C   Initial Definitions
      PARAMETER (ZERO=0.0D0, ONE=1.0D0, TWO=2.0D0)
      E_11=props(1)
      E_perp=props(2)
      G=props(3)
      Groll=props(4)
      f_t0=props(5)
      f_c0=props(6)
      f_t90=props(7)
      f_c90=props(8)
      f_v=props(9)
      f_roll=props(10)
      G_f0=props(11)
      G_f90=props(12)
      G_fv=props(13)
      G_froll=props(14)
      viNU=props(15)
      PoiRatio_12=props(16)
      PoiRatio_13=props(17)
```

```
      PoiRatio_23=props(18)
      PoiRatio_21=E_perp/E_11*PoiRatio_12
      PoiRatio_31=E_perp/E_11*PoiRatio_13
      PoiRatio_32=PoiRatio_23
C
      CapDelta=ONE/(ONE-PoiRatio_12*PoiRatio_21-PoiRatio_13
     1     *PoiRatio_31-PoiRatio_23*PoiRatio_32-TWO*PoiRatio_13
     2     *PoiRatio_21*PoiRatio_32)
C
      DO km=1,nblock
        DO i=1,ndir+nshr
          ExpectedStrain(i)=stateOld(km,(30+i))+strainInc(km,i)
        ENDDO
      stateNew(km,31)=ExpectedStrain(1)
      stateNew(km,32)=ExpectedStrain(2)
      stateNew(km,33)=ExpectedStrain(3)
      stateNew(km,34)=ExpectedStrain(4)
      stateNew(km,35)=ExpectedStrain(5)
      stateNew(km,36)=ExpectedStrain(6)
      ExpectedStress(1)=ExpectedStrain(1)
     1     *(ONE-PoiRatio_23*PoiRatio_32)*CapDelta*E_11
     2     +ExpectedStrain(2)
     3     *(PoiRatio_21+PoiRatio_31*PoiRatio_23)*CapDelta*E_11
     4     +ExpectedStrain(3)
     5     *(PoiRatio_31+PoiRatio_21*PoiRatio_32)*CapDelta*E_11
      ExpectedStress(2)=ExpectedStrain(2)
     1     *(ONE-PoiRatio_13*PoiRatio_31)*CapDelta*E_perp
     2     +ExpectedStrain(1)
     3     *(PoiRatio_12+PoiRatio_13*PoiRatio_32)*CapDelta*E_perp
     4     +ExpectedStrain(3)
     5     *(PoiRatio_32+PoiRatio_31*PoiRatio_12)*CapDelta*E_perp
      ExpectedStress(3)=ExpectedStrain(3)
     1     *(ONE-PoiRatio_12*PoiRatio_21)*CapDelta*E_perp
     2     +ExpectedStrain(1)
     3     *(PoiRatio_13+PoiRatio_12*PoiRatio_23)*CapDelta*E_perp
     4     +ExpectedStrain(2)
     5     *(PoiRatio_23+PoiRatio_13*PoiRatio_21)*CapDelta*E_perp
      ExpectedStress(4)=ExpectedStrain(4)*2*G
      ExpectedStress(5)=ExpectedStrain(5)*2*Groll
      ExpectedStress(6)=ExpectedStrain(6)*2*G
C   FAILURE CRITERIA
C      Initializion
      Ft0=ZERO
      Fc0=ZERO
      Ft90R=ZERO
      Fc90R=ZERO
```

```
      FvR=ZERO
      Ft90T=ZERO
      Fc90T=ZERO
      FvT=ZERO
C     Calculation
      Ft0=ExpectedStress(1)/f_t0
      Fc0=-ExpectedStress(1)/f_c0
      Ft90R=ExpectedStress(4)**2/f_v**2
      IF (ExpectedStress(2).ge.ZERO) THEN
        Ft90R=Ft90R+ExpectedStress(2)**2/f_t90**2
      ENDIF
        Fc90R=-ExpectedStress(2)/f_c90
        FvR=ExpectedStress(4)**2/f_v**2
     1   +ExpectedStress(5)**2/f_roll**2
      Ft90T=ExpectedStress(6)**2/f_v**2
      IF (ExpectedStress(3).ge.ZERO) THEN
        Ft90T=Ft90T+ExpectedStress(3)**2/f_t90**2
      ENDIF
        Fc90T=-ExpectedStress(3)/f_c90
        FvT=ExpectedStress(6)**2/f_v**2
     1   +ExpectedStress(5)**2/f_roll**2
C     History Variables
      K_t0=max(ONE, stateOld(km,1), Ft0)
      K_c0=max(ONE, stateOld(km,2), Fc0)
      K_t90R=max(ONE, stateOld(km,3), Ft90R)
      K_c90R=max(ONE, stateOld(km,4), Fc90R)
      K_t90T=max(ONE, stateOld(km,5), Ft90T)
      K_c90T=max(ONE, stateOld(km,6), Fc90T)
      K_vR=max(ONE, stateOld(km,7), FvR)
      K_vT=max(ONE, stateOld(km,8), FvT)
C
      stateNew(km,1)=K_t0
      stateNew(km,2)=K_c0
      stateNew(km,3)=K_t90R
      stateNew(km,4)=K_c90R
      stateNew(km,5)=K_t90T
      stateNew(km,6)=K_c90T
      stateNew(km,7)=K_vR
      stateNew(km,8)=K_vT
C   DAMAGE VARIABLES
      d_t0=max(ZERO, (ONE-ONE/(f_t0**2-TWO*G_f0*E_11)*(f_t0**2-TWO
     1     *G_f0*E_11/K_t0)), stateOld(km,9))
      d_c0=max(ZERO,(ONE-ONE/K_c0), stateOld(km,10))
      d_t90R=max(ZERO, (ONE-ONE/(f_t90**2-TWO*G_f90*E_perp)*(f_t90**2
     1     -TWO*G_f90*E_perp/K_t90R)), stateOld(km,11))
      d_c90R=max(ZERO,(ONE-ONE/K_c90R), stateOld(km,12))
```

```
      d_t90T=max(ZERO, (ONE-ONE/(f_t90**2-TWO*G_f90*E_perp)*(f_t90**2
     1      -TWO*G_f90*E_perp/K_t90T)), stateOld(km,13))
      d_c90T=max(ZERO,(ONE-ONE/K_c90T), stateOld(km,14))
      d_vR1=max(ZERO, (ONE-ONE/(f_v**2-TWO*G_fv*G)*(f_v**2
     1      -TWO*G_fv*G/K_vR)), stateOld(km,15))
      d_vT1=max(ZERO, (ONE-ONE/(f_v**2-TWO*G_fv*G)*(f_v**2
     1      -TWO*G_fv*G/K_vT)), stateOld(km,16))
C     Imposed maximum value and storage
      d_t0=min(d_t0,0.9999995)
      d_c0=min(d_c0,0.9999995)
      d_t90R=min(d_t90R,0.9999995)
      d_c90R=min(d_c90R,0.9999995)
      d_t90T=min(d_t90T,0.9999995)
      d_c90T=min(d_c90T,0.9999995)
      d_vR1=min(d_vR1,0.9999995)
      d_vT1=min(d_vT1,0.9999995)
      stateNew(km,9)=d_t0
      stateNew(km,10)=d_c0
      stateNew(km,11)=d_t90R
      stateNew(km,12)=d_c90R
      stateNew(km,13)=d_t90T
      stateNew(km,14)=d_c90T
      stateNew(km,15)=d_vR1
      stateNew(km,16)=d_vT1
C     Composite variables, with maximums built in
      d_vR=min((ONE-(ONE-d_t90R)*(ONE-d_vR1)), 0.9999995)
      d_vT=min((ONE-(ONE-d_t90T)*(ONE-d_vT1)),0.9999995)
      d_roll=max(ZERO, (ONE-(ONE-d_t90R)*(ONE-d_vR1)*(ONE-d_t90T)
     1      *(ONE-d_vT1)), stateOld(km,17))
      d_roll=min(d_roll,0.9999995)
      stateNew(km,17)=d_roll
C     Assignment of active axial damage variables
      IF (ExpectedStress(1).ge.ZERO) THEN
        d_0=d_t0
      ELSEIF (ExpectedStress(1).lt.ZERO) THEN
        d_0=d_c0
      ENDIF
      IF (ExpectedStress(2).ge.ZERO) THEN
        d_90R=d_t90R
      ELSEIF (ExpectedStress(2).lt.ZERO) THEN
        d_90R=d_c90R
      ENDIF
      IF (ExpectedStress(3).ge.ZERO) THEN
        d_90T=d_t90T
      ELSEIF (ExpectedStress(3).lt.ZERO) THEN
        d_90T=d_c90T
```

```
      ENDIF
C   VISCOUS STABILIZATION
      IF (viNU.ne.ZERO) THEN
        dv_t0=max(ZERO,stateOld(km,21),viNU/(dt+viNU)*stateOld(km,21)
     1          +dt/(dt+viNU)*d_t0)
        dv_c0=max(ZERO,stateOld(km,22),viNU/(dt+viNU)*stateOld(km,22)
     1          +dt/(dt+viNU)*d_c0)
       dv_t90R=max(ZERO,stateOld(km,23),viNU/(dt+viNU)*stateOld(km,23)
     1          +dt/(dt+viNU)*d_t90R)
       dv_c90R=max(ZERO,stateOld(km,24),viNU/(dt+viNU)*stateOld(km,24)
     1          +dt/(dt+viNU)*d_c90R)
       dv_t90T=max(ZERO,stateOld(km,25),viNU/(dt+viNU)*stateOld(km,25)
     1          +dt/(dt+viNU)*d_t90T)
       dv_c90T=max(ZERO,stateOld(km,26),viNU/(dt+viNU)*stateOld(km,26)
     1          +dt/(dt+viNU)*d_c90T)
        dv_vR1=max(ZERO,stateOld(km,27),viNU/(dt+viNU)*stateOld(km,27)
     1          +dt/(dt+viNU)*d_vR1)
        dv_vT1=max(ZERO,stateOld(km,28),viNU/(dt+viNU)*stateOld(km,28)
     1          +dt/(dt+viNU)*d_vT1)
        dv_roll=max(ZERO, (ONE-(ONE-dv_t90R)*(ONE-dv_vR1)*(ONE-
     1      dv_t90T)*(ONE-dv_vT1)), stateOld(km,29))
        dv_roll=min(dv_roll,0.9999995)
C
         stateNew(km,21)=dv_t0
         stateNew(km,22)=dv_c0
         stateNew(km,23)=dv_t90R
         stateNew(km,24)=dv_c90R
         stateNew(km,25)=dv_t90T
         stateNew(km,26)=dv_c90T
         stateNew(km,27)=dv_vR1
         stateNew(km,28)=dv_vT1
         stateNew(km,29)=dv_roll
C
         dv_vR=min((ONE-(ONE-dv_t90R)*(ONE-dv_vR1)), 0.9999995)
         dv_vT=min((ONE-(ONE-dv_t90T)*(ONE-dv_vT1)),0.9999995)
C
         IF (ExpectedStress(1).ge.ZERO) THEN
           dv_0=dv_t0
         ELSEIF (ExpectedStress(1).lt.ZERO) THEN
           dv_0=dv_c0
         ENDIF
         IF (ExpectedStress(2).ge.ZERO) THEN
           dv_90R=dv_t90R
         ELSEIF (ExpectedStress(2).lt.ZERO) THEN
           dv_90R=dv_c90R
         ENDIF
```

```
          IF (ExpectedStress(3).ge.ZERO) THEN
             dv_90T=dv_t90T
          ELSEIF (ExpectedStress(3).lt.ZERO) THEN
             dv_90T=dv_c90T
          ENDIF
C      Reassignment of damage variables
          d_0=dv_0
          d_90R=dv_90R
          d_90T=dv_90T
          d_vR=dv_vR
          d_vT=dv_vT
          d_roll=dv_roll
       ENDIF
C   Store Combined Axial Damage
       stateNew(km,18)=d_0
       stateNew(km,19)=d_90R
       stateNew(km,20)=d_90T
C   Compliance Matrix 3x3 Construction
       ComM(1,1)=ONE/(ONE-d_0)/E_11
       ComM(1,2)=-PoiRatio_21/E_perp
       ComM(1,3)=-PoiRatio_31/E_perp
       ComM(2,1)=-PoiRatio_12/E_11
       ComM(2,2)=ONE/(ONE-d_90R)/E_perp
       ComM(2,3)=-PoiRatio_32/E_perp
       ComM(3,1)=-PoiRatio_13/E_11
       ComM(3,2)=-PoiRatio_23/E_perp
       ComM(3,3)=ONE/(ONE-d_90T)/E_perp
C   Initialize 0's in Stiffness Matrix
       DO i=1,ndir+nshr
          DO j=1,ndir+nshr
             Stiffness(i,j)=ZERO
          END DO
       ENDDO
C   Determinate of 3x3 for Stiffness Matrix
       detinv =ONE/(ComM(1,1)*ComM(2,2)*ComM(3,3)-ComM(1,1)
     1    *ComM(2,3)*ComM(3,2)-ComM(1,2)*ComM(2,1)*ComM(3,3)
     2    +ComM(1,2)*ComM(2,3)*ComM(3,1)+ComM(1,3)*ComM(2,1)
     3    *ComM(3,2)-ComM(1,3)*ComM(2,2)*ComM(3,1))
C   Calculate the inverse of the matrix, and the decoupled shear terms
      Stiffness(1,1) =detinv*(ComM(2,2)*ComM(3,3)-ComM(2,3)*ComM(3,2))
      Stiffness(2,1) =-detinv*(ComM(2,1)*ComM(3,3)-ComM(2,3)*ComM(3,1))
      Stiffness(3,1) =detinv*(ComM(2,1)*ComM(3,2)-ComM(2,2)*ComM(3,1))
      Stiffness(1,2) =-detinv*(ComM(1,2)*ComM(3,3)-ComM(1,3)*ComM(3,2))
      Stiffness(2,2) =detinv*(ComM(1,1)*ComM(3,3)-ComM(1,3)*ComM(3,1))
      Stiffness(3,2) =-detinv*(ComM(1,1)*ComM(3,2)-ComM(1,2)*ComM(3,1))
      Stiffness(1,3) =detinv*(ComM(1,2)*ComM(2,3)-ComM(1,3)*ComM(2,2))
```

```
      Stiffness(2,3) =-detinv*(ComM(1,1)*ComM(2,3)-ComM(1,3)*ComM(2,1))
      Stiffness(3,3) =detinv*(ComM(1,1)*ComM(2,2)-ComM(1,2)*ComM(2,1))
      Stiffness(4,4) =(ONE-d_vR)*2*G
      Stiffness(5,5) =(ONE-d_roll)*2*Groll
      Stiffness(6,6) =(ONE-d_vT)*2*G
C Deletion check, with compression disabled
       Deletion=1
       IF (d_0.ge.(0.999995).AND.ExpectedStress(1).ge.ZERO) THEN
          Deletion=0
       ELSEIF (d_90R.ge.(0.999995).AND.ExpectedStress(2).ge.ZERO) THEN
          Deletion=0
       ELSEIF (d_90T.ge.(0.999995).AND.ExpectedStress(3).ge.ZERO) THEN
          Deletion=0
       ELSEIF (d_vR.ge.(0.9999995)) THEN
          Deletion=0
       ELSEIF (d_vT.ge.(0.9999995)) THEN
          Deletion=0
       ELSEIF (d_roll.ge.(0.9999995)) THEN
          Deletion=0
       ENDIF
       stateNew(km,30)=Deletion
C   Update Stress
       stressNew(km,1)=Stiffness(1,1)*ExpectedStrain(1)+Stiffness(1,2)*
     1      ExpectedStrain(2)+Stiffness(1,3)*ExpectedStrain(3)
       stressNew(km,2)=Stiffness(2,1)*ExpectedStrain(1)+Stiffness(2,2)*
     1      ExpectedStrain(2)+Stiffness(2,3)*ExpectedStrain(3)
       stressNew(km,3)=Stiffness(3,1)*ExpectedStrain(1)+Stiffness(3,2)*
     1      ExpectedStrain(2)+Stiffness(3,3)*ExpectedStrain(3)
       stressNew(km,4)=Stiffness(4,4)*ExpectedStrain(4)
       stressNew(km,5)=Stiffness(5,5)*ExpectedStrain(5)
       stressNew(km,6)=Stiffness(6,6)*ExpectedStrain(6)
     ENDDO
     RETURN
     END
```

APPENDIX F: FINITE ELEMENT ANALYSIS RESULTS

F.1 Model GL1.1

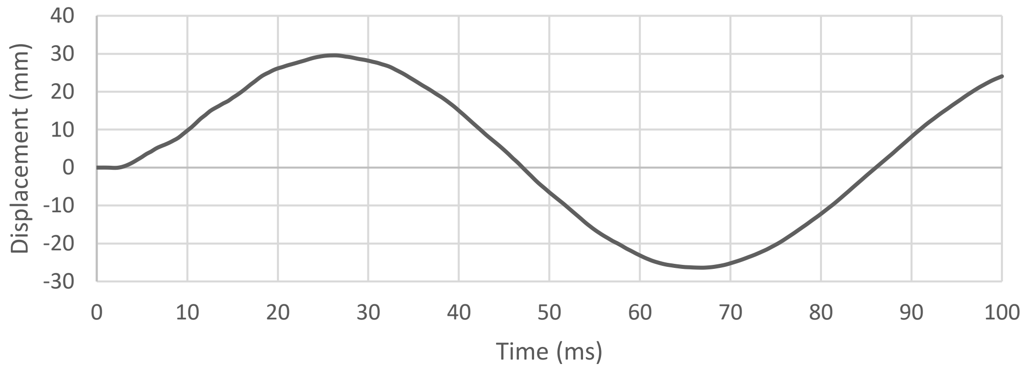

Figure F.1: Displacement results for finite element model GL1.1

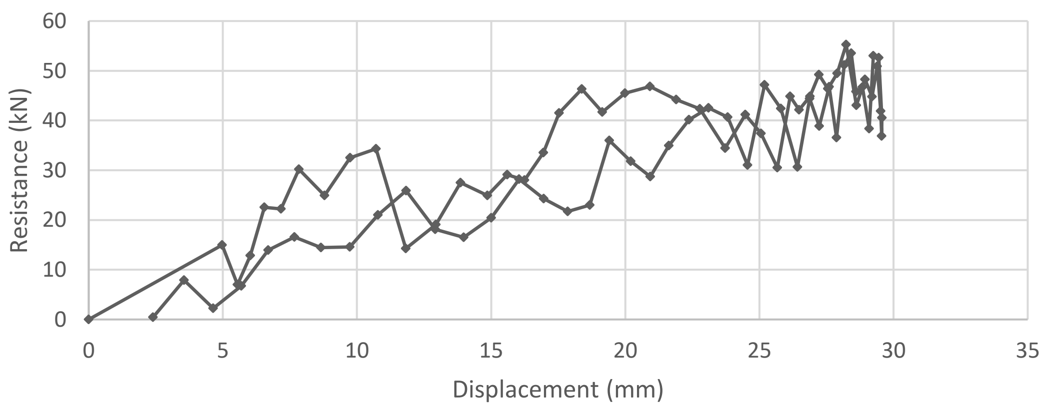

Figure F.2: Analytical resistance curve for GL1.1

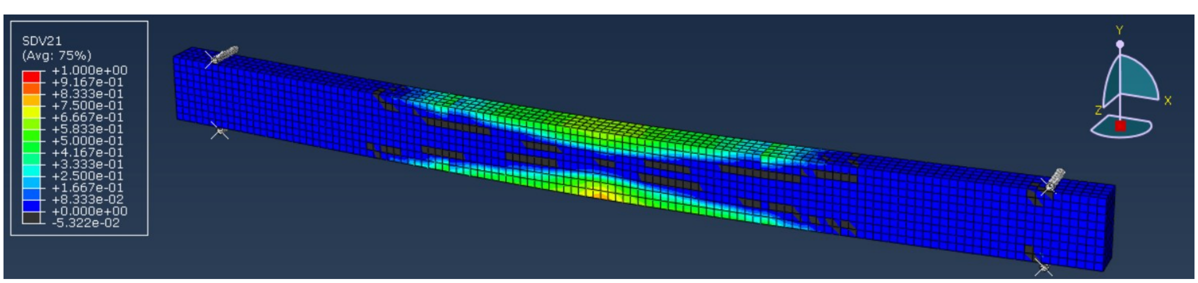

Figure F.3: End state of model GL1.1, tension parallel to grain displayed

F.2 Model GL2.1

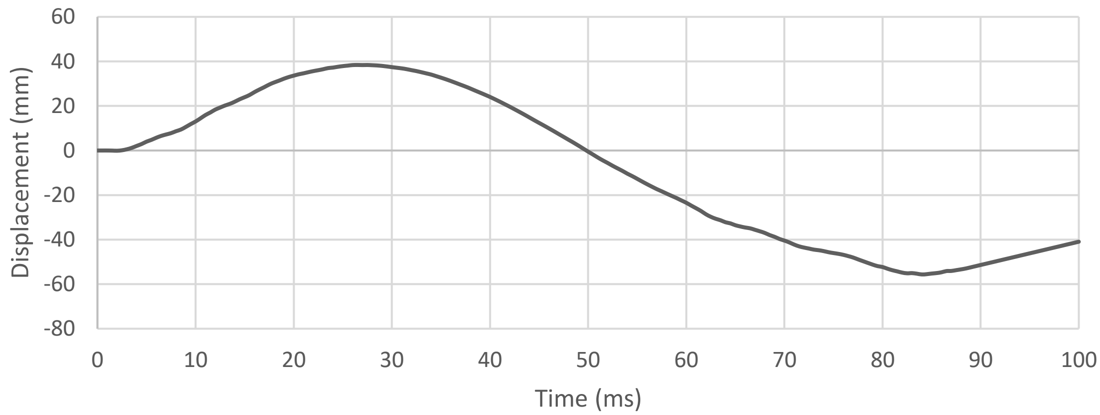

Figure F.4: Displacement results for finite element model GL2.1

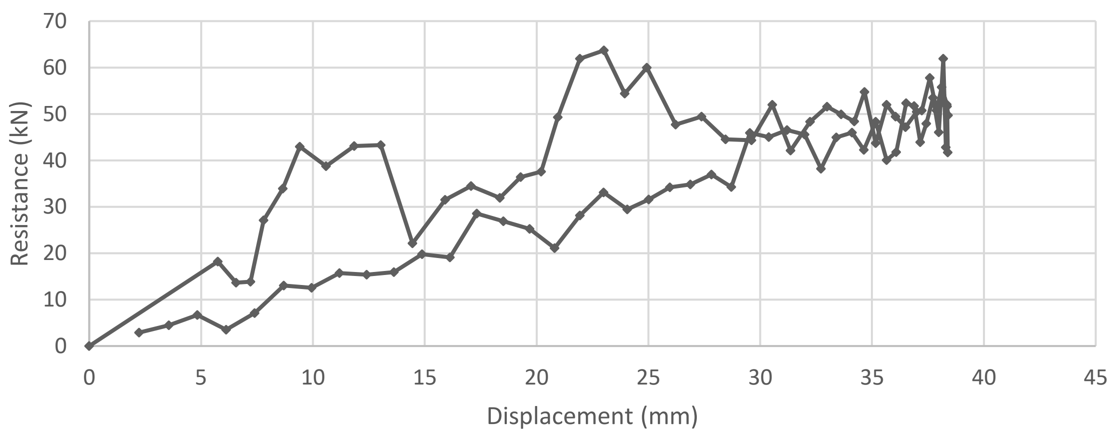

Figure F.5: Analytical resistance curve for GL2.1

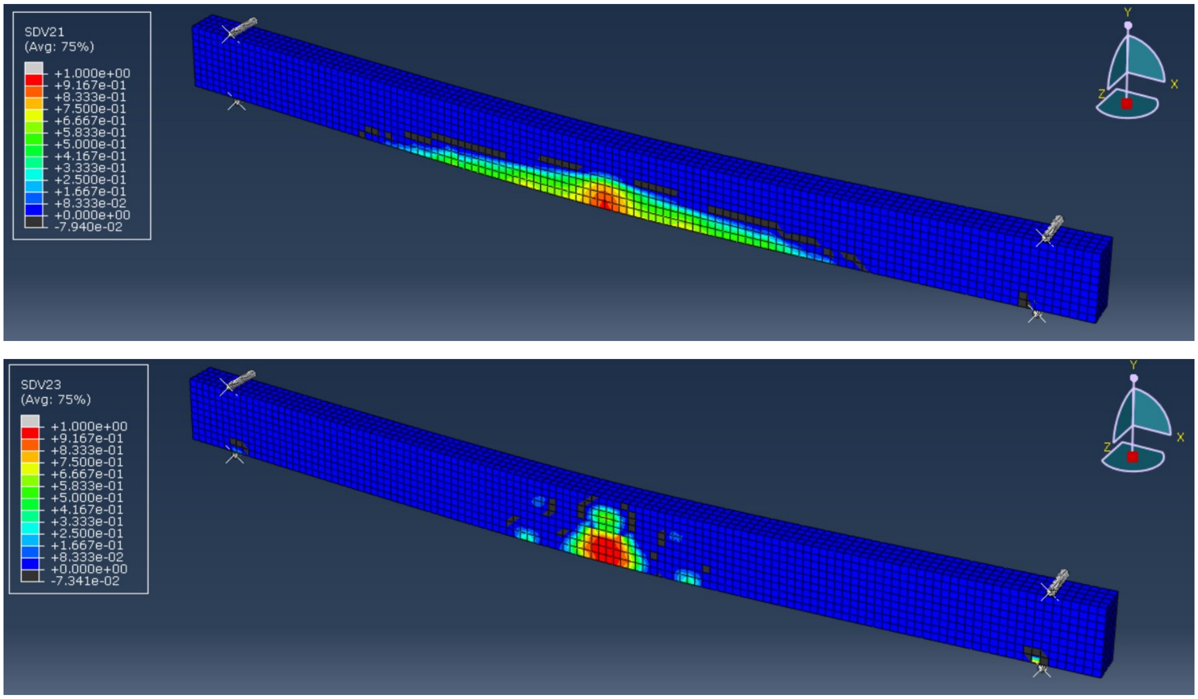

Figure F.6: Total damage for model GL2.1: a) Tension parallel to grain b) Tension perpendicular to grain (Global Y)

F.3 Model GL2.2

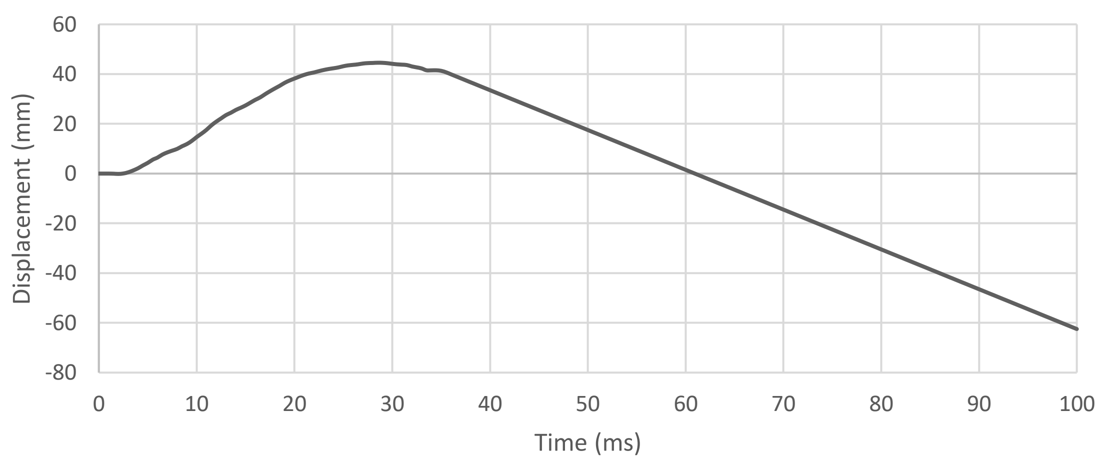

Figure F.7: Displacement results for finite element model GL2.2

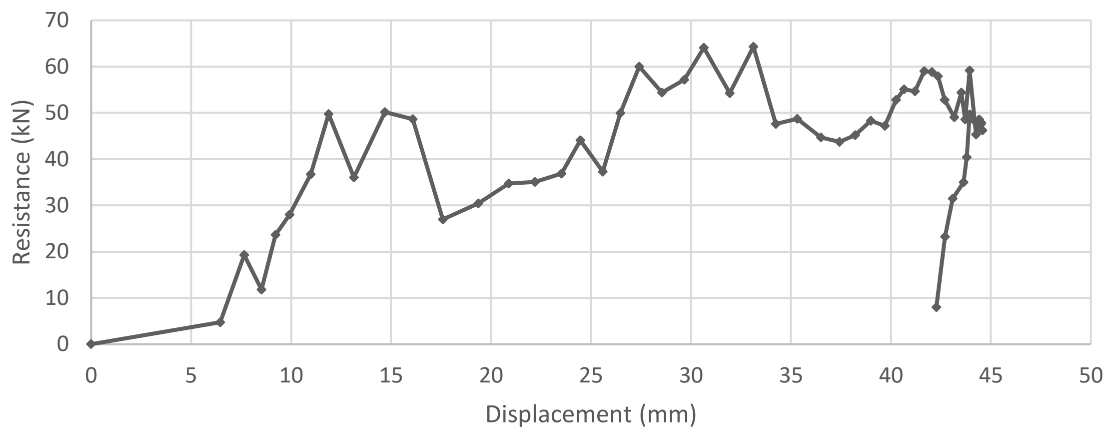

Figure F.8: Analytical resistance curve for GL2.2

a)

b)

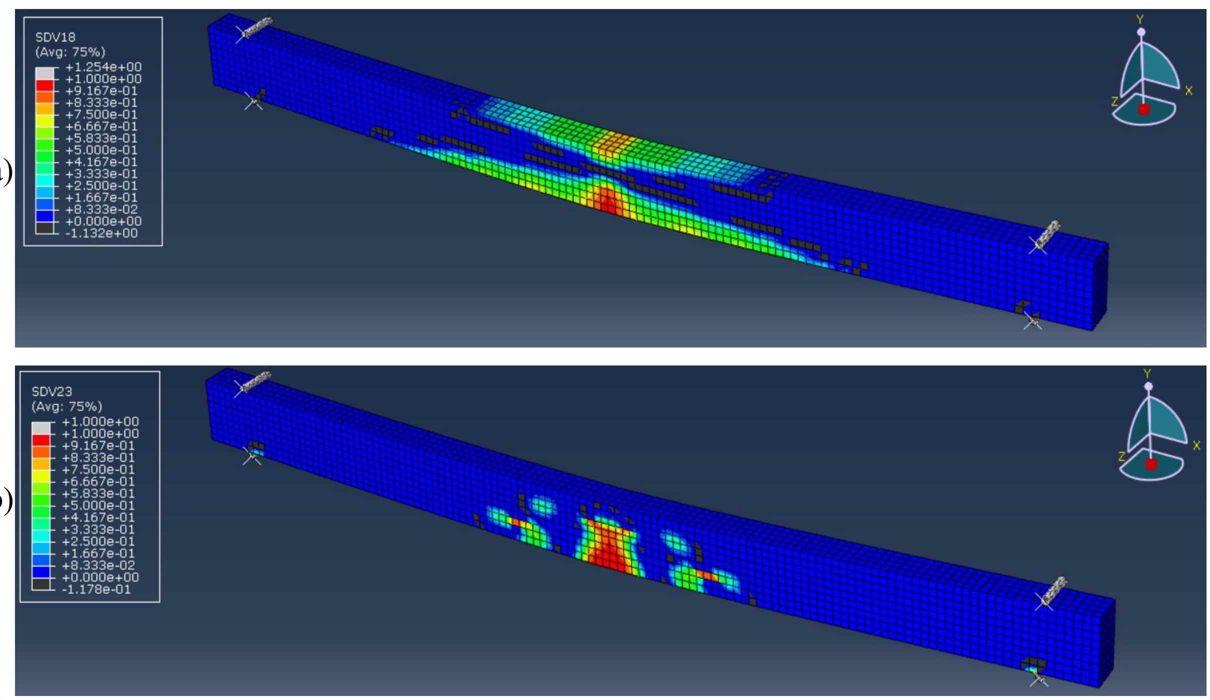

Figure F.9: Damage immediately before deletion in model GL2.2: a) Combined damage parallel to grain b) Tensile damage perpendicular to grain (Global Y)

a)

b)

c)

d)

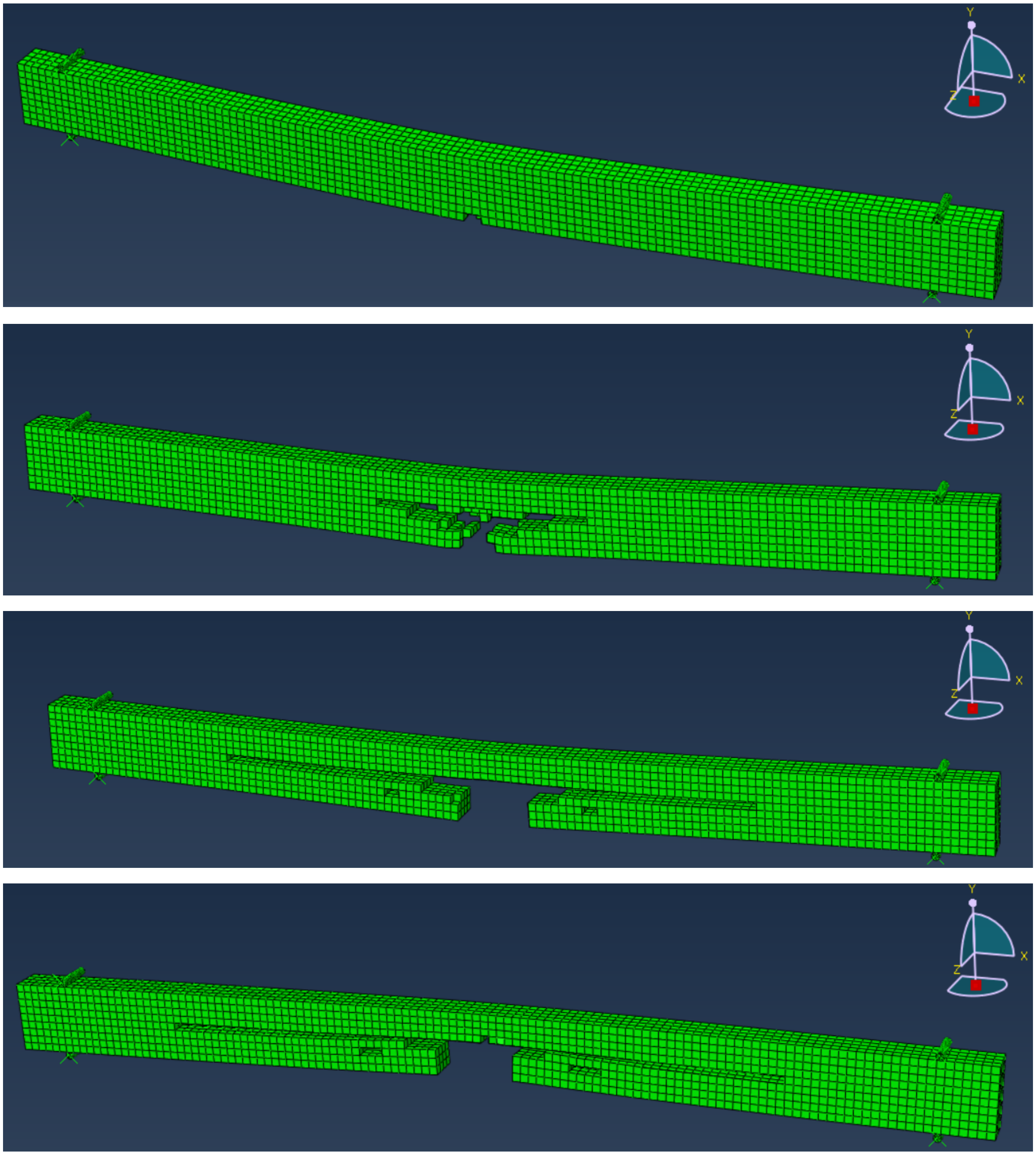

Figure F.10: Failure progression in model GL2.2: a) Initial deletion b) Central point deletion c) End of deletion towards supports d) Final state

F.4 Model GL3.1

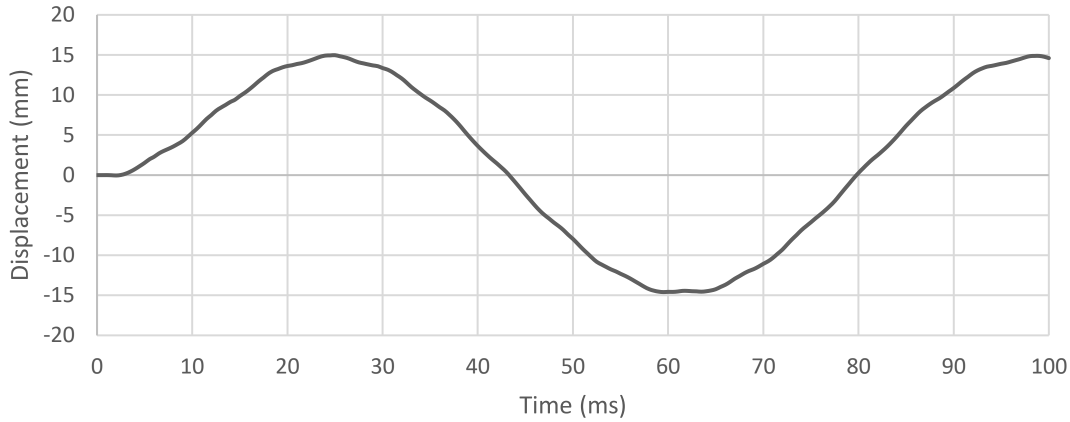

Figure F.11: Displacement results for finite element model GL3.1

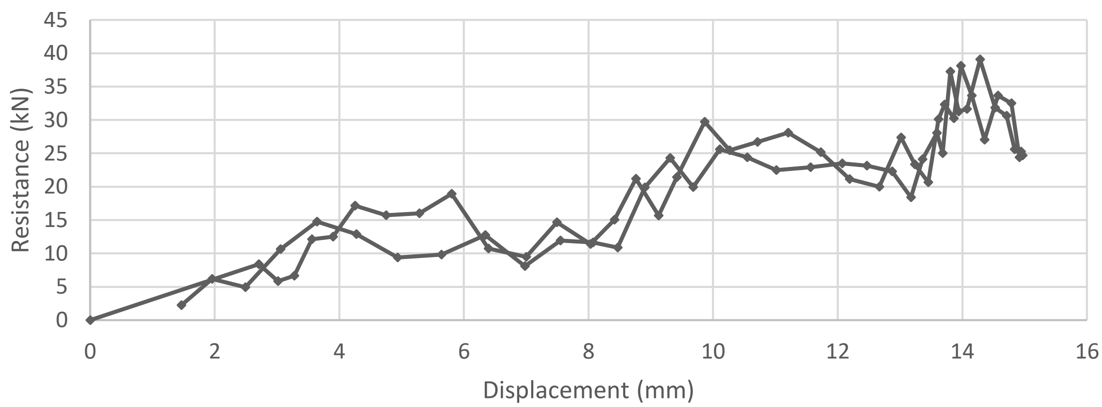

Figure F.12: Analytical resistance curve for GL3.1

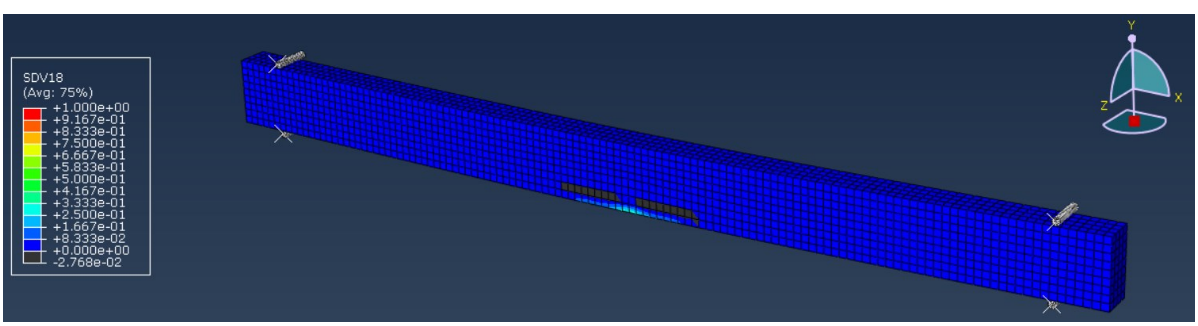

Figure F.13: Final state of model GL3.1, displaying tensile damage parallel to grain

F.5 Model GL3.2

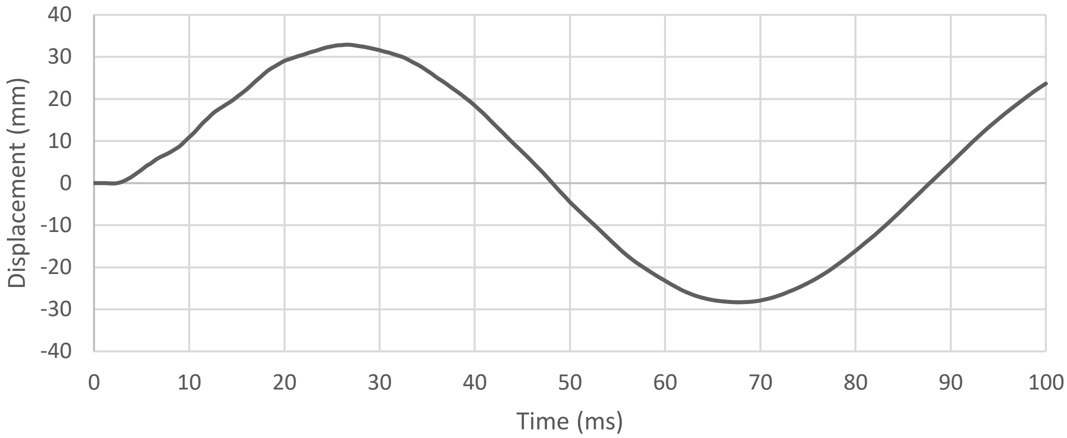

Figure F.14: Displacement result for finite element model GL3.2

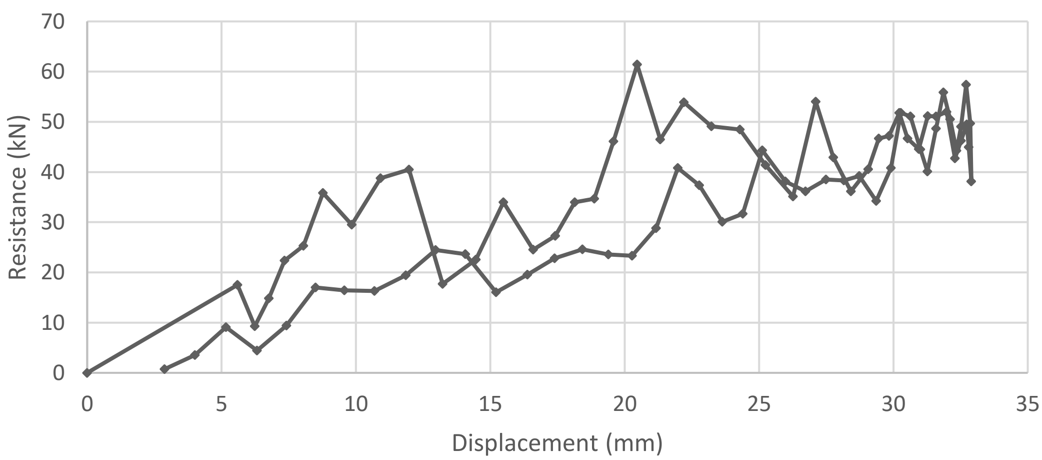

Figure F.15: Analytical resistance curve for GL3.2

a)

b)

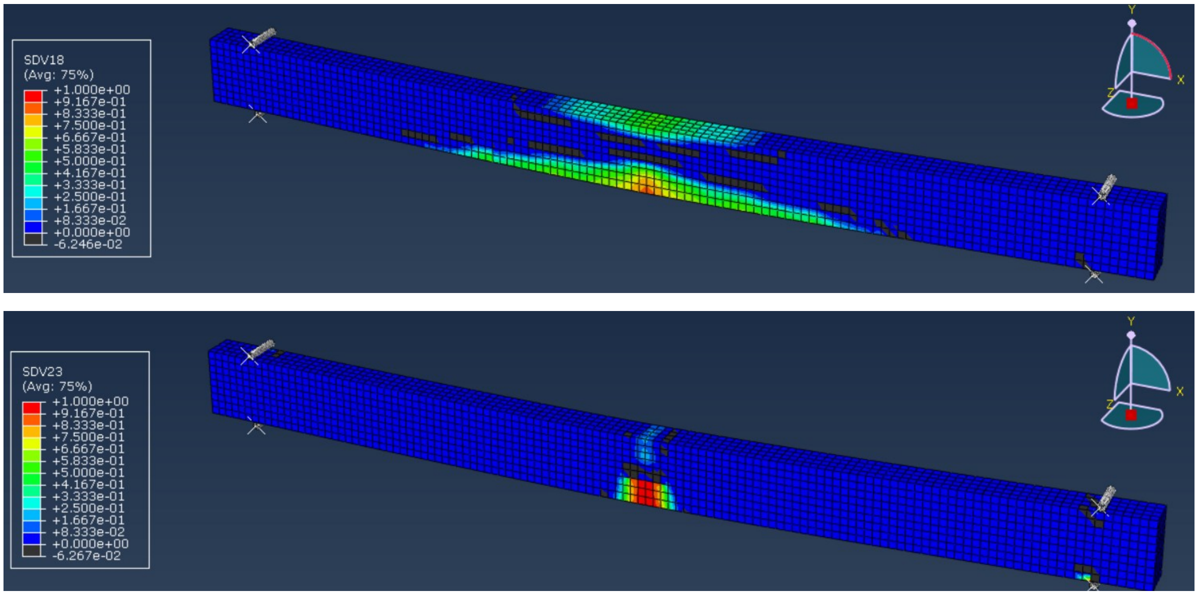

Figure F.16: Final state of model GL2.2, displaying: a) Combined damage parallel to grain b) Tensile damage perpendicular to grain (Global Y)

F.6 Model GL3.3

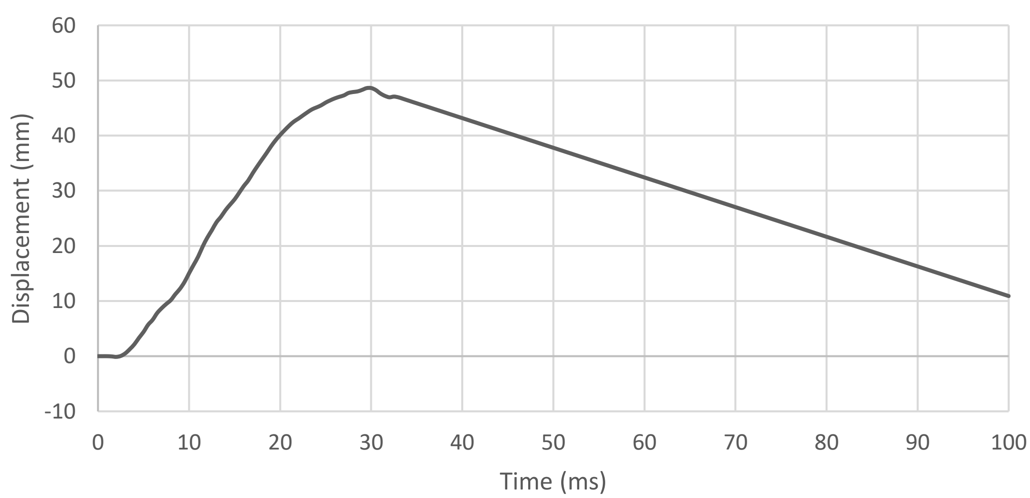

Figure F.17: Displacement result for finite element model GL3.3

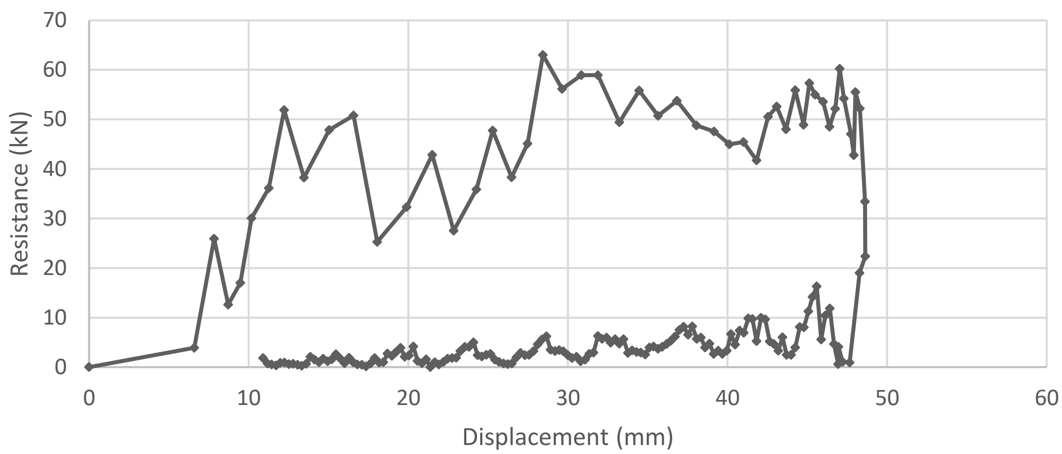

Figure F.18: Analytical resistance curve for GL3.3

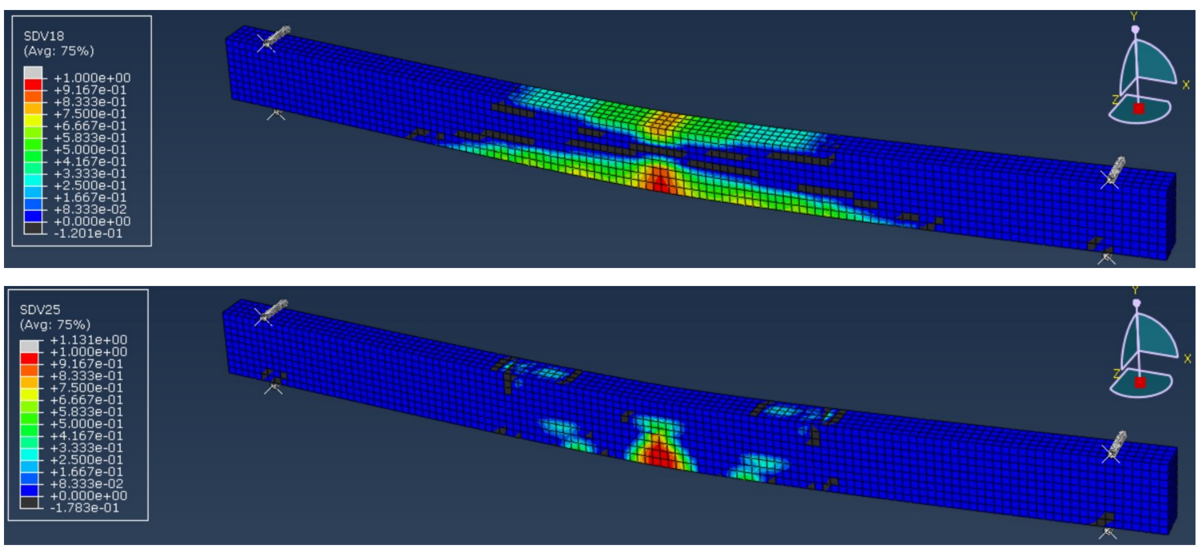

Figure F.19: Damage immediately before deletion in model GL3.3: a) Combined damage parallel to grain b) Tensile damage perpendicular to grain (Global Z)

a)
b)
c)
d)

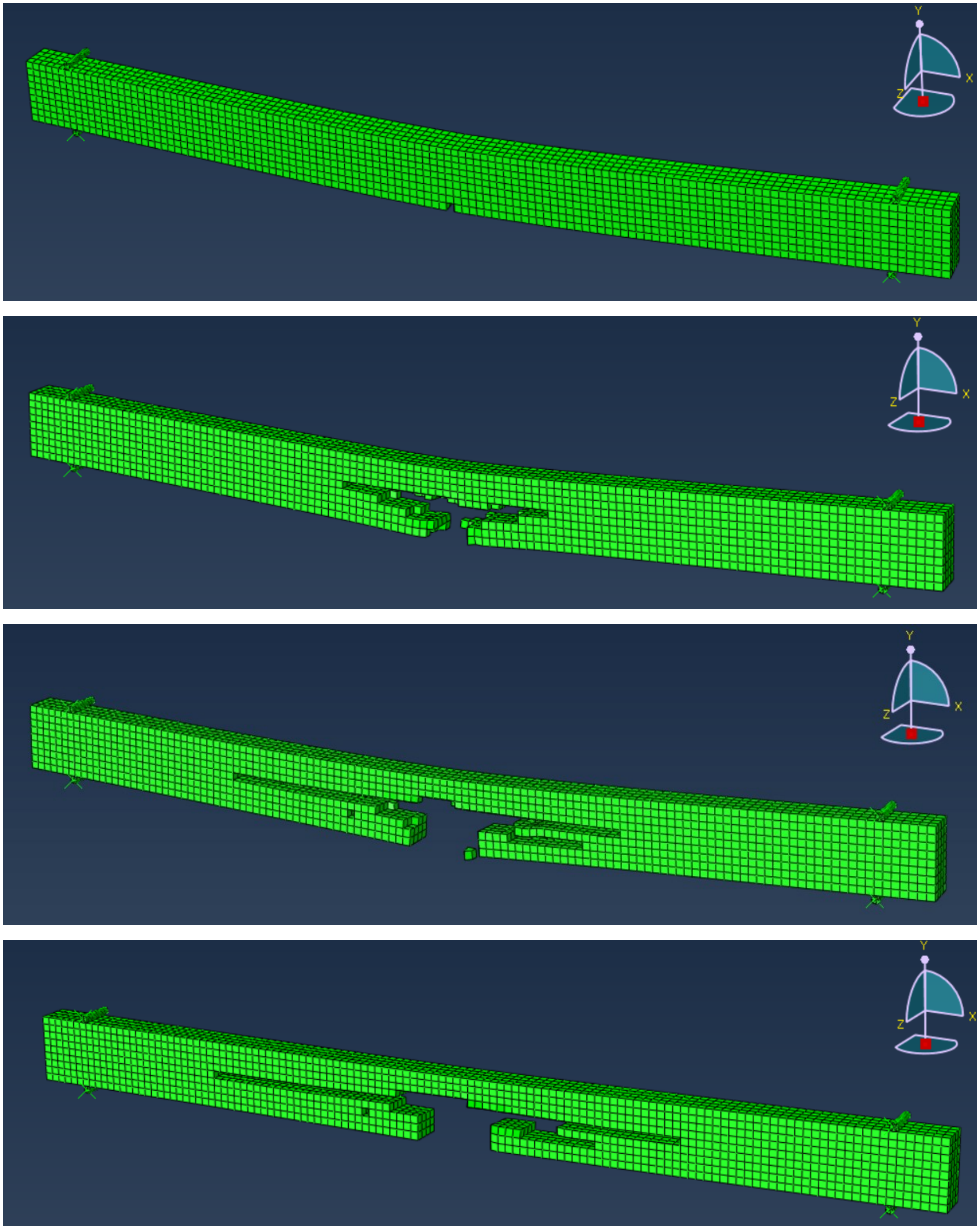

Figure F.20: Failure progression in model GL2.2: a) Initial deletion b) Central point deletion c) Spread of deletion towards supports d) Final state

F.7 Model CLT1.1

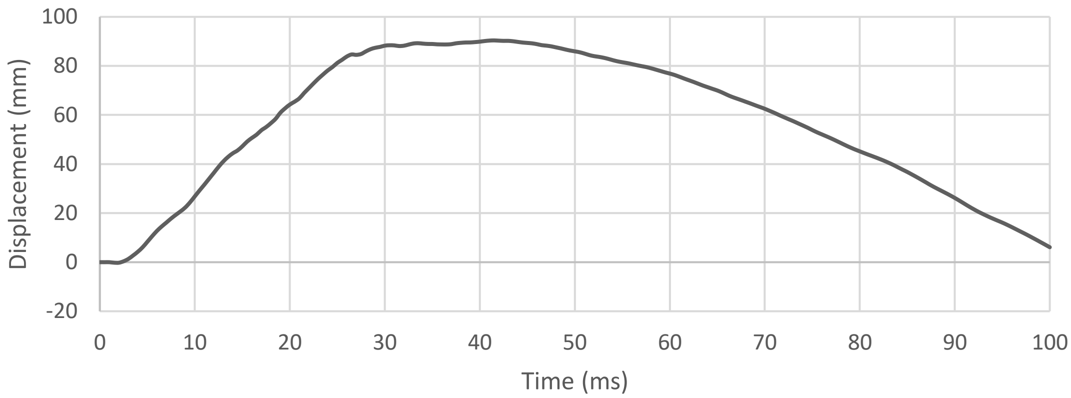

Figure F.21: Displacement results for finite element model of CLT1.1

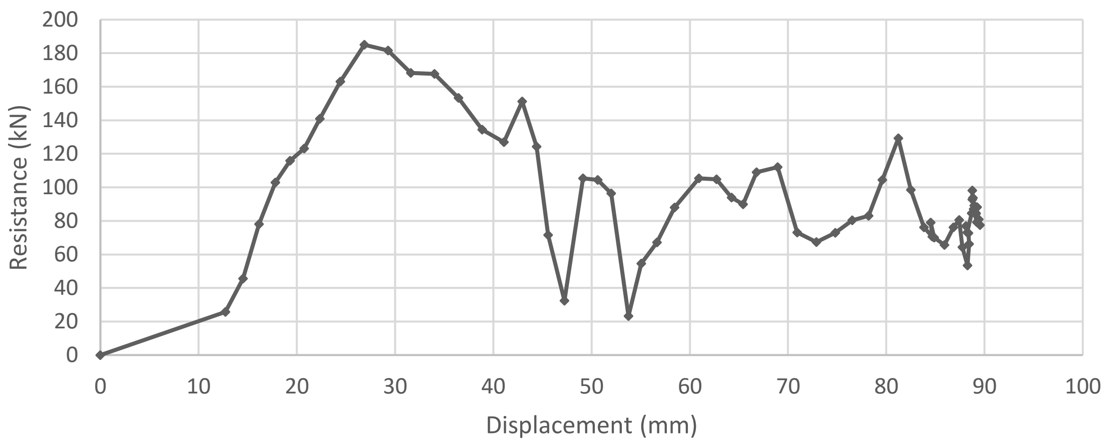

Figure F.22: Analytical resistance curve for CLT1.1

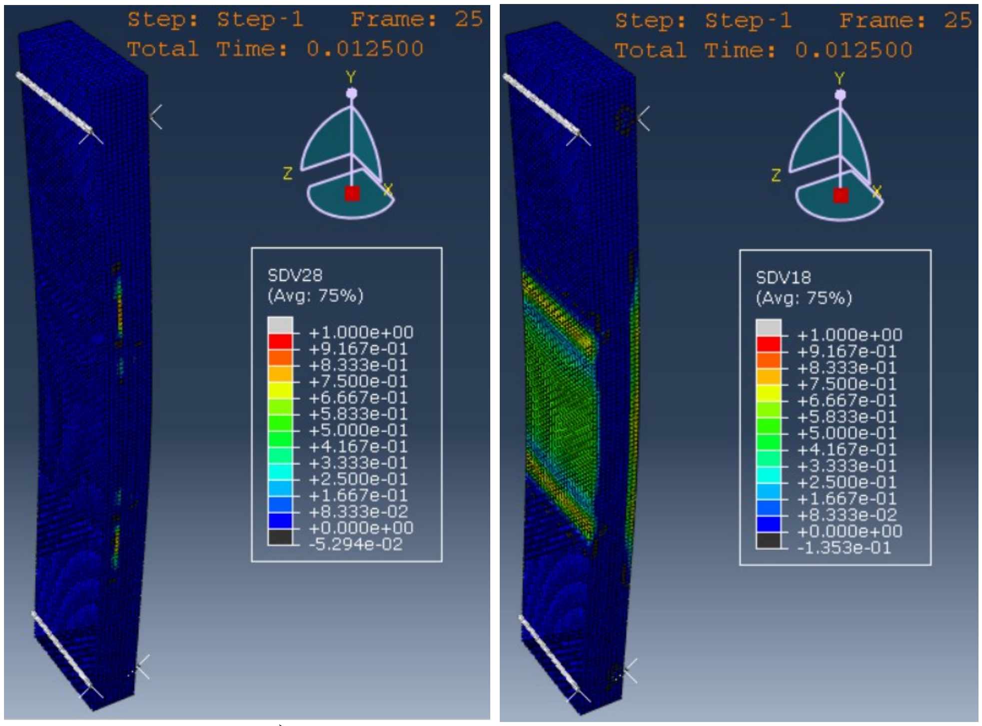

a) b)

Figure F.23: a) Initiation of rolling shear damage in model CLT1.1 b) Combined damage parallel to grain

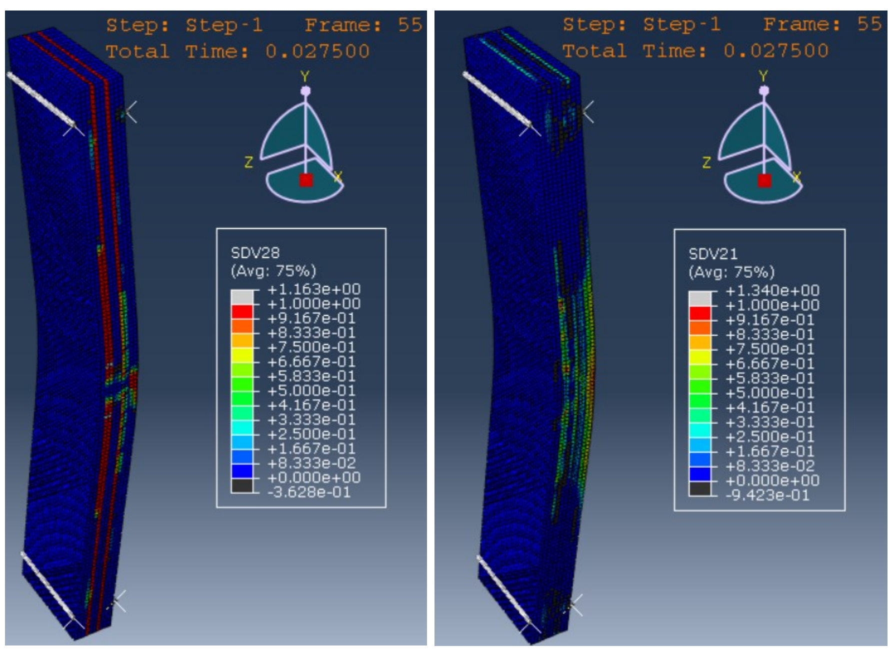

a) b)

Figure F.24: State of model CLT1.1 immediately before deletion a) Shear damage b) Tensile damage parallel to grain

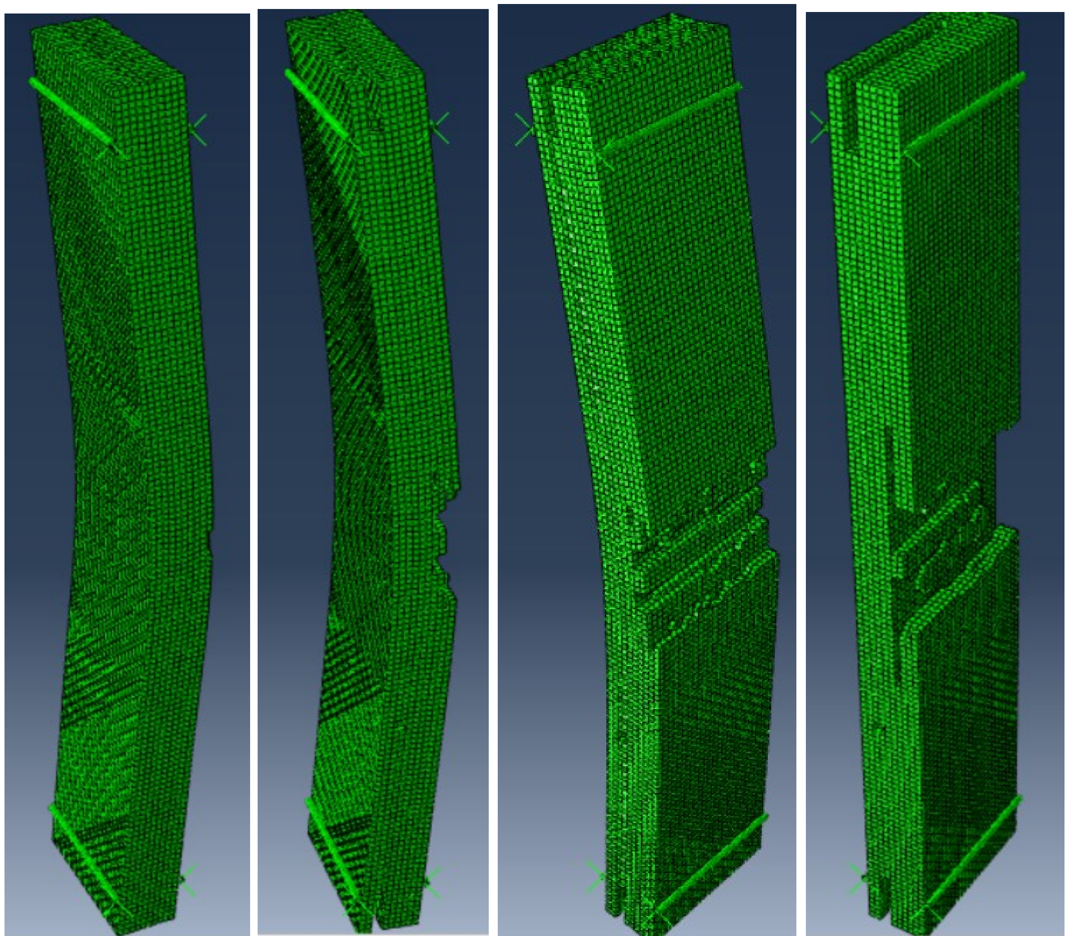

a) b) c) d)

Figure F.26: Failure progression in model CLT1.1: a) Initial deletion b) Propagation of failure into the 4th ply c) Rear view of failure propagation d) Final state of model

F.8 Model CLT2.1

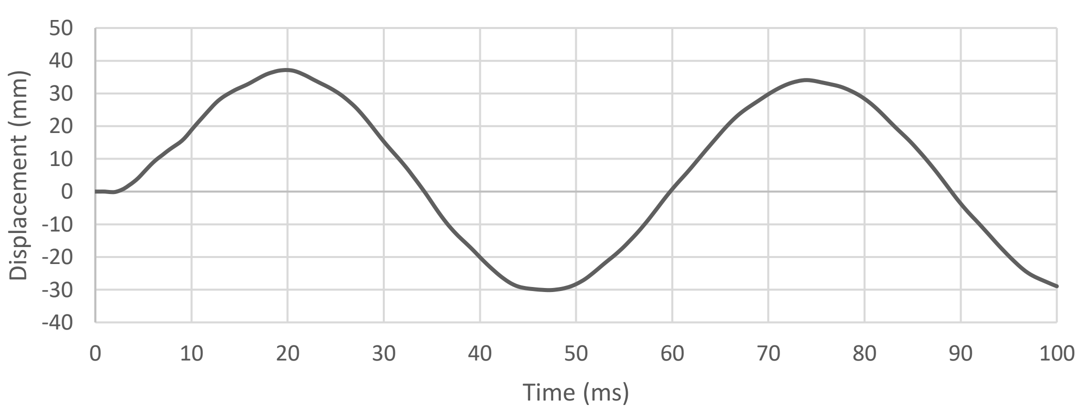

Figure F.27: Displacement results for finite element model CLT2.1

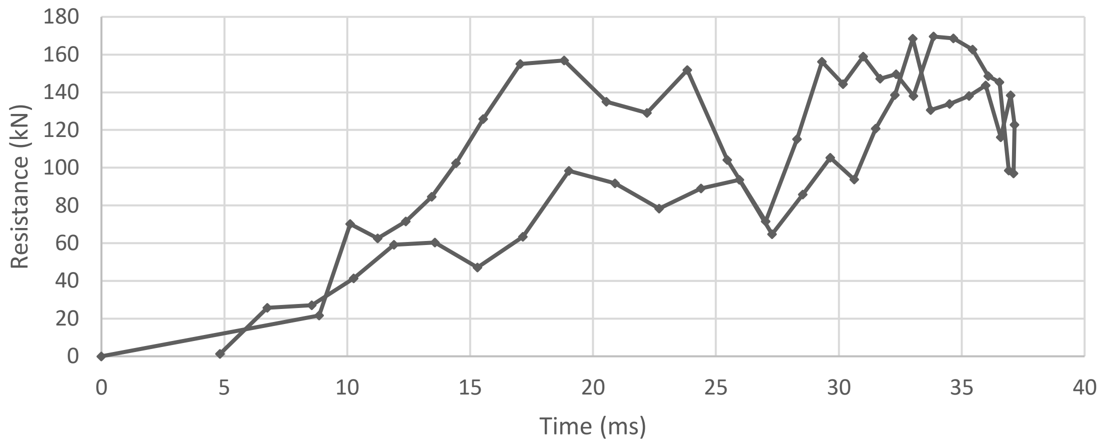

Figure F.28: Analytical resistance curve for CLT2.1

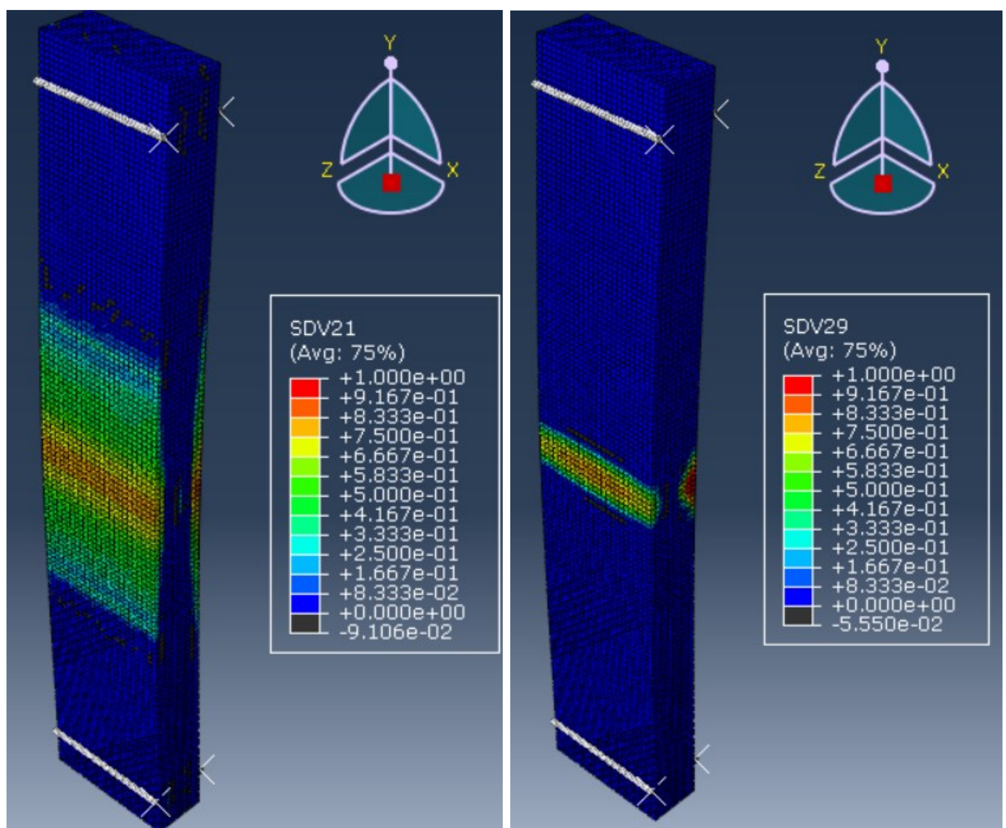

a) b)

Figure F.29: Final state of model CLT2.1: a) Tensile damage parallel to grain b) Rolling shear damage (caused by stress redistribution)

F.9 Model CLT3.1

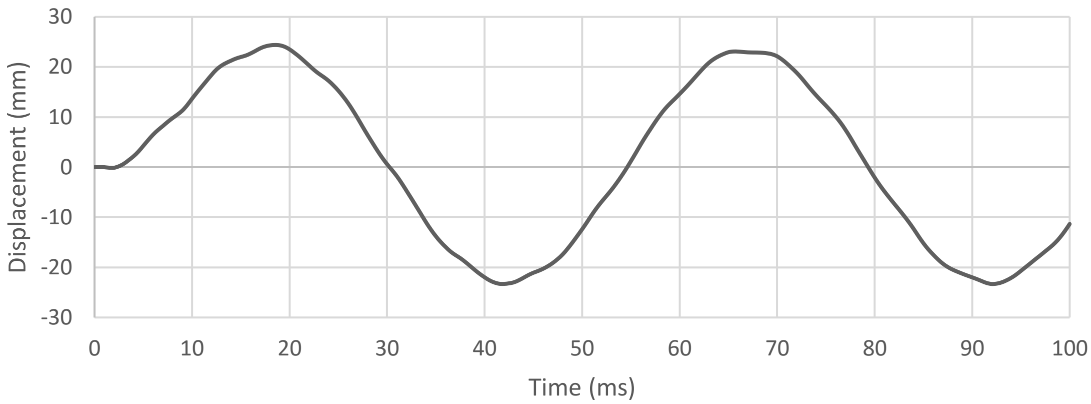

Figure F.30: Displacement results for finite element model CLT3.1

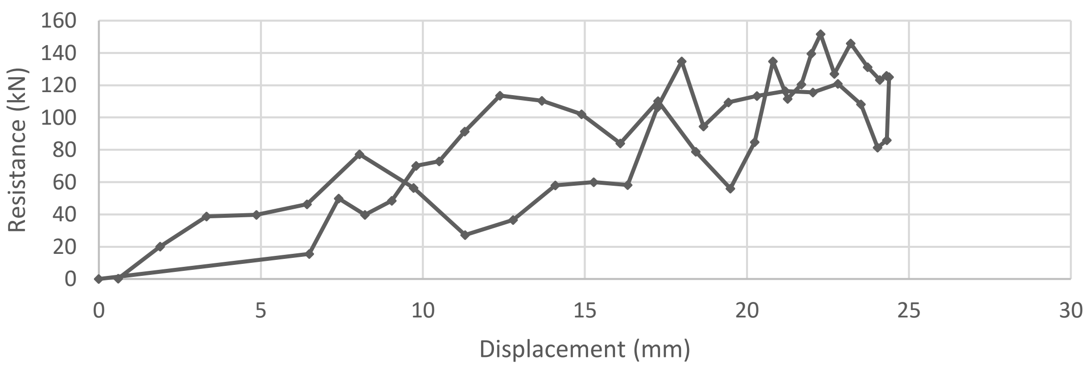

Figure F.31: Analytical resistance curve for CLT3.1

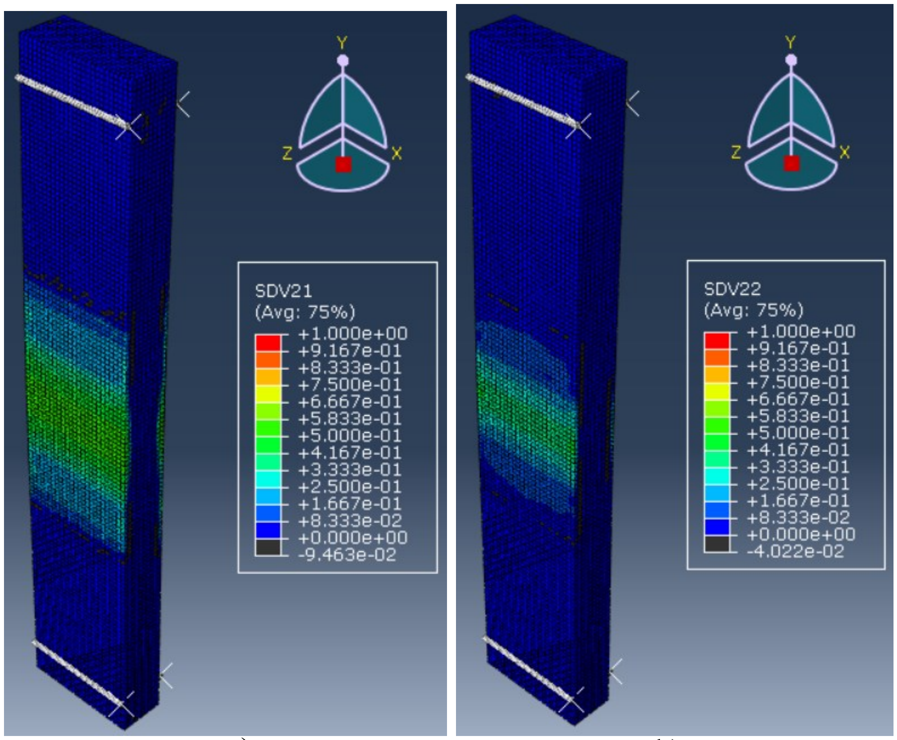

a) b)

Figure F.32: Final state of model CLT3.1: a) Tensile damage parallel to grain b) Compressive damage parallel to grain

F.10 Mesh Size Comparison

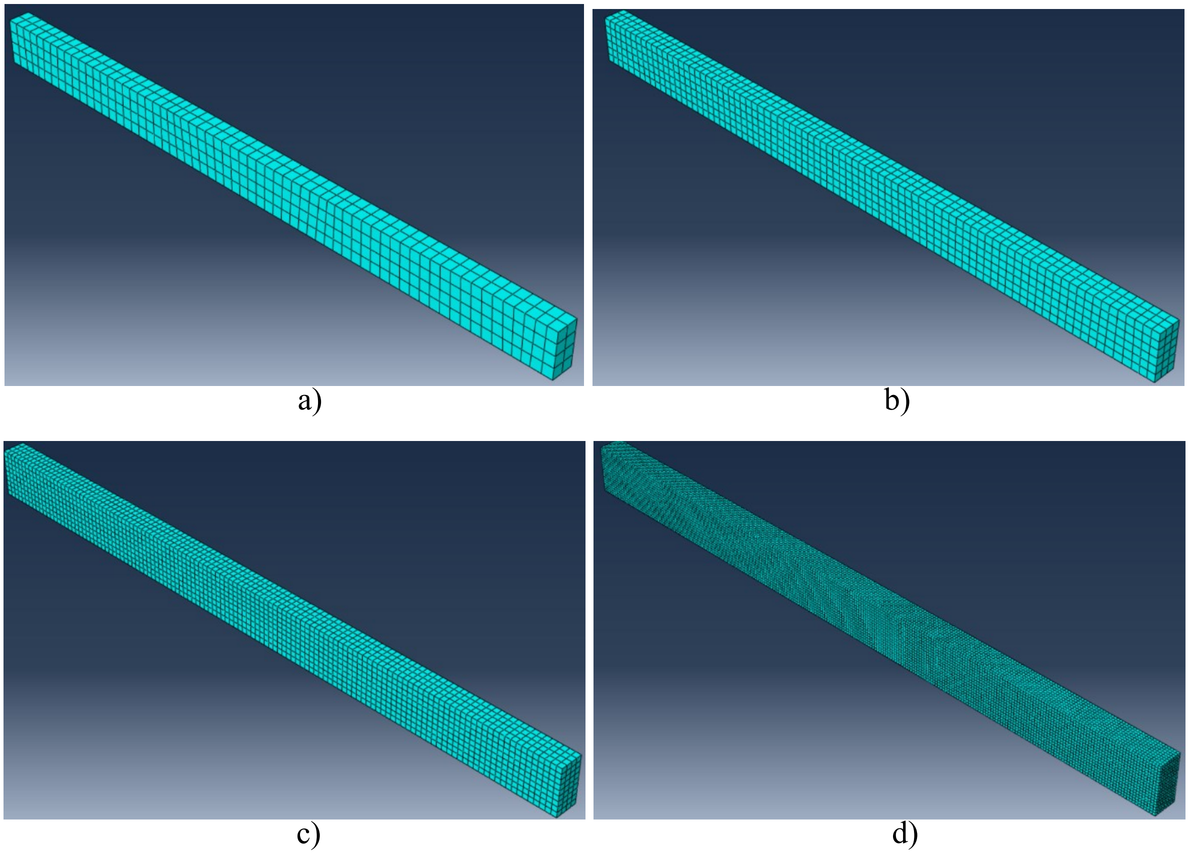

a) b) c) d)

Figure F.33: Investigated mesh sizes for glulam: a) 40 mm b) 30 mm c) 20 mm d) 10 mm

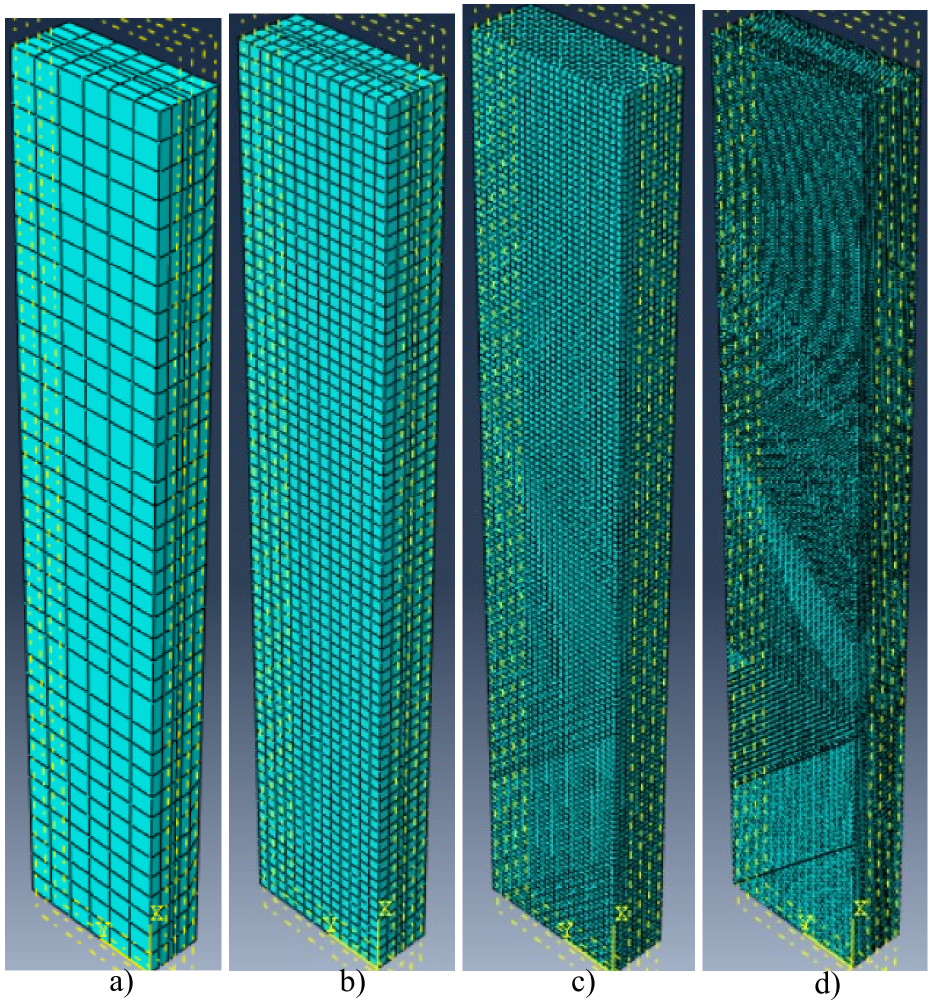

Figure F.34: Investigated mesh sizes for CLT: a) 75 mm b) 35 mm c) 17.5 mm d) 9 mm